Advanced Numerical Analysis of Tunnel Behaviour in Structured Clayey Soils under Seismic Loading

Lowell Tan Cabangon

BS Civil Engineering

MSc International Construction Management & Engineering

MAS Tunnelling

A thesis submitted for the degree of Doctor of Philosophy in the

School of Civil Engineering and Geosciences

Newcastle University

Newcastle upon Tyne

NE1 7RU

April 2019

Abstract

Tunnels are crucial components of transportation networks and considered as "lifeline" utilities as their continued operation is of vital importance during and in the immediate aftermath of an earthquake. It is, therefore, imperative to assess the engineering performance of such important geotechnical structures to ensure their resilience during and after seismic events. To achieve an accurate prediction of the tunnel behaviour during earthquake, a better approach should be implemented that can capture the multi-directional propagation of the seismic waves and the realistic soil response to seismic loads.

Seismic wave propagation has an arbitrary direction with respect to the axis of the structure that causes multi-directional loading for the soil deposit and tunnel lining. Two-dimensional (2D) simplifications of these three-dimensional (3D) effects can impact the seismic response of tunnels and underestimate the lining forces. Furthermore, most natural soils particularly natural clays are characterised by high stiffness and peak strength due to initial structure. Extreme events such as an earthquake can induce sufficient stiffness degradation in the soil associated to strain-softening processes. Under such condition, the initial structure and its progressive destructuration may significantly alter the soil behaviour and its interaction with the tunnels.

This dissertation investigates and presents novel results from advanced numerical simulations of the behaviour of shallow circular tunnels in natural clays accounting for soil structure degradation induced by earthquake loading. Moreover, it adopts 3D space model applying multi-directional seismic input motions. Notably, the results show that the soil destructuration facilitates the transmission of higher loads in the longitudinal lining forces while reducing the transverse lining forces. All these studies highlight for the first time the importance of the initial structure and its degradation and the benefits of the 3D approach in controlling the magnitude of the tunnel lining forces and, consequently, the overall seismic tunnel design.

This PhD dissertation is dedicated to my wonderful mom, Gloria and to my loving sister, Carmencita, who never fail to point me to the right direction.

Acknowledgements

At this stage of the work it is with great pleasure I write the acknowledgements. It has been my good fortune to work with people whose insights have helped me to combine the important with the interesting and exciting.

I would like first and foremost to thank my supervisors, Dr Gaetano Elia and Dr Mohamed Rouainia for giving me the opportunity to conduct the research. I am indebted to them for guiding me enthusiastically through the whole research process by unselfishly sharing their vast knowledge; providing the necessary materials and advice; for stimulating, challenging and influencing my thinking throughout my research; and for introducing me to the world of geomechanics and geotechnical seismic engineering.

I also like to express my heartfelt gratitude to my PhD buddies, Dr Tom Charlton and Dr Yusuf Guzel not only for their enlightening discussions, expert advice and wonderful company, but also for helping me in my work in numerous ways.

Special thanks go to the CEG-IT team, Dr Stuart Petch, Mr Graham Patterson and Mr Iain Woodfine for their unyielding support and assistance with PLAXIS and IT issues.

I also want to thank all the people who crossed my path, both friends and foes who inspired and motivated me to get to where I am today.

Last but not the least, I would like to thank my mom Gloria for her trust, encouragement and constant support in any endeavour that I undertake and for staying beside me for better for worst.

Table of Contents

List of Figures

List of Tables

List of Papers and Publications

Cabangon, L.T., Elia, G. and Rouainia, M. (2017) 'Advanced numerical modelling of the transverse behaviour of tunnels under seismic loading', *Proceedings of the Fourth International Conference on Computational Methods in Tunneling and Subsurface Engineering (EURO:TUN 2017)*. Innsbruck, Austria, 18-20 April 2017. pp. 729-737.

Cabangon, L.T., Elia, G. and Rouainia, M. (2018) '3D Numerical Analysis of tunnel behaviour in clayey soils under seismic loads', *16th European Conference on Earthquake Engineering (16ECEE)* Thessaloniki, Greece, 18-21 June 2018.

Cabangon, L.T., Elia, G. and Rouainia, M. (2019) 'Modelling the transverse behaviour of circular tunnels in structured clayey soils during earthquakes', *Acta Geotechnica*, 14(1), pp. 163-178.

Chapter 1. Project introduction

1.1 Background and motivation

Current predictions indicate an increasing trend in urban population and expect to surpass six and a half billion by 2050 (DESA, 2019). As a result, urban areas will face numerous challenges in meeting the needs of their growing urban populations, including housing, transportation, infrastructure and services (electricity, water, sanitation, etc.). To meet this growing demand, the need for space within cities becomes increasingly important. "Managing urban areas has become one of the most important development challenges of the 21st century. Our success or failure in building sustainable cities will be a major factor in the success of the post-2015 UN development agenda," said John Wilmoth, Director of United Nations Department of Economic and Social Affairs' (DESA) Population Division in the 2014 revision of the division's 'World Urbanization Prospects' report (DESA, 2014).

For hundreds of thousands of years, our natural domain has been principally two-dimensional space: the surface of the ground. The lack of surface space leads to the exploration of subsurface as a means to expand the urban facilities and expanding to a third dimensional space for future growth. The International Tunnelling Association (ITA) published a booklet titled *Why Go Underground* prepared by Godard (2002), past Vice-President of ITA, citing the social, environmental and economic reasons to use underground space. It elaborates further the advantages and subsequent benefits of utilising underground space. One of the key uses of underground space is tunnels for transport and storage use.

Tunnels constitute a major part of civil infrastructure and serve as public transportation facilities, highways and railways, sanitation and irrigation utilities, water supply and storage places (Cilingir and Madabhushi, 2011). Dense urban environments particularly mega cities such as London, New York, Paris, Tokyo, Taipei, Hong Kong, Beijing, Singapore and Bangkok have found the use of tunnels to solve traffic congestion, poor environmental conditions due to noise and air pollution, crowding and lack of space for work and recreation, sewage conveyance and treatment thus

improving the quality of life and ensure sustainability for the next generation. With an increased awareness and realisation of these benefits, particularly long-term improvements of the environmental impacts and more effective and efficient use of space and resources, other cities including Jakarta, Istanbul, Los Angeles, Copenhagen, Madrid, Seoul, Kuala Lumpur, Sydney, Riyadh, Seattle, Doha and Auckland follow suit as construction of new underground services and transport links in urban cities continues to grow. Many of these tunnels are constructed in countries of known high seismicity such as China, Indonesia, Turkey, India, Japan, Western USA, Taipei and New Zealand.

The tunnel operation massively contributes in running city businesses and in sustaining the normal everyday life activities of the city's population consequently fostering the city's economic growth and improving the quality of life. These huge advantages are highlighted in Broere (2016). Thus, urban tunnels are considered ''lifeline'' utilities as their continued operation is of vital importance during and in the immediate aftermath of an earthquake. It is, therefore, imperative to assess the engineering performance of such important geotechnical structures to ensure their resilience during and after seismic events.

1.1.1 *Performance of tunnels during seismic event*

Failures of geotechnical structures due to earthquake events, with huge consequences in terms of fatalities, disruption to transport networks and huge financial cost and economic loss, have been widely documented in recent years. These failures are often associated with significant deformation of soil deposits due to amplification of the ground motion which can cause major damage to buildings, bridges, houses and other surface infrastructure facilities. Some of those catastrophic failures caused by some of the major and most fatal earthquakes in the last 22 years are shown in Figure 1.1. On the contrary, dynamic effects on underground structures have often been neglected based on the assumption that their response to earthquake loading is relatively safe.

2016 Taiwan EQ (M6.4)

1999 Taiwan EQ (M7.6)

2010 Chile EQ (M8.8)

1995 Kobe EQ (M6.9)

Photo Credit:
http://www.scmp.com/, http://tunneltalk.com/, http://syurati.wordpress.com/, http://www.reddit.com/

Figure 1.1 Major historic earthquakes causing catastrophic failures on above-ground structures

Historically, underground facilities have experienced a lower rate of damage than surface structures and the recorded cases may sound not as fatal as those above ground. This is due to the fact that deep buried structures, especially flexible ones, are confined within the soil and therefore not expected to oscillate independently of the surrounding ground (Kolymbas, 2005). Nevertheless, several examples of recorded damage to underground structures for which seismic forces were not considered in the original design can be found in the literature. Hashash *et al.* (2001) described the collapse of the Daikai subway station in Kobe during the 1995 Hyogoken-Nambu earthquake (Figure 1.2), the damages to highway tunnels in Central Taiwan during the 1999 Chi-Chi earthquake and the collapse of the Bolu tunnel in Turkey during the 1999 Düzce earthquake (Figure 1.3). Twelve per cent of the mountain tunnels in the epicentral area were heavily damaged during the Kobe earthquake (Yashiro *et al.*, 2007), while after the Chi-Chi earthquake 26% of the 50 tunnels located within 25 km of the rupture zone were severely damaged and 22% moderately damaged (Wang *et al.*, 2001). More recently, Li (2012) reported the investigation of seismic damages to 11 highway tunnels in the Yingxiu Town area during the Wenchuan earthquake which

occurred on May 2008: 4 were seriously damaged, 3 moderately damaged and 4 slightly damaged. The main causes of damage in these case histories were the shallow depth of tunnels, the poor geological conditions (i.e. soft soils with high plasticity, weak rocks), the displacement of active faults crossing the tunnel and pre-existing structural defects in the tunnel lining.

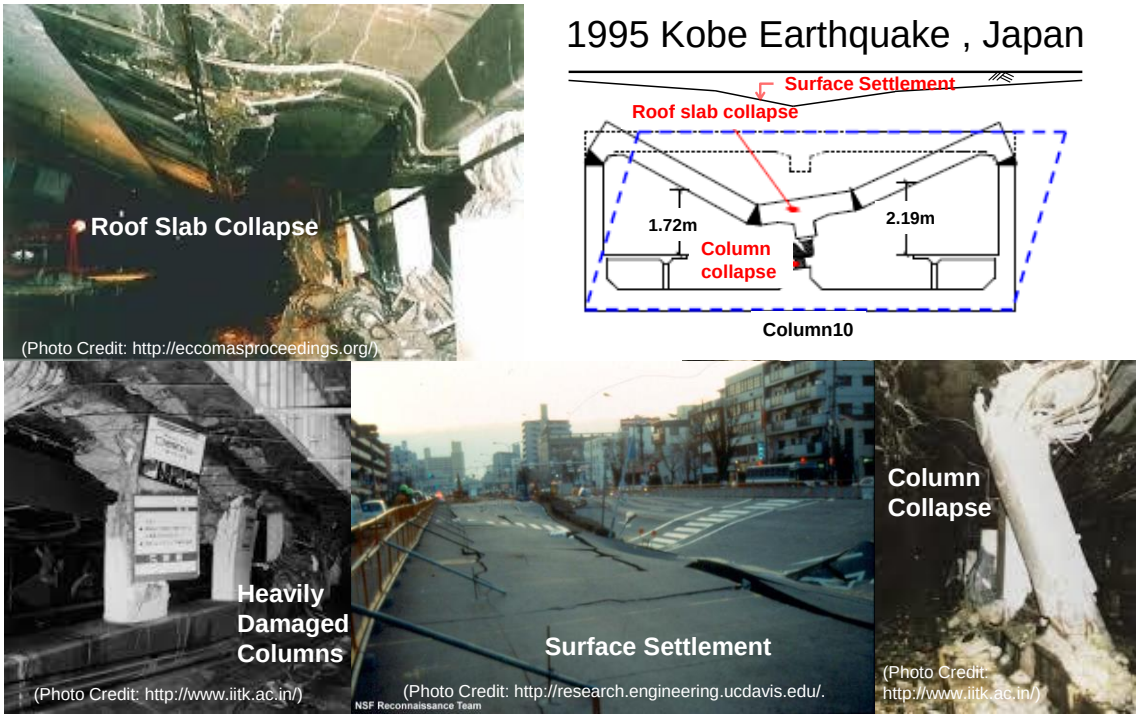

Figure 1.2 Collapse of Daikai subway in Kobe in 1995

During a seismic event, tunnels are subjected to axial compression and extension, longitudinal bending and ovaling or racking of the tunnel lining (Owen and Scholl, 1981). Underground facilities constructed in soft soils or weak rocks, such as urban tunnels, can be expected to suffer more damage compared to openings constructed in competent rocks (Hashash *et al.*, 2001). Ovaling and racking of the tunnel lining are reported to be the most critical sources of damage (Penzien, 2000), although longitudinal effects may have a significant impact on the response of long underground structures [(Hwang and Lysmer, 1981), (Hashash *et al.*, 2001)].

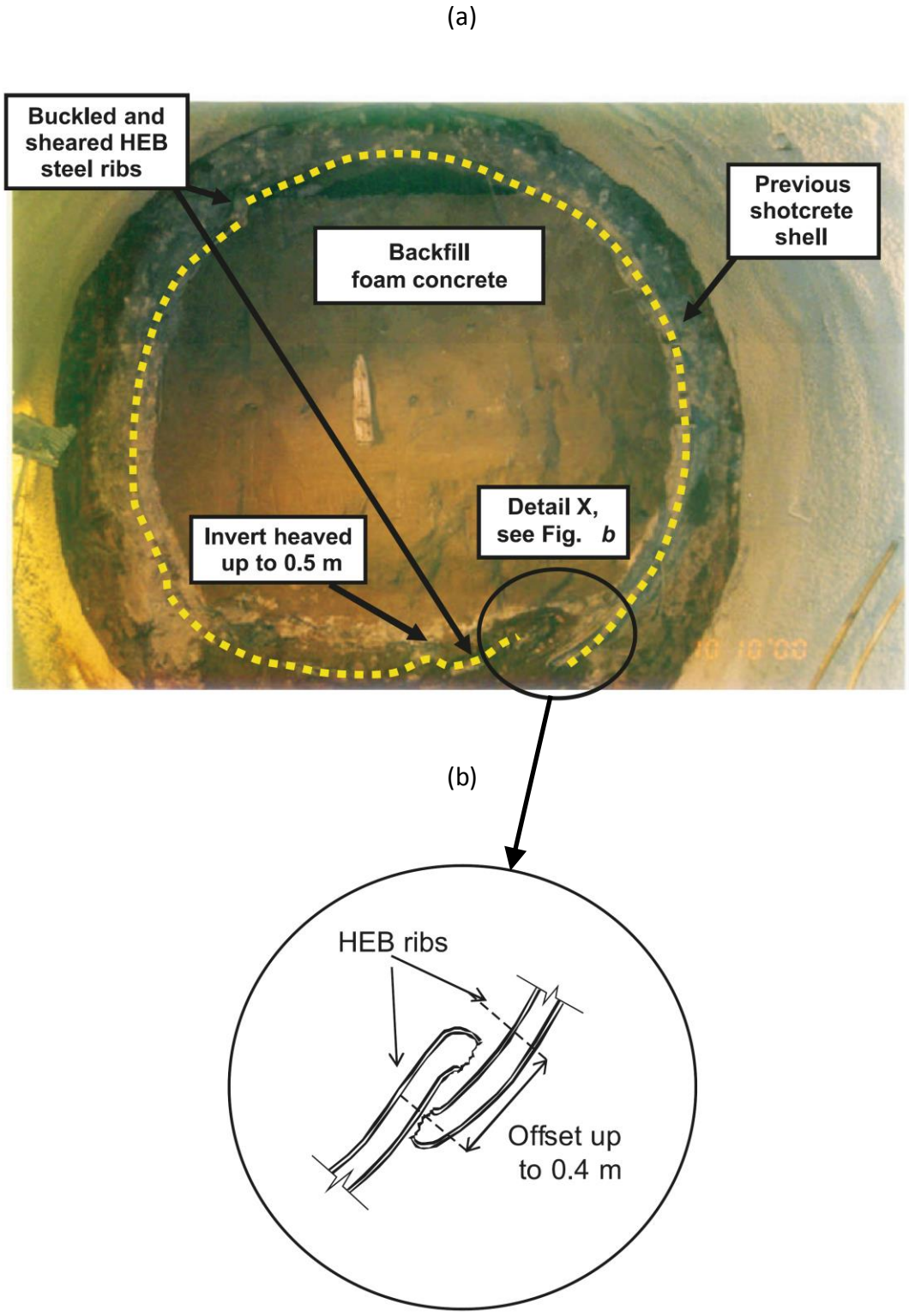

Figure 1.3 Collapse of Bolu tunnel in Turkey in 1999 (Kontoe *et al.*, 2008)

1.1.2 *Engineering approach to seismic analysis and design*

The seismic design of tunnels has been addressed in the past by a number of researchers [e.g. (Wang, 1993), (Penzien, 2000), (Hashash *et al.*, 2001), (Hung *et al.*, 2009)] who have proposed solutions based on analytical or numerical methods. The

analytical design methods typically rely on elasticity solutions to calculate the dynamic lining forces a tunnel experiences during an earthquake event and ignore the inertial effects. The Soil-Structure Interaction (SSI) approach has, instead, the ability to consider relatively complex conditions in terms of heterogeneity of soil strata, non-regularity of tunnel geometry, pre-existence of surface and sub-surface structures and ground water flow. In such cases, the analysis of SSI can take advantage of the use of numerical two-dimensional (2D) and three-dimensional (3D) approaches, such as the Finite Difference Method (FDM), Boundary Element Method (BEM) and the Finite Element Method (FEM).

Most commonly, the soil and tunnel are modelled in the transverse direction only, assuming plane strain conditions [e.g. (Khoshnoudian and Shahrour, 2002), (Pakbaz and Yareevand, 2005), (Liu and Song, 2005), (Amorosi and Boldini, 2009), (Azadi and Hosseini, 2010), (Shahrour *et al.*, 2010), (Kontoe *et al.*, 2011)]. However, when the direction of wave propagation is arbitrary with respect to the axis of the structure, which causes multi-directional loading for the soil deposit and the tunnel lining, longitudinal effects (e.g. spatial incoherence, axial compression and extension, longitudinal bending, construction sequence) can impact the response of the tunnel structure (Hashash *et al.*, 2001). Thus, the problem becomes three-dimensional and relatively few contributions studying this aspect can be found in literature [e.g. (Stamos and Beskos, 1995), (Stamos and Beskos, 1996), (Yang *et al.*, 2004), (Gazetas *et al.*, 2005), (Hatzigeorgiou and Beskos, 2010)].

Seismic numerical analyses are often performed using a 2D approach which has grown in popularity for the last two decades. This approach, however, requires simplifications to solve 3D problems. It assumes plane strain condition in the longitudinal direction which may not represent the actual condition during seismic event particularly for non-homogeneous surrounding medium and cases of ground motion incoherence (Zlatanović *et al.*, 2013). Such approximations can impact the response of the tunnel structure and may lead to un-conservative design.

Although the use of 3D methods to study soil–structure interaction under earthquake excitation has the appeal that some of these modelling and simplification errors from 2D are reduced, it suffers from the important disadvantages that the solution time and

the complexity of the analysis are substantially increased. However, with the emergence of high-performance computers with increased computing capacity at reduced computing time, 3D approaches in predicting seismic performance of tunnels are now frequently explored as evident from works by Ohbo *et al.* (2004), Dobashi *et al.* (2008), Yamada *et al.* (2008), Yu *et al.* (2009b), Park *et al.* (2009), Sliteen *et al.* (2011), Dobashi *et al.* (2011), Yu *et al.* (2013b), Sahoo *et al.* (2014) and Fabozzi and Bilotta (2016). Within this context along with the fact that multi-directional loading and longitudinal effects can impact the response of the tunnel structure, there has been a greater demand for accuracy and reliability of numerical results in predicting the seismic performance of tunnels. Therefore, it is most appropriate and rational to approach seismic simulation of tunnels using 3D methods.

An accurate prediction of tunnel behaviour during earthquake can be achieved not only by simulating the problem in a 3D space but also by capturing a realistic soil response to seismic loads. State dependency, early irreversibility, non-linearity, anisotropy, non-coaxiality, structure degradation (destructuration), decrease of nominal stiffness and related hysteretic energy dissipation in the mechanical behaviour of soils under cyclic loading are evident in a number of experimental results presented in Roscoe *et al.* (1967), Sangrey *et al.* (1969), Castro and Christian (1976), Arthur *et al.* (1980), Oda *et al.* (1985), Alawaji *et al.* (1990), Leroueil and Vaughan (1990), Vucetic and Dobry (1991), Cotecchia and Chandler (1997) and Gutierrez and Ishihara (2000). Only some of these features can be simulated by adopting simple constitutive assumptions in the framework of linear-visco-elastic assumption and elasto-plasticity theory (e.g. Linear isotropic elasticity, Ramberg-Osgood, Mohr-Coulomb, Modified Cam Clay, Drucker-Prager) thus needing more advanced constitutive models to simulate them.

A primary limitation of single surface models in the context of dynamic analysis is related to their inability to reproduce the observed hysteretic dissipation. This is caused by the unrealistically large extent of their yield surfaces, which leads to limited accumulation of plastic strain during cycles as opposed to gradual accumulation of irrecoverable plastic strain and accompanying energy dissipation at pre-yield stage normally observed on soils subjected to cyclic loading. As a consequence, the use of simple models in FEM dynamic analyses requires the superposition of an often large,

fictitious viscous damping (Woodward and Griffiths, 1996). This ingredient of the analysis is difficult to quantify a priori and, at the same time, can have a crucial influence on the results of numerical simulations. Moreover, natural soils are often characterised by a preferential orientation at microscopic level, deriving from both the geologic processes acting during the deposit formation and the stresses induced in the soil by engineering structures. In both cases, the existence of such an orientated microstructure leads to an anisotropic behaviour at the macroscopic level, as the mechanical response of the soil depends on the relative orientation of the external stresses and the internal soil microstructure [(Oda *et al.*, 1985), (Alawaji *et al.*, 1990)]. Recent work suggests that ignoring the anisotropic soil behaviour would lead to unsafe design in practice and is therefore potentially risky [e.g. (Yu, 2008)].

Another advanced soil attribute normally ignored by simple constitutive models is the initial soil structure and its subsequent degradation which is innate in natural soils. Destructuration may significantly alter the soil behaviour and its interaction with any substructure, an aspect which this project will primarily focus on. Its existence and effects will be explored in detail in subsequent chapters.

Advanced constitutive models can be employed nowadays in FEM dynamic analyses of earth structures in order to properly predict the main features of the soil behaviour mentioned above. Despite their more complex mathematical formulation, these models can simulate inherent and induced anisotropy, non-coaxiality, early development of irreversible strains, decrease of nominal stiffness due to hysteretic energy dissipation, structure degradation and permanent pore water pressures build up in undrained loading conditions, thus resulting in a better prediction of the anisotropic and cyclic behaviour of soils.

In all cases above, the analysis can take advantage of the use of numerical three-dimensional approach. With this approach, both the transversal and the longitudinal directions of the tunnel can be modelled and analysed simultaneously, taking into account the complicated soil deposit geometry, the non-linear behaviour of the soil and the structure using appropriate constitutive relationships and the behaviour of the soil-structure interface (Pitilakis and Tsinidis, 2014). The capabilities of such numerical approaches to improve the accuracy and reliability in the assessment of tunnel

behaviour under seismic loading have not been fully exploited yet. This approach requires the use and calibration of advanced constitutive models to appropriately describe the soil stress-strain behaviour during the dynamic action in conjunction with a realistic description of the three-dimensional soil-structure interaction. In particular, the evolution of microstructure (destructuration) induced in natural soil deposits by the seismic action and its effect on the soil-tunnel dynamic behaviour has not been investigated before. Hence the primary objective of the project is to fill in that gap in the numerical approach.

1.2 Aim and objectives

1.2.1 *Overall aim*

The primary aim of the project as diagrammatically shown in Figure 1.4 is to improve the design of underground structures in natural clayey soils subjected to earthquake loading by increasing the accuracy and reliability through better prediction of tunnel and soil behaviour during seismic action. Together with the use of reliable and accepted design codes and guidelines which has to be continually improved based on lessons learnt from past earthquake experience, this project can lead to economical design benefit while reducing risk and ensuring safety in design.

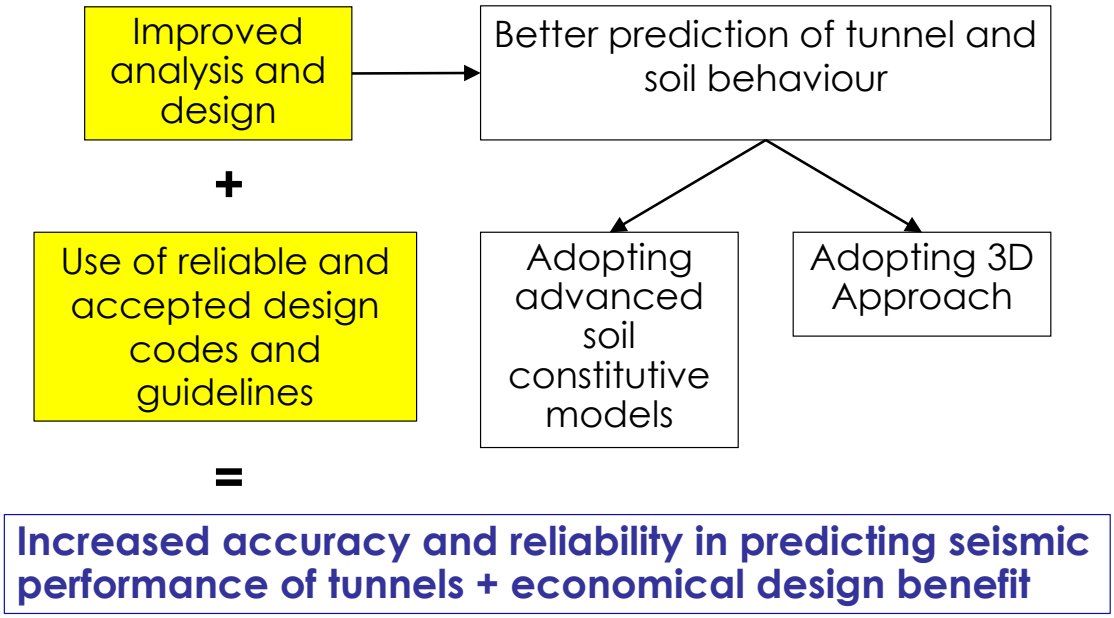

Figure 1.4 Primary aim of the project

The aim will be achieved through the following objectives.

1.2.2 *Specific objectives*

- To identify an appropriate advanced non-linear soil constitutive model considered to produce the most accurate prediction for the soil stress-strain behaviour of natural clayey soils during seismic action.
- To generate two- and three-dimensional numerical models of an ideal underground structure in natural clayey deposits using soil data calibrated from existing case studies and laboratory results found in literature.
- To examine the benefits and limitations of adopting a 2D versus a 3D approach.
- To investigate the influence of the non-linear advanced soil constitutive model on the results of two- and three-dimensional model of an ideal underground structure in natural clayey soils in earthquake condition.
- To investigate the effects of multi-directional application of earthquake ground motion compared to traditional one-directional application.
- To examine the impact and relative merit of this new approach on the tunnel design.

1.3 Thesis layout

1.3.1 *Chapter 2*

Chapter 2 lays down the approach and methods pursued by the author through the whole course of the project in order to achieve its aim and objectives.

1.3.2 *Chapter 3*

Chapter 3 presents a literature review on the soil behaviour under earthquake loading and the nature of initial soil structure and its degradation as well as previous research on tunnel-soil behaviour in static and dynamic conditions. It also covers the identification and selection process for the most appropriate soil constitutive model and geotechnical engineering software for the project. It includes an outline of the most advanced soil constitutive models that can capture the essential features to produce a realistic response of natural soils under earthquake loading.

1.3.3 *Chapter 4*

Chapter 4 emphasises the advantages of using advanced non-linear soil constitutive model and highlights for the first time the importance of the initial structure of natural

clayey soils and its eventual degradation in controlling the magnitude of the tunnel lining forces and, consequently, the overall seismic tunnel design.

In this chapter the dynamic performance of a shallow circular tunnel in a natural clay deposit is analysed by means of a 2D FEM approach. It includes the calibration of an advanced kinematic hardening multi-surface soil model RMW against real laboratory data. Different soil constitutive models both simple and advanced and different rates of destructuration of the soil's initial structure are investigated and compared within the context of the effects they induced on the soil-tunnel behaviour in dynamic conditions.

The chapter also discusses the optimisation of the geometry of the numerical model and the selection strategies for the definition of the bedrock input motions. The results of the 2D simulations are then presented and discussed and some conclusions are drawn at the end.

1.3.4 *Chapter 5*

Chapter 5 demonstrates the benefits of extending the 2D approach into 3D utilising the advanced soil constitutive model RMW. Following the work done in Chapter 4, the 2D FEM model is translated into a 3D FEM model inheriting all the properties from the previous 2D works.

In this chapter, the 3D FEM model is subjected to multi-directional earthquake loading. The chapter covers the validation of the 3D model against a simplified 2D model. The results of the 3D simulations are then presented, discussed and compared with those from one-directional earthquake loading traditionally adopted in 2D and some conclusions are drawn at the end.

1.3.5 *Chapter 6*

Chapter 6 provides a summary of the project and concludes with an outline of the findings from the studies. The chapter also discusses the relative strengths and weaknesses of this new advanced approach on the tunnel design as well as lessons learnt and provides recommendations for further research work.

Chapter 2. Methodology

2.1 Overview

The project is consist of the following 5 tasks:

Task 1: Extensive literature review for identification and selection of the appropriate soil constitutive model;

Task 2: Generation of 2D and 3D numerical models

- 2a: Evaluation of different geotechnical engineering software currently available and selection of the appropriate tool which meets the project's objectives;
- 2b: Generating and simulating 2D & 3D numerical models using the chosen numerical analysis tool and validating the models;
- 2c: Examine the benefits of adopting advanced soil constitutive model and the influence of degradation of soil's initial structure (destructuration);

Task 3: 3D numerical simulation using adopted non-linear soil constitutive model

- 3a: Simulating the 3D model with the adopted soil constitutive model and examining the benefits and limitations of adopting 2D versus 3D approach;
- 3b: Investigating the influence of 3D multi-directional application of earthquake ground motion compared to the traditional one-directional 2D approach;

Task 4: Examination of the impact and relative merit of this new approach on the tunnel design;

Task 5: Summary of findings and recommendations for future research work.

These tasks are discussed in detail below.

2.2 Approach and methods

2.2.1 *Identification of an appropriate non-linear advanced constitutive model*

The initial phase (Task 1) of the research focuses on the examination of all existing and known soil constitutive models through extensive literature review in conjunction with advice from the supervisory team. The models are shortlisted to those which can characterise the advanced mechanical behaviour of soil under cyclic loads (i.e. state dependency, early irreversibility, non-linearity, anisotropy, non-coaxiality, structure degradation, decrease of nominal stiffness and related hysteretic energy dissipation). One of these models is the Rouainia and Wood (2000) (RMW) model. A final evaluation and selection of the soil constitutive model deemed to be the most appropriate model to accurately predict the real soil stress-strain behaviour during dynamic action is conducted. Single element simulations using the cyclic direct simple-shear test in SoilTest within PLAXIS and single element driver SM2D are performed with the selected soil constitutive model to calibrate against known cyclic/dynamic laboratory tests (resonant column/torsional shear and cyclic triaxial tests) results from real soil samples and to verify its performance prior to its full use. Calibration was also performed against the results from the undrained triaxial compression tests of the same soil samples. This soil constitutive model then serves as an input component in the simulations of both 2D and 3D models.

2.2.2 *Generation of 2D and 3D numerical models*

The second phase (Task 2) involves generating 2D and 3D models of an ideal circular tunnel in typical clayey deposit using numerical tools of FEM or FDM type such as FLAC, PLAXIS, LS-DYNA, SWANDYNE, MIDAS GTS or Opensees (Open System for Earthquake Engineering Simulation). The choice of the numerical analysis tools depends on cost, availability, functionality, capability, ease of use, adaptability and technical support. Therefore, a study and evaluation of these tools precedes any activity prior to their use. This is concurrent with activities from Task 1. Once the tool is chosen, some period is spent in learning and familiarising with the selected tool and its functionalities (e.g. model setup, mesh generation, element build-up, choosing boundary conditions and material behaviour, applying seismic load, etc.) through formal training. This period has also been spent learning numerical strategies for

modelling the soil-structure interaction with earthquake loading through available literature. The chosen tool is used to set up and simulate the 2D and 3D models mentioned above. A parametric study has been performed to determine the optimum size of the model whereby free-field conditions are reproduced near the lateral boundaries. In order to validate the models from the simulations, the results are compared to agree with those from one-dimensional 1D soil response (i.e. free-field conditions) simulations. Using the 2D model, a case study involving different soil constitutive models which include the selected advanced soil constitutive model and a parametric study with different rates of destructuration of the soil initial structure are then performed to evaluate the effects they induced on the soil–tunnel behaviour in dynamic conditions

2.2.3 *3D Numerical simulation implementing non-linear constitutive model on soil-tunnel interaction problem*

In the third phase (Task 3), the simulation of the 3D model using the adopted soil constitutive model identified in Task 1 is performed and validated using results from the 2D model. To determine the appropriate size of the 3D model, a parametric study of the model length and width is conducted to ensure sufficient distance to the lateral boundaries of the mesh to simulate properly the free-field conditions. The author then analyses the simulation results to determine the benefits and limitations of adopting 2D versus 3D models as well as the influence of multi-directional earthquake loading and longitudinal effects (e.g. axial compression and extension, longitudinal bending, construction sequence) on the soil-tunnel behaviour.

2.2.4 *Examine impact and relative merit of new 3D approach on tunnel design*

The fourth phase (Task 4) examines in detail the impact and benefit (if any) of adopting the developed 3D approach on tunnel design. The seismic acceleration and shear strain in soil as well as the forces (bending, shear, axial) in the tunnel lining from the developed 3D one-directional earthquake simulation in Task 3 have been assessed and compared with those from the 2D in Task 2 to determine its impact on the soil-tunnel behaviour. Similar comparative approach has been conducted between the results of 3D models in Task 3 when only one-directional earthquake acceleration is applied at the bedrock against the case of imposing bi-directional earthquake motion including

any variation of lining forces along the tunnel length resulting from the propagation of the seismic waves. The author also examines other relative merits and challenges for using this approach.

2.2.5 *Summary of findings and recommendations for future research work.*

The last phase (Task 5) summarises and concludes with an outline of the principal findings from the studies. These include the relative strengths and weaknesses of the new 3D approach as well as lessons learnt and provides recommendations for further research work.

Chapter 3. Literature review

3.1 Introduction

The aim of this chapter is to provide the basis for the selection of an appropriate soil constitutive model and geotechnical software for the project as well as to present a short background on the significance of initial soil structure and subsequent destructuration. This chapter also provides an outline of the most relevant advanced soil constitutive models that have been developed in recent years.

The literature review comprises of three parts. The first part covers an overview of the soil behaviour under cyclic loading and the initial structure of natural soils and its destructuration process. It includes research conducted and salient findings on the structure of natural soils. It also reviews literature works undertaken on tunnel-soil behaviour in static and dynamic conditions. The second part presents the steps that the author undertook to select an appropriate constitutive model that can capture the advanced attributes of natural soils under earthquake condition. A brief description of the most advanced soil constitutive models from the sifted list is given including their similarities and differences. The last part presents the identification and selection process for the adopted geotechnical engineering software for the project.

3.2 Seismic behaviour of natural soils

Cyclic loading is defined as a periodic action which tends to change, and usually reverse, the stress and strain state of soils over time (Pinto, 2012). The most recognisable form of cyclic loading in soils occurs during an earthquake. An earthquake is a propagation of seismic waves that radiate from an underground source which in most cases related to plate tectonics. These seismic waves can impose large-scale soil movements that are both erratic and unpredictable. It is common knowledge that earthquakes can have devastating effects on human lives, as it can cause deaths, injuries, and property and infrastructure damage, sometimes with disastrous consequences. Thus, the study of soil properties and behaviour during earthquakes is very important in order to understand their influence on the seismic waves and possibly reduce the impact of earthquake on infrastructure.

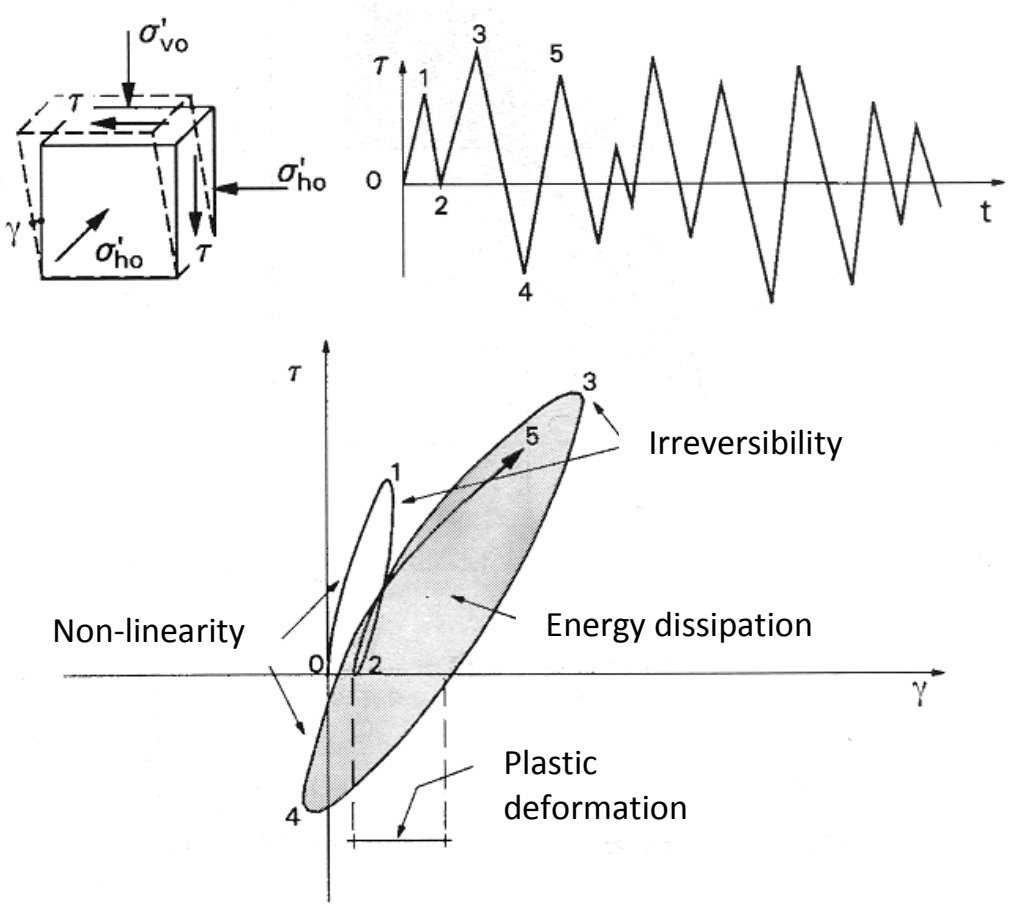

Figure 3.1 Soil behaviour under seismic loading [modified from Lanzo and Silvestri (1999)]

Soil behaviour under earthquake loading is significantly different and complex from that observed under monotonic loading as shown in Figure 3.1. Some of those differences are listed here which include:

- strong non-linearity [Amorosi *et al.* (2010), Shahrour *et al.* (2010)];
- early irreversibility [Elia and Rouainia (2010), Shahrour *et al.* (2010)];
- decrease of nominal shear stiffness with consequent hysteretic energy dissipation during cycles [Borja *et al.* (2001), Amorosi *et al.* (2010)];
- pore pressure buildup in undrained condition due to hysteretic action [Borja *et al.* (2001), Conti *et al.* (2014)];
- dependence on past stress-history [Amorosi *et al.* (2010), Elia and Rouainia (2010)]; and
- structure degradation [Elia and Rouainia (2010), Elia and Rouainia (2014), Elia and Rouainia (2016)].

These attributes except structure degradation have been identified in the past through extensive laboratory investigation on reconstituted soil samples by a number of researchers including Vucetic and Dobry (1991), Sangrey *et al.* (1969), Matasovic and Vucetic (1995), Castro and Christian (1976), Yasuhara *et al.* (1992), Lee and Sheu (2007) and Gu *et al.* (2012). However, recent advances in experimental and constitutive modelling of natural soils have uncovered the importance of structure and its subsequent degradation. This attribute and its significance are discussed further in the succeeding sections. Ideally, the inclusion of all these advanced attributes in a soil constitutive model allows an increased accuracy and reliability in predicting realistic response of natural soils during earthquake.

3.2.1 *Definition of dynamic soil parameters*

The response of the soil in cyclic loading conditions is normally presented as a shear stress (τ) - shear strain (γ) curve which can be divided into two basic components: the path of first loading defined by a backbone curve and the unloading and reloading path which form the hysteresis loop as illustrated in Figure 3.2. This response is strongly controlled by the mechanical properties of the soil. The most important of which to characterise the dynamic behaviour of soils are the shear modulus and damping. Both these properties are affected by the effective stress and over-consolidation ratio.

The shear stiffness of the soil is defined by a parameter called the secant shear modulus, G. It can be determined by measuring the slope of the hysteresis loop or extreme points of the hysteresis loop as shown in Figure 3.2 and is numerically expressed as:

$$G = \frac{\tau_a}{\gamma_a} \qquad 3.1$$

At very small strains when the hysteresis loop is linear elastic, the shear modulus of a soil is at its maximum. This modulus is called the maximum or initial shear modulus, G_0 (see Figure 3.2). Figure 3.3 shows that every shear strain amplitude produces distinct hysteresis loop with corresponding secant stiffness, i.e. secant shear modulus. It can be seen that the hysteresis loops become wider and flatter on the horizontal axis with the increase in the strain amplitude. This is an effect of the immediate past history of the soil. The locus of points corresponding to the tips or extreme points of hysteresis

loops form the backbone curve (also called skeleton curve or initial loading curve) shown as a black dashed line in Figure 3.3, which is essential to describe the soil behaviour subject to initial loading.

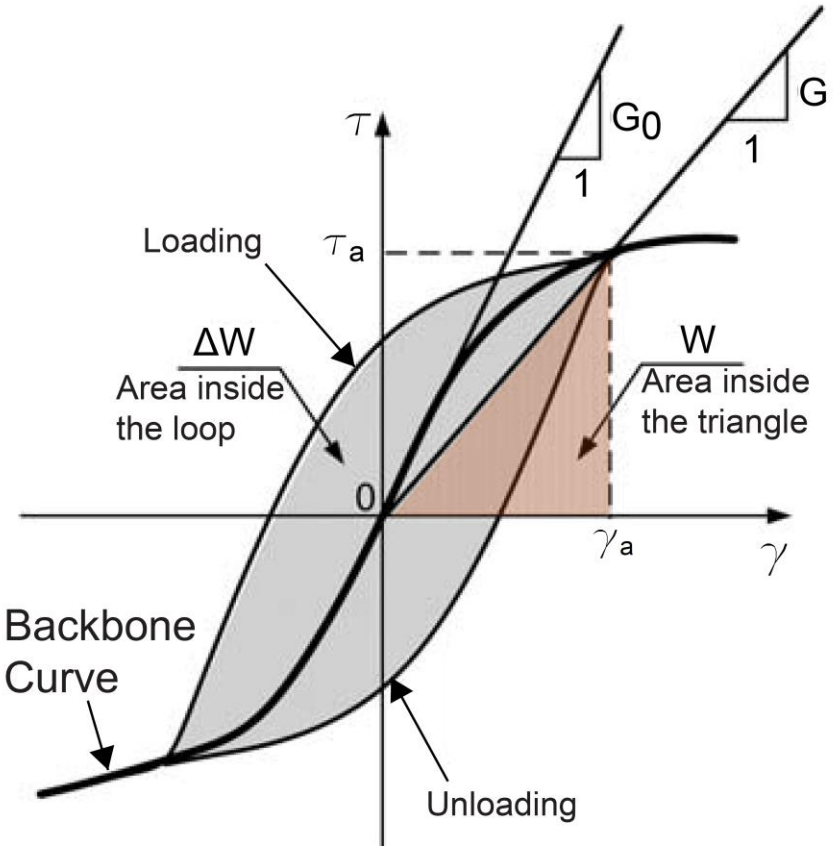

Figure 3.2 Schematic representation of secant shear modulus (*G*), elastic stored strain energy (*W*) and dissipation energy (*ΔW*) (Assimaki *et al.*, 2008)

As the strain amplitude increases (which subsequently increases the size of the cyclic shear stress-strain curve represented by the ellipses), it can be discerned in Figure 3.3 that the shear modulus ratio, G/G_0, which is equal to unity for zero shear strain amplitude, gradually reduces. The change of the modulus ratio with shear strain is often presented using a modulus reduction curve (also called normalised shear modulus) which describes the shear stiffness degradation of soils. An example of a modulus reduction curve is shown in Figure 3.4.

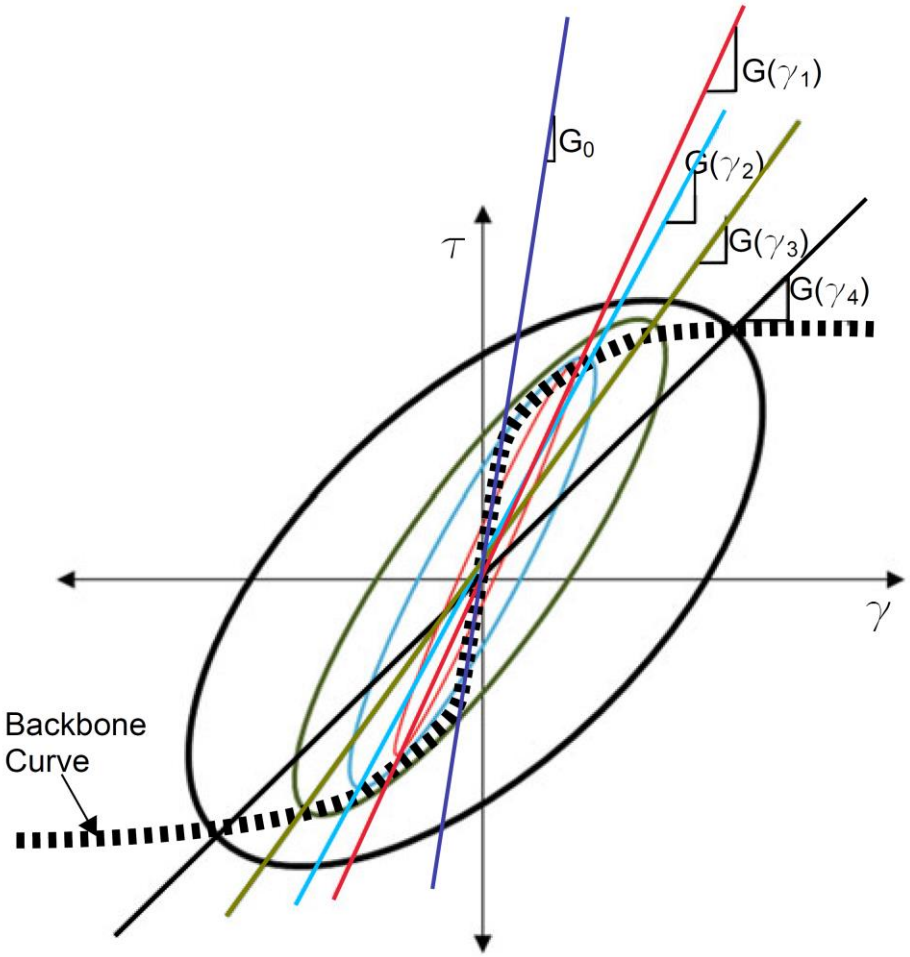

Figure 3.3 Variations in secant shear modulus (*G*) for different shear strain amplitudes and the corresponding backbone curve (Jia, 2018)

Soils under cyclic loading show a tendency to dissipate energy, even at low strains (Kramer, 1996). This dissipation of energy happens due to material damping. Soil damping generally termed as hysteretic damping allows excitation introduced by dynamic loading such as an earthquake to decrease over time. The soil's hysteretic damping ability is defined by a parameter called the damping ratio ξ. It is proportional to the ratio of the energy loss per cycle ΔW, and the maximum elastic energy that can be stored in a unit volume of a viscoelastic body W, mathematically expressed in Equation 3.2.

$$\xi = \frac{\Delta W}{4\pi W} \qquad 3.2$$

where ΔW = area bounded by the hysteresis loop and W = area of the triangle bounded by a straight line defining the secant modulus at the point of maximum strain as illustrated in Figure 3.2 and expressed below.

$$W = \frac{1}{2}\tau_a \gamma_a \qquad 3.3$$

Soils tend to dissipate more energy in a loading cycle though hysteretic damping with increasing shear strain, i.e. as shear strain amplitude increases the damping ratio ξ also increases, as shown in Figure 3.4. Results from experiments by various researchers including Vucetic and Dobry (1991), Ishibashi and Zhang (1993), among others, show that the plasticity of the soil has a significant effect on the evolution of damping with strain. The damping ratio tends to increase generally as the plasticity index increases, especially at small strain levels. The damping behaviour is also influenced by the effective confining pressure as demonstrated from experimental results by several authors including Ishibashi and Zhang (1993) and Darendeli (2001). The higher the effective confining pressures, the less the energy dissipation exhibited by the soil.

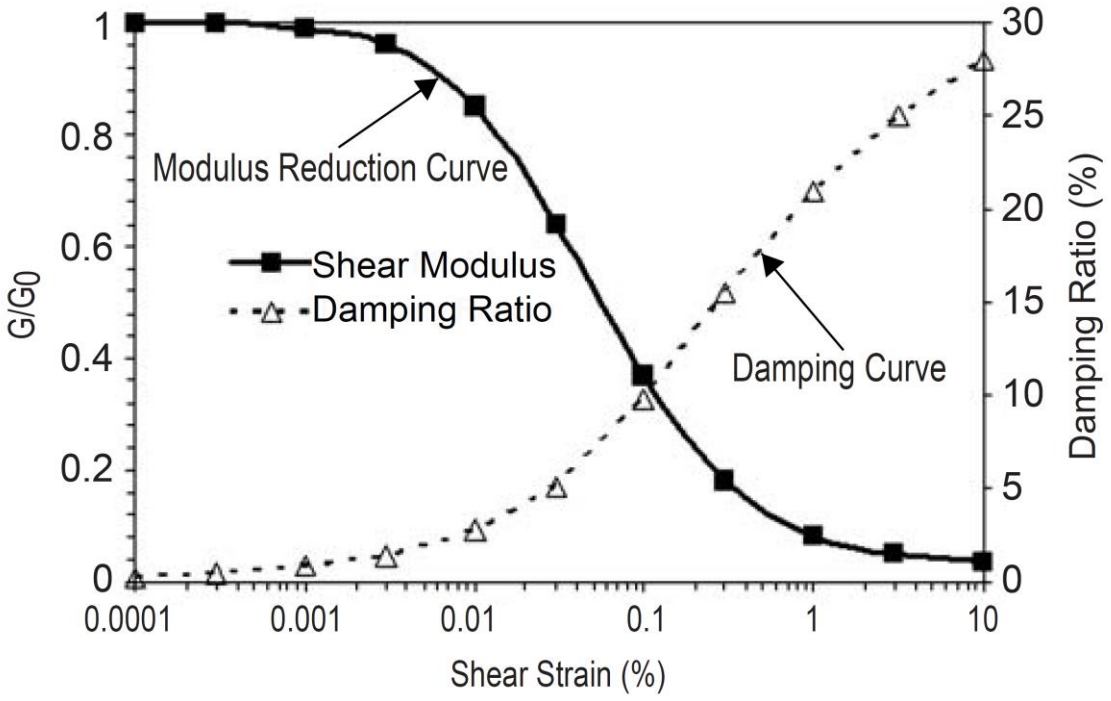

Figure 3.4 Curves of normalised shear modulus (G) and damping ratio (ξ) as a function of shear strain (γ) (Stupazzini *et al.*, 2009)

3.3 Structure in natural soils

It has been well recognised by several authors [e.g. Burland (1990), Leroueil and Vaughan (1990)] that there are significant differences between natural and reconstituted or remoulded soils. Intact natural soils particularly structured clays have

initial structure which enables it to exist at states outside the state boundary surface for the remoulded soil, resulting in greater peak undrained strength and yield stress at a given void ratio than for the same clay when reconstituted (Nash *et al.*, 2007).

The term 'structure' was defined by Lambe and Whitman (1969) to describe the combination of 'fabric', which is characterised by the distinctive arrangement of the clay particles, and 'bonding' defined as forces interacting to connect those particles, which are not of a purely frictional nature. Fabric includes in-homogeneities, layering and distribution of the soil particles and fissures (Coop *et al.*, 1995). The soil's initial structure is the result of deposition, consolidation, aging, thixotropy, and cementation (Leroueil *et al.*, 1979).

Geotechnical loading and disturbance including sampling can cause substantial irrecoverable plastic strains thereby inducing degradation of the initial soil structure. This behaviour was verified by experimental studies conducted by several authors including Burland (1990), Leroueil and Vaughan (1990), Cotecchia and Chandler (1997), Leroueil *et al.* (1979) and Callisto and Calabresi (1998). The studies showed that the behaviour of natural clays at their structured state are different and more fragile compared to their remoulded states. As destructuration progresses, the structured clay evolves to its destructured state such that the interparticle bonding of soil deteriorates producing significant changes on the mechanical behaviour of clays including reduction in strength in the overconsolidated state and strong reductions in shear and bulk moduli.

As plastic straining further develops, the accumulated strain gradually destroys the microstructure as established by test results conducted on Bothkennar clay by Clayton *et al.* (1992) and Hight *et al.* (1992). As a consequence, the destructuration process shrinks the bounding surface towards that of the reconstituted clay as indicated in Figure 3.5. In the figure, the stresses are normalised by p'_e, the value of mean effective stress at the appropriate void ratio on the normal consolidation line for the reconstituted material. The reconstituted state is reached when sufficient mechanical energy is imparted to the clay mass to reduce its strength to a minimum. This can be achieved through intense dynamic movement such as an earthquake event which can

cause the destructuration to accelerate and thereby alter the performance of any critical substructure bounded by the soil such as a transport tunnel.

Nash *et al.* (2007) suggested that the main indicators to assess destructuration are change of state (reduction of void ratio at a given stress state), increase of creep rate, changes of small strain shear stiffness G_0, changes of small and intermediate strain axial stiffness E_v and volumetric stiffness K, reduction of yield stress, and reduction of undrained strength.

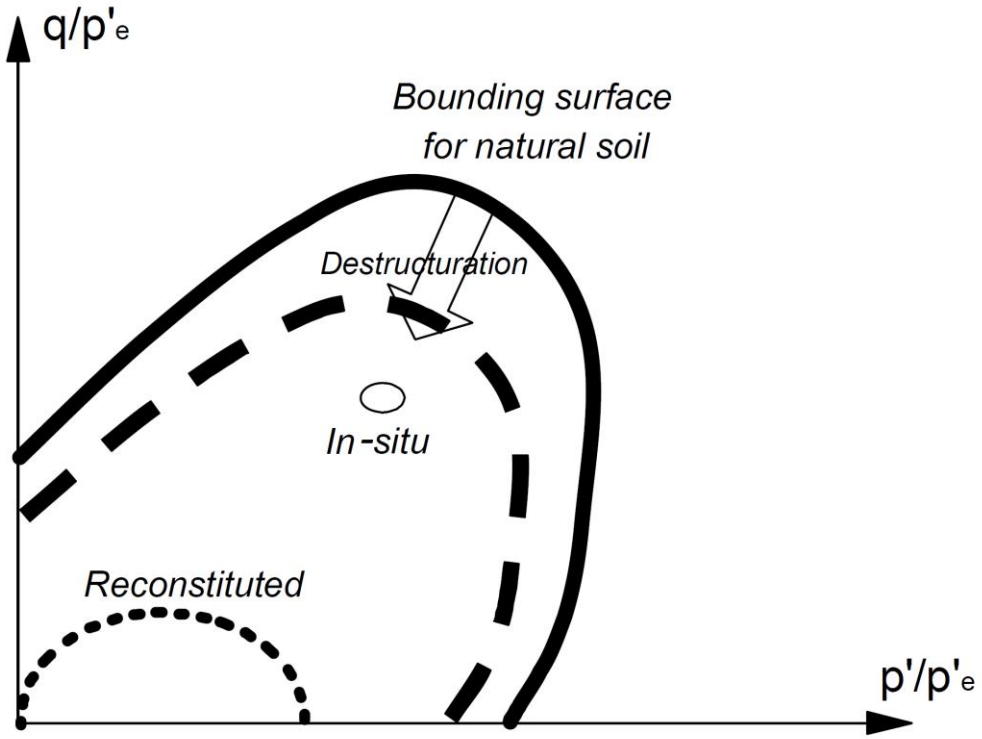

Figure 3.5 Bounding surface of natural clay showing effect of destructuration (Nash *et al.*, 2007)

During deposition, all normally consolidated insitu clays follow 'a sedimentation compression curve' (SC curve) in the e-σ'_v plane (Terzaghi, 1941) under one-dimensional compression. The SC curves for a natural clay and for the same clay when reconstituted and compressed in the laboratory, are shown in Figure 3.6. In these figures, Cotecchia and Chandler (2000) illustrated the differing responses of both natural and reconstituted clay at their normally consolidated and overconsolidated conditions. The plots show the reduced void ratio of the reconstituted soil compared to its intact natural state. Although both clays have identical mineralogical composition, the difference in the positions of their SC curves are attributed to the

differences in their sedimentation structures. For simply overconsolidated case in Figure 3.6 (b), if reloaded one-dimensionally, both natural and reconstituted clays will return to their sedimentation structure as it reaches the SC curve (Y & Y* in Figure 3.6) at a stress σ'_{vy} & σ^*_{vy} which is close to the preconsolidation stress σ'_{vc} & σ^*_{vc}. However, for natural clay, its curve path will continue depending on the reloading rate. At relatively high loading rates (e.g. geotechnical loading & disturbance), the oedometer compression curve falls below the SC curve (path Y-Z_2) while at geological time-scale rates (e.g. natural deposition), the curve will follow the SC curve (path Y-Z_1). This does not apply to reconstituted clay which is unlikely to suffer diagenesis or cementation such that the post-sedimentation structure of reconstituted clays is generally due either to unloading or to creep. At gross yield (which refer to a state in effective stress space outside the elastic domain, at which soil stiffness falls significantly with accompanying increase in the plastic strain increments inducing degradation of the initial soil structure), the oedometer compression curve for the natural clay crosses the SC curve, moving some distance to the right (path O-Y, Figure 3.6 (c)) and subsequently follows a path steeper than the SC curve (path Y-Z_3). Those plots clearly show a marked difference on the behaviour of natural clays at their structured state compared to their remoulded states irrespective of the stress state of clay (i.e. normally consolidated or overconsolidated or at gross yield). When plotted in *q- p'-v* space, it clearly demonstrates that the bounding surface for a natural clay (SBS – state boundary surface) shrinks when the same clay has been remoulded (SBS*) due to degradation of the soil structure as shown in Figure 3.7. These have been validated by experimental test results on Pappadai clay by Cotecchia and Chandler (1997). Figure 3.8 shows the plots of the void index I_v against the effective vertical stress σ'_v wherein the reconstituted Pappadai clay has lower void index compared to its natural structured state under similar effective vertical stress while Figure 3.9 shows the normalised *p'-q* curve for intact and remoulded clays wherein the bounding surface of the reconstituted clays has shrunk compared to its natural state. The void index I_v which is conceptually similar to liquidity index is defined by the equation below (Burland, 1990).

$$I_v = \frac{e - e^*_{100}}{e^*_{100} - e^*_{1000}} \qquad 3.4$$

where e = the void ratio and e^*_{100} & e^*_{1000} are the void ratios when compressed one-dimensionally to a vertical effective stress of 100 and 1000 kPa, respectively.

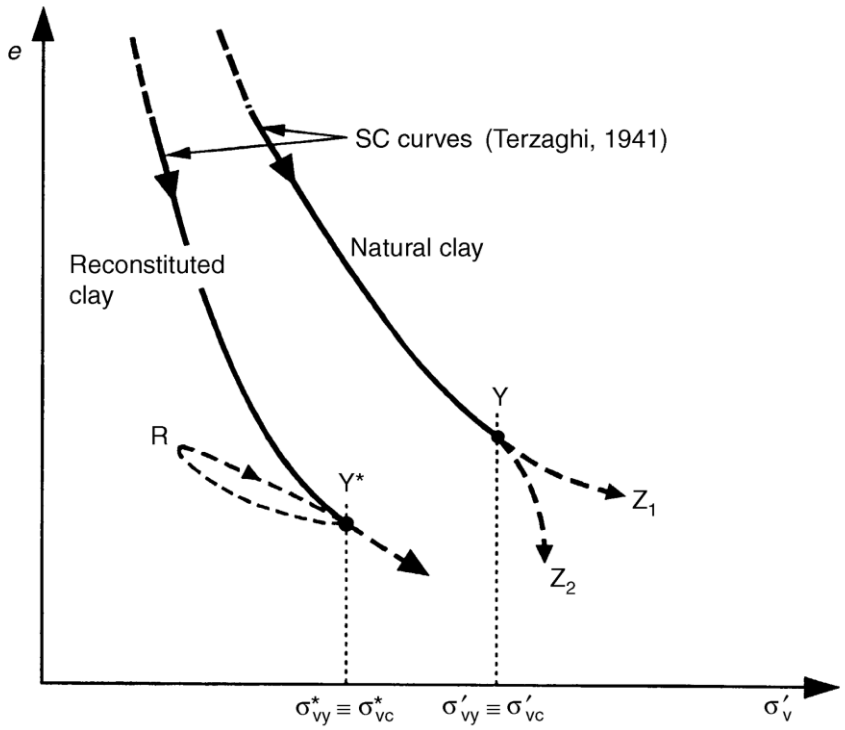

(a)

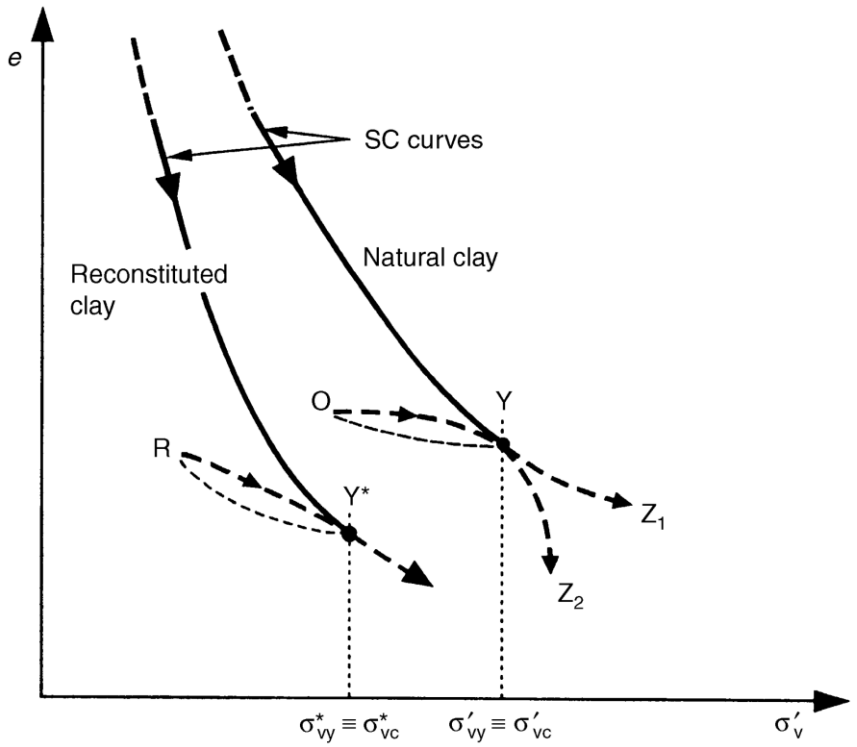

(b)

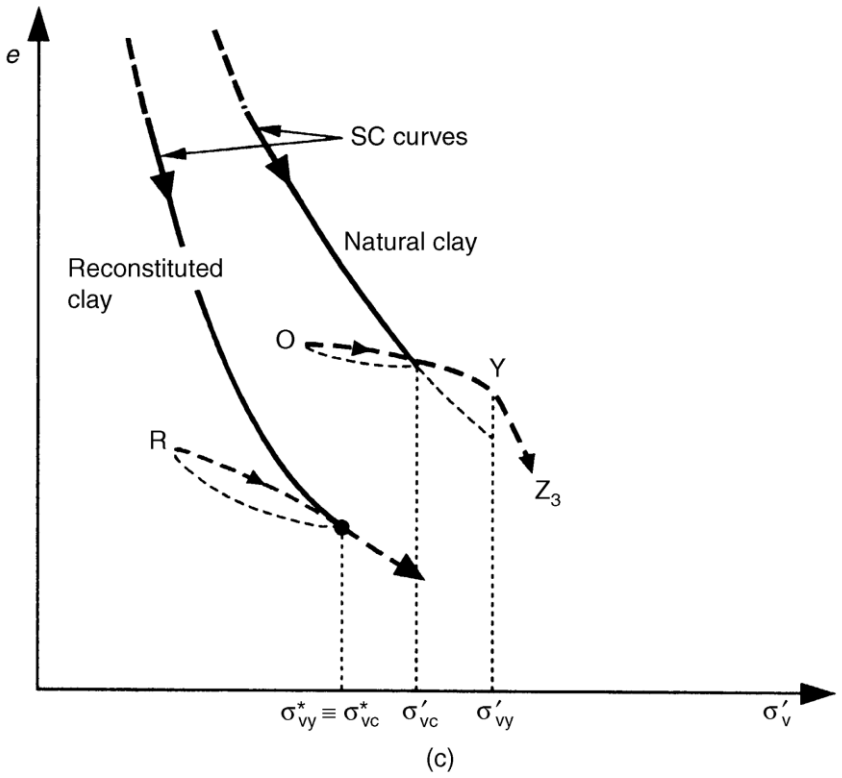

Figure 3.6 Response of clays to one-dimensional compression. The natural clay is (a) normally consolidated with a sedimentation structure; (b) simply overconsolidated; (c) overconsolidated with a post-sedimentation structure at gross yield (Cotecchia and Chandler, 2000)

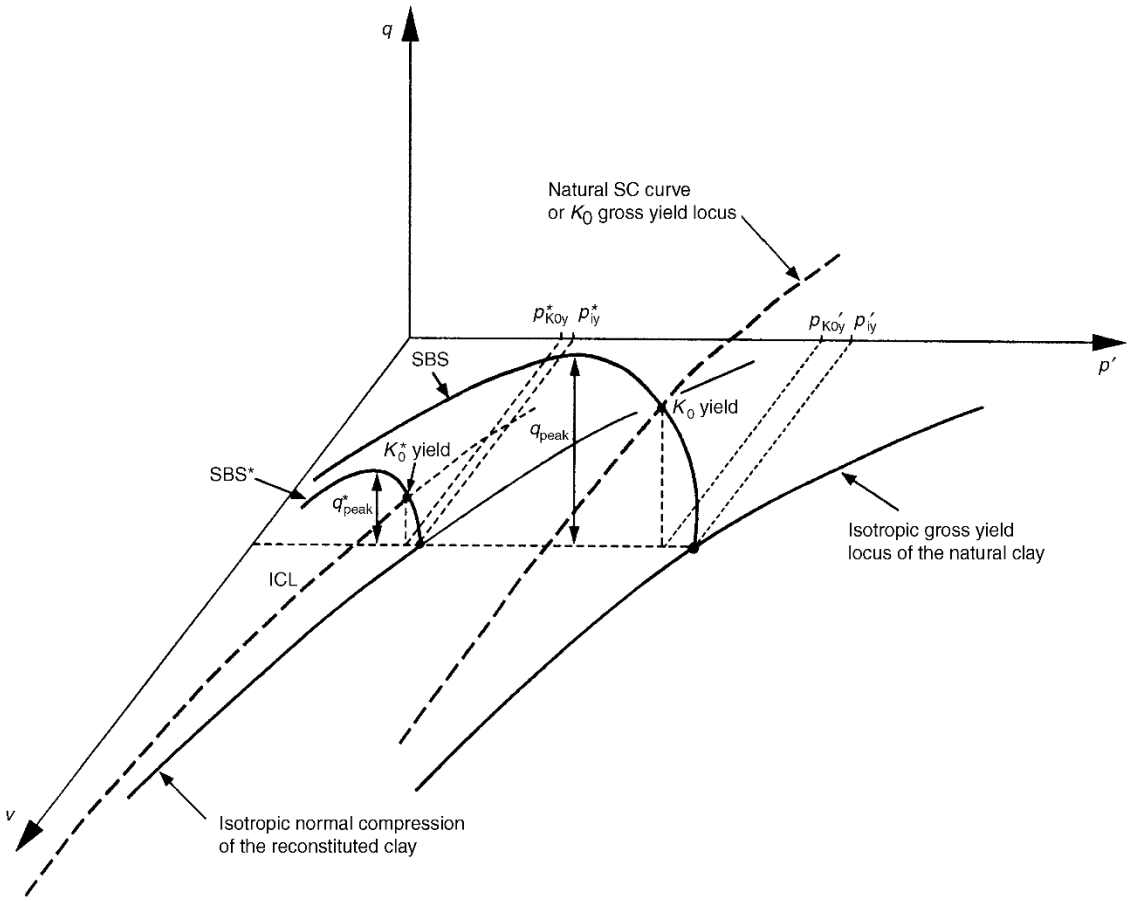

Figure 3.7 Idealised behaviour of a natural clay and of the same clay when reconstituted (Cotecchia and Chandler, 2000)

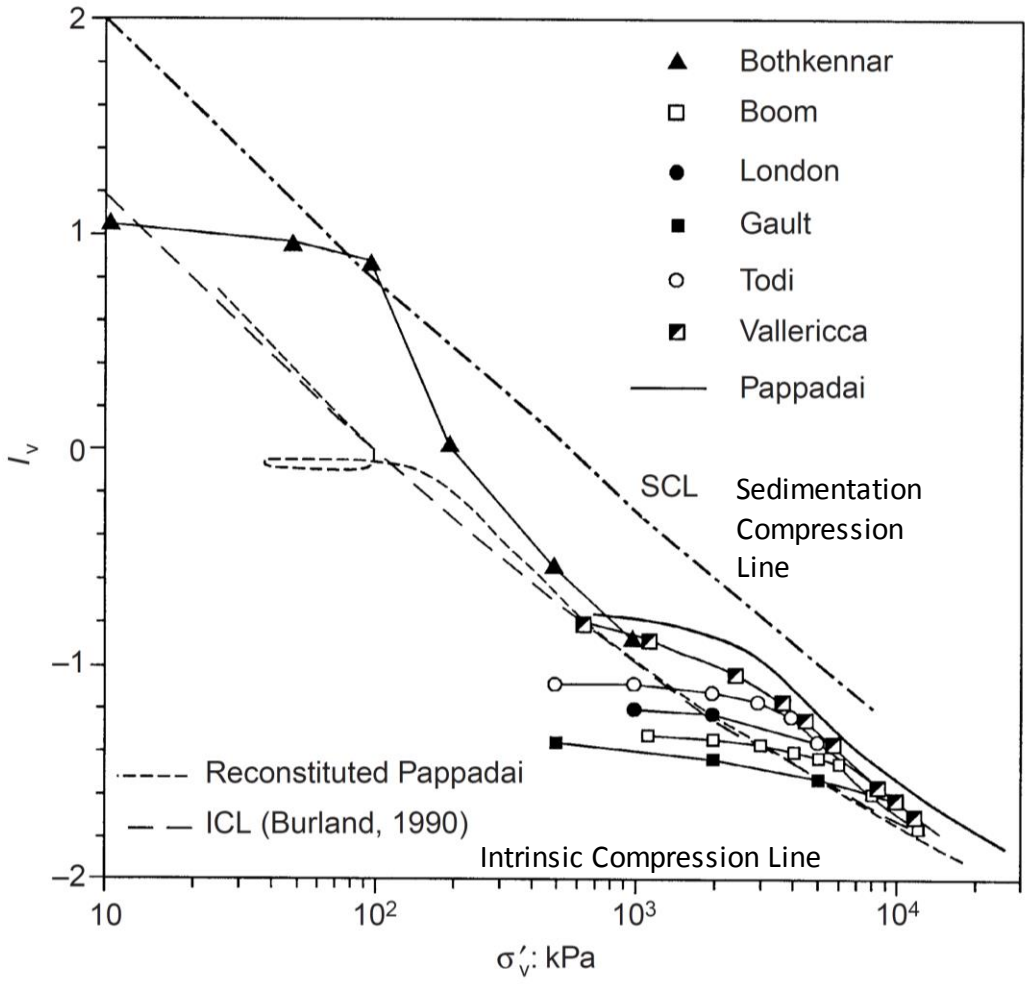

Figure 3.8 One-dimensional compression of natural and reconstituted clays plotted against the void index (Cotecchia and Chandler, 2000)

The difference in the fabric arrangement of Pappadai clay in its natural and reconstituted state has been examined using a Cambridge 500 scanning electron microscope (Cotecchia and Chandler, 1997). As shown in Figure 3.10, the fabric of natural clay is densely packed while that of the reconstituted clay appears more open than the natural clay, reflecting the considerable difference in the pre-consolidation pressures of the two clays.

Following the works of Burland (1990), Burland *et al.* (1996), Cotecchia and Chandler (1997) and Cotecchia and Chandler (2000), Low (2004) in his master's thesis explored the effect of soil structure on the behaviour of Pulau Tekong (PT) clay. This Singapore marine clay generally consists of two distinct members, the upper marine clay (upper PT) and the lower marine clay (lower PT) separated by a stiffer intermediate layer, widely considered to be the desiccated crust of the lower PT. The lower PT was deposited sometime between 12,000 to 18,000 years ago, at the end of the

Pleistocene epoch while the upper PT is deposited after the last Ice Age (Holecene epoch) and usually thought to be younger than 10,000 years (Pitts, 1992). To compare the undrained shear strength between natural and reconstituted clay, tests conducted on PT clay include constant volume direct shear test (DST), unconfined compression test (UCT) and unconsolidated undrained tests (UU). The test results as plotted in Figure 3.11 show the normalised peak undrained shear strength against normalised effective vertical stress for natural and reconstituted PT clay.

In both graphs, natural PT clay samples have a higher shear strength at a given effective vertical stress than reconstituted PT clay. A similar trend has been observed when the undrained shear strength is plotted against shear strain as shown in Figure 3.12 and normalised Young's modulus against insitu vertical stress as shown in Figure 3.13. Clearly, the natural PT clay are much stiffer than the reconstituted PT clay and reached the peak undrained shear strength at a displacement or strain lower than the reconstituted sample. The post peak behaviour, however, shows that the reconstituted PT is ductile compared to a more brittle behaviour at its natural state.

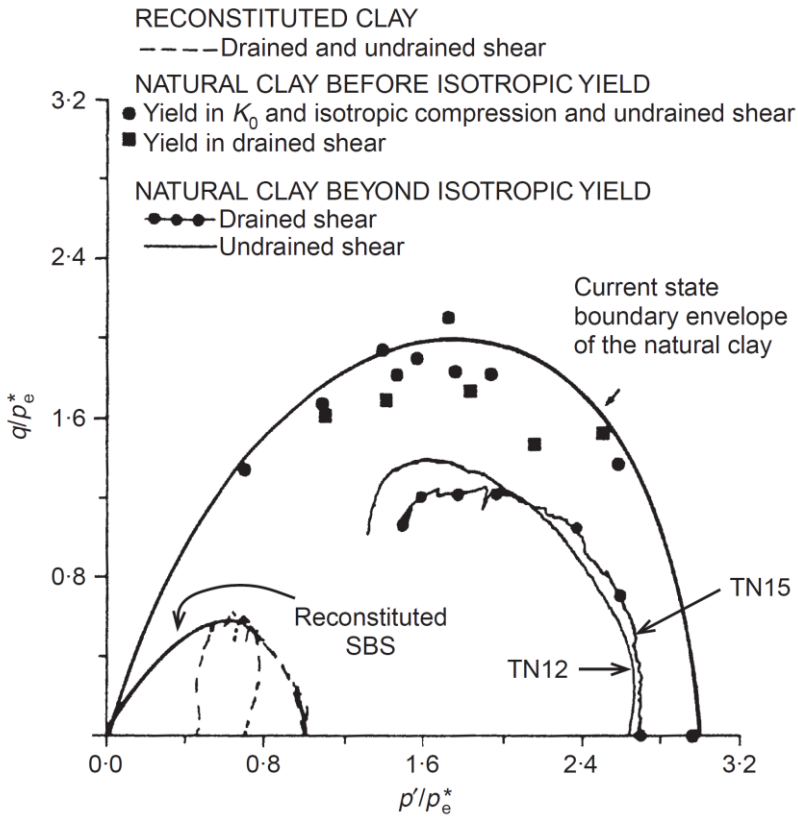

Figure 3.9 Pappadai clay: gross yield states of the natural clay, stress paths of the clay compressed beyond isotropic gross yield, and stress paths of the reconstituted clay (Cotecchia and Chandler, 1997)

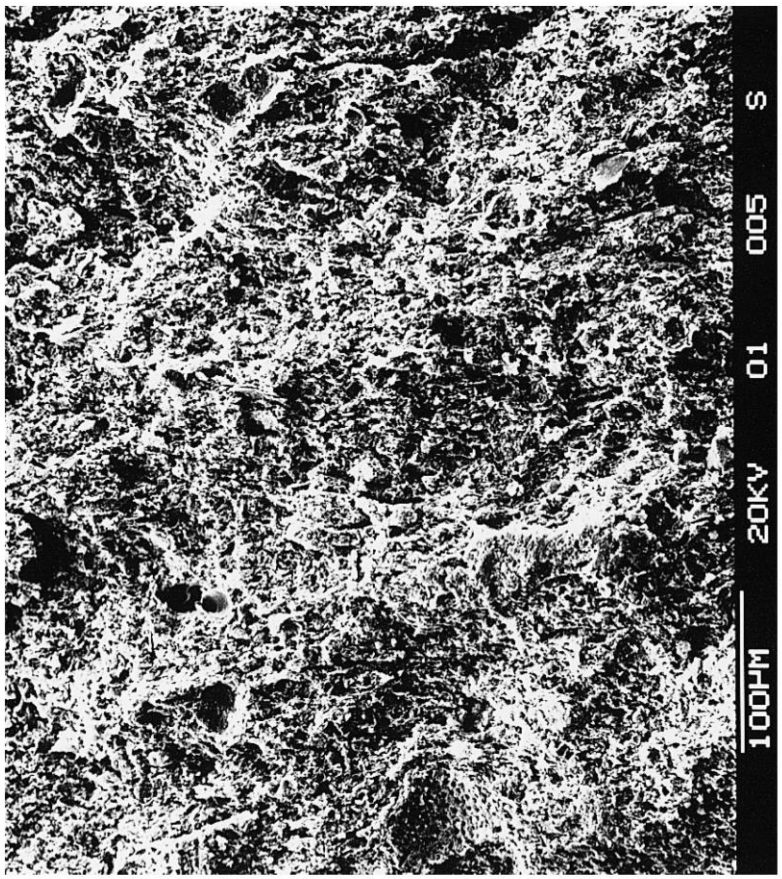

(a)

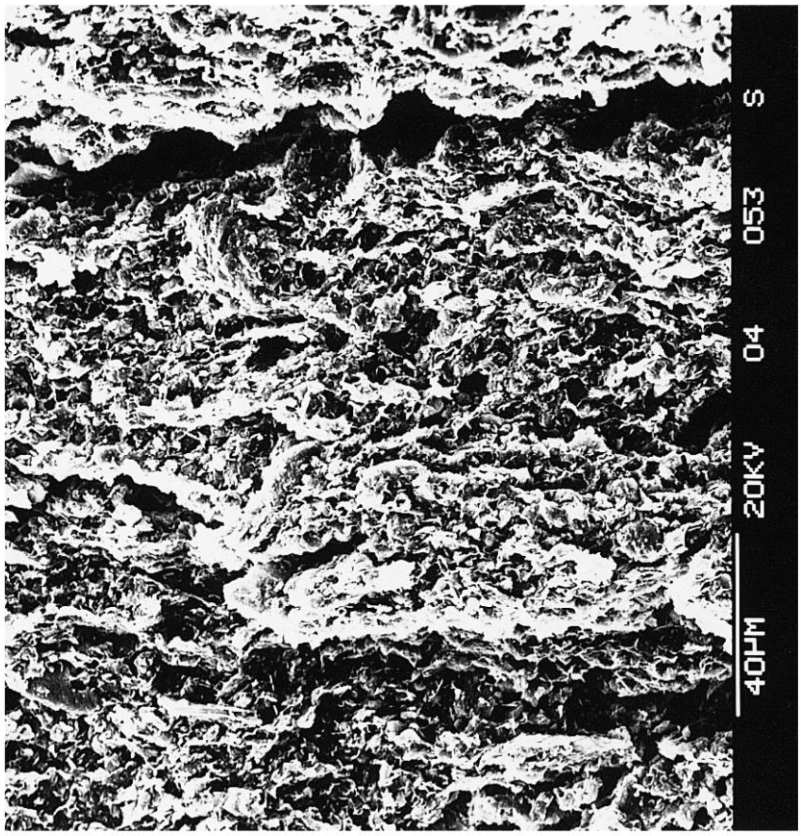

(b)

Figure 3.10 Pappadai Clay: fabric on a vertical fracture of (a) undisturbed clay and (b) reconstituted clay (Cotecchia and Chandler, 1997)

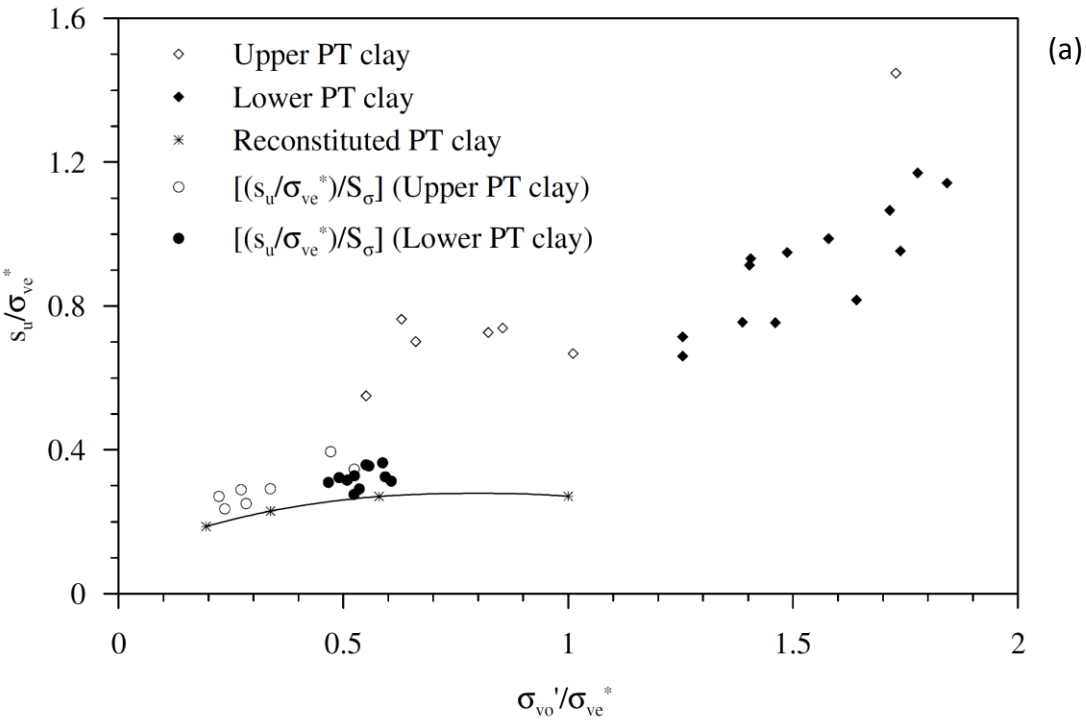

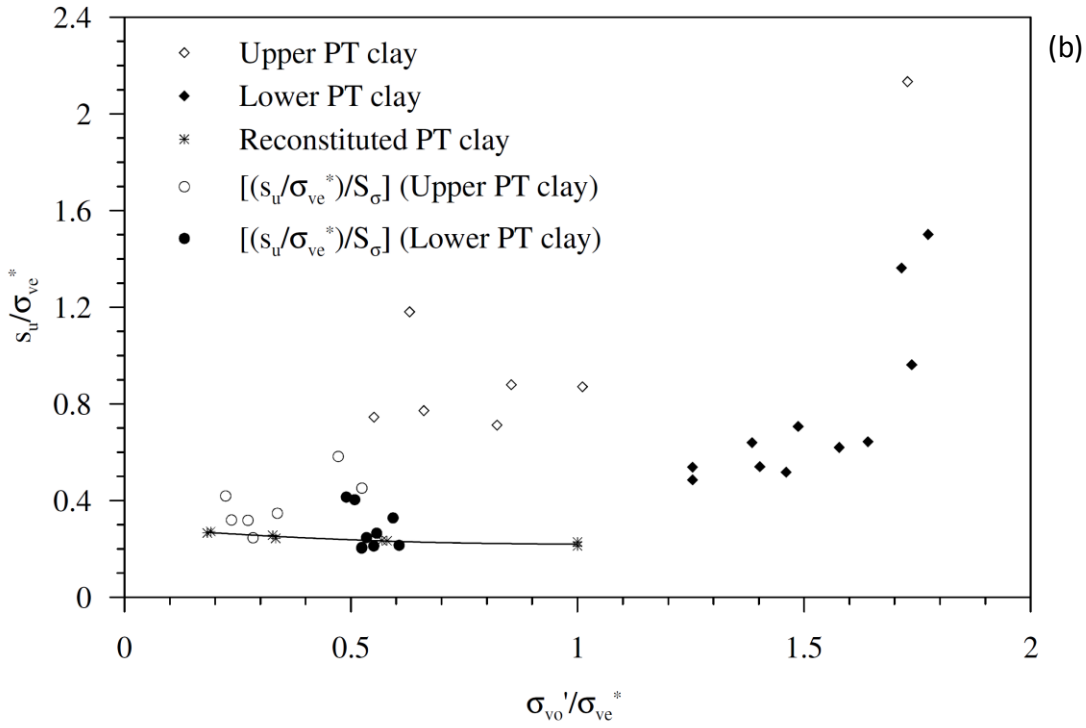

Figure 3.11 Peak strength envelope obtained by (a) DST for natural and reconstituted PT clay and (b) UCT for natural PT clay and by UU for reconstituted PT clay (Low, 2004)

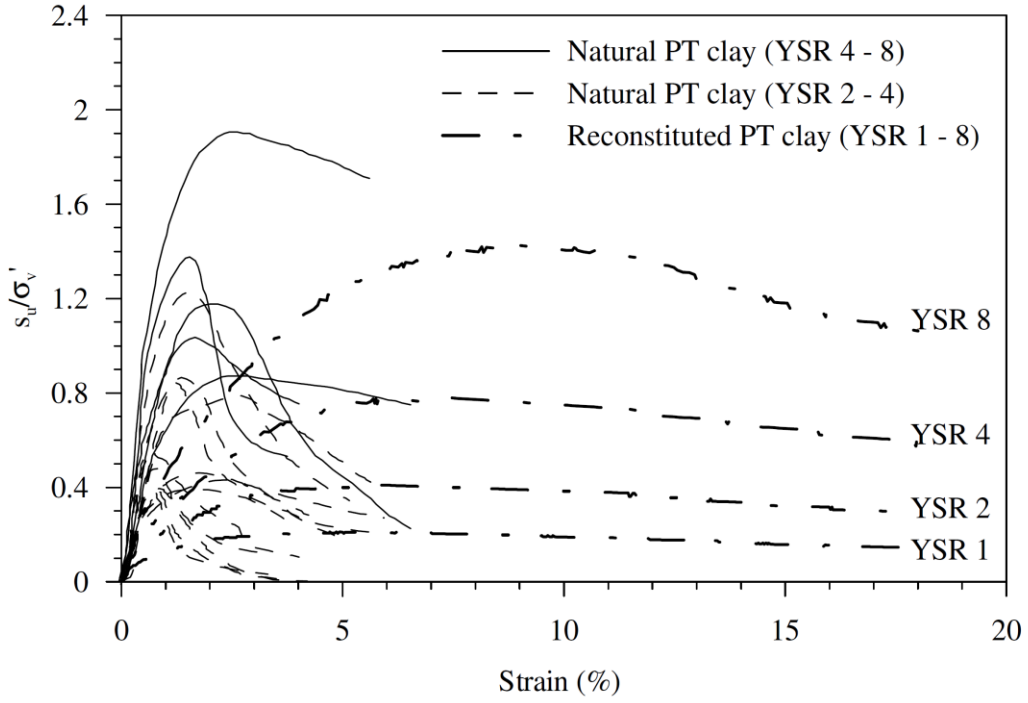

Figure 3.12 Stress-strain curves for natural PT clay obtained by UCT and for reconstituted PT clay obtained by UU (Low, 2004)

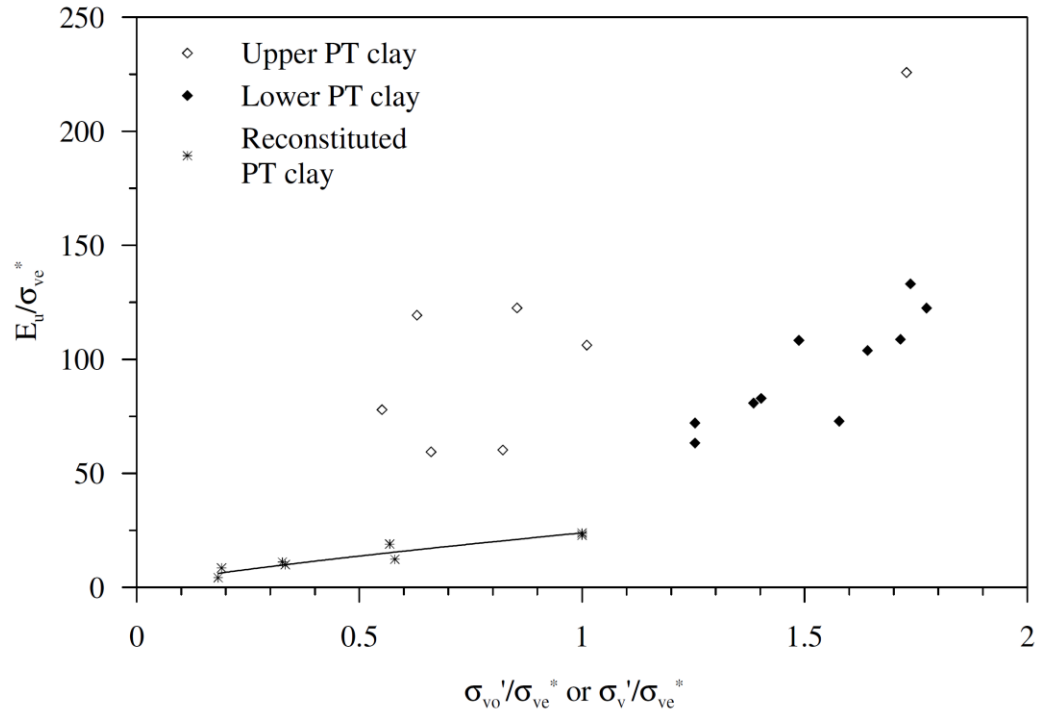

Figure 3.13 Normalised Young's modulus versus insitu vertical stress (Low, 2004)

Those earlier laboratory tests were conducted under monotonic loading which fairly represent soil conditions under static loading. More recent testing programme on structure degradation have also included dynamic tests, e.g. resonant column (RC) and

torsional shear (TS) tests, to determine the dynamic/cyclic properties of soils. However, there are very few laboratory data available in the literature comparing the dynamic/cyclic behaviour of natural and reconstituted soils. One of those studies is by d'Onofrio *et al.* (1998) wherein a reconstituted and natural sample of Bisaccia clay were tested using resonant column and torsional shear device at the same mean confining pressure. The test results have shown that the normalised shear stiffness of the natural sample degrades faster than the corresponding reconstituted material as shown in Figure 3.14 (a) due to destructuration caused by the increased loading throughout the test. A similar trend was obtained by Rampello (1993) from results of resonant column and torsional shear tests on natural and reconstituted samples of overconsolidated Vallericca clay shown in Figure 3.14 (b). Nonetheless, the natural clay material shows higher initial small-strain stiffness than the reconstituted sample. This has been similarly observed by Brosse *et al.* (2017) while examining the shear stiffness characteristics of UK stiff clays using triaxial bender element and resonant column tests which demonstrated a higher shear moduli for the natural clays as compared to their reconstituted counterparts as shown in Figure 3.15 to Figure 3.17.

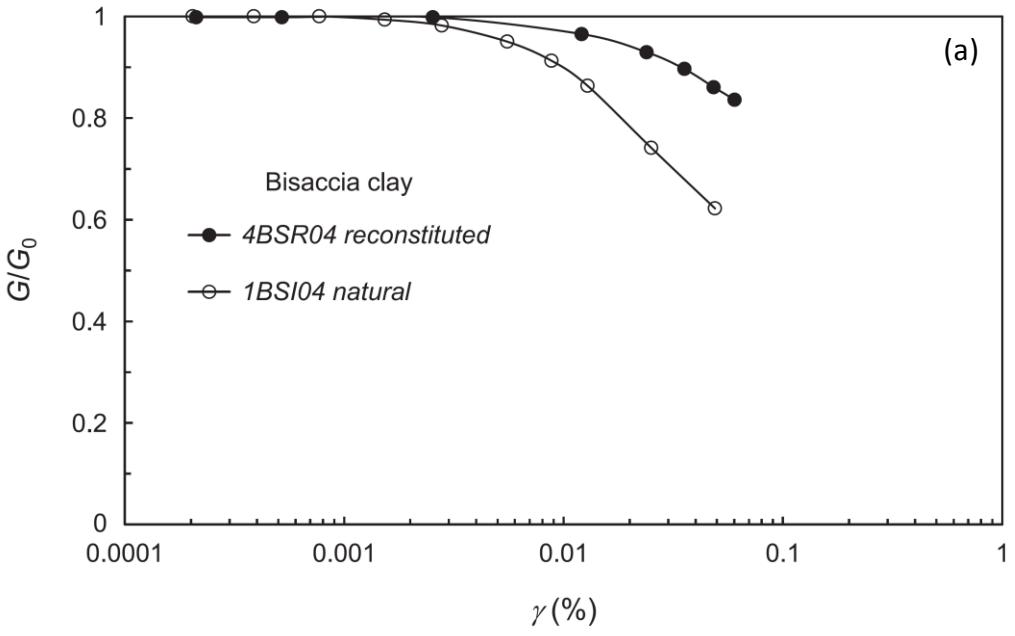

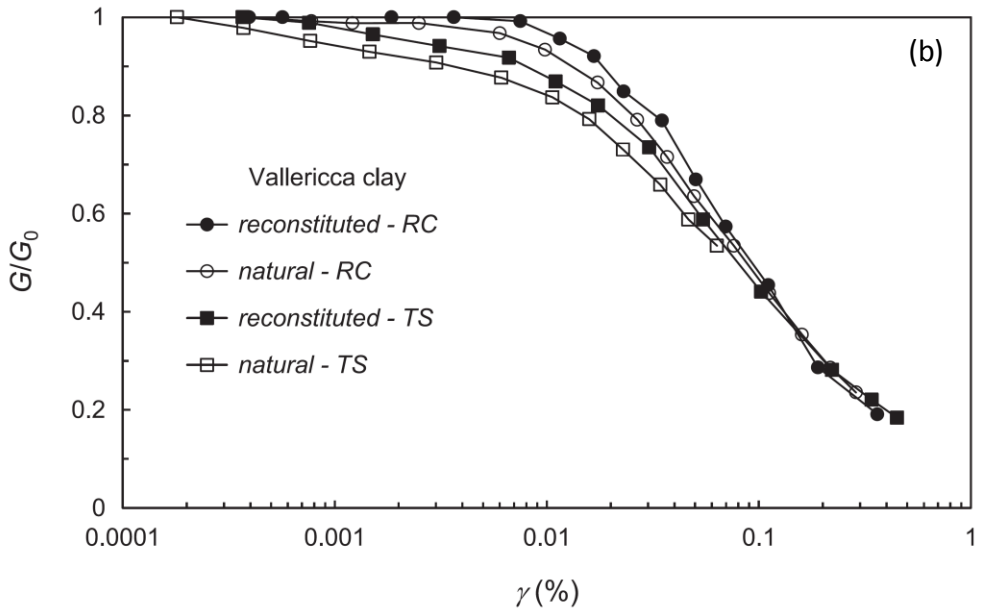

Figure 3.14 Normalised shear modulus against shear strain of (a) Bisaccia clay and (b) Vallericca clay (Elia and Rouainia, 2016)

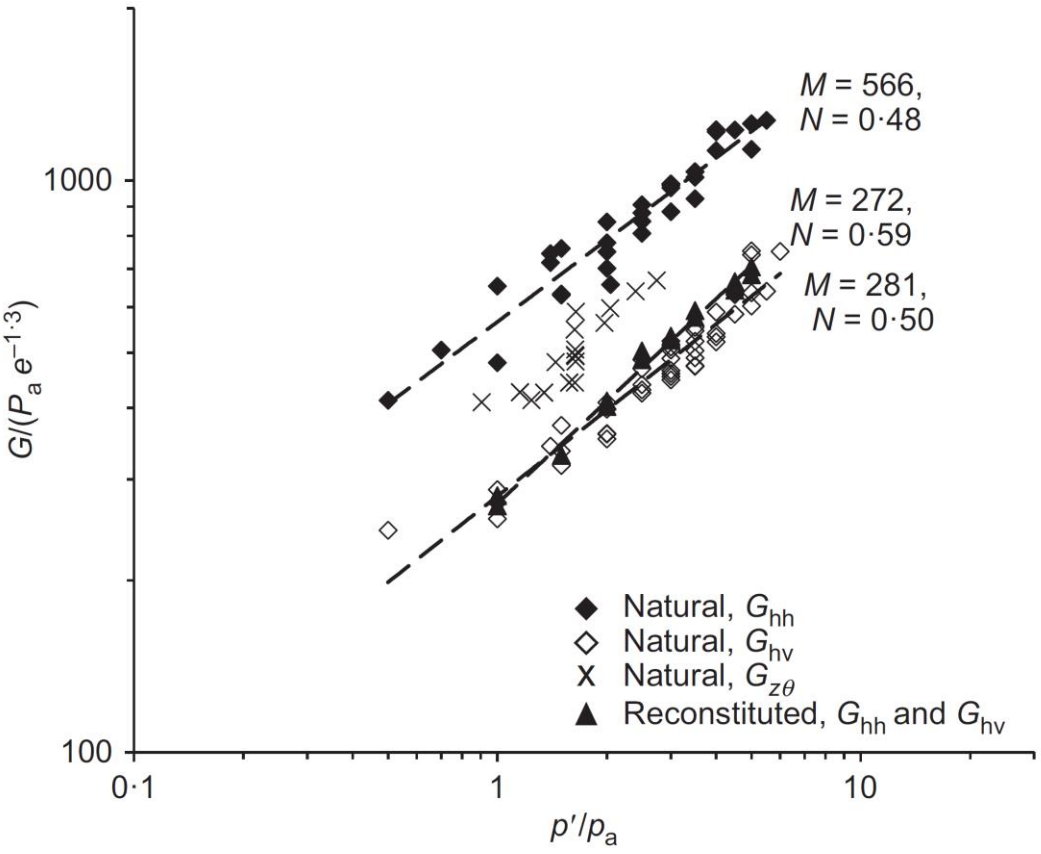

Figure 3.15 Elastic shear stiffness G_{hh} and G_{hv} measurements made by bender element tests on natural and reconstituted Gault clay, along with HCA resonant column $G_{\theta z}$ trends; normalised for void ratio (Brosse *et al.*, 2017)

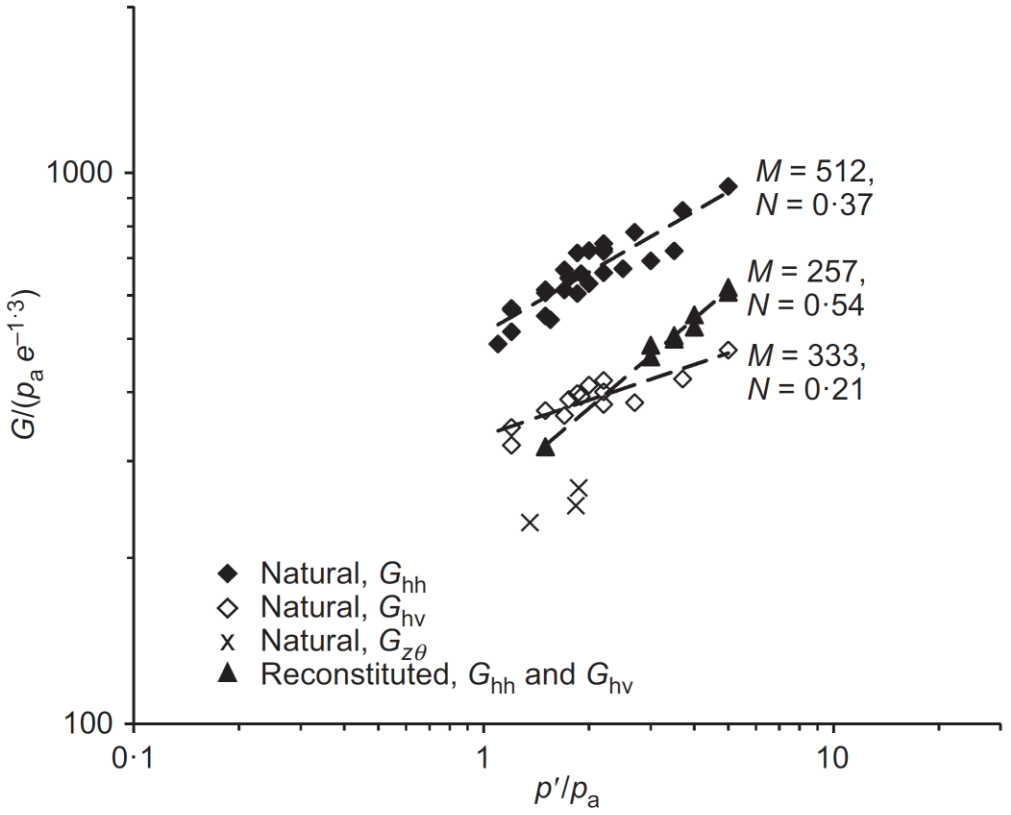

Figure 3.16 Elastic shear stiffness G_{hh} and G_{hv} measurements made by bender element tests on natural and reconstituted Kimmeridge clay, along with HCA resonant column $G_{\theta z}$ trends; normalised for void ratio (Brosse *et al.*, 2017)

Nash *et al.* (2007), on the other hand, has carried out a systematic investigation of the effects of destructuration on properties of the Bothkennar clay using changes of small strain shear stiffness G_0 as an indicator of damage. Testing was carried out in a Bishop-Wesley stress path apparatus on cylindrical samples fitted with mid-height pore pressure transducers and bender elements enabling measurements to be made on three shear wave velocities. The findings have shown that destructuration by undrained shearing results in a reduction of G_0.

Research by other authors such as investigation on Ballina clay by Pineda *et al.* (2016), have followed the same observation and conclusion where destructuration has resulted to reduction of void ratio at a given stress state, changes in small strain shear stiffness G_0, changes to soil's stiffness and moduli, shrinkage of state boundary surface, reduction of yield stress, and reduction of undrained strength.

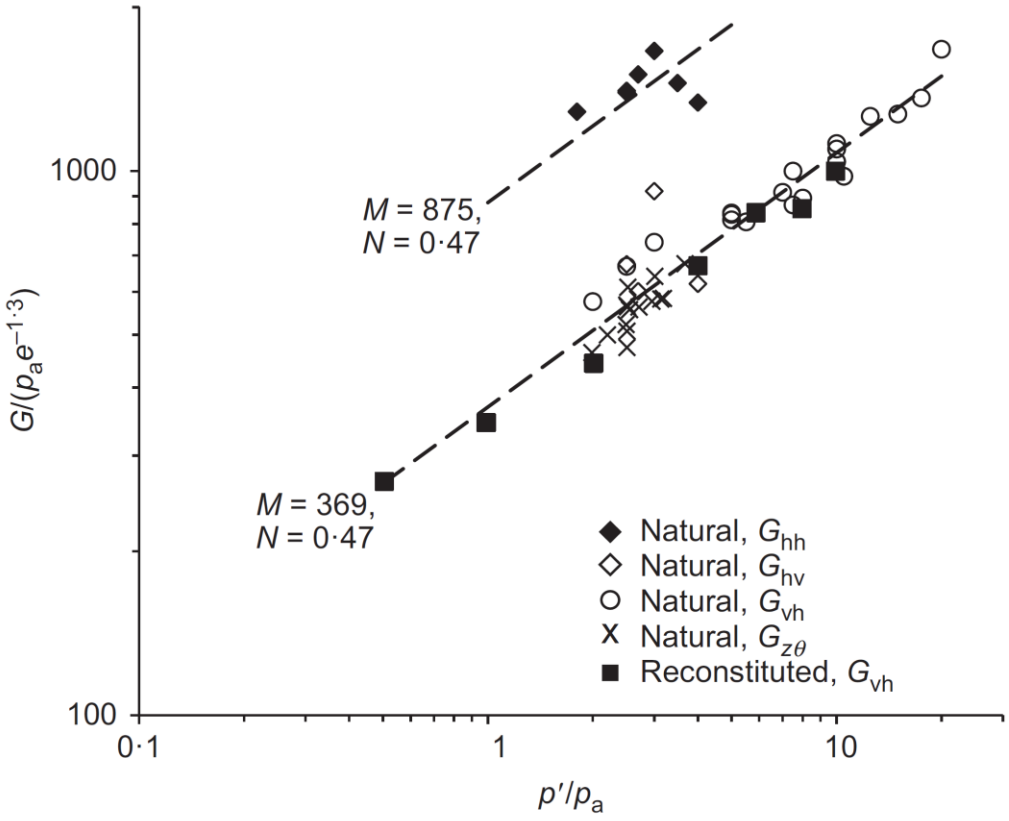

Figure 3.17 Elastic shear stiffness G_{hh} and G_{hv} measurements made by bender element tests on natural and reconstituted Oxford clay, along with HCA resonant column $G_{\theta z}$ trends; normalised for void ratio (Brosse *et al.*, 2017)

All these studies confirm the dependency of the soil's intact properties on the initial structure and the significance of destructuration in changing the stiffness and strength of natural clays. Given that many geotechnical systems are embedded into the soil mass, this can lead to a different response in the soil-structure interaction under both static and dynamic conditions.

Most of the studies on the effect of destructuration on geotechnical systems have focused on static loading in clay deposits, such as on shallow foundations [e.g. Lagioia and Potts (1999)], earth embankments [e.g. Panayides *et al.* (2012)] and tunnels [e.g. González *et al.* (2012)]. In contrast, relatively few contributions studying this aspect as applied to dynamic conditions, e.g. earthquake event, can be found in the literature [e.g. Elia and Rouainia (2014)].Thus the need to explore this subject further. The author aims to contribute to this less ventured subject by investigating the effect of progressive destructuration of natural soils, particularly highly structured clay, on

tunnels brought about by intense dynamic actions, i.e. earthquake loading and its subsequent influence on the behaviour of these substructures.

3.4 Researches on tunnel-soil behaviour in static and dynamic conditions

For centuries, the design and construction of tunnels merely relied on actual experience. It was only around the 1900s that research on the mechanical processes started as evident from studies by Kommerell (1912), Wiesmann (1909) and Leon and Willheim (1910) where the development of stresses around the tunnel was investigated as shown in Figure 3.18. Research on tunnel behaviour has since evolved with an increased effort in establishing theoretical background for the analysis and design of tunnel to the use of analytical tools in the 1st half of the 20th century and numerical methods (e.g. FEM, FDM, BEM) in the 2nd half of the 20th century due to the availability of computers (Schubert and Beer, 2003).

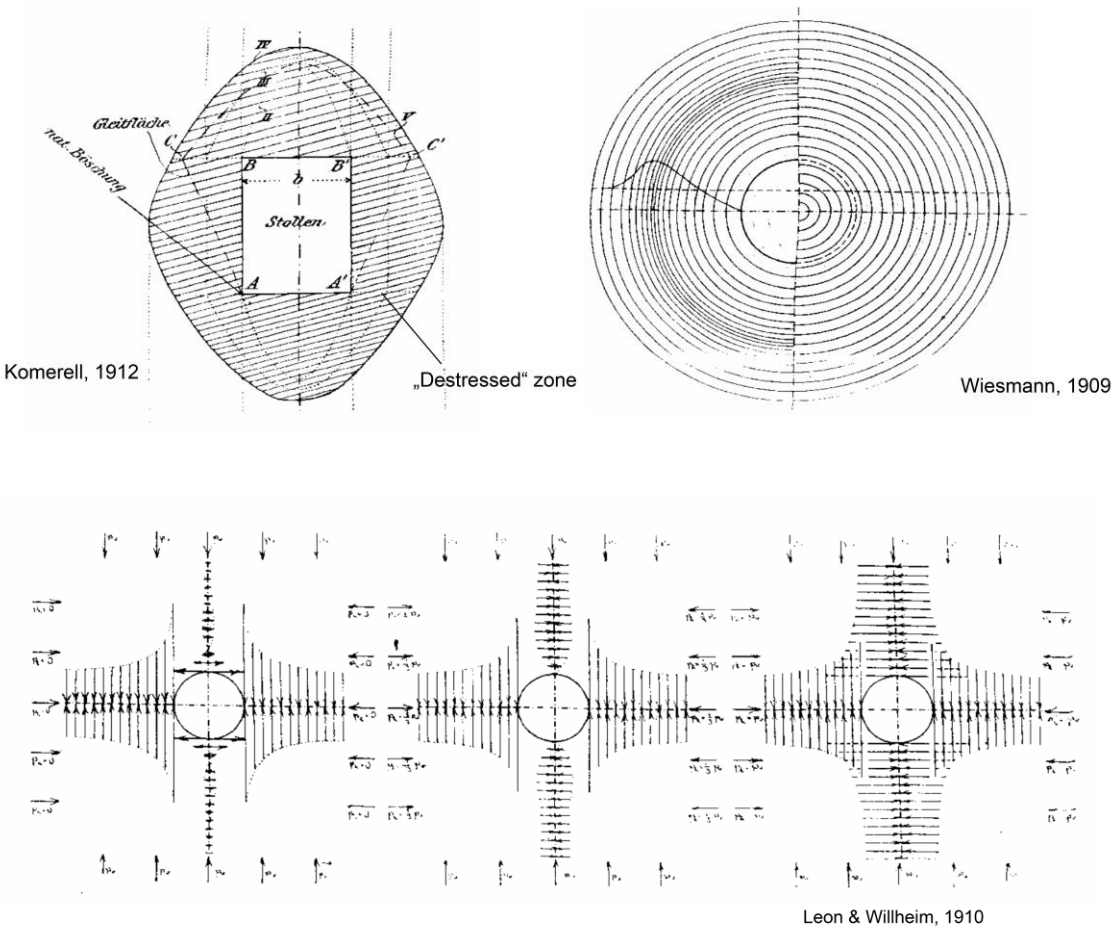

Figure 3.18 Early studies on the mechanical processes in tunnelling

Nowadays, there has been abundant research in the literature exploring tunnel-soil behaviour in static conditions in both 2D and 3D. This research has covered a wide range of topics from continuous refinement of analytical methods [e.g. Curtis (1976), Muir-Wood (1975)] to further advancement in numerical approaches [e.g. Moldovan and Popa (2012), Namazi *et al.* (2012)]. Moreover, researchers have also explored the use of simple soil constitutive models [e.g. Oettl *et al.* (1998)] to advanced models ([e.g. González *et al.* (2012)], from single tunnel [e.g. Surarak (2011)] to multiple tunnels [e.g. Laver and Soga (2012), Koungelis and Augarde (2004)] and with different arrangements [e.g. Shalabi (2017)]. Cases of an ideal single layer of soil [e.g. Flores and Mayoral (2011)] to multi-layers [e.g. Zhang *et al.* (2015), González *et al.* (2012)] have also been investigated as well as the tunnel's interaction with adjacent structures [e.g. Mroueh and Shahrour (2003)]. There are also various published studies for special cases such as rectangular [e.g. Huang *et al.* (2018)], double-O [e.g. Chen *et al.* (2016)] and horseshoe-shaped tunnels [e.g. Goit *et al.* (2011)] which are commonly used in the sequential excavation method (SEM) known as the New Austrian Tunneling Method (NATM). In contrast, research in dynamic conditions are less extensive, less so with cases using advanced soil constitutive models with 3D modelling.

Although some early studies in the seismic performance of underground structures were known, it was not until late 1960s that the focus on this topic started to flourish (Hashash *et al.*, 2001). One of the first underground facilities that took seismic effects into consideration was the Bay Area Rapid Transit (BART) system in San Francisco, California, USA (Kuesel, 1969). By 1973, Okamoto *et al.* (1973) demonstrated through model tests and measurements of the seismic response of an immersed tunnel in Tokyo that the tunnel behaviour is dominated by the deformations and strains imposed on the structure by the surrounding ground which relate to the dynamic properties of the soil and not the inertial properties of the tunnel structure itself. These findings have led to the development of design methods, such as the Seismic Deformation Method [e.g. Kawashima (2000)] which focused on the free-field deformation of the ground and its interaction with the underground structure. However, in many cases particularly in soft soils, the free-field deformation approach resulted in overly conservative designs due to lack of consideration on the stiffness of the tunnel structure. As such, several authors including St John and Zahrah (1987),

Wang (1993), Peck *et al.* (1972), Penzien and Wu (1998), Penzien (2000), Power *et al.* (1996), among others, have then incorporated the tunnel lining stiffness in the design and proposed closed-form and analytical solutions to determine the thrusts, bending moments and displacements of the tunnel under seismic loading based on the soil-structure interaction concept. This method, however, does not consider dynamic or wave propagation effects.

Thereafter advances in the computer and software technology have opened the doors to numerical analysis in the seismic performance of tunnels. Numerical approaches using FEM, FDM and BEM dominated the scene with several researchers including industry practice focusing on 2D approach [e.g. Khoshnoudian and Shahrour (2002), Pakbaz and Yareevand (2005), Liu and Song (2005), (Hashash *et al.*, 2005), Bolouri Bazaz and Besharat (2008), Amorosi and Boldini (2009), Azadi and Hosseini (2010), Shahrour *et al.* (2010), Kontoe *et al.* (2011)] to replace the closed-form and analytical solutions. An example of which is shown in Figure 3.19. Hashash *et al.* (2005), Pakbaz and Yareevand (2005) and Bolouri Bazaz and Besharat (2008), in particular, have compared the results of the tunnel lining forces from closed-form and analytical solutions with those from 2D pseudo-static numerical approaches. The studies highlight the limitations of the analytical solutions particularly the Penzien's solutions which highly underestimate the axial thrust in the tunnel lining for the no-slip condition. It also highlights the influence of the flexibility ratio (relative rigidity between the ground and the tunnel) on the magnitude of error between the analytical and numerical solutions and similarly on the tunnel lining forces. As the flexibility ratio increases, the difference between the results of the analytical and numerical solutions also increases but the bending moment and shear force decreases.

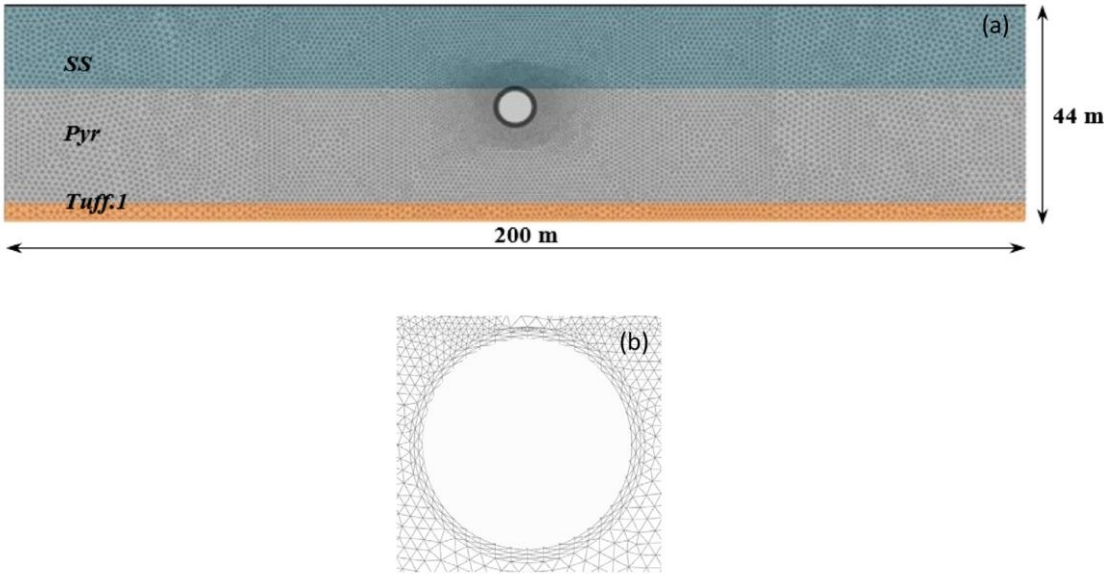

Figure 3.19 Example of 2D approach in tunnel seismic design: (a) 2D finite element model of the soil-tunnel system; (b) Detail of the mesh around the tunnel (Fabozzi *et al.*, 2017)

Some of the most recent researches in tunnel dynamics which took advantage of this 2D approach include Fabozzi *et al.* (2017) which uses this approach to predict the seismic behaviour of a tunnel in Napoli, Italy. In this paper, comparison was made between pseudo-static analysis (where the effect of an earthquake is simulated with an equivalent seismic load, statically applied to the boundaries of the numerical model as a distribution of peak free field displacements) and full dynamic analysis (where the force increments in the lining due to an earthquake are directly obtained from the simulation of the ground motion of the coupled soil-structure interaction in a time domain). The comparison shows that the pseudo-static analysis underestimates the increment of forces in the tunnel lining with respect to the full dynamic analysis. The difference in the magnitude was found to be strongly dependent on the interface behavior and lining flexibility with the tendency to increase with the lining flexibility and for a condition closer to ‘‘no slip” interaction. This follows on similar findings from previous studies by Bilotta *et al.* (2007), Argyroudis and Pitilakis (2012) and Tsinidis *et al.* (2016) which reinforces the need to perform full dynamic analysis to take into account the influence of pre-existing stress state around the tunnel and the permanent ground deformation during earthquake.

Another recent paper by Patil *et al.* (2018) & Choudhury *et al.* (2019) has explored the seismic responses by varying the shapes of tunnel enclosed in soft soil as well as the

tunnel embedment ratio, soil-tunnel interface conditions, lining thickness and input ground motion. It was observed from the results that circular tunnel performs better than other tunnel shapes under seismic loading in terms of development of stress and that the distortion of tunnels substantially decreases when embedment ratio is greater than 2. The results also show the contribution of the soil-tunnel interface conditions to the reduction of the distortion in the tunnel lining. The distortion in the full-slip interface condition was found to be 6% to 18% more than that in the no-slip interface condition. Regardless of the interface conditions, the internal forces in the tunnel lining increase with the lining thickness, as similarly observed by Bilotta *et al.* (2007), indicating the increasing effect of soil-structure interaction due to increase in flexural rigidity. The study also indicates the significant dependence of the induced dynamic earth pressure at the tunnel lining on the input motion characteristics, i.e. the higher the magnitude of the earthquake base acceleration, the higher will be the earth pressure. However, the location where the maximum incremental dynamic earth pressure occurs is constantly observed at the shoulder and knee regions of the tunnel lining.

Other researchers like Bilotta (2018) have integrated numerical modeling with physical centrifuge testing of tunnel under seismic actions emphasising the benefits of using well-defined and controlled experiments to calibrate the numerical model thereby increasing the reliability of any numerical study particularly where advanced soil constitutive models are used. Zhang and Liu (2018), on the other hand, investigated numerically the performance of a rectangular subway tunnel subjected to a far-field ground motion using finite element method incorporated with random fields. In the study, the effects of the uncertainty in soil property on the seismic response of the soil-tunnel system are examined by imposing spatial randomness in the shear modulus of soil. The results suggest that the randomness in small-strain shear modulus of clay can significantly affect the seismic responses (i.e. bending moment, shear force and lateral deformation) of rectangular tunnel walls in varying degrees. However, the average results from the random field was found to be identical to that computed from the deterministic case which also suggest that the randomness in the maximum shear modulus of soil introduces unbiased effects on the seismic response of tunnels.

Most recently, the author has published studies on the seismic performance of circular tunnel in structured clay [Cabangon *et al.* (2017), Cabangon *et al.* (2019)] using 2D FEM which are presented in Chapter 4 of this dissertation. In Cabangon *et al.* (2017) paper, a shallow circular tunnel in a typical soft clay deposit was subjected to earthquake loading to investigate the effect of an advanced kinematic-hardening multi-surface soil model and its reduced single surface version on dynamic soil-tunnel interaction. The results confirm the findings drawn by Kontoe *et al.* (2011) that single surface models can significantly over-predict the permanent increments of lining forces at the end of the seismic action with respect to kinematic-hardening models, thus highlighting the benefits of using more advanced constitutive models in tunnel design practice. A further study was conducted by Cabangon *et al.* (2019) to investigate the influence of soil structure degradation induced by earthquake loading on the transverse behaviour of shallow circular tunnels in natural structured clays. In the study, it was found that although a natural clay deposit is characterized by high stiffness and peak strength due to its initial degree of structure, seismic loads can induce sufficient stiffness degradation associated with strain-softening which facilitate transmission of higher tunnel lining loads. Both studies use 2D approach which inherently considers wave propagation effects. However, it requires simplifications to solve 3D problems by assuming plane strain conditions in the longitudinal direction which may not represent the actual response of the tunnel during a seismic event. Furthermore, seismic wave propagation has an arbitrary direction with respect to the axis of the structure that causes multi-directional loading for the soil deposit and tunnel lining, thus the need for a three-dimensional representation.

With the continued growth of high-performance computers and extensive software development, the use of 3D numerical approach in tunnel dynamics has increasingly becoming attractive as evident from works by Ohbo *et al.* (2004), Dobashi *et al.* (2008), Yamada *et al.* (2008), Yu *et al.* (2009b), Park *et al.* (2009), Sliteen *et al.* (2011), Gregor and Shobayry (2011), Dobashi *et al.* (2011), Yu *et al.* (2013b), (Yu *et al.*, 2013a), Sahoo *et al.* (2014) and Fabozzi and Bilotta (2016). For instance, Sliteen *et al.* (2011) evaluated the effects of the non-linear and irreversible behaviour of the soil on the seismic response of tunnel embedded in soft soils modelled in a 3D FDM by employing non-linear non-associated Mohr-Coulomb soil model and comparing the results with

those from purely elastic soil model. The results showed huge disparity between Mohr-Coulomb and purely elastic model proving the insufficiency of purely elastic soil model to determine the seismic induced response of soil-tunnel system. The study, thus, emphasises the importance of using non-linear soil model to capture more realistic results in soil-tunnel seismic cases.

Normally in numerical analysis, the seismic ground motion is applied uniformly. In reality, the ground motions are not uniform and display spatially variable characteristics. To account for the spatial incoherence (i.e. wave scattering, wave passage, site response and attenuation effects) including the variation in the amplitudes and frequency contents of the ground motion, Park *et al.* (2009) subjected a tunnel in both uniform and non-uniform (differing soil properties) ground under spatially varying ground motions to determine the seismic behaviour of the tunnel under such conditions. The study uses the longitudinal displacement profile, which has been developed from spatially variable ground motion time histories. This cannot be represented accurately in 2D and requires 3D modelling. The results of the analyses demonstrate that spatially varying ground motions causes longitudinal bending of the tunnel and can induce substantial axial stress on the tunnel lining in the longitudinal direction. The results also demonstrate significant increase in the axial stress and moment in the tunnel lining when the shear modulus of the ground decreases due to higher strains developed at softer ground. In addition, high axial stress and moment in the longitudinal direction can develop at the boundary between different soil conditions. The study was performed using pseudo-static 3D FEM, instead of full dynamic analysis, which is simplistic and ignored the variation in the ground motion displacement along the depth of the soil.

As mentioned earlier in the 2D cases, pseudo-static analysis underestimates the increment of forces in the tunnel lining with respect to the full dynamic analysis. Gregor and Shobayry (2011), on the other hand, used full dynamic analysis to compare the relative displacements between the bored tunnel and the station box structure when the earthquake ground motion is applied either uniformly or spatially varying. Comparing the results from the two types of ground motion, it was observed that there is no disparity in differential displacement for the uniform and spatially varying cases when the earthquake motion was applied transversely. This is not the case

though when the earthquake motion was applied longitudinally where there is notable increase in the differential displacement for spatially varying case compared to the uniform case. These findings might explain the significant increase in the axial stress generated in the tunnel lining from the results of Park *et al.* (2009).

Taking advantage of the availability of high-performance computers with enhanced mass storage capabilities, Ohbo *et al.* (2004) and similarly Dobashi *et al.* (2008), Yamada *et al.* (2008), Yu *et al.* (2009b), Dobashi *et al.* (2011), Yu *et al.* (2013b) and Yu *et al.* (2013a), utilised large-scale three-dimensional dynamic analysis to investigate the seismic performance of complex tunnel structures such as an underground motorway junction as shown in Figure 3.20 and a long-distance water conveyance tunnel connected to three working shafts with refined model including bolts and joints as shown in Figure 3.21. These large-scale 3D models capture not only the complicated geometric configurations of the tunnel but also the spatial variations of the ground and the tunnel conditions (Figure 3.22). Such complexities cannot be reflected accurately and evaluated rationally in a 2D or even a small-scale 3D soil-structure analysis. In their works, Ohbo *et al.* (2004), Dobashi *et al.* (2008), Yamada *et al.* (2008) and Dobashi *et al.* (2011) investigated the responses of a complex road tunnel configuration in a large-scale 3D model by full dynamic analysis. The model has considered the non-linear behaviour of the soil and comprises of more than two million nodes and elements. The ground input motion was applied parallel and perpendicular to the tunnel axis separately. The results confirmed earlier findings that the seismic response behavior of the tunnel structure significantly changes depending on the characteristics such as direction, acceleration and frequency of input earthquake ground motion. It also shows that ground motion applied in the longitudinal direction produces tensile and compressive stress in the longitudinal direction while the transverse earthquake motion produces not only transverse stresses but also longitudinal stresses (longitudinal bending, longitudinal shear and torsion). These orthogonal stresses and corresponding strains which cannot be predicted in 2D can have substantial effect on the design of the tunnel lining and therefore should not be ignored. As similarly observed by Park *et al.* (2009), the response is small for the tunnel located in hard ground, while the response is large in soft ground in the vicinity of the surface. When the results of the 3D analysis were compared with those of the 2D, the responses of

the tunnel from both analyses agree very well for the section located in hard ground but do not agree for the section in soft soil layer. It was also observed that the maximum response displacement between the two analyses occurs at different time steps. These disparities between 2D and 3D responses for tunnels in soft soil, which can be attributed to a higher strain in the soft soil together with the 3D interaction of the soil and the tunnel structure, can be significant in terms of stresses in the tunnel lining, thus, can prove critical to the lining design. All these findings illustrate the benefits of 3D analysis for an adequate and rational evaluation of the earthquake behaviour and the seismic response of a tunnel particularly those located in soft ground.

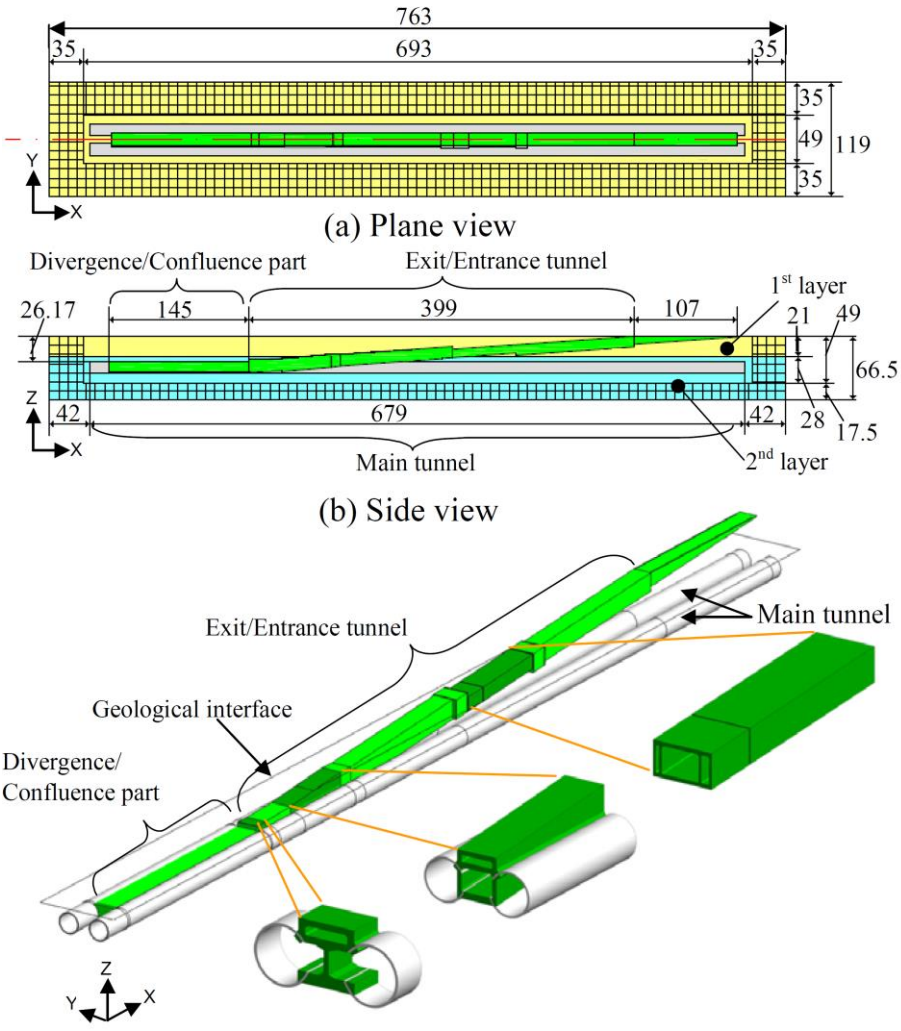

Figure 3.20 Numerical model of the underground motorway junction of the Yamate tunnel in Japan (Dobashi *et al.*, 2011)

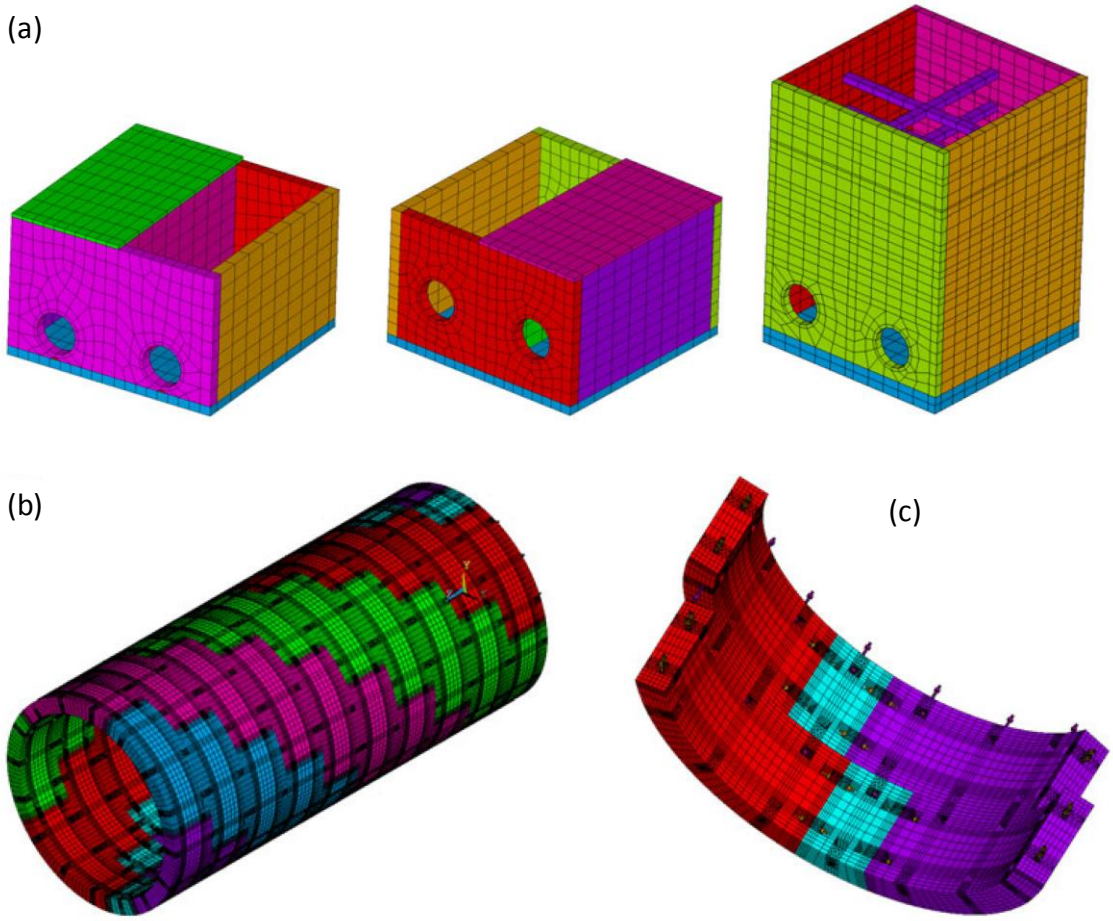

Figure 3.21 Water conveyance tunnel system: (a) Coarse-mesh model for the working shafts; (b) Coarse-mesh model for the tunnel; and (c) Refined-mesh model for the tunnel including bolts and joints (Yu *et al.*, 2009a)

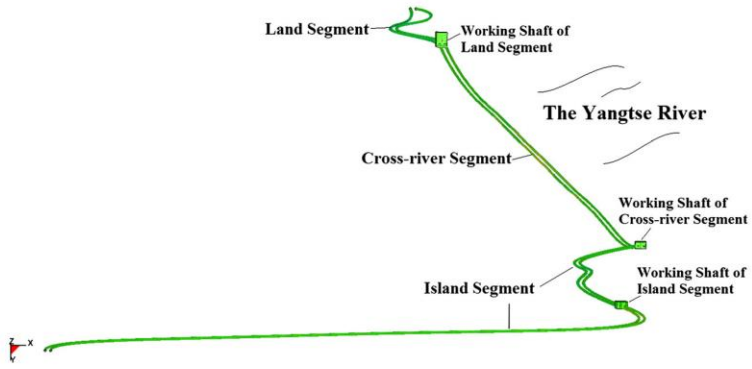

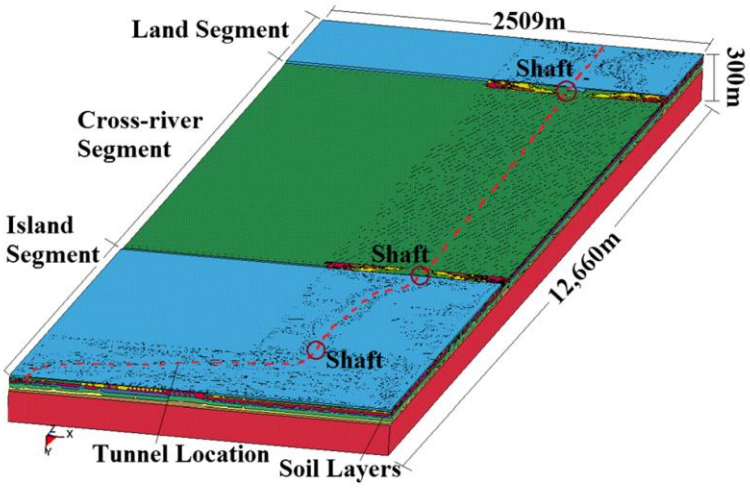

Figure 3.22 Coarse-scale soil and tunnel model (Yu *et al.*, 2013a)

In the case of the 14km water conveyance tunnel connected to three working shafts with refined model including bolts and joints, Yu *et al.* (2013b) and Yu *et al.* (2013a) employed a two-step multi-scale method to reduce the computational costs for such a large-scale 3D model. The final size of the 3D model is 12,660m x 2,509 m x 300 m (length x width x depth) and has a total of 2,503,632 nodes and 4,671,362 elements. The two-step multi-scale involves concurrent discretization of the entire domain with both coarse-scale and fine-scale finite element meshes. In the first step, a coarse-scale mesh is employed to identify the seismic response characteristics of the integral system and areas of interest where detailed analysis is required, whereas in the second step, a refined-scale mesh replaces the coarse-scale mesh in those areas of interest (e.g. inclusion of bolts, joints and contact interfaces) and a new simulation with the composite model is carried out to determine in detail the dynamic response in positions of potential damage or interest. The approach went one step further by including both material (Ramberg-Osgood, a nonlinear hysteretic soil constitutive model) and contact interface nonlinearities in the multi-scale model and applying simultaneously both the longitudinal and transverse directions of the seismic ground motion either uniformly or spatially varying. Previous research has indicated that the largest demand on the tunnel is obtained when the seismic accelerations, imposed at bedrock, propagate along both the longitudinal and transverse directions [(Yu *et al.*, 2009a), (Hashash *et al.*, 2001)]. Similar to the underground motorway junction case, the results confirmed that the seismic response of the tunnel (i.e. deformations and stresses) depends on the characteristics (e.g. spectral shape) of the input ground

motion. The results show that seismically induced stress increments are dependent to both the tunnel depth and the wavelength of incident waves and that amplification of the seismically induced stress is more pronounced when the tunnel is located at a depth of around one quarter of the wavelength. The studies also show that the displacement demands under the spatially varying earthquake motion are larger than those under the uniform earthquake excitation, and thus serious deformation and stress responses of the tunnel are expected. In addition, the application of flexible joints in the tunnel lining reduces the stresses on the tunnel but may result in larger local deformation particularly at the joints thereby requiring more attention on the water-proofing design.

Current commercially available 3D analysis software and computing resources, however, still have limitations in the model size and computing capability particularly when using user-defined soil models and large number of time steps to fully capture the corresponding earthquake input signals. Also, high-performance computing in a supercomputer environment is not widely available yet due to the huge computational costs to use those machines. Another downside of the 3D approach is the need to create large size models and finer mesh sizes employing massive number of nodes and elements to achieve an acceptable accuracy in the results. This in turn, increases the computational time and complexity of the analysis and thus the computational costs. 3D large-scale calculations normally require cluster of supercomputer work stations running continuously for a long period of time and produce enormous amount of input and output data [(Yu *et al.*, 2009b), (Ichimura *et al.*, 2016)]. In general, the 3D approach is still in present-day considered computationally inefficient.

On the other hand, 3D models can account for the seismic wave propagation effects and can consider the construction sequence along the length scale of the tunnel which can only be approximated but cannot be reproduced realistically in 2D models. Some of the studies proposed to tackle these computational issues include using the earlier mentioned multi-scale method, image-based modeling and sophisticated approximation techniques [e.g. Yu *et al.* (2013b), Yu *et al.* (2013a), Ichimura *et al.* (2016), Yu *et al.* (2017)]. The image-based modelling and sophisticated approximation techniques are discussed in detail in Ichimura *et al.* (2016). In the case of the 3D large-scale underground motorway junction, a combination of structured (first-order shape

elements used outside of the complex region) and non-structured elements (normally second-order shape elements used within the complex region) was employed to reduce the computational cost in evaluating the stiffness matrix of element and the memory storage. To further reduce the computational costs, Ichimura *et al.* (2016) performed multi-scale method, image-based modeling and sophisticated approximation techniques to simulate the same model. The enhanced approach successfully reproduce the dynamic behavior of a full 3D model with good accuracy while considerably reducing the time to generate the finite element model from more than 2 months to 3 hours and the time to solve the resulting problem from 18,991.5 node hours on the K supercomputer to 257.5 node hours on a small PC cluster system. However, with the limited availability of high-performance computing to run large-scale modelling, the simplest method commonly used to reduce the computing cost is to optimise the size of the model by parametric studies subject to the capability of the numerical software and computing power. This can reduce though the accuracy of the solution. Hence, the small-scale 3D approach requires a good compromise between an acceptable accuracy and optimal computational time within the available computing capacity.

More recent papers that employ small-scale 3D full dynamic approach in simulating tunnels in seismic conditions considering the soil-structure interaction include Fabozzi and Bilotta (2016), Yue and Ang (2017), Zhou *et al.* (2018) and Cabangon *et al.* (2018). Fabozzi and Bilotta (2016) compared the seismic demand of a continuous and a segmental reinforced concrete lining. The 3D numerical model was calibrated against experimental centrifuge data and subjected to a transversal ground motion. Unlike the other studies mentioned previously, the model utilised a more advanced soil constitutive model, the Hardening Soil with small strain (HSS), an elastic-plastic isotropic-deviatoric hardening model which include non-linearity, hysteretic behaviour and strong stiffness variation with increasing shear strain amplitudes in the domain of small strains. In the study, HSS was able to capture the permanent increments of lining forces at the end of the seismic motion due to the accumulation of plastic deformation in the soil deposit which confirm the experimental evidences obtained by Lanzano *et al.* (2012). The result establishes the need to use a non-linear elasto-plastic hysteretic soil model to replicate a realistic response of the soil during earthquake even for

simple ground conditions, consistent with the findings by Sliteen *et al.* (2011), Amorosi and Boldini (2009) and Shahrour *et al.* (2010). Also, it was evident in the results that pre-seismic conditions (initial stress state), such as excavation and construction sequence, increase the seismic demand in the tunnel lining, as similarly observed by Bilotta (2018). This is due to the reduction of the soil stiffness around the tunnel during excavation which subsequently reduces the flexibility ratio during earthquake resulting to an increase in the internal forces of the tunnel lining. As such, the pre-seismic conditions must always be considered in the analysis. On the other hand, flexible joints in the segments reduce the internal forces in the lining compared to a continuous lining but increase the relative rotation between segments which can cause potential issue to segment gaskets, as similarly observed by Yu *et al.* (2013b).

Other studies such as works by Yue and Ang (2017) have explored the stochastic response and reliability of the tunnel system by modelling the elastic modulus and yield stress of the surrounding soil as a random field. The 3D soil-structure FEM model established for this study, as shown in Figure 3.23, was subjected to transverse earthquake ground motion. Two cases were compared. Case I considers only the elastic modulus as a random field while in Case II, both the elastic modulus and the yield stress of the soil are assumed as random fields. The analysis results show that the hoop forces, shear forces and bending moments of the tunnel lining along the longitudinal direction are not uniformly distributed due to the spatial variability in the soil parameter and the tunnel stresses are higher in Case II than those in Case I. However, the reliability of the tunnel in Case II is lower than that of Case I. Also, when compared with 3D, the results obtained with a 2D model of the soil–tunnel system are misleading or erroneous because 2D model ignores the strengths of the adjacent sections of the soil–tunnel system, thus stressing the significance of relying on 3D model to obtain realistic results.

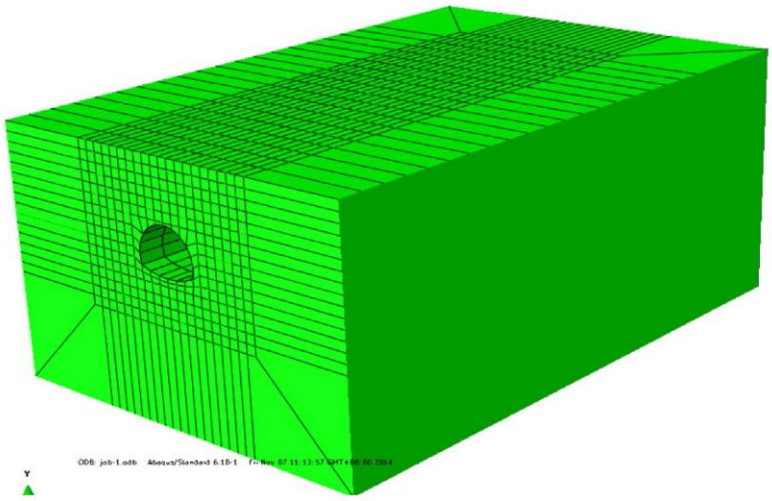

(a) soil-tunnel system

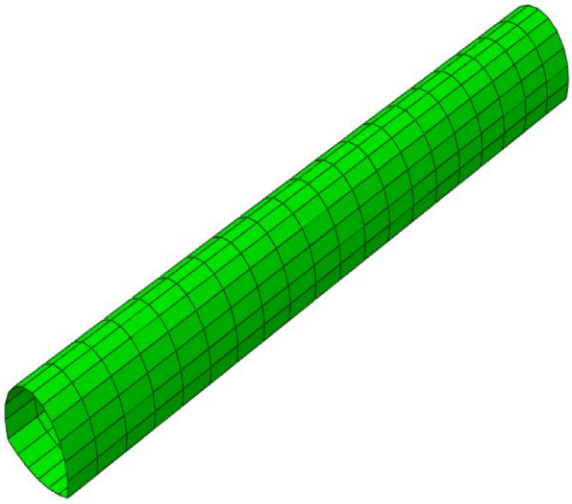

(b) tunnel model

Figure 3.23 3D finite element method applied to soil-tunnel dynamic system (Yue and Ang, 2017)

Following the works of Yu *et al.* (2013b) and Yu *et al.* (2013a), Zhou *et al.* (2018) studied the effects of spatially varying seismic ground motions and incident angles on the behavior of long tunnels using a small-scale 3D model. The studies confirm the findings by Yu *et al.* (2013b) that the response of the tunnel under the spatially varying earthquake motion is greater than those under the uniform input seismic motion. Moreover, in the case of uniform seismic input simulations, the maximum radial strain rate occurred at the middle point of the long tunnel and the radial strain rates were symmetrically distributed on the left and right sides of the tunnel while in the case of spatially varying seismic ground motions, the radial strain rate distribution is

asymmetric along the tunnel length. In terms of the effects of the incident angle, the values of maximum tensile/compressive stresses in the lining decrease with increasing incident angles. Cabangon *et al.* (2018), on the other hand, extended his earlier 2D works (Cabangon *et al.*, 2017), into 3D by investigating the effects of simultaneous application of multi-directional (transverse and longitudinal) seismic loading compared to uni-directional (transverse) earthquake motion. The 3D results are comparable to 2D in the transverse direction but generally lower due to the dissipation of the earthquake accelerations in the longitudinal direction. Consequently, longitudinal lining forces (i.e. axial compression and extension, torsional force and longitudinal bending moment) are produced which cannot be obtained using a 2D approach. It is also evident from the study that the transverse earthquake motion dictates the forces in the transverse direction. This observation justifies and validates the common use of a 2D model to design a tunnel section to account for ovaling/racking effects. In addition, the simultaneous application of a transverse and a longitudinal earthquake event at bedrock effectively reproduce a seismic motion acting at an angle with the tunnel axis. This allows to predict an increase in the longitudinal axial forces, in-plane shear and longitudinal bending moments in the lining. Ignoring these forces with a 2D approach can lead to un-conservative design, compromising the integrity and thereby the safety of the tunnel. These are all discussed in detail in Chapter 5.

It was observed from the reviewed papers and various other literature that simple linear-visco-elastic or elasto-plastic soil constitutive models (e.g. Linear isotropic elasticity, Ramberg-Osgood, Mohr-Coulomb, Modified Cam Clay, Drucker-Prager) have been heavily utilised in analysing the tunnel behaviour subjected to cyclic/dynamic conditions even for small-scale 3D models. This might be due to ease in obtaining the soil model parameters through conventional laboratory tests and the simplicity in formulating those constitutive models leading to reduced computing costs. However, for the case of soils under cyclic loading, it is necessary to employ advanced soil constitutive model to accurately predict the tunnel behaviour during earthquake which will be further discussed in Section 3.5. Only a few studies have considered soil constitutive models that include some or most of the advanced attributes observed during cycling loading as defined in Section 3.2 to determine the tunnel behaviour. Nevertheless, their application has been limited mostly to static or settlement analysis.

Some of which can be found in the works by Amorosi and Boldini (2005) (MSS), Dang and Meguid (2008) (Multilaminate), Valls-Marquez (2009) ("Bubble", S-CLAY1), Surarak (2011) (HS-Small), González *et al.* (2012) (RMW), Fernández Ruiz and Medina Rodríguez (2015) (HS-Small), Bian *et al.* (2016), Barciaga *et al.* (2016) (SANICLAY), Chen *et al.* (2016) (HS-Small). A further few exceptions have explored the dynamic application of these advanced soil models in tunnels which include Kontoe *et al.* (2008) (M2-SKH), Shahrour *et al.* (2010) (MODSOL), Kontoe *et al.* (2011) (M2-SKH), Tsinidis *et al.* (2013) (Modified kinematic hardening model combined with a Von-Mises failure criterion), Bilotta *et al.* (2014) (Hypoplastic, Bounding surface plasticity) and more recently by Cabangon *et al.* (2019) (RMW), Zhang and Liu (2018) (Hyperbolic-hysteretic), Mohammadi-Haji and Ardakani (2018) (Hypoplastic) and Fabozzi *et al.* (2017) (HS-Small).

These advanced soil models are able to appropriately capture features of the soil behaviour under seismic excitation, such as pore pressure generation, hysteretic damping and plastic deformation during unloading, at varying degree. Consequently, these models gave reasonable predictions for the seismically induced loads in the tunnel lining. Some of the major observations from those research include the ability of these models to predict permanent increments of hoop force, bending moment and shear force at the end of the seismic motion due to accumulation of plastic deformations as a result of the irreversible plastic behaviour of the soil [(Kontoe *et al.*, 2011), (Tsinidis *et al.*, 2013), (Bilotta *et al.*, 2014), (Cabangon *et al.*, 2019), (Bilotta, 2018)] as confirmed by experimental data (Bilotta *et al.*, 2014). This behaviour is not evident in visco-elastic models [(Amorosi and Boldini, 2009), (Tsinidis *et al.*, 2013)]. Plastic deformations can lead to a significant reduction in the seismic amplification, thereby reducing the seismic-induced bending moment in the tunnel lining (Shahrour *et al.*, 2010). Kontoe *et al.* (2011), Cabangon *et al.* (2017) and Mohammadi-Haji and Ardakani (2018) also observed that simple elasto-plastic models (e.g. Mohr-Coulomb, Modified Cam Clay) generally overpredict the transient loads acting on the tunnel lining during earthquake and underestimate the small-strain stiffness (Bilotta *et al.*, 2014) with respect to advanced soil constitutive models.

Normally, simple elasto-plastic models do not provide adequate small-strain damping, thus cannot reproduce hysteretic behaviour at small strains, leading to substantial

overestimation of the seismic loads acting on the tunnel lining. This is usually compensated for by the use of Rayleigh damping. Rayleigh damping approximates the material damping which is difficult to quantify a priori and can have a crucial influence on the results of numerical simulations as proven by Kontoe *et al.* (2011), Bilotta *et al.* (2014) and Bilotta (2018). Small Rayleigh damping, however, can help to overcome unrealistic amplification at high frequency (Bilotta *et al.*, 2014) even for advanced soil models. On the other hand, advanced constitutive models can reproduce hysteretic damping in both small and large strain ranges irrespective of the initial stress state of the soil [(Kontoe *et al.*, 2011), (Mohammadi-Haji and Ardakani, 2018)], although some models may show a more pronounced stiffness decay and increase in damping at smaller strain levels (Bilotta *et al.*, 2014). One key aspect that Bilotta *et al.* (2014) observed is that advanced models that allow coupling between plastic shear and volume strains can better simulate the volumetric plastic straining induced by cyclic shear loads which significantly improve the prediction of surface settlement. The absence of this feature in simple elasto-plastic models can lead to substantial underestimation of surface settlement at the end of ground motion (Mohammadi-Haji and Ardakani, 2018). All these highlight the inadequacy of simple elasto-plastic models for dynamic analysis.

Two crucial factors that affects the numerical results for tunnels under cyclic loading are (i) the relative flexibility of the structure and the ground and (ii) the interface characteristics between the structure and the surrounding soil (Tsinidis *et al.*, 2013) as similarly observed by Fabozzi *et al.* (2017). Results from Bilotta *et al.* (2014), Tsinidis *et al.* (2013) and Fabozzi *et al.* (2017) show how the lining forces are highly affected by the assumption on the soil–lining interface confirming its significance in obtaining accurate output. Soil-tunnel interface closer to no slip condition tends to produce higher thrust force than those in full slip condition.

In spite of the variability among the numerical results between advanced soil models, the results, in general, show good agreement with the field [(Kontoe *et al.*, 2008), (Kontoe *et al.*, 2011)] and experimental data [(Tsinidis *et al.*, 2013), (Bilotta *et al.*, 2014), (Mohammadi-Haji and Ardakani, 2018)]. Thus, with proper input data and appropriate soil-tunnel interface condition, it can be seen that the use of advanced soil constitutive models can better reproduce and simulate the soil and tunnel behaviour

under dynamic loading, thereby increasing the accuracy in determining the tunnel lining forces during earthquake.

Out of all these researchers, only Fabozzi and Bilotta (2016) (HS-Small) and Bilotta (2018) (HS-Small) have ventured to the 3D approach. This depicts the scarcity of research attempt to use a 3D approach with advanced soil constitutive model to investigate its effects on the seismic performance of tunnels. As such, this project will attempt to fill that gap and contribute to this subject matter.

Similarly, the use of advanced soil constitutive models to highlight the effects of the evolution of microstructure (destructuration) induced in natural soil deposits (discussed earlier in Section 3.3) as applied to soil-tunnel interaction has been limited exclusively to static and settlement analysis [e.g. Dang and Meguid (2008), (González *et al.*, 2012), Bian *et al.* (2016), Barciaga *et al.* (2016)]. The author will go one step further by exploiting this intrinsic soil attribute using an advanced soil constitutive model and scrutinise its impact on the soil-tunnel response in a seismic environment, in conjunction with 3D approach, which has never been explored before. This will be discussed in detail in Chapter 5.

3.5 Soil constitutive models

Following the major damage experienced by underground structures in recent large earthquakes, these events raised great concerns regarding the performance of underground structures and expressed necessity to explicitly account for seismic loading in the design of underground structures. These failures are often associated with significant deformation of soil deposits which can cause major collapse of the tunnels and subsequent damage to buildings and infrastructure facilities. To guarantee the safe performance of tunnels, the designer needs to capture a realistic soil response to seismic loads in order to accurately predict the tunnel behaviour during earthquake. This can only be achieved by adopting an appropriate soil constitutive model.

Simple constitutive assumptions in the framework of linear-visco-elastic and elasto-plasticity theories (e.g. Linear isotropic elasticity, Ramberg-Osgood, Mohr-Coulomb, Modified Cam Clay, Drucker-Prager) are commonly used to model the soil stress-strain behaviour during earthquake. However, these assumptions are not adequate to

simulate advanced features in the mechanical behaviour of soils under cyclic loading (e.g. non-linearity, material anisotropy, non-coaxiality, early irreversibility, structure degradation or destructuration, state dependency, decrease of nominal stiffness and related hysteretic energy dissipation), thus the need for an advanced non-linear soil constitutive model. These advanced features are evident in results from studies and experiments conducted by several authors including Leroueil and Vaughan (1990), Vucetic and Dobry (1991), Cotecchia and Chandler (1997) and Gutierrez and Ishihara (2000). As illustrated in Section 3.3, some of these intrinsic features particularly the initial structure and its destructuration may significantly alter the soil behaviour and thereby lead to either overly conservative estimate of ground deformations leading to uneconomical design of the tunnel or underestimate the ground deformations leading to unsafe design.

To identify soil constitutive models which capture these advanced behaviours, the author examined and listed all known models from the simplest (e.g. linear and non-linear elastic models) to advanced (e.g. cyclic, non-linear, elasto-plastic models, critical state models) to complex models (e.g. double surface plasticity models, multiple surface kinematic models, bounding surface plasticity models, nested surface plasticity model). By exploring numerous studies, the author identified and extracted known qualities and behaviour of these soil models. The initial selection provides the basis for the next step in the selection process. It includes an early indication on the extent of capabilities for each listed soil constitutive model.

Borja *et al.* (2001) stated that for loading histories with repetitive loading action the mechanical behaviour of soils is dominated by hysteretic motion. Hence, proper account must be taken of material anisotropy as well as the accompanying stiffness degradation and pore pressure build-up (for saturated soils) during cyclic loading. Recognising the contribution of initial structure in the stiffness and strength of natural soils and the vital effects of structure degradation under cyclic loading, this essential behaviour must be equally considered. In principle, the required constitutive model should at least reproduce adequately and exhibit:

1. Non-linear behaviour of soil;
2. Structure degradation;

3. Stiffness reduction leading to hysteretic energy dissipation;
4. Pore pressure build-up in undrained condition due to hysteretic action; and
5. Material anisotropy.

Using these five main criteria as well as their applicability to the soil type (clay) in the project scope, the initial list of constitutive models has been narrowed down to advanced models (i.e. advanced critical state models) and complex models (i.e. multi-surface kinematic models, bounding surface plasticity models, nested surface plasticity models). Other essential features/behaviours of soils under cyclic loading are then considered such as dependence on past stress history, early irreversibility, kinematic hardening, non-coaxiality, coupled volumetric-deviatoric plastic deformation and non-linear stiffness at small strain as well as specific requirements for the project which include 3D capability and past successful implementation in software. The author has to conduct further literature review to establish some of these features/behaviours which are not immediately apparent. The shortlist selection where further research and examination has been conducted to establish their advanced capabilities is tabled in Appendix A. One point is given for every existing feature within each constitutive model. The points are then added up and the soil constitutive models were ranked according to the most number of capabilities as summarised in Figure 3.24. The whole process resulted in identifying the four most reliable and efficient soil constitutive models that can simulate many of these complex behaviours under cyclic loading as follows:

<u>Multi-surface kinematic models</u>

Two-surface

- RMW (Kinematic Hardening Structure Model) by Rouainia and Muir-Wood
- MSS (Model for Structured Soils) by Kavvadas and Amorosi

Three-surface

- S3-SKH by Baudet and Stallebrass

<u>Advanced critical state and bounding surface plasticity model</u>

- B-SCLAY1S by Karstunen & Sivasithamparam

The author focused his final assessment on the qualitative nature of the four models based on:

- Ease in obtaining the input parameters required for the model;
- Availability of the programming code for the model;
- Ease of implementation into the chosen software;
- Successful application to different geotechnical problems.

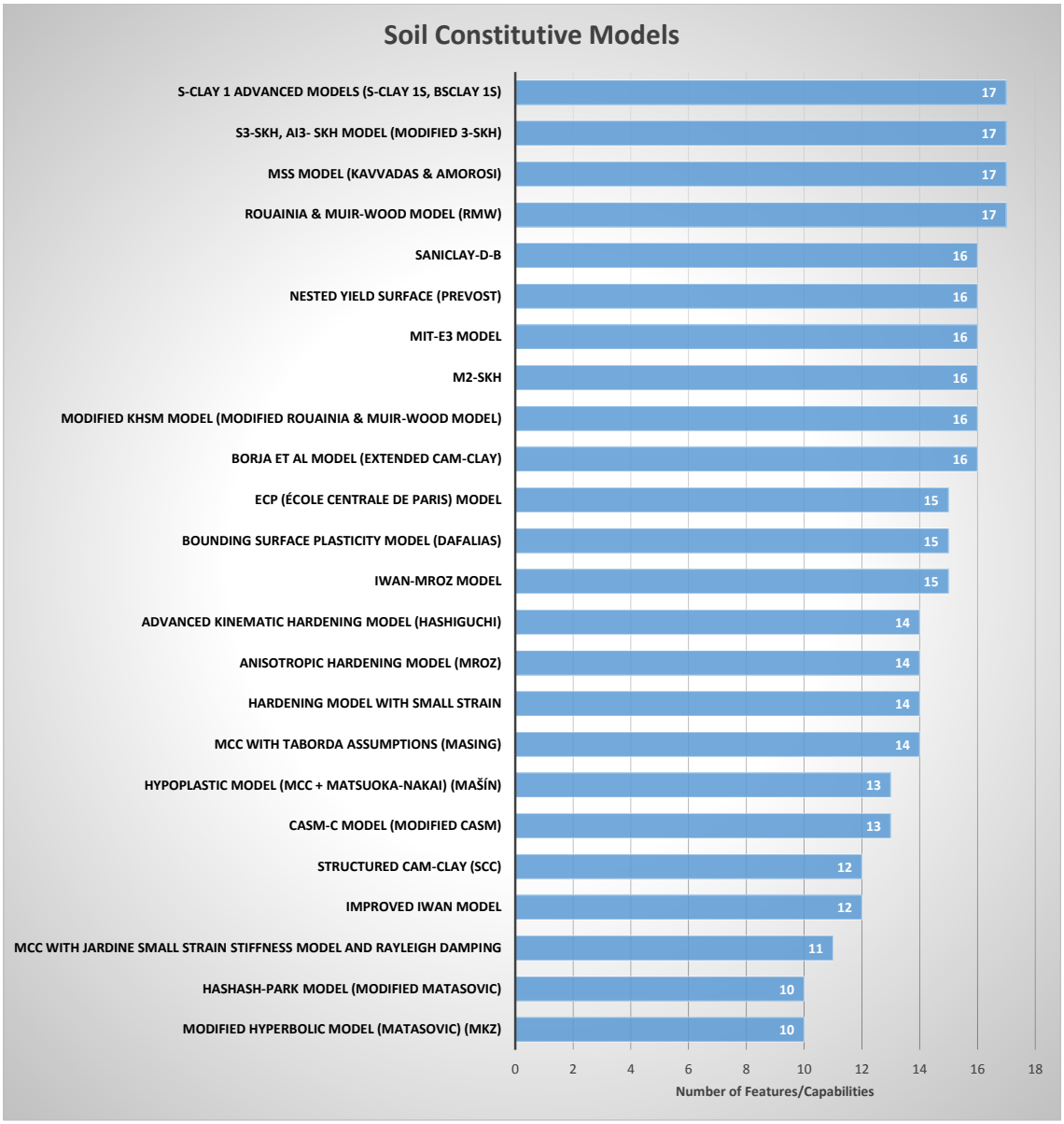

Figure 3.24 Summary of soil constitutive model shortlist selection

Based on those criteria, RMW has been chosen as the most appropriate one to adopt and utilise in generating both 2D and 3D tunnel models. In addition, the author's supervisory team has vast experience and expertise with RMW model. The basic input

parameters for RMW model can be derived from Modified Cam Clay parameters which can be easily obtained from conventional soil laboratory tests while the other parameters can be calibrated from results of standard cyclic tests.

Those four soil constitutive models including RMW are discussed further in the succeeding sections. Some background of Cam Clay and the "Bubble" model which form the basis for the four constitutive models and their development is also presented.

3.5.1 *Definition of stress and strain variables*

The formulation of the constitutive models in this chapter is based on three parameters: the mean effective stress *p'*, the deviatoric stress *q* and the void ratio *e*. They are defined as follows,

$$p' = \frac{1}{3}(\sigma'_1 + \sigma'_2 + \sigma'_3) = \frac{1}{3}(\sigma_1 + \sigma_2 + \sigma_3) - u \tag{3.5}$$

$$p' = \tfrac{1}{3}(\sigma'_1 + 2\sigma'_3) \text{ for conventional triaxial space} \tag{3.6}$$

$$q = \left[\frac{(\sigma'_1 - \sigma'_2)^2 + (\sigma'_2 - \sigma'_3)^2 + (\sigma'_3 - \sigma'_1)^2}{2}\right]^{1/2} \tag{3.7}$$

$$q = \left[\frac{(\sigma'_x - \sigma'_y)^2 + (\sigma'_y - \sigma'_z)^2 + (\sigma'_z - \sigma'_x)^2}{2} + 3\left(\tau_{xy}{}^2 + \tau_{yz}{}^2 + \tau_{zx}{}^2\right)\right]^{1/2} \tag{3.8}$$

$$q = \sigma'_1 - \sigma'_3 \text{ for conventional triaxial space} \tag{3.9}$$

where σ_x, σ_y, σ_z = total normal stresses; σ'_x, σ'_y, σ'_z = effective normal stresses; τ_{xy}, τ_{yz}, τ_{zx} = shear stresses; σ_1, σ_2, σ_3 = total principal stresses; σ'_1, σ'_2, σ'_3 = effective principal stresses; and u = pore water pressure.

Another parameter required to describe the stress state in the deviatoric plane is the Lode's angle θ defined as:

$$\theta = \tan^{-1}\left[\frac{1}{\sqrt{3}}\left(2\frac{\sigma'_2 - \sigma'_3}{\sigma'_1 - \sigma'_3} - 1\right)\right] = -\frac{1}{2}\sin^{-1}\left(\frac{27\det s}{2q^3}\right) \tag{3.10}$$

where

$$\det s = \begin{vmatrix} \sigma'_x - p' & \tau_{xy} & \tau_{zx} \\ \tau_{xy} & \sigma'_y - p' & \tau_{yz} \\ \tau_{zx} & \tau_{yz} & \sigma'_z - p' \end{vmatrix} \quad 3.11$$

The corresponding strains are the volumetric strain ε_v and the deviatoric (distortional) strain ε_q which are mathematically represented below.

$$\varepsilon_v = \varepsilon_1 + \varepsilon_2 + \varepsilon_3 = \varepsilon_x + \varepsilon_y + \varepsilon_z \quad 3.12$$

$$\varepsilon_v = \varepsilon_1 + 2\varepsilon_3 \text{ for conventional triaxial space} \quad 3.13$$

$$\varepsilon_q = \frac{\sqrt{2}}{3}[(\varepsilon_1 - \varepsilon_2)^2 + (\varepsilon_2 - \varepsilon_3)^2 + (\varepsilon_3 - \varepsilon_1)^2]^{1/2} \quad 3.14$$

$$\varepsilon_q = \frac{2}{3}(\varepsilon_1 - \varepsilon_3) \text{ for conventional triaxial space} \quad 3.15$$

where ε_x, ε_y, ε_z = normal strains and ε_1, ε_2, ε_3 = principal strains.

The basic elasto-plastic assumption is that the strain rate $\dot{\boldsymbol{\varepsilon}}$ (in tensor form) is comprised of the combination of the elastic strain rate $\dot{\boldsymbol{\varepsilon}}^e$ and plastic strain rate $\dot{\boldsymbol{\varepsilon}}^p$ as shown below, where the superimposed dot denotes time differentiation. All tensor quantities are denoted by bold-faced characters. For a purely elastic model, $\dot{\boldsymbol{\varepsilon}}^p = 0$.

$$\dot{\boldsymbol{\varepsilon}} = \dot{\boldsymbol{\varepsilon}}^e + \dot{\boldsymbol{\varepsilon}}^p \quad 3.16$$

The incremental stress-strain relationship is then given by the following equation.

$$\dot{\boldsymbol{\sigma}} = \boldsymbol{D}^e : \dot{\boldsymbol{\varepsilon}}^e + \boldsymbol{D}^p : \dot{\boldsymbol{\varepsilon}}^p \quad 3.17$$

where $\dot{\boldsymbol{\sigma}}$ = stress tensor; $\boldsymbol{D}^e$ = the tensor of elastic moduli, being in general a function of the elastic bulk modulus K and elastic shear modulus G; $\boldsymbol{D}^p$ = the tensor of plastic moduli; and the colons denote the inner product.

3.5.2 *Cam Clay model*

Cam Clay was developed from the Critical State Theory proposed by Roscoe *et al.* (1958). The theory was founded from observations on triaxial compression tests on saturated clays which exhibited a pattern of behaviour of clay according to its shear strength and deformation relationship. The critical state was defined as the stress state

at which plastic shearing of the soil under sustained loading will continue indefinitely without any changes in volume and effective stresses. This perfectly plastic state is given by the following equation:

$$\frac{dp'}{d\varepsilon_q} = \frac{dq}{d\varepsilon_q} = \frac{dv}{d\varepsilon_q} = 0 \qquad 3.18$$

where p' = the mean effective stress; q = the deviatoric stress defined as the difference between major and minor principal stresses; v is the specific volume of the soil = 1 + e; and ε_q = the deviatoric strain.

In the original Cam Clay model, this critical state is represented by the yield surface in the form of a logarithmic curve in p'-q stress space as shown in Figure 3.25. When the soil specimen is loaded the stress path will approach and consequently converge to a point on that yield surface. When the stress state remains within the yield surface, the behaviour of the soil is purely elastic, hence the deformation is recoverable. On contact with the yield surface, the soil behaviour becomes elasto-plastic, with a portion of the strains being plastic and therefore irrecoverable. When the critical state is reached, the stress state for a given clay soil forms a unique line in p'-q-v space referred to as the critical state line (CSL). The CSL is a straight line passing through the origin when projected on the p'-q space with a slope equal to M as shown in Figure 3.25. The yield surface for the original Cam Clay model is mathematically expressed as:

$$F = q + Mp' \ln \frac{p'}{p'_c} = 0 \qquad 3.19$$

where F is the yield function and p'_c is known as the yield stress or pre-consolidation pressure which controls the size of the yield surface.

It was clearly evident that the biggest drawback of the original Cam Clay model is the discontinuity and singularity of the yield surface at q = 0. With this condition, Roscoe and Burland (1968) pointed out that an infinite number of points normal to the yield surface are produced, thus an infinite number of flow directions of plastic increments (flow rule) could be defined at these points. Furthermore, with the associated flow rule (i.e. F = P, where F is the yield function and P is the plastic potential function) assumed for the model, any isotropic stress changes lead to the development of non-zero shear

strains. When compared to experimental results, this model predicts incorrectly the stress paths during K_0 (coefficient of earth pressure at rest) consolidation at zero lateral strain condition due to the shape of the yield surface (Valls-Marquez, 2009). As such, only the isotropic consolidation case can be properly reproduced.

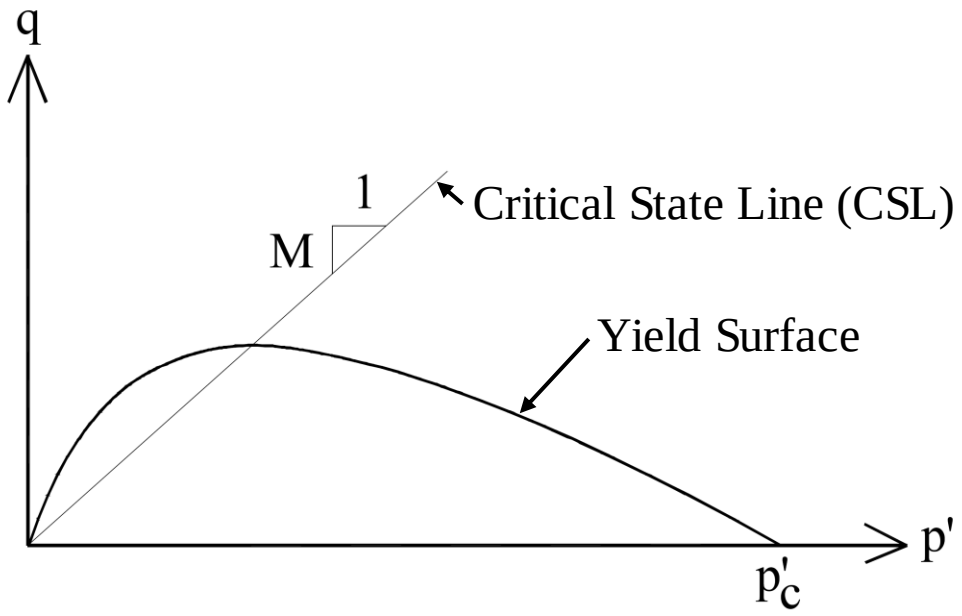

Figure 3.25 Original Cam Clay yield surface (Valls-Marquez, 2009)

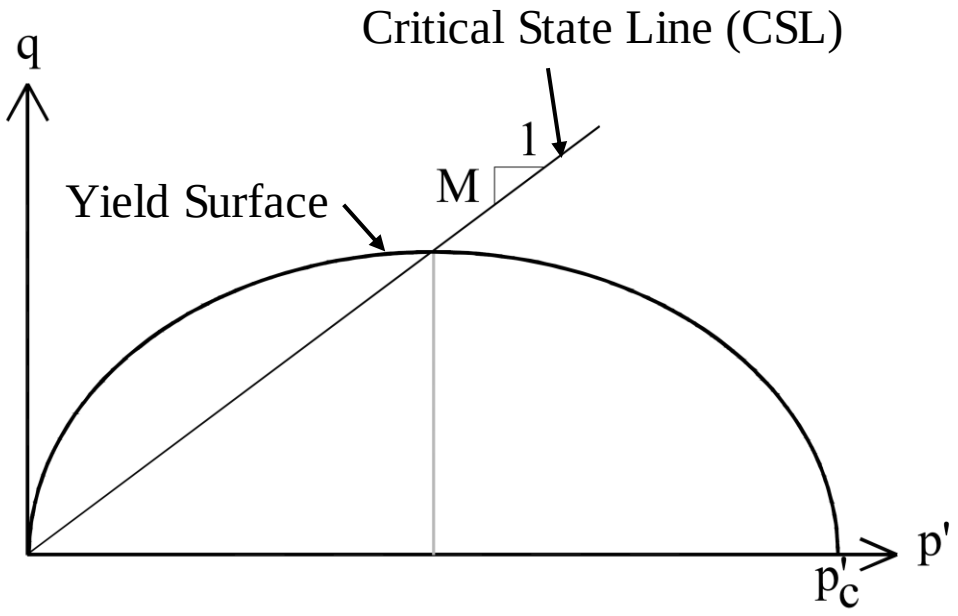

Figure 3.26 Modified Cam Clay yield surface (Valls-Marquez, 2009)

To overcome these issues, Roscoe and Burland (1968) proposed an improved version known as the Modified Cam Clay (MCC) model adopting an elliptical shape yield surface as shown in Figure 3.26 which has the following mathematical expression:

$$F = q^2 - M^2 p'(p'_c - p') = 0 \qquad 3.20$$

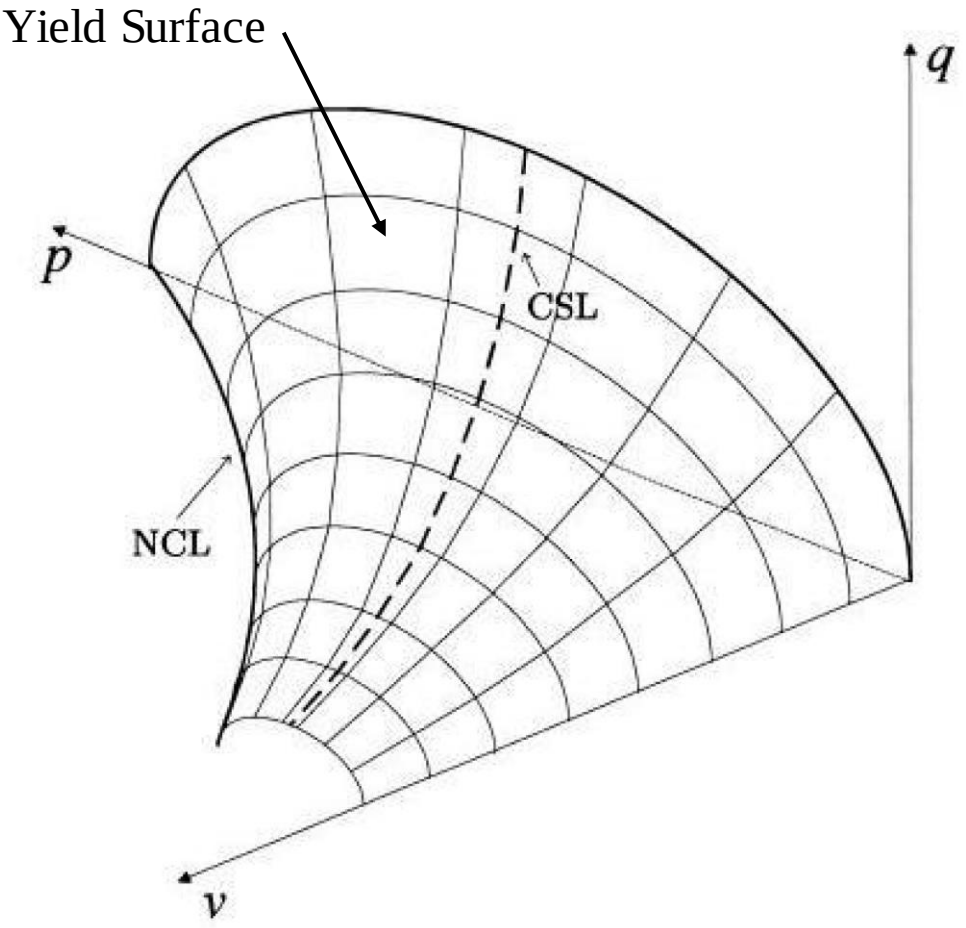

Figure 3.27 Yield or state boundary surface for the Modified Cam Clay model in *p'-q-v* space (Elia, 2015)

The yield or state boundary surface for the Modified Cam Clay model in *p'-q-v* space as shown in Figure 3.27 can expand isotropically (same in all directions) without changing its position in stress space. The isotropic hardening is given by Equation 3.21 where p'_c= the size of the yield surface, v = specific volume of the soil, λ & κ are Cam Clay parameters and ε_v^p = plastic volumetric strain.

$$dp'_c = p'_c \frac{v}{\lambda - \kappa} d\varepsilon_v^p \qquad 3.21$$

Within the yield surface, the elastic stress behaviour of the soil accompanied with an elastic change in volume is defined by the elastic bulk modulus $K = \frac{vp'}{\kappa}$ and the elastic shear modulus $G = \frac{3(1-2\mu)}{2(1+\mu)}K$ such that the incremental constitutive relationship for the elastic response is:

$$\begin{bmatrix} d\varepsilon_v{}^e \\ d\varepsilon_q{}^e \end{bmatrix} = \begin{bmatrix} 1/K & 0 \\ 0 & 1/3G \end{bmatrix} \begin{bmatrix} dp' \\ dq \end{bmatrix} \quad 3.22$$

where $\varepsilon_v{}^e$ = elastic volumetric strain; $\varepsilon_q{}^e$ = elastic distortional strain.

The flow rule (which determines the direction of plastic increments) associated with the yield surface, i.e. the plastic strain increment vector is normal to the yield surface and the corresponding plastic stress-strain response are given by Equations 3.23 and 3.24 respectively.

$$\frac{d\varepsilon_v{}^p}{d\varepsilon_q{}^p} = \frac{M^2 - \eta^2}{2\eta} \quad 3.23$$

$$\begin{bmatrix} d\varepsilon_v{}^p \\ d\varepsilon_q{}^p \end{bmatrix} = \frac{1}{H} \begin{bmatrix} (M^2 - \eta^2) & 2\eta \\ 2\eta & 4\eta^2/(M^2 - \eta^2) \end{bmatrix} \begin{bmatrix} dp' \\ dq \end{bmatrix} \quad 3.24$$

where H = plastic modulus is given by Equation 3.25; e = void ratio of soil; $\varepsilon_v{}^p$ = plastic volumetric strain; $\varepsilon_q{}^p$ = plastic distortional strain; and stress ratio $\eta = \frac{q}{p'}$.

$$H = \frac{(1+e)p'(M^2 + \eta^2)}{\lambda - \kappa} \quad 3.25$$

Both Cam Clay models require five material parameters as follows:

1. λ = the slope of the normal compression (virgin consolidation) line and critical state line (CSL) in v-ln p' space as illustrated in Figure 3.28
2. κ = the slope of a swelling (reloading-unloading) line in v-ln p' space as illustrated in Figure 3.28
3. M = the slope of the CSL in p'-q space
4. N = the specific volume of the normal compression line at unit mean effective stress as illustrated in Figure 3.28 or Γ = the specific volume of the CSL at unit mean effective stress

5. μ = Poisson's ratio or G = shear modulus.

The initial state of consolidation of such materials must also be specified. This can be achieved by obtaining either p'_c = the preconsolidation pressure or *OCR* = the overconsolidation ratio: the ratio of the previous maximum mean effective stress (p'_c) to the current mean effective stress.

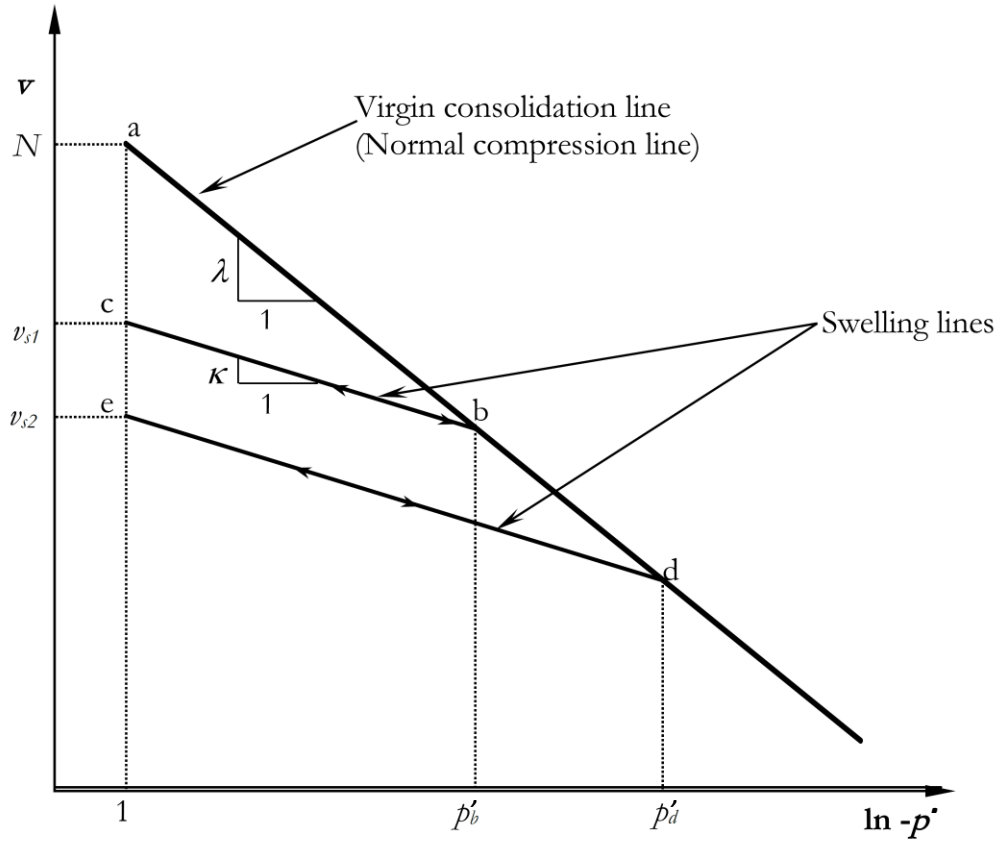

Figure 3.28 Typical behaviour of clays in consolidation (oedometer) test

The revised formulations for MCC undoubtedly resolved the issue on discontinuity and singularity occurring in the original Cam Clay model. It also managed to capture experimentally observed yield loci and was able to reasonably simulate the behaviour of normally and lightly overconsolidated clays. It is capable in capturing many important features of soil behaviour such as pressure sensitivity, hardening response with plastic volumetric compaction, softening response with plastic dilation and coupled volumetric-deviatoric plastic deformations (Borja *et al.*, 2001). However, it still inherits some of the limitations of the original Cam Clay. Some of these limitations are briefly described below.

1. The MCC model may allow for unrealistically large ratios of shear stress over mean stress when the stress state is above CSL. Furthermore, the model predicts a softening behaviour on the dry side of the yield surface. Without special considerations, the softening behaviour leads to mesh dependency and possible lack of convergence in a finite element analysis.
2. The transition from elastic (stress within the bounding surface) to elasto-plastic phase (stress upon contact with the yield surface) is sudden and abrupt resulting to a sharp drop in the stiffness of the soil. This characteristic was not consistent with observations from real soil behaviour, as yielding of soils was far more gradual, with a smooth transition in stiffness as the soil moves from the elastic to the elasto-plastic phase.
3. The MCC model overestimates the failure stresses on the 'dry' or supercritical side (i.e. yielding occurs to the left of the intersection of the CSL) (Potts and Zdravković, 1999); thus, it overestimates the peak strength in undrained highly overconsolidated clay.
4. Subsequent changes in the loading direction, e.g. unload-reload cycles, within the bounding surface, produced only purely elastic strains and constant excess pore pressure response after the first loading cycle.
5. MCC model cannot replicate the behaviour of clays that are subjected to cyclic loading particularly gradual accumulation of irrecoverable plastic strains and accompanying energy dissipation, associated with hysteretic behaviour, as well as accumulation of excess pore water pressures. This is caused by the unrealistically large extent of the yield surface, which leads to limited accumulation of plastic strain during cycles.
6. The yield loci of the Cam Clay models retained the same shape and expanded uniformly when the soil yielded, hence their behaviour is isotropic. However, due to the modes of deposition, natural soils exhibit anisotropic characteristics as observed from laboratory investigations including works by Graham and Houlsby (1983) on Winnipeg clay (see Figure 3.29) where the yield loci were found to be rotated from the isotropic axis and centred on the K_0-line.
7. The model does not consider the initial structure of natural soils and its degradation process. The influence and importance of which have been highlighted in Section 3.3.

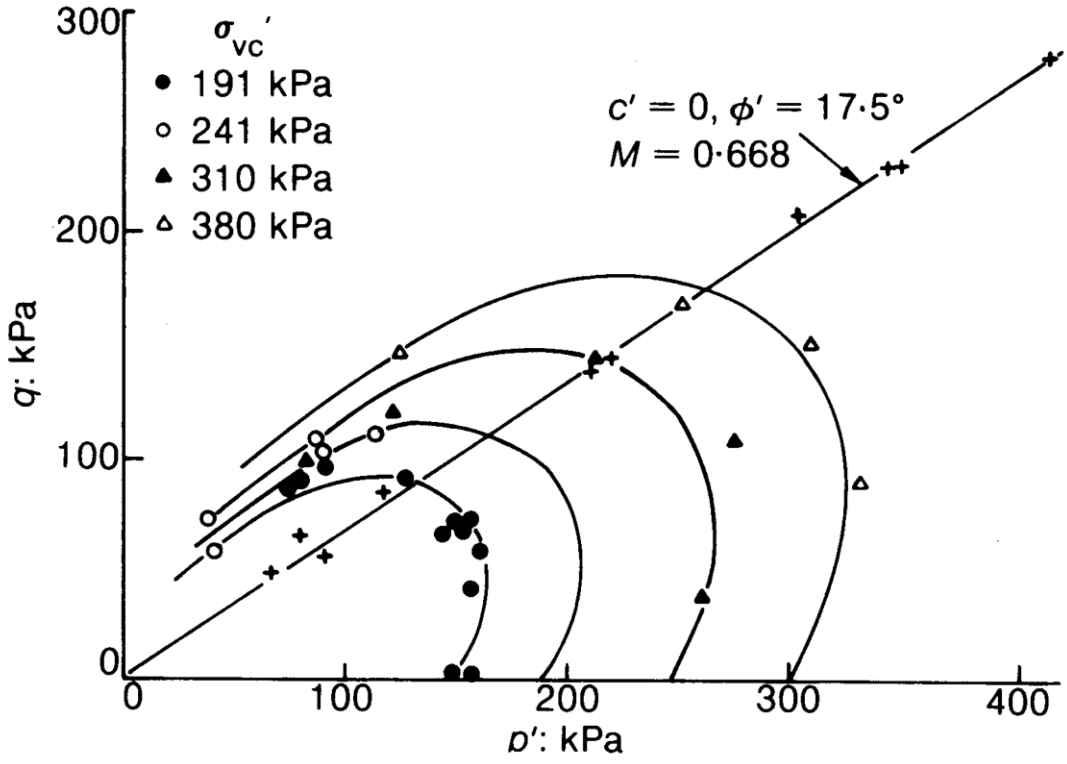

Figure 3.29 Yield curves observed from triaxial tests on undisturbed Winnipeg clay (Graham and Houlsby, 1983)

3.5.3 *"Bubble" Model*

The "bubble" model by Al-Tabbaa and Wood (1989) is an extension of the single surface Modified Cam Clay model and formulated within the kinematic hardening framework similar to the two-surface model proposed by Mróz *et al.* (1979). The term "bubble" comes from the single inner yield surface introduced into the Modified Cam Clay bounding surface with associated plasticity of the same shape as that of the bounding surface as illustrated in Figure 3.30 (a) and (b). The "bubble" model was formulated based on results from tests on slow cyclic response of Speswhite Kaolin clay. The yield surface can expand or contract and translate (isotropic and kinematic hardening) within the bounding surface while maintaining the ratio of the size of the yield surface to that of the bounding surface. This relative size was given by parameter R. The yield surface of the bubble is defined by Equation 3.26 where p_c = stress variable controlling size of the surfaces and (p'_α, q_α) is the centre of the kinematic yield surface. Variables p', q and material parameter M are the same as those of Modified Cam Clay model.

$$f_b = (p' - p'_\alpha)^2 + \frac{(q - q_\alpha)^2}{M^2} - R^2 {p_c}^2 = 0 \qquad 3.26$$

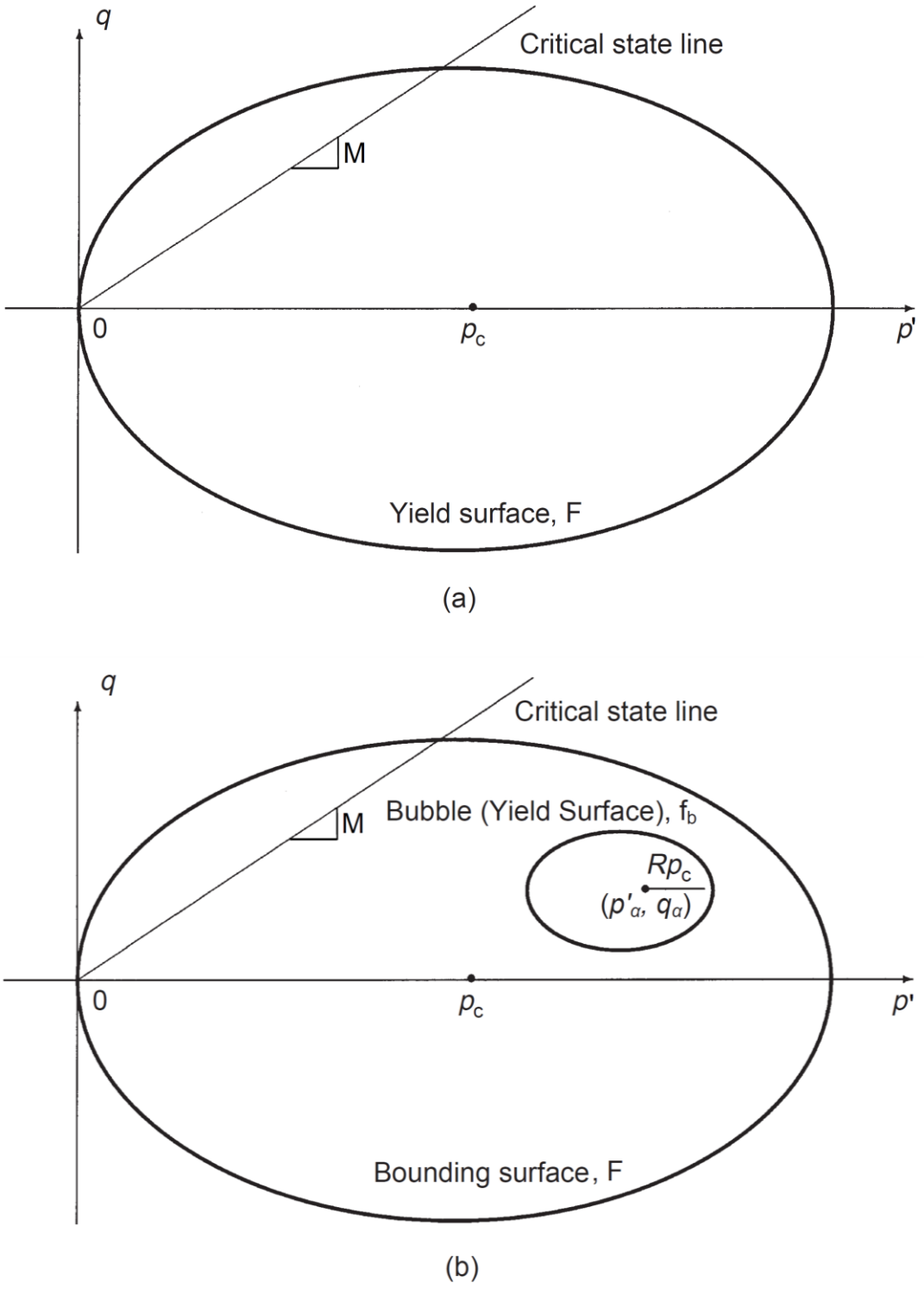

Figure 3.30 Evolution of the "Bubble" model: (a) Modified Cam Clay model; (b) "Bubble" model (Rouainia and Wood, 2000)

The bounding surface can also expand or contract but not translate (isotropic hardening). The bounding surface is represented by the Modified Cam Clay yield surface and defined by Equation 3.27.

$$F = (p' - p_c)^2 + \frac{q^2}{M^2} - {p_c}^2 = 0 \qquad 3.27$$

Within the kinematic bubble, the behaviour was assumed to be isotropic elastic and defined by the linear-elastic bulk modulus *K* expressed in Equation 3.28 and linear-elastic shear modulus *G* expressed in Equation 3.29 where κ^* is the slope of the swelling (reloading-unloading) line on the ln *v*-ln *p'* plane (instead of using the *v*-ln *p'* plane as in the Cam Clay models) such that $\kappa^* = \frac{\kappa}{1+e}$. The elastic incremental formulation follows that of MCC as given in Equation 3.22.

$$K = \frac{p'}{\kappa^*} \qquad 3.28$$

$$G = \frac{3(1-2\mu)}{2(1+\mu)}K \qquad 3.29$$

Changing in size and movement of the bubble within the bounding surface is governed by a kinematic hardening rule similar to the translation rule proposed by Hashiguchi (1985). The rule ensures that the bubble and the bounding surface engage at a common point but under no circumstances they intersect. This was made possible by associating each point on the bubble surface with the corresponding conjugate points on the bounding surface [Mróz (1967), Hashiguchi (1985)] such that their outward normal had the same direction.

The equation to describe the kinematic hardening rule is given below.

$$\begin{bmatrix} dp'_\alpha \\ dq_\alpha \end{bmatrix} = \frac{dp_c}{p_c}\begin{bmatrix} p'_\alpha \\ q_\alpha \end{bmatrix} + S\begin{bmatrix} \frac{p' - p'_\alpha}{R} - (p' - p_c) \\ \frac{q - q_\alpha}{R} - q \end{bmatrix} \qquad 3.30$$

The first term in the equation corresponds to the change in size of the bubble due to isotropic expansion or contraction of the bounding surface while the second term corresponds to translation of the bubble within the bounding surface.

The scalar quantity *S* is derived from the following equation.

$$S = \frac{\left(p' - p'_{\alpha}\right)\left[dp' - \frac{dp_c}{p_c}p'\right] + \frac{q - q_{\alpha}}{M^2}\left[dq - \frac{dp_c}{p_c}q\right]}{\left(p' - p'_{\alpha}\right)\left[\frac{p' - p'_{\alpha}}{R} - (p' - p_c)\right] + \frac{(q - q_{\alpha})}{M^2}\left[\frac{q - q_{\alpha}}{R} - q\right]} \qquad 3.31$$

The isotropic hardening rule of the bounding surface is the same as that of the Modified Cam Clay model as defined in Equation 3.32. The only difference is that λ and κ are replaced by λ^* and κ^* respectively, where λ^* is the slope of the normal compression line in ln *v*-ln *p'* compression plane.

$$dp_c = \frac{p_c}{(\lambda^* - \kappa^*)} d\varepsilon_v{}^p \qquad 3.32$$

The model follows an associated flow rule similar to the MCC model (Equation 3.23). As a consequence, in the special case when the two surfaces are in contact the plastic strain increments on the kinematic yield surface are formed as follows:

$$\begin{bmatrix} d\varepsilon_v{}^p \\ d\varepsilon_q{}^p \end{bmatrix} = \frac{1}{h_0}\begin{bmatrix} \left(p' - p'_{\alpha}\right)^2 & \left(p' - p'_{\alpha}\right)\frac{q - q_{\alpha}}{M^2} \\ \left(p' - p'_{\alpha}\right)\frac{q - q_{\alpha}}{M^2} & \left(\frac{q - q_{\alpha}}{M^2}\right)^2 \end{bmatrix}\begin{bmatrix} dp' \\ dq \end{bmatrix} \qquad 3.33$$

where h_0, determined by Equation 3.34, controls the plastic strain increments when the yield surface is in contact with the bounding surface.

$$h_0 = \frac{(p' - p'_{\alpha})}{(\lambda^* - \kappa^*)}\left[p'\left(p' - p'_{\alpha}\right) + \frac{q(q - q_{\alpha})}{M^2}\right] \qquad 3.34$$

In order to calculate the plastic strains in any cases whether or not the kinematic yield surface and the bounding surface are in contact, Al-Tabbaa (1987) replaced h_o in Equation 3.33 with a more general expression for the hardening modulus. To achieve this, the hardening modulus should be dependent on the distance between the two surfaces and thereby expressed in Equation 3.35 below.

$$h = h_0 + H \qquad 3.35$$

The plastic modulus *H*, which is a function of the stress state, determines the response of the model when plastic strains occur irrespective of the position of the yield surface relative to the bounding surface. The equation for *H*, given in Equation 3.36, ensures a

smooth reduction of the stiffness as the yield surface approaches the bounding surface.

$$H = \left[\frac{{p_c}^3}{(\lambda^* - \kappa^*)}\right]\left(\frac{b}{b_{max}}\right)^{\psi} \quad 3.36$$

where b = normalised distance between yield surface and bounding surface; b_{max} = maximum value of b; and ψ = an interpolation exponent determined from experimental results of the soil type under consideration.

The values for b are calculated from Equation 3.37 while the values for b_{max} are given by Equations 3.38 and 3.39.

$$b = \frac{1}{Rp_c}\left[\left(p' - {p'}_{\alpha}\right)\left[\frac{p' - {p'}_{\alpha}}{R} - (p' - p_c)\right] + \frac{(q - q_{\alpha})}{M^2}\left[\frac{(q - q_{\alpha})}{R} - q\right]\right] \quad 3.37$$

$$b_{max} = 2p_c(1 - R) \text{ for } M < 1 \quad 3.38$$

$$b_{max} = 2p_c M(1 - R) \text{ for } M \geq 1 \quad 3.39$$

Outside the yield surface but within the bounding surface of the "bubble" model, progressive plastic deformations occur resulting in a non-linear stress-strain behaviour during loading and unloading. The model therefore exhibits non-linear plasticity to describe the pre-yield behaviour compared to the non-linear elasticity displayed by the Jardine (1985) and Jardine (1991) models.

The "bubble" model requires six soil parameters: λ^*, κ^*, M, μ, R, ψ; and one additional parameter that defines the initial stress conditions of the soil and fixes the model in the ln v-ln p' space, i.e. N (a parameter of Modified Cam Clay). The first four parameters are typical of MCC model. The model degenerates to Modified Cam Clay model when the two surfaces are in contact and yielding continually occurs. Similar to Cam Clay models, M is considered to be the same for extension and compression, but this model theoretically improves the prediction of the overconsolidated response due to the definition of the hardening rule (Valls-Marquez, 2009). The "bubble" model managed to address aspects of soil behaviour that were missing or inadequately described by Cam Clay models such as hysteretic non-linear behaviour with accumulation of permanent strains during cyclic loading and a failure envelope for

overconsolidated soils. Despite its huge advancement from Cam Clay models, there are still existing limitations within its framework that needs improvement. Some of these observed limitations are listed below.

1. Inability to simulate anisotropic characteristics;
2. Does not consider the non-linear small-strain stiffness required for the dynamic and small-strain cyclic loading of soils;
3. Limited capability to model the effect of recent history;
4. Non-smooth elasto-plastic transition, hence an abrupt change in stiffness, when the stress state reaches the kinematic yield surface (Grammatikopoulou, 2004);
5. Inability to capture the effects of structure in natural soils.

3.5.4 *MSS (Model for Structured Soils)*

MSS (Model for Structured Soils) proposed by Kavvadas and Amorosi (2000) is based on the theory of incremental plasticity and critical state concepts. It is a two-surface constitutive model for structured soils that combine features such as:

1. Non-linear stiffness in the elastic domain;
2. Refinement of the soil's memory of its stress history by adding a number of `yield' or `history' surfaces which record key characteristics of the stress path; and
3. Inclusion of the effects of the structure in natural soils and the consequent damage to it due to loading.

The model has two characteristic surfaces: an internal plastic yield envelope (PYE) and an external bond strength envelope (BSE) shown in Figure 3.31. The internal plastic surface (PYE) controls the transition from the elastic to the plastic state. The term ‘plastic’ was designated to the ‘yield surface’ to point out the difference between plastic yielding (which may occur at small strains) and large-scale yielding which lead to destructuration of the soil (Jardine, 1991).The external bond strength surface is the bounding surface which corresponds to the initial or current structured state of the soil. Plastic strains are allowed to develop inside the bounding surface and hence

activate the mechanism that can lead to the gradual loss of the initial structure based on the proposed destructuration law.

The mathematical expression for the ellipsoidal BSE is given below.

$$F = \frac{1}{c^2}(\boldsymbol{s} - \boldsymbol{s}_K) : (\boldsymbol{s} - \boldsymbol{s}_K) + (\sigma - \sigma_K)^2 - \alpha^2 = 0 \qquad 3.40$$

where $\boldsymbol{s}$ = deviatoric stress tensor and σ = mean stress. The symbol ':' indicates a summation of products.

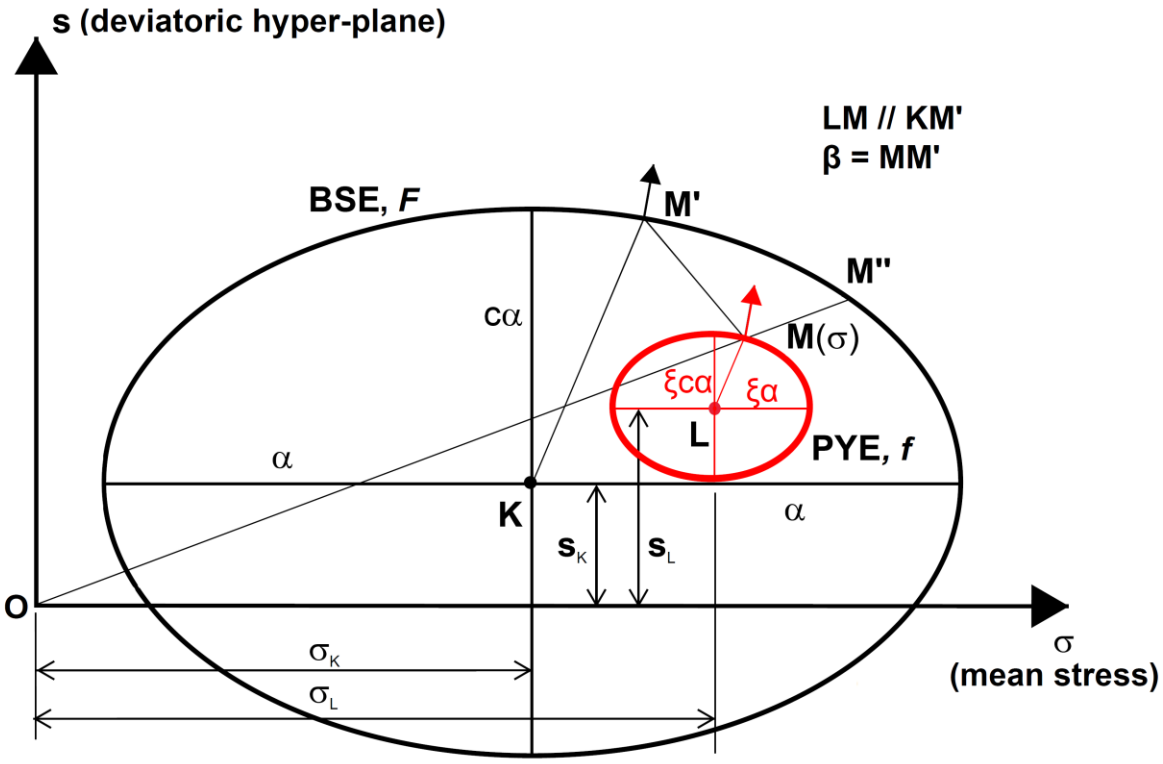

Figure 3.31 Schematic diagram of the model for structured soils MSS (Elia, 2012)

The ellipsoid is centred at point K with the length of the half-axes along the isotropic axis equal to α and along each of the deviatoric axes equal to $c\alpha$ where c is the eccentricity of the BSE. The dimension of the BSE along all deviatoric axes need not be the same, i.e. the ellipsoid does not need to be symmetric about the isotropic axis. As the bounding surface is centred off the mean stress axis (isotropic axis), the model does accommodate the effects of anisotropy. The model also allows some degree of tensile strength, with the surface permitted to exist in negative mean stress space similar to the model formulated by Mróz (1967).

The plastic yield envelope (PYE) is centred at point L and retained the same geometric shape as the bounding surface BSE, but was scaled down by a factor ξ. Thus, its size along the isotropic axis is equal to $\xi\alpha$ and along each of the deviatoric axes equal to $\xi c\alpha$ as shown in Figure 3.31. The scaling factor ξ which is the ratio of the sizes of the BSE and PYE is a very small number of the order of 0.001. The smaller the yield surface, the more non-linear the behaviour of the model. The equation for the PYE is given below.

$$f = \frac{1}{c^2}(\boldsymbol{s} - \boldsymbol{s}_L) : (\boldsymbol{s} - \boldsymbol{s}_L) + (\sigma - \sigma_L)^2 - (\xi\alpha)^2 = 0 \qquad 3.41$$

In this model, the destructuration law is incorporated within the isotropic hardening function as demonstrated in Equation 3.42. Thus, the change in size $\dot{\alpha}$ of the BSE correlates to the loss of structure caused by the accumulation of both plastic volumetric and deviatoric strains. Equation 3.42 reduces to the hardening rule of the MCC model when all structure degradation parameters are equal to zero.

$$\dot{\alpha} = \alpha\left[\left\{\left(\frac{1+e}{\lambda-\kappa}\right) - \zeta_v exp(-\eta_v, {\varepsilon_v}^p)\right\}{\dot{\varepsilon}_v}^p + \left\{\theta_q - \zeta_q exp\left(-\eta_q, {\varepsilon_q}^p\right)\right\}{\dot{\varepsilon}_q}^p\right] \qquad 3.42$$

where (ζ_v, η_v) and (ζ_q, η_q) = the rate of volumetric and deviatoric structure degradation respectively; and θ_q = steady-state deviatoric structure degradation/ hardening parameter (usually $\theta_q = 0$).

Similar to the "bubble" model by Al-Tabbaa and Wood (1989), the kinematic hardening relates to the translation of the characteristic surfaces (BSE and PYE) in the stress space and is achieved by controlling the movement of their centres K and L. It also defines the evolution of the material anisotropy during plastic deformation. The centre K of the BSE moves as follows:

For stress states inside the BSE:

$$\dot{\boldsymbol{\sigma}}_K = \frac{\dot{\alpha}}{\alpha}\boldsymbol{\sigma}_K \qquad 3.43$$

The model reduces to the MCC model when $\boldsymbol{\sigma}_K = \alpha\boldsymbol{I}$ where $\boldsymbol{I}$ is the isotropic unit tensor.

For stress states on the BSE (i.e. the two characteristic surfaces are in contact):

$$\dot{\boldsymbol{\sigma}}_K = \frac{\dot{\alpha}}{\alpha}\boldsymbol{\sigma}_K + \psi\frac{\dot{\alpha}}{\alpha}\left(\boldsymbol{s} - \chi\frac{\sigma}{\sigma_K}\boldsymbol{s}_K\right) \tag{3.44}$$

where (χ, ψ) = parameters controlling the evolution of material anisotropy

The movement of centre L of the PYE is dictated by the position of K as expressed below.

For stress states on the BSE

$$\boldsymbol{\sigma}_L = (1-\xi)\boldsymbol{\sigma} + \xi\boldsymbol{\sigma}_K \tag{3.45}$$

For stress states inside the BSE

$$\dot{\boldsymbol{\sigma}}_L = \frac{\dot{\alpha}}{\alpha}\boldsymbol{\sigma}_L + \dot{\mu}\boldsymbol{\beta} \tag{3.46}$$

where $\boldsymbol{\beta}$ = MM' and the factor $\dot{\mu}$ is evaluated below.

$$\dot{\mu} = \frac{\frac{1}{c^2}(\boldsymbol{s}-\boldsymbol{s}_L):\left[\dot{\boldsymbol{s}} - \frac{\dot{\alpha}}{\alpha}\boldsymbol{s} + (\sigma-\sigma_L)\left(\dot{\sigma} - \frac{\dot{\alpha}}{\alpha}\sigma\right)\right]}{\xi\alpha^2 - \left[\frac{1}{c^2}(\boldsymbol{s}-\boldsymbol{s}_L):(\boldsymbol{s}-\boldsymbol{s}_K) + (\sigma-\sigma_L)(\sigma-\sigma_K)\right]} \tag{3.47}$$

The associated flow rule for the PYE which determines the plastic strain increment is generally expressed in the following form.

$$\dot{\boldsymbol{\varepsilon}}^p = \lambda\boldsymbol{P} \qquad \lambda = \frac{1}{H}(\boldsymbol{Q}:\dot{\boldsymbol{\sigma}}) \tag{3.48}$$

where scalar λ and plastic potential $\boldsymbol{P}$ gives the magnitude and direction of the plastic strain increment; $\boldsymbol{\sigma}$ and $\dot{\boldsymbol{\sigma}}$ are the effective stress and the corresponding effective stress increment respectively; $\boldsymbol{Q} = \frac{\partial f}{\partial \boldsymbol{\sigma}}$ is the gradient of the PYE; and H as defined below is the plastic modulus when the two characteristic surfaces are not in contact.

$$H = H'' + |H''|\left[\left(1 - \frac{\delta}{\delta_0}\right)^{-\gamma} - 1\right] \tag{3.49}$$

where H'' = the value of the plastic modulus at point M'' where vector $\overrightarrow{\mathrm{OM}}$ intersects the BSE (refer to Figure 3.31); δ = the normalised length of MM'' (M is the current state); δ_0 = the value of δ upon onset of yielding; and γ = material parameter

controlling the degradation of the plastic modulus H in the early stages of destructuration (i.e. before the BSE is engaged). The value of H ranges between ∞ (upon onset of yielding, i.e. $\delta/\delta_0 = 1$) and H'' (when the stress state reaches the BSE, i.e. the two surfaces are in contact, thus $\delta/\delta_0 = 0$).

The deformation inside the PYE is considered elastic similar to "bubble" model. The model allows choice between poro-elasticity principles (similar to MCC) or hyper-elasticity formulations developed by Houlsby (1985) (Equations 3.50 and 3.51).

$$\dot{\boldsymbol{\sigma}} = p_r exp\left(\frac{{\varepsilon_v}^e}{\kappa^*}\right)\left\{\frac{1}{\kappa^*}\left[1 + \left(\frac{3\alpha^*}{2\kappa^*}\right)\left({\varepsilon_q}^e\right)^2\right]\dot{\boldsymbol{\varepsilon}}_v{}^e + \left(\frac{2\alpha^*}{\kappa^*}\right)\left(\boldsymbol{e}^e \cdot \dot{\boldsymbol{e}}^e\right)\right\} \quad 3.50$$

$$\dot{\boldsymbol{s}} = p_r exp\left(\frac{{\varepsilon_v}^e}{\kappa^*}\right)\left\{\left(\frac{2\alpha^*}{\kappa^*}\right)\boldsymbol{e}^e\dot{\boldsymbol{\varepsilon}}_v{}^e + 2\alpha^*\dot{\boldsymbol{e}}^e\right\} \quad 3.51$$

where p_r = a reference pressure; κ^* is similar to the "bubble" parameter; α^* = hyper-elastic shear parameter; $\boldsymbol{\sigma}$ = effective stress tensor; $\boldsymbol{s}$ = deviatoric stress tensor; and $\boldsymbol{e}$ = deviatoric strain tensor.

One advantage of hyper-elasticity over poro-elasticity is the introduction of coupled volumetric and shear components in the stress-strain relationships. Another advantage is the ability to predict the development of shear-induced excess pore pressures during elastic undrained loading, thereby improving the predicted effective stress path.

The MSS model requires the following thirteen parameters, four of which are MCC parameters, while the remaining seven control the structure degradation and anisotropic characteristics of the soil.

1. κ or κ^* = poro-elastic or hyper-elastic compressibility, respectively;
2. G/K or α^* = elastic shear parameter in poro-elasticity or hyper-elasticity, respectively;
3. λ = intrinsic compressibility;
4. c = eccentricity of the BSE;
5. (ζ_v, η_v) and (ζ_q, η_q) = volumetric and deviatoric structure degradation parameters;
6. (χ, ψ) = parameters controlling the evolution of material anisotropy, that is the motion of the BSE in the deviatoric space;

7. γ = parameter controlling the variation of the elasto-plastic modulus (H) in the early stages of structure degradation;
8. ξ = ratio of the sizes of the BSE and PYE typically ranges from 0.005 to 0.05;
9. θ_q = steady-state deviatoric structure degradation/hardening parameter usually equal to zero.

In addition, the model requires the initial state condition of the soil by specifying the following state variables.

1. $\boldsymbol{\sigma}$ = effective stress components;
2. e = void ratio;
3. α = size of the BSE;
4. σ_K = position of the centre of the BSE which controls the primary structure anisotropy;
5. σ_L = position of the centre of the PYE which controls the secondary anisotropy

The model has been calibrated against laboratory tests on the stiff overconsolidated Vallericca clay (isotropic and anisotropic consolidation tests, anisotropically consolidated triaxial shearing at both low and high pressures).

One main criticism of MSS model is the large number of material parameters and variables required to establish the model as well as the difficulty in obtaining them from laboratory tests. Also, because the model itself is generally complicated, the numerical computation is then quite complex requiring considerable memory for the configuration of the sub-yield and stress reversal surface (Suebsuk, 2010). This drawback, however, is similarly observed from other kinematic hardening models and generally in most advanced and complex constitutive models.

MSS model has been utilised in the works by Amorosi *et al.* (2011), Elia *et al.* (2010) and Elia *et al.* (2011) particularly for soils under dynamic conditions. The model exhibits advanced soil characteristics such as non-linear behaviour, hysteretic action, stiffness degradation, pore pressure build-up for saturated soils and material anisotropy as well as allowing for the early development of early strains, the response in the small strain region and the effects of damage to structure caused by irrecoverable plastic strains. It has a distinct advantage in providing a smooth

transition of stiffness as the effective stress path moves from elastic to elasto-plastic region upon reaching the edge of the PYE by using a unique hardening function (Ni, 2007). Also, it proves to be capable to reproduce the non-coaxial behaviour of soils, typically observed in unconventional laboratory tests on cohesive and granular soils.

An improved MSS model named MSS-2 was proposed by Kavvadas and Belokas (2000) which incorporates: (a) rotated distorted ellipsoids for the bounding and the yield surfaces to cover both structure- and stress-induced anisotropy; (b) an improved damage type mechanism to model structure degradation; (c) the Intrinsic Strength Envelope as a reference envelope that delimits all possible unbonded states, representing a lower bound (structureless state) of the bounding surface; and d) a non-associated flow rule controlled by structure. Details of this model can be found in Belokas and Kavvadas (2010). Further improvements were made by Sitarenios *et al.* (2013) incorporating new isotropic and kinematic hardening rules. The improvements aimed to address the most common shortcomings of anisotropic models including: (a) the inability to reproduce compression lines that depend on the level of induced anisotropy; (b) the inability to reproduce unique critical state conditions; and finally (c) the inability to simulate strain softening response usually observed under triaxial compression after K_0 consolidation. Details of those improved formulations can be found in Sitarenios *et al.* (2013).

3.5.5 *S3-SKH*

S3-SKH is an extension of 3-SKH, a three-surface model originally proposed by Stallebrass (1990) and further developed by Stallebrass and Taylor (1997). Baudet and Stallebrass (2004) extended 3-SKH to S3-SKH to include structure degradation. The original 3-SKH is also an extension of the "bubble" model by Al-Tabbaa and Wood (1989) which apart from the bubble yield surface which marks the onset of plastic deformations, another kinematic yield surface (history surface) is introduced into the model to represent the influence of recent stress history on stiffness and shear-volumetric response of soil as shown in Figure 3.32 (a). The model consists of three characteristic surfaces: the history and yield surfaces nested within a natural state boundary surface. The model utilised an associated flow rule. In addition, the translation and hardening rule in this model is also associated with the history surface.

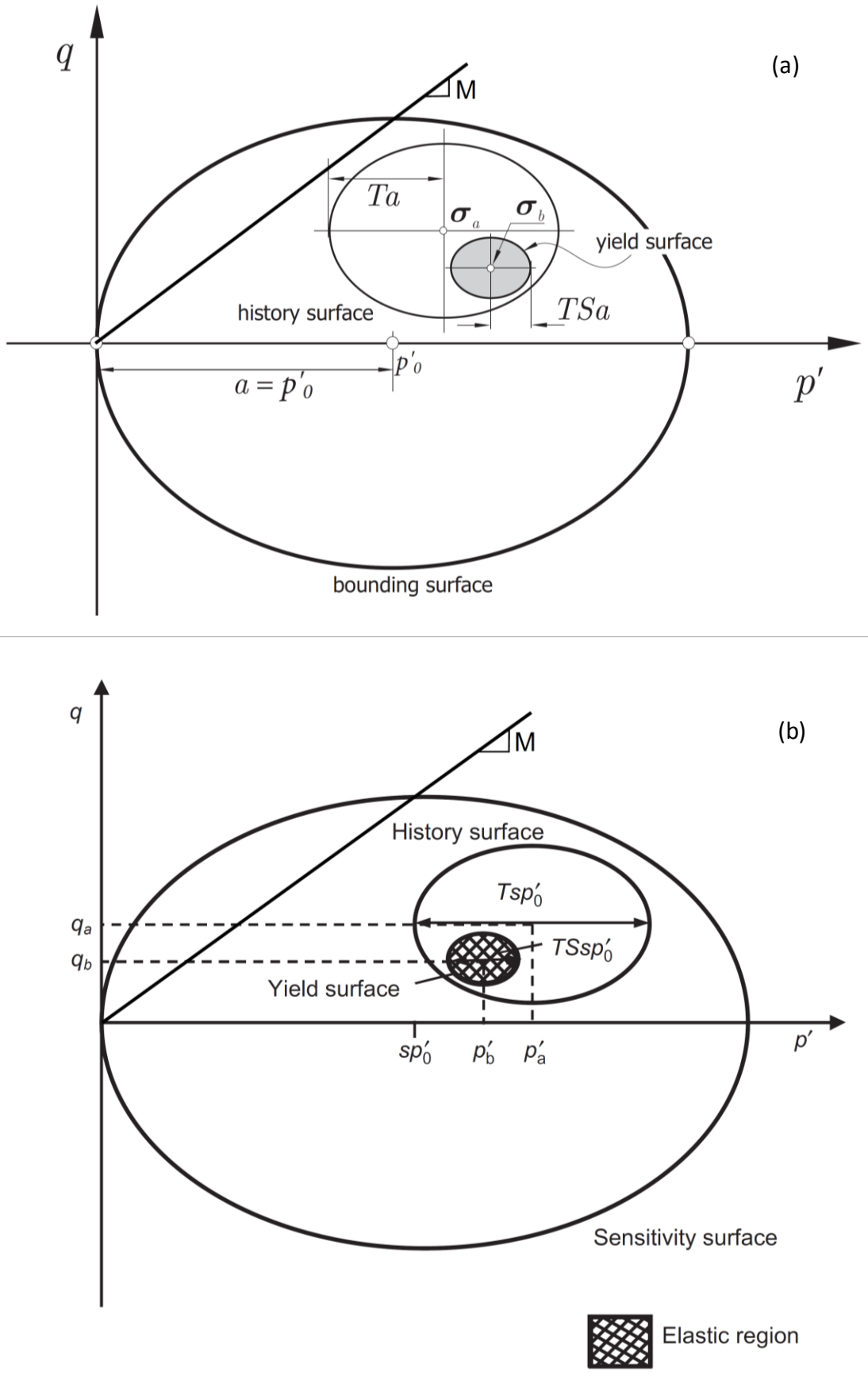

Figure 3.32 Schematic diagrams of the characteristic surfaces of the (a) 3–SKH model (Tamagnini *et al.*, 2006) and (b) S3-SKH model (Baudet and Stallebrass, 2004)

In S3-SKH model, the basic forms of the translation rules and hardening rule used in the 3-SKH model are retained. The key improvement was the incorporation of the effects of structure in the size of the bounding surface, which is represented by the product of the sensitivity parameter *s* which decreases exponentially with plastic strain and the centre of the intrinsic bounding surface p'_0 as illustrated in Figure 3.32 (b). In this model, the bounding surface is called the sensitivity surface as it is related to the sensitivity of soil and its size changes as plastic strain occurs (destructuration) similar to the MSS model. The three characteristic surfaces of the S3-SKH model are shown in Figure 3.32 (b).

The sensitivity surface is mathematically expressed as:

$$(p' - sp'_0)^2 + \frac{q^2}{M^2} = (sp'_0)^2 \qquad 3.52$$

where *s* = the sensitivity parameter which is equal to the ratio between the sizes of the sensitivity and equivalent intrinsic bounding surfaces, p'_0 = the centre of the intrinsic bounding surface and sp'_0 = the centre of the sensitivity surface.

The sensitivity surface formulation is exactly similar to that of the bounding surface for the "bubble" and 3-SKH models except the p'_0 is factored by the sensitivity parameter which represents the structure of the soil. The history and yield surfaces are defined in Equations 3.53 and 3.54 respectively.

$$(p' - p'_a)^2 + \frac{(q - q_a)^2}{M^2} = (Tsp'_0)^2 \qquad 3.53$$

$$(p' - p'_b)^2 + \frac{(q - q_b)^2}{M^2} = (TSsp'_0)^2 \qquad 3.54$$

where (p'_a, q_a) and (p'_b, q_b) = the stress state at the centre of the history and yield surfaces respectively; *T* = ratio of the size of the history surface to that of the sensitivity surface; *S* = ratio of the size of the yield surface to that of the history surface; and *M* = slope of the critical state line in q-p' space.

Within the yield surface, the soil deformation is assumed to be isotropic elastic with the following equation.

$$\begin{bmatrix} \dot{\boldsymbol{\varepsilon}}_v{}^e \\ \dot{\boldsymbol{\varepsilon}}_q{}^e \end{bmatrix} = \begin{bmatrix} \kappa^*/p' & 0 \\ 0 & 1/3G'_e \end{bmatrix} \begin{bmatrix} \dot{\boldsymbol{p}}' \\ \dot{\boldsymbol{q}} \end{bmatrix} \quad 3.55$$

where G'_e = elastic shear modulus and λ^*, κ^* = gradients of the normal compression line and elastic swelling lines in ln v-ln p' space respectively.

It was suggested by Baudet and Stallebrass (2004) to use the expression for the small-strain stiffness variation G_0 by Viggiani and Atkinson (1995) (Equation 3.56) for G'_e as it has been used successfully in the numerical analyses by Stallebrass and Taylor (1997). Equation 3.56 is based on the principle of hypo-elasticity and shows the dependency of the small-strain shear modulus G_0 on the mean effective stress, the plasticity index and overconsolidation ratio as shown below. This expression for G_0 was found to apply generally even at larger strains. In this formulation, the shear modulus is treated independently of the bulk modulus.

$$\frac{G_0}{p_{ref}} = A_g \left(\frac{p'}{p_{ref}}\right)^{n_g} {R_0}^{m_g} \quad 3.56$$

where A_g, n_g and m_g are dimensionless parameters which depend on the plasticity index, p_{ref} is a reference pressure equal to 1kPa, p' is the mean pressure and R_0 is the overconsolidation ratio in terms of mean effective stress = $2p_c/p'$.

Based on data from Bothkennar and Pisa clays, Baudet and Stallebrass (2004) observed that there is direct proportionality between the normalised decrement of sensitivity and increment of a damage strain when all effects of destructuration are assumed to be included in the current size of the bounding surface. This led to the formulation of sensitivity s given in Equation 3.57 considering the physical significance of sensitivity, which for natural clays is typically greater than 1.

$$\frac{\dot{\boldsymbol{s}}}{s-1} = \chi \dot{\varepsilon}_d \quad 3.57$$

where $\dot{\boldsymbol{s}}$ = the increment of current sensitivity for a given strain increment; s = the initial sensitivity; χ = a factor of proportionality that is always negative; and $\dot{\varepsilon}_d = \sqrt{(\dot{\varepsilon}_v{}^p)^2 + \left(\dot{\varepsilon}_q{}^p\right)^2}$ = increment of damage strain or the rate of destructuration strain.

Unlike the MSS model where the rates of volumetric and deviatoric structure degradation in the destructuration law can be varied, the plastic volumetric and shear strains in S3-SKH are treated as equally important.

Equation 3.57 is used as the basic form for destructuration but adjusted to include the fact that for natural clays with stable components of structure, sensitivity should reduce to a value greater than unity. Thus, the S3-SKH destructuration law is expressed as follows:

$$\dot{\boldsymbol{s}} = \frac{k}{\lambda^* - \kappa^*}(s - s_f)\dot{\varepsilon}_d \qquad 3.58$$

where k = a parameter that controls the rate of destructuration and s_f = the ultimate sensitivity, which represents the stable elements of structure. Both parameters k and s_f can be obtained from a standard isotropic compression test.

The translation rule is similar to the 3-SKH model and has the same form as those used in the two-surface model developed by Mróz *et al.* (1979) and Al-Tabbaa (1987). This rule controls the movement of the two kinematic surfaces inside the sensitivity surface during loading ensuring that the surfaces do not intersect. It is achieved by defining the centre of a surface such that it always moves along a vector joining the current stress state to its conjugate point on the next surface, as shown in Figure 3.33. The conjugate point is defined as the point on the surface with the same outwards normal. The model reduces to the MCC model when all the surfaces are in contact.

The translation of the history surfaces is expressed in Equation 3.59. The first term corresponds to isotropic hardening, i.e. movement due to the expansion or contraction of surface and the second term corresponds to kinematic hardening, i.e. movement of the surface along the vector β (see Figure 3.33) when it is dragged by the current stress state.

$$\begin{bmatrix} dp'_a \\ dq_a \end{bmatrix} = \frac{d(sp'_0)}{sp'_0}\begin{bmatrix} p'_a \\ q_a \end{bmatrix} + W\begin{bmatrix} \frac{p' - p'_a}{T} - (p' - sp'_0) \\ \frac{q - q_\alpha}{T} - q \end{bmatrix} \qquad 3.59$$

The scalar quantity W can be obtained through Equation 3.60.

$$W = \frac{(p' - p'_a)\left[dp' - \frac{d(sp'_0)}{sp'_0}p'\right] + \frac{q - q_a}{M^2}\left[dq - \frac{d(sp'_0)}{sp'_0}q\right]}{(p' - p'_a)\left[\frac{p' - p'_a}{T} - (p' - sp'_0)\right] + \frac{(q - q_a)}{M^2}\left[\frac{q - q_a}{T} - q\right]} \quad 3.60$$

When the history surface is in contact with the sensitivity surface, the translation rule for the history surface becomes:

$$\begin{bmatrix} dp'_a \\ dq_a \end{bmatrix} = (1 - T)\begin{bmatrix} dp' \\ q \end{bmatrix} + T\begin{bmatrix} d(sp'_0) \\ 0 \end{bmatrix} \quad 3.61$$

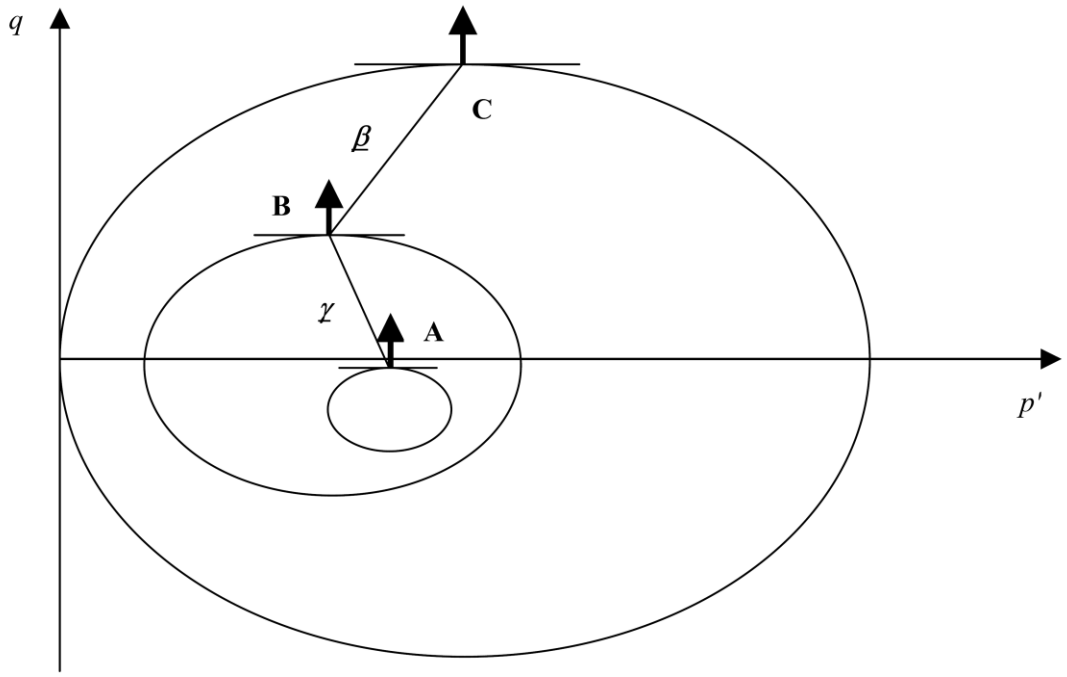

Figure 3.33 Conjugate stresses and vectors of movement of the kinematic surfaces (Stallebrass and Taylor, 1997)

Similar to the translation rule for the history surface, the translation rule for the yield surface given in Equation 3.62 is expressed in terms of the combined isotropic hardening (first term), i.e. movement due to the expansion or contraction of surface and kinematic hardening (second term), i.e. movement of the surface along vector *γ* (see Figure 3.33) when it is dragged by the current stress state.

$$\begin{bmatrix} dp'_b \\ dq_b \end{bmatrix} = \frac{d(sp'_0)}{sp'_0}\begin{bmatrix} p'_b \\ q_b \end{bmatrix} + Z\begin{bmatrix} \frac{p' - p'_b}{S} - (p' - p'_a) \\ \frac{q - q_b}{S} - (q - q_a) \end{bmatrix} \quad 3.62$$

The scalar quantity *Z* is calculated from Equation 3.63.

$$Z = \frac{\left(p' - p'_b\right)\left[dp' - \frac{d(sp'_0)}{sp'_0}p'\right] + \frac{q - q_b}{M^2}\left[dq - \frac{d(sp'_0)}{sp'_0}q\right]}{\left(p' - p'_b\right)\left[\frac{p' - p'_b}{S} - \left(p' - p'_a\right)\right] + \frac{(q - q_b)}{M^2}\left[\frac{q - q_b}{S} - (q - q_a)\right]} \qquad 3.63$$

Similarly, when the yield surface is in contact with the history surface, the translation rule for the yield surface becomes:

$$\begin{bmatrix} dp'_b \\ dq_b \end{bmatrix} = (1 - S)\begin{bmatrix} dp' \\ q \end{bmatrix} + S\begin{bmatrix} dp'_a \\ dq_a \end{bmatrix} \qquad 3.64$$

The hardening rule consists of two competing terms as suggested by Gens and Nova (1993). The first term is similar to the volumetric hardening rule of the "bubble" model given in Equation 3.32. The second term is the destructuration law given in Equation 3.58, which links change in sensitivity to change in damage strain. The hardening rule governs the variation in size of the sensitivity surface while constraining its form to be consistent with the volumetric hardening of the yield surface. Adopting the MCC model approach, S3-SKH assumes an associated flow rule such that the vector of plastic strain increments is always normal to all three current surfaces (Equation 3.23).

In general, the constitutive relationship for plastic strain increments on the yield surface is similar to the "bubble" model as expressed below.

$$\begin{bmatrix} d\varepsilon_v{}^p \\ d\varepsilon_q{}^p \end{bmatrix} = \frac{1}{h_0}\begin{bmatrix} \left(p' - p'_b\right)^2 & \left(p' - p'_b\right)\frac{q - q_b}{M^2} \\ \left(p' - p'_b\right)\frac{q - q_b}{M^2} & \left(\frac{q - q_b}{M^2}\right)^2 \end{bmatrix}\begin{bmatrix} dp' \\ dq \end{bmatrix} \qquad 3.65$$

However, the equation for h_0 has been modified to include the current sensitivity as shown below.

$$h_0 = \frac{(p' - p'_b)}{(\lambda^* - \kappa^*)}\left[p'\left(p' - p'_b\right) + \frac{q(q - q_b)}{M^2}\right]\left[1 - \frac{k}{p' - p'_b}\left(1 - \frac{s_f}{s}\right)\sqrt{\left(p' - p'_b\right)^2 + \left(\frac{q - q_b}{M^2}\right)^2}\right] \qquad 3.66$$

In order to formulate a general expression for the plastic strain increments which covers any positions between the characteristic surfaces, Stallebrass (1990) replaced h_0 in Equation 3.65 by the hardening modulus defined by the function $h = h_0 + H_1 + H_2$,

where H_1 and H_2 = functions of the position of the history surface and the yield surface respectively, as expressed below.

$$H_1 = \frac{1}{(\lambda^* - \kappa^*)} \left(\frac{b_1}{b_{1max}}\right)^{\psi} (sp'_0)^3 S^2 \quad 3.67$$

$$H_2 = \frac{1}{(\lambda^* - \kappa^*)} \left(\frac{Tb_2}{b_{2max}}\right)^{\psi} (sp'_0)^3 \quad 3.68$$

where b_1 = normalised distance between history and sensitivity surface; b_{1max} = maximum value of b_1; b_2 = normalised distance between yield and history surface; b_{2max} = maximum value of b_2; and ψ = an interpolation exponent determined from experimental results of the soil type under consideration which determines the rate of stiffness decay with strain.

The values for b_1 and b_2 are calculated from Equations 3.69 and 3.70 while the values for b_{1max} and b_{2max} are given by Equations 3.71 and 3.72. The distances b_1, b_2, b_{1max} and b_{2max} are defined geometrically in Stallebrass (1990).

$$b_1 = \frac{1}{Tsp'_0}\left\{\frac{(p' - p'_b)}{S}\left[\frac{p' - p'_b}{TS} - \left(\frac{p' - p'_b}{S} + p'_a - sp'_0\right)\right] + \frac{(q - q_b)}{SM^2}\left[\frac{(q - q_b)}{TS} - \left(\frac{q - q_b}{S} + q_a\right)\right]\right\} \quad 3.69$$

$$b_2 = \frac{1}{TSsp'_0}\left\{(p' - p'_b)\left[\frac{p' - p'_b}{S} - (p' - p'_a)\right] + \frac{(q - q_b)}{M^2}\left[\frac{(q - q_b)}{S} - (q - q_a)\right]\right\} \quad 3.70$$

$$b_{1max} = 2sp'_0(1 - T) \quad 3.71$$

$$b_{2max} = 2Tsp'_0(1 - S) \quad 3.72$$

S3-SKH model reduces to "bubble" model when the yield and history surfaces are in contact, i.e. $b_2 = 0$ and $H_2 = 0$. It reduces further to a Modified Cam Clay model when all surfaces are in contact, i.e. $H_1 + H_2 = 0$.

The model requires ten parameters, three of which, λ^*, κ^*, M are common with Modified Cam Clay, one elastic modulus parameter G'_e which can be derived from

Viggiani and Atkinson (1995) equation (Equation 3.56), three (T, S, ψ) are from the original 3-SKH model and three additional parameters (k, s_0, s_f) to represent the structure of the soil and the destructuration rate. One additional parameter is required to fix the model in ln v-ln p' space usually taken as the specific volume of the isotropic compression line at p' = 1KPa, i.e. N.

S3-SKH can simulate similar cyclic behaviours as the MSS model. However, as the bounding surface is centred at the mean stress axis (isotropic axis), the model cannot capture the effects of anisotropy. To take into account the material anisotropy, a modification was introduced by Mašín (2003) to 3-SKH model to predict the behaviour of anisotropically consolidated clays (AI3-SKH) by assuming a non–associated flow rule. McDowell and Hau (2003) also proposed a simple non-associated flow rule to improve the 3-SKH model in predicting the coefficient of earth pressure at rest (K_0) under one-dimensional normal compression.

The model was used to simulate drained probing tests and undrained triaxial tests on natural specimens of Bothkennar clay (Baudet and Stallebrass, 2004) as well as the behaviour of deep-sea sediments (Baudet and Ho, 2005). Nevertheless, there are no sufficient existing data to be able to evaluate the S3-SKH model exhaustively as stated by Baudet and Stallebrass (2004). Moreover, no practical application of the model to any geotechnical systems has been found in the literature.

3.5.6 *S-CLAY1S and B-SCLAY1S*

B-SCLAY1S is based on the S-CLAY1S model using critical state theory and bounding surface plasticity. The anisotropic elasto-plastic model S-CLAY1, developed at Glasgow and Helsinki, is an extension of conventional critical state models, i.e. Modified Cam Clay model, with anisotropy of plastic behaviour represented through an inclined yield surface and a rotational component of hardening to model the development or erasure of fabric anisotropy during plastic straining (Wheeler *et al.*, 2003a) as shown in Figure 3.34 (a). The S-CLAY1 model was originally proposed by Wheeler (1997) and subsequently modified to its current form based on experimental data obtained from triaxial tests on a natural soft Finnish clay (Naatänen *et al.*, 1999). Results from the tests and model simulations conducted on this clay suggested that the S-CLAY1 captured anisotropy very well, but there were a number of weaknesses in the

modelling identified. The main drawback of the model is its inability to accommodate the effects of soil structure and subsequent destructuration. The S-CLAY1S model was then proposed in the works by Koskinen *et al.* (2002) and Wheeler *et al.* (2003a) to take into account the influence of destructuration based on the concept of intrinsic yield surface by Gens and Nova (1993) while retaining all of the components of the S-CLAY1 model. The model aims to maintain a degree of simplicity with parameters that can be readily deduced from standard laboratory tests.

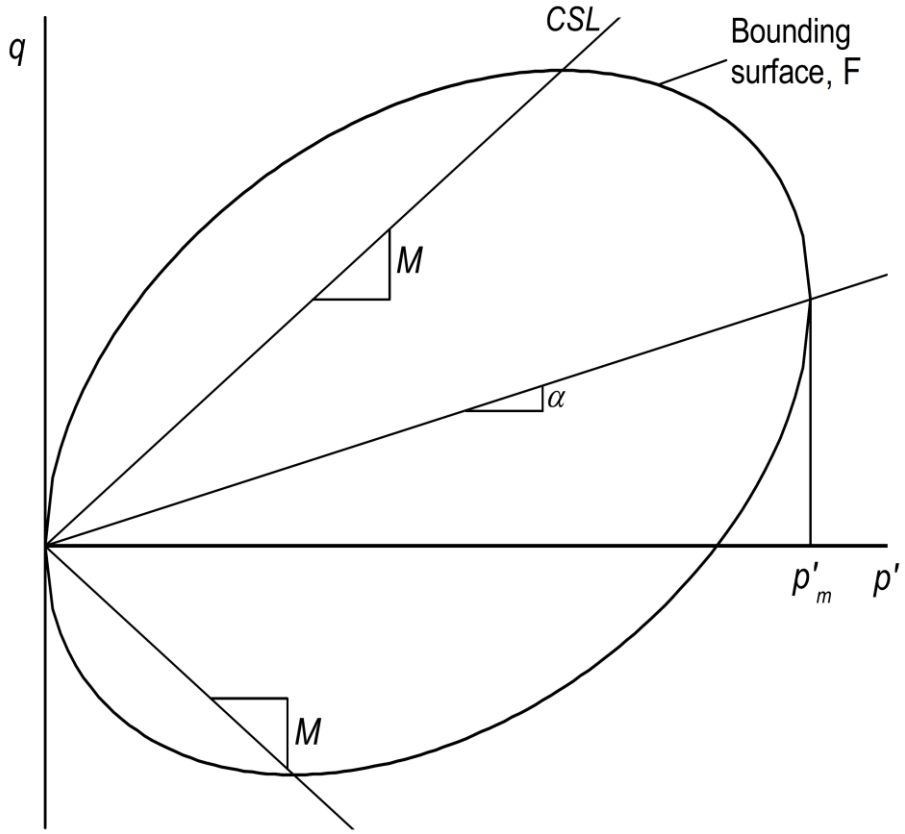

(a)

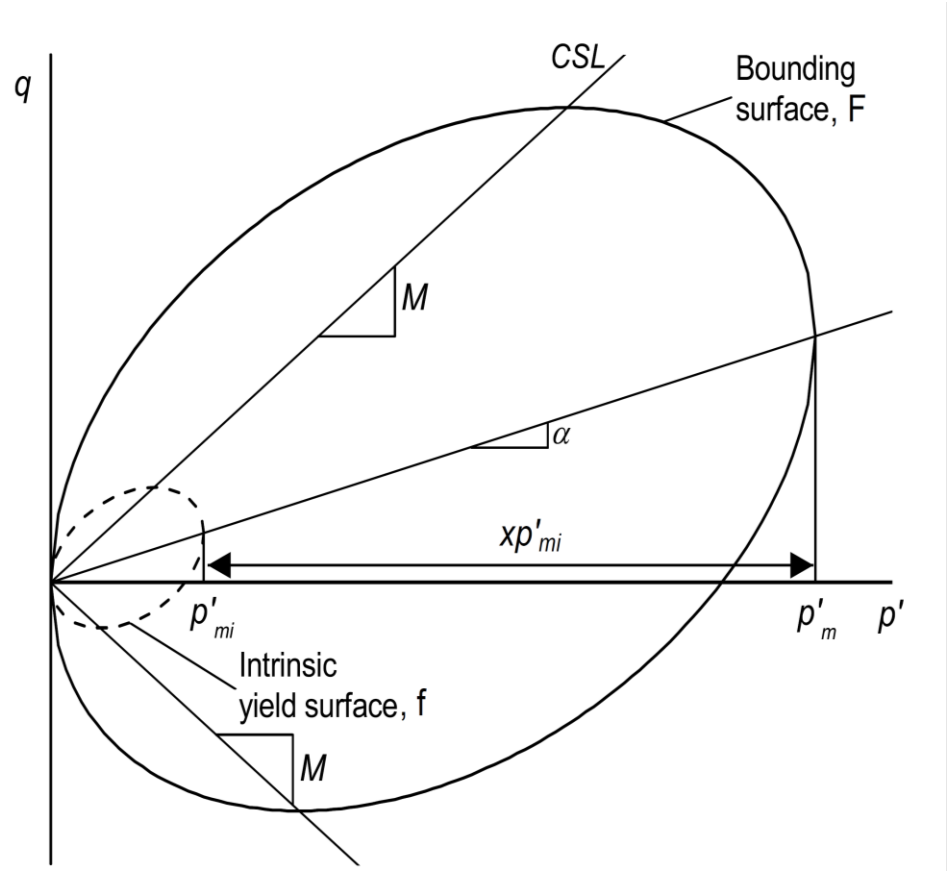

(b)

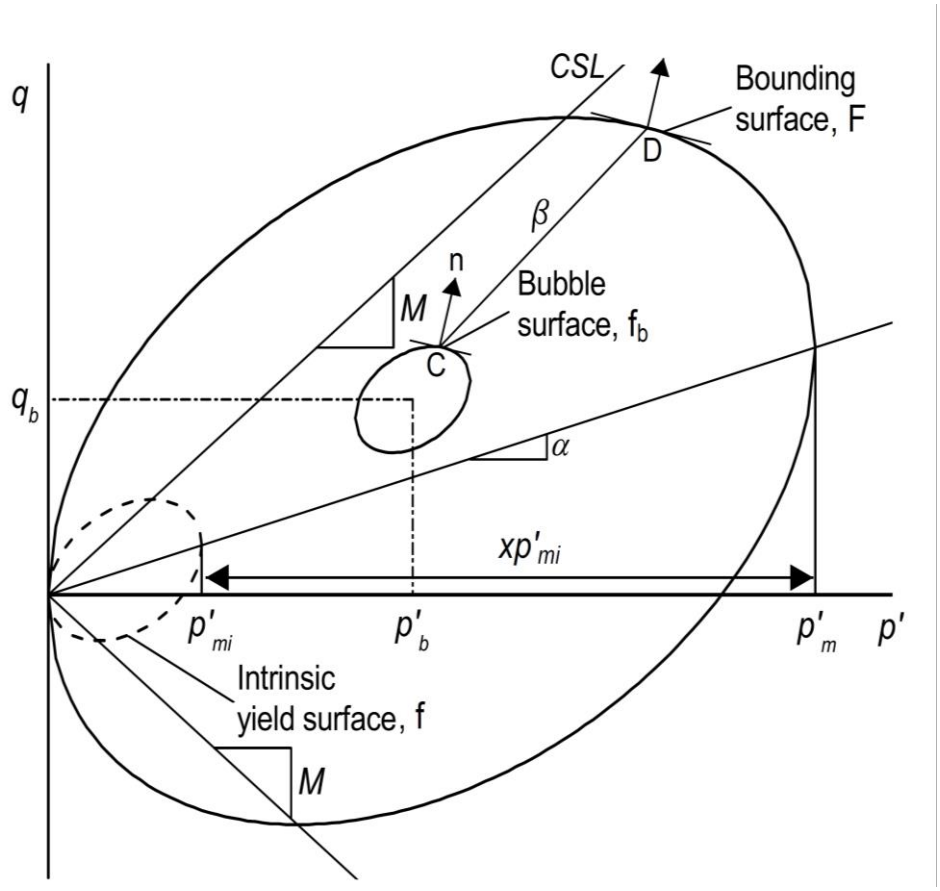

(c)

Figure 3.34 Evolution of B-SCLAY1S model: (a) S-CLAY1 model: (b) S-CLAY1S model; and (c) B-SCLAY1S model [modified from Sivasithamparam and Karstunen (2012)]

The S-CLAY1S model (and similarly the S-CLAY1) was developed for normally or lightly overconsolidated soils where plastic strains are dominant and elastic strains are relatively insignificant, such that the assumption of isotropic elasticity is sufficient. The assumed form of isotropic elastic behaviour is adopted from the Modified Cam Clay model which is expressed numerically in Equation 3.22. Likewise, an associated flow rule has been utilised, hence the plastic potential is the same as the bounding yield surface. The yield function for the bounding surface shown in Figure 3.34 (b) which represents the bonded soil has a shape of a sheared ellipse identical to the model proposed by Dafalias (1987) and Korhonen and Lojander (1987). The yield function is given below.

$$F = (q - \alpha p')^2 - (M^2 - \alpha^2)\left(p'_m - p'\right)p' = 0 \qquad 3.73$$

where M = slope of the critical state line; p'_m = size of the bounding surface or natural yield surface related to the soil's preconsolidation pressure; and α = orientation of the natural yield surface which is a measure of the degree of plastic anisotropy of the soil.

To define the destructured state of the soil, an equivalent unbonded soil represented by an intrinsic yield surface is added to S-CLAY1 model with the same orientation α as the bounding surface, but of smaller size, p'_{mi} as illustrated in Figure 3.34 (b). Thus, the equation for the intrinsic yield surface can be derived from Equation 3.73 as written below.

$$f = (q - \alpha p')^2 - (M^2 - \alpha^2)\left(p'_{mi} - p'\right)p' = 0 \qquad 3.74$$

The relative size of the bounding and intrinsic yield surfaces is linked to a bonding parameter x, such that the size of the bounding surface is now given by the equation below.

$$p'_m = (1 + x)p'_{mi} \qquad 3.75$$

where p'_{mi} = size of the intrinsic yield surface and x = amount of structure bonding.

S-CLAY1S incorporates three hardening rules: the first one (the "isotropic hardening rule") describes the change in size of the yield surface; the second one (the "rotational hardening rule") describes the change of orientation of the yield surface with plastic

straining; and the third one (the "destructuration rule") describes the degradation of structure bonding.

The isotropic hardening rule as given below relates to volumetric hardening and has the same formulation as the S-CLAY1 and MCC models but instead accounts for the change in size of the intrinsic yield surface rather than the yield surface for the bonded soil.

$$dp'_{mi} = p'_{mi}\frac{v}{\lambda_i - \kappa}d\varepsilon_v{}^p \qquad 3.76$$

where v = the specific volume; λ_i = the gradient of the intrinsic compression line in v-ln p' plane, i.e. the slope of the normal compression line for unstructured/unbonded soil and κ = the slope of the swelling line in v-ln p' space.

The rotational hardening rule which describes the rotation of bounding surface due to plastic volumetric and plastic shear straining also retains the same form as that of S-CLAY1 model and is defined below.

$$d\alpha = \mu\left[\left(\frac{3\eta}{4} - \alpha\right)\langle d\varepsilon_v{}^p\rangle + \beta\left(\frac{\eta}{3} - \alpha\right)\left|d\varepsilon_q{}^p\right|\right] \qquad 3.77$$

where $\eta = \frac{q}{p'}$ is the stress ratio; β = a soil parameter that controls the relative effectiveness of plastic shear strains and plastic volumetric strains in rotating the bounding surface and μ = a soil parameter that controls the absolute rate at which α heads towards its current target value. The parameter β can be determined in the same way as in S-CLAY1 as defined in Equation 3.78.

$$\beta = \frac{3\left(4M^2 - 4\eta_{K_0}{}^2 - 3\eta_{K_0}\right)}{8\left(\eta_{K_0}{}^2 - M^2 + 2\eta_{K_0}\right)} \qquad 3.78$$

where η_{K_0} = the stress ratio (i.e q/p') during K_0 consolidation which is a function of soil's friction angle.

The value of parameter μ can be obtained by simulation of experimental data as discussed by Wheeler *et al.* (2003b). The initial orientation of the bounding surface is determined from the equation below.

$$\alpha_{K_0} = \frac{\left(\eta_{K_0}{}^2 + 3\eta_{K_0} - M^2\right)}{3} \quad 3.79$$

The orientation of the bounding surface can be assumed to have been created by normally consolidated K_0 loading. Hence, the value of η_{K_0} can then be calculated from the K_{0NC} (coefficient of earth pressure at rest in normally consolidated conditions) as given below.

$$\eta_{K_0} = \frac{3(1 - K_{0nc})}{1 + 2K_{0nc}} \quad 3.80$$

When the orientation of the bounding surface α and the rate parameter μ are set to zero, the model reduces to the MCC model.

The destructuration rule describes the degradation of soil structure with plastic straining, i.e. both plastic volumetric and plastic shear strains, which tends to reduce the bonding parameter x towards zero as follows:

$$dx = -ax\left(|d\varepsilon_v{}^p| + b\left|d\varepsilon_q{}^p\right|\right) \quad 3.81$$

where a = a soil parameter that controls the absolute rate of destructuration and b = a soil parameter that controls the relative effectiveness of plastic deviatoric strains and plastic volumetric strains in destroying the bonding. These two soil parameters can be derived through the procedures outlined in Karstunen *et al.* (2005).

Despite the advanced features of S-CLAY1S model, it fails to reproduce some of the important characteristics of soil behaviour as listed below.

1. non-linearity and plasticity from early stages of loading; and
2. hysteretic behaviour of soil subjected to cyclic loading particularly gradual accumulation of irrecoverable plastic strains and accompanying energy dissipation, as well as accumulation of excess pore water pressures

To overcome these shortcomings, Sivasithamparam and Karstunen (2012) extended S-CLAY1S model into B-SCLAY1S by introducing a bubble surface within the bounding surface to enclose a truly elastic region based on the works of Al-Tabbaa (1987) as demonstrated in Figure 3.34 (c). The kinematic bubble surface has a similar shape to the bounding surface, but smaller in size and formulated as follows:

$$f_b = \frac{[(q - p'\alpha) - (q_b - p'_b\alpha)]^2}{M^2 - \alpha^2} + (p' - p'_b)^2 - R^2\left(\frac{p'_m}{2}\right)^2 \qquad 3.82$$

where (p'_b, q_b) = centre of the kinematic bubble surface; and R = the ratio of the size of the kinematic bubble surface to that of the bounding surface. M is assumed to be the same in compression and extension.

The kinematic bubble surface can translate within the bounding surface and can change size simultaneously (combined kinematic and isotropic hardening). The combination of the kinematic and isotropic hardening forms the fourth hardening rule, which is the "translation rule" of the kinematic bubble surface. Two different translation rules are adopted, one for the case when the bubble moves within the bounding surface (first translation rule) and one for the case when the two surfaces are in contact (second translation rule), which are all based on the works of Al-Tabbaa (1987). The rule is formulated to ensure that the bubble and the bounding surface engage at a common point but under no circumstances they intersect. This is achieved by defining the centre of the kinematic bubble surface such that it always moves along a vector β joining the current stress state C to its conjugate point D on the bounding surface, as shown in Figure 3.34 (c). When the bubble is not in contact with the bounding surface, no rotation is allowed.

The first translation rule is expressed in Equation 3.83 and comprised of two components: the first term in the equation corresponds to the change in size of the bubble due to isotropic expansion or contraction of the bounding surface while the second term corresponds to translation of the bubble along the vector β when it is dragged by the current stress state.

$$\begin{bmatrix} dp'_b \\ dq_b \end{bmatrix} = \frac{dp'_m}{p'_m}\begin{bmatrix} p'_b \\ q_b \end{bmatrix} + S\begin{bmatrix} \frac{p' - p'_b}{R} - (p' - p'_m) \\ \frac{(q - p'\alpha) - (q_b - p'_b\alpha)}{R} - (q - p'\alpha) \end{bmatrix} \qquad 3.83$$

where S = scalar quantity which can be derived from the consistency condition of the bubble surface.

The second translation rule describes the movement of the bubble when the two surfaces are in contact at the current stress state such that vector β becomes zero and Equation 3.83 is reduced to:

$$\begin{bmatrix} dp'_b \\ dq_b \end{bmatrix} = \frac{dp'_m}{p'_m} \begin{bmatrix} p'_b \\ q_b \end{bmatrix} \tag{3.84}$$

When the two surfaces are in contact the hardening modulus h_0 is given by the following equation:

$$h_0 = \frac{4v}{\lambda_i - \kappa} \left[\left(p' - \frac{p'_m}{2} \right) - \frac{(q - \alpha p')}{M^2 - \alpha^2} (\alpha) \right] \left[\frac{(q - \alpha p')^2}{M^2 - \alpha^2} + \left(p' - \frac{p'_m}{2} \right) p' \right] \tag{3.85}$$

To formulate a general expression for the plastic strain increments which covers any position between the two surfaces, either these surfaces are in contact or not, Al-Tabbaa (1987) replaced h_0 by a more general expression for the hardening modulus defined by the function $h = h_0 + H$ where H = function of a measure of the proximity of the bubble surface to the bounding surface. The details for calculating H can be found in Sivasithamparam (2012). Similar to S-CLAY1S, B-SCLAY1S adopts an associated flow rule; thus, the plastic strain increment vector is always normal to the kinematic yield surface at the current stress state.

The BS-CLAY1S model requires ten soil constants and 3 state variables. Four of the soil constants (λ_i, κ, M, Poisson's ratio) are from the MCC model which can be determined from conventional laboratory tests. Two (R, ψ) are introduced by the "bubble" model which can be obtained from simple standard tests or multi-stage tests using the triaxial apparatus. Two additional soil constants (μ and β) incorporates the evolution of anisotropy and two more soil constants (a and b) relates to the destructuration process. The procedures for determining the values of parameters of a and b are explained in Karstunen *et al.* (2005) while for μ and β can be found in Wheeler *et al.* (1999) and Wheeler *et al.* (2003b). The three state variables needed are the initial void ratio e_0, the initial anisotropy α_0 which gives the initial orientation of the bounding surface and the initial bonding x_0 which relates to the initial structure of the natural soil and can be estimated by the sensitivity S_t of the soil.

The model reduces to S-CLAY1S model by setting R equal to one and subsequently to S-CLAY1 by setting the relevant structure parameters to zero. Furthermore, if the initial anisotropy α_0 and μ are equal to zero, the model reverts back to the isotropic MCC model.

With the introduction of the bubble, B-SCLAY1S managed to address those aspects of soil behaviour not reproduced by the S-CLAY1S model, while keeping the rest of essential behaviours including material anisotropy and structure degradation. Hence, B-SCLAY1S model has all the necessary ingredients that would be ideal for simulating the behaviour of overconsolidated soils and/or the cyclic response of soils just like the MSS and S3-SKH models. However, ratcheting features have been observed by Sivasithamparam *et al.* (2010) during cyclic loading simulations which may over-predict the shear strain after large number of cycles. Also, due to the rotated yielding surface in the model, the pore water pressures during the undrained shearing stage have been observed to be underestimated while the initial stiffness was greatly overestimated (Valls-Marquez, 2009). In addition, it does not incorporate non-linearity of small strain stiffness stating that in many practical problems involving soft clays, the primary requirement for accurate numerical analysis is likely to be successful modelling of the onset of large plastic strains and the subsequent pattern of plastic straining (Wheeler *et al.*, 2003b).

Instead of introducing a bubble, Rezania *et al.* (2014) proposed a different improvement to S-CLAY1S by enhancing the bounding surface formulations for a better prediction of the cyclic behaviour in natural soils by capturing non-linearity and plasticity from the early stages of loading. The extended model referred to as SCLAY1S-BS model adopted a mapping rule to project the current stress state to an image point, where the origin of the stress space is assumed to be the fix projection centre in the unloading-reloading condition. Also, in this model, the plastic hardening modulus, which is related to a corresponding image point on the bounding surface, has different formulations for loading and unloading conditions. The details of the formulations are presented in Rezania *et al.* (2014). By comparing the results of cyclic loadings on Kaolin Clay against those from S-CLAY1S, the model shows much improved capability in simulating the gradual accumulation of permanent strains within the yield surface.

The B-SCLAY1S model has been verified by simulating slow cyclic loading on Kaolin clay (Sivasithamparam *et al.*, 2010) and Bothkennar clay (Sivasithamparam and Karstunen, 2012). No practical application of the model to any geotechnical systems has been found in the literature except in the works of Karstunen *et al.* (2005) where the behaviour of a test embankment in a soft clay has been investigated using the S-CLAY1S model.

3.5.7 *RMW (Kinematic Hardening Structure Model)*

RMW (Kinematic Hardening Structure Model) proposed by Rouainia and Wood (2000) as an extension of the "bubble" model by Al-Tabbaa and Wood (1989) is a rate-independent model. Similar to MSS, S3-SKH and B-SCLAY1S models, it takes into account the effects of damage to structure caused by irrecoverable plastic strains, resulting from geotechnical loading or disturbance such as sampling or an earthquake event (Elia and Rouainia, 2010). The model has been utilised by many authors and has been applied to different geotechnical structures such as shallow foundations [e.g. Elia and Rouainia (2014)], earth embankments [e.g. Panayides *et al.* (2012)] and tunnels [e.g. González *et al.* (2012)]. Its performance on cyclic/dynamic conditions has also been explored by authors including Elia and Rouainia (2012), Elia and Rouainia (2014), Elia and Rouainia (2016), Cabangon *et al.* (2017) and Cabangon *et al.* (2019).

The model has three yield surfaces, i.e. reference surface (f_r), bubble (f_b) and structure surface (F) as shown in Figure 3.35 (a) and (b), which have the same elliptical shape. The material parameter m in Figure 3.35 (b) represents the convexity of the surfaces and links M_ϑ and M. It is the ratio between the radii of the sections through the surface for axisymmetric extension and compression in the deviatoric plane and is equal to α^4 in Equation 3.87. To ensure convexity, m should be between 1 and 0.7. Although the model has three surfaces, it is still a two-surface model like MSS as the reference surface is neither involved in the kinematic hardening rule nor the hardening function. The reference surface, which passes through the stress origin, is used to model the intrinsic behaviour of the reconstituted or completely remoulded soil. It is always centred on the p' axis in the p'-q plane in the similar fashion to the Modified Cam Clay model and is expressed mathematically in Equation 3.86.

$$f_r = \frac{3}{2{M_\theta}^2}\boldsymbol{s}:\boldsymbol{s} + (p' - p_c)^2 - {p_c}^2 = 0 \qquad 3.86$$

where $\boldsymbol{s}$ = deviatoric stress tensor and M_θ = slope of the critical state line in triaxial space expressed as a function of Lode's angle θ. The symbol '**:**' indicates a summation of products. M_θ affects the three surfaces in the deviatoric plane and is derived from the following equation.

$$M_\theta = M\left[\frac{2\alpha^4}{1 + \alpha^4 + (1 - \alpha^4)\sin 3\theta}\right]^{\frac{1}{4}} \qquad 3.87$$

where M = the slope of the critical state line for triaxial compression and α = a material parameter which sets the shape of the reference surface. When the parameter α = (3 - sin φ)/(3 + sin φ) (where φ is the friction angle of the soil at critical state), the reference surface coincides with the Mohr-Coulomb hexagon at all vertices in the deviatoric plane and when α = 1 the surface follows the Drucker-Prager compression circle (as originally assumed in Modified Cam Clay).

The Lode's angle θ is related to the second stress invariant $J_2 = (\frac{1}{2}\boldsymbol{s}:\boldsymbol{s})$ and third stress invariant $J_3 = (\frac{1}{3}s_{ij}s_{jk}s_{ki})$ such that:

$$\frac{-\pi}{6} \leq \theta = \frac{1}{3}\sin^{-1}\left[\frac{-3\sqrt{3}J_3}{2{J_2}^{3/2}}\right] \leq \frac{\pi}{6} \qquad 3.88$$

The bubble is the yield surface separating regions of elastic and plastic response and moving with the current stress. It has the same role as the internal plastic surface (PYE) in the MSS model. When the stress path engages the bubble, its size changes according to an isotropic hardening rule and translates inside the structure surface according to a kinematic hardening rule similar to the "bubble" model. The equation of the bubble surface is:

$$f_b = \frac{3}{2{M_\theta}^2}(\boldsymbol{s} - \boldsymbol{s}_{\bar{\alpha}}):(\boldsymbol{s} - \boldsymbol{s}_{\bar{\alpha}}) + (p' - p_{\bar{\alpha}})^2 - (Rp_c)^2 = 0 \qquad 3.89$$

where R = the ratio between the sizes of the bubble surface and the reference surface and $\{p'_{\bar{\alpha}}, \boldsymbol{s}_{\bar{\alpha}}\}^T = \bar{\alpha}$ denotes the location of the centre of the bubble in the stress space. When the stress state is situated inside the bubble, the response of the model is

isotropic elastic, with the elastic part expressed in the original formulation in terms of the linear bulk and shear moduli, *K* and *G* as previously defined in Equations 3.28 and 3.29.

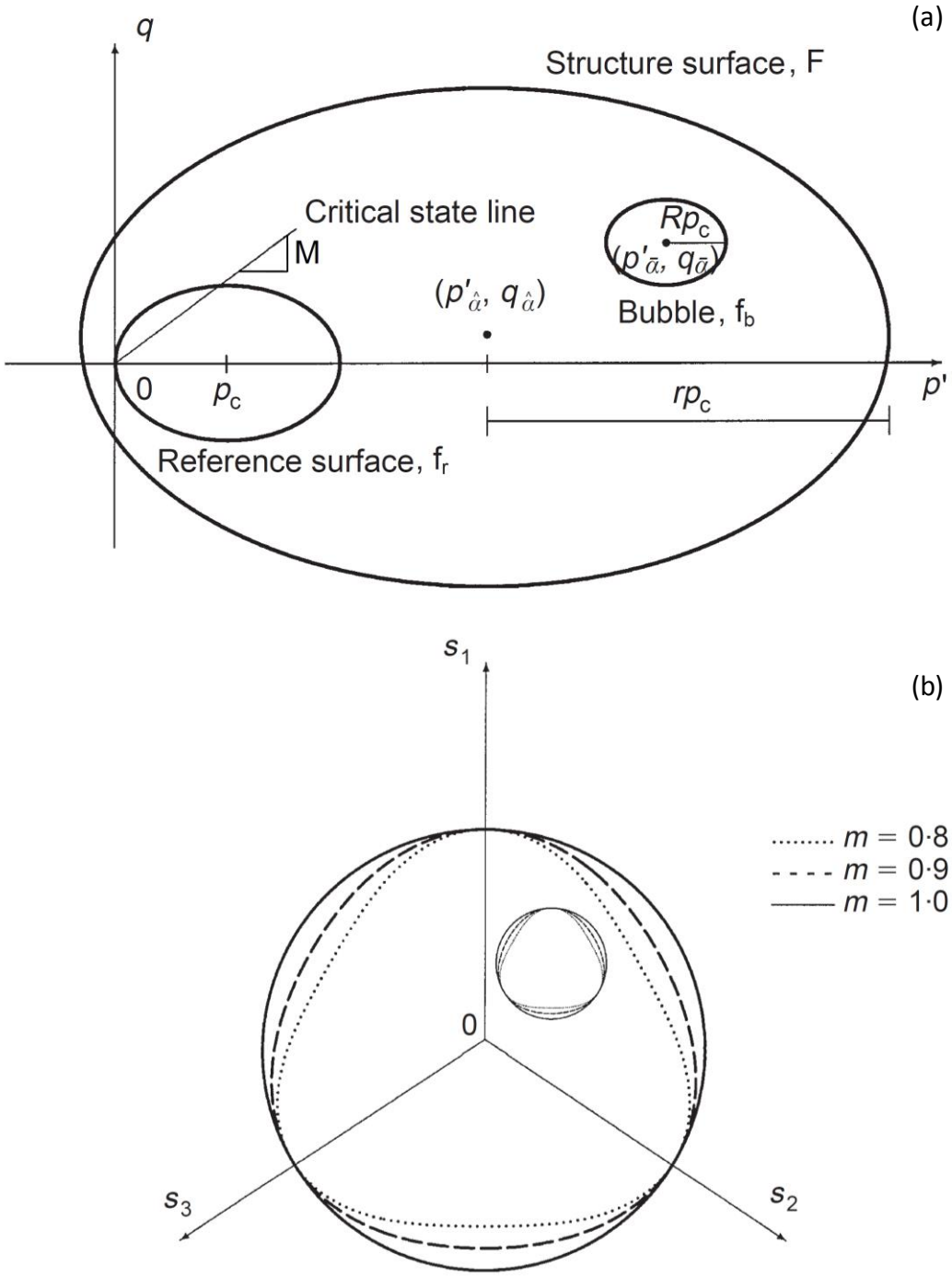

Figure 3.35 (a) Schematic diagram of the RMW model; (b) Deviatoric section through bubble and structure surface (Rouainia and Wood, 2000)

The shear modulus *G* was modified in the later publications by González *et al.* (2011), Panayides *et al.* (2012), González *et al.* (2012), Panayides (2014) and Elia and Rouainia

(2016) using non-linear stiffness of soil at very small strain introduced by Viggiani and Atkinson (1995) (Equation 3.56).

The model also allows choice of the formulations developed by Houlsby *et al.* (2005) based on the principle of hyper-elasticity. The formulations focused on deriving elasticity models that would obey the laws of thermodynamics. By adopting the hyper-elastic approach, a reversible response can be derived based on the existence of an energy potential. It avoids the issue with hypo-elastic models where application of multiple cycles on soils can lead to the continuous production of energy. Details of these formulations can be found in the above reference.

The structure surface acts as a bounding surface similar to the external bond strength surface (BSE) in the MSS model and contains information about the initial or current stress state of the soil including the current magnitude and anisotropy of structure. This surface controls the process of destructuration through its interaction with the bubble. As plastic straining occurs, the destructuration process proceeds such that this structure surface collapses towards the reference surface. The surface structure is described by Equation 3.90.

$$F = \frac{3}{2M_\theta{}^2}[\boldsymbol{s} - (r-1)\eta_0 p_c]:[\boldsymbol{s} - (r-1)\eta_0 p_c] + (p' - rp_c)^2 - (rp_c)^2 = 0 \qquad 3.90$$

where η_0 = a dimensionless deviatoric tensor controlling the structure surface and $\{rp_c, (r-1)\eta_0 p_c\}^T = \hat{\alpha}$ denotes the centre of the structure surface. The centre of the structure surface can be situated off the mean effective stress axis, allowing the model to accommodate the inherent anisotropy, which is commonly exhibited by natural structured clays. The anisotropy is captured by the position of the structure surface according to the parameter η_0. The scalar variable r is the size of the structure surface relative to the reference surface and calculated by Equation 3.91. It represents the progressive destructuration of a structured soil and is assumed to be a monotonically decreasing function of the plastic strain.

$$r = 1 + (r_0 - 1)exp\left[\frac{-k\varepsilon_d}{\lambda^* - \kappa^*}\right] \qquad 3.91$$

where r_0 = the initial structure (similar to the sensitivity parameter s in S3-SKH model) and k = a parameter defining the rate of destructuration with strain. The incremental form of Equation 3.91 is written as,

$$\dot{r} = -\frac{k}{\lambda^* - \kappa^*}(r-1)\dot{\varepsilon}_d \tag{3.92}$$

Similar to the MSS model, both compression and shearing contribute to the soil destructuration, therefore the rate of the destructuration strain $\dot{\varepsilon}_d$, expressed below in incremental form, comprises both plastic volumetric strain rate $\dot{\varepsilon}_v{}^p$ and equivalent plastic shear strain rate $\dot{\varepsilon}_q{}^p$.

$$\dot{\varepsilon}_d = \left[(1-A)(\dot{\varepsilon}_v{}^p)^2 + A\left(\dot{\varepsilon}_q{}^p\right)^2\right]^{1/2} \tag{3.93}$$

where A = a non-dimensional scaling parameter indicating the proportion of volumetric and shear strains on the degree of destructuration. For A = 1 the destructuration is purely distortional, while for A = 0 the destructuration is purely volumetric. The equations for the plastic volumetric strain rate and equivalent plastic shear strain rate are given below.

$$\dot{\varepsilon}_v{}^p = \frac{1}{3} tr(\dot{\boldsymbol{\varepsilon}}^p) \tag{3.94}$$

$$\dot{\varepsilon}_q{}^p = \left[\frac{2}{3}(\dot{\boldsymbol{\varepsilon}}^p : \dot{\boldsymbol{\varepsilon}}^p)\right]^{1/2} \tag{3.95}$$

where $\dot{\boldsymbol{\varepsilon}}^p$ = plastic strain rate tensor and *tr* is the trace operator.

The associated flow rule when the bubble surface is engaged, i.e. f_b = 0, marking the onset of plastic deformation is given by Equation 3.96.

$$\dot{\boldsymbol{\varepsilon}}^p = \dot{\gamma}\overline{\boldsymbol{n}} \tag{3.96}$$

where $\dot{\gamma}$ = plastic multiplier; $\overline{\boldsymbol{n}}$ = a unit vector representing the normalised stress gradient on the bubble at the current stress state and $\|\overline{\boldsymbol{n}}\| = |\overline{\boldsymbol{n}} : \overline{\boldsymbol{n}}|^{1/2}$ is a unit vector. The calculation of $\overline{\boldsymbol{n}}$ involves the derivatives of Lode's angle with respect to the stress as given below.

$$n_{ij} = \frac{\partial f_b}{\partial \sigma_{ij}} = \frac{-6}{{M_\theta}^3} J_2 \frac{\partial M_\theta}{\partial \sigma_{ij}} + \frac{3}{{M_\theta}^2} \frac{\partial J_2}{\partial \sigma_{ij}} + 2(p' - {p'}_{\bar{\alpha}}) \frac{\partial p'}{\partial \sigma_{ij}} \qquad 3.97$$

The plastic multiplier can be computed as:

$$\dot{\gamma} = \frac{1}{H}(\bar{\boldsymbol{n}} : \dot{\boldsymbol{\sigma}}') = \frac{1}{H_c}(\bar{\boldsymbol{n}} : \dot{\boldsymbol{\sigma}}'_c) \qquad 3.98$$

where $\dot{\boldsymbol{\sigma}}'$ and $\dot{\boldsymbol{\sigma}}'_c$ are the stress tensor and conjugate stress tensor respectively while H and H_c are the associated scalar plastic hardening moduli. The conjugate stress tensor $\dot{\boldsymbol{\sigma}}'_c$ is defined as the stress point on the structure surface with similar outward normal as the current stress point $\dot{\boldsymbol{\sigma}}'$ on the bubble as shown in Figure 3.36.

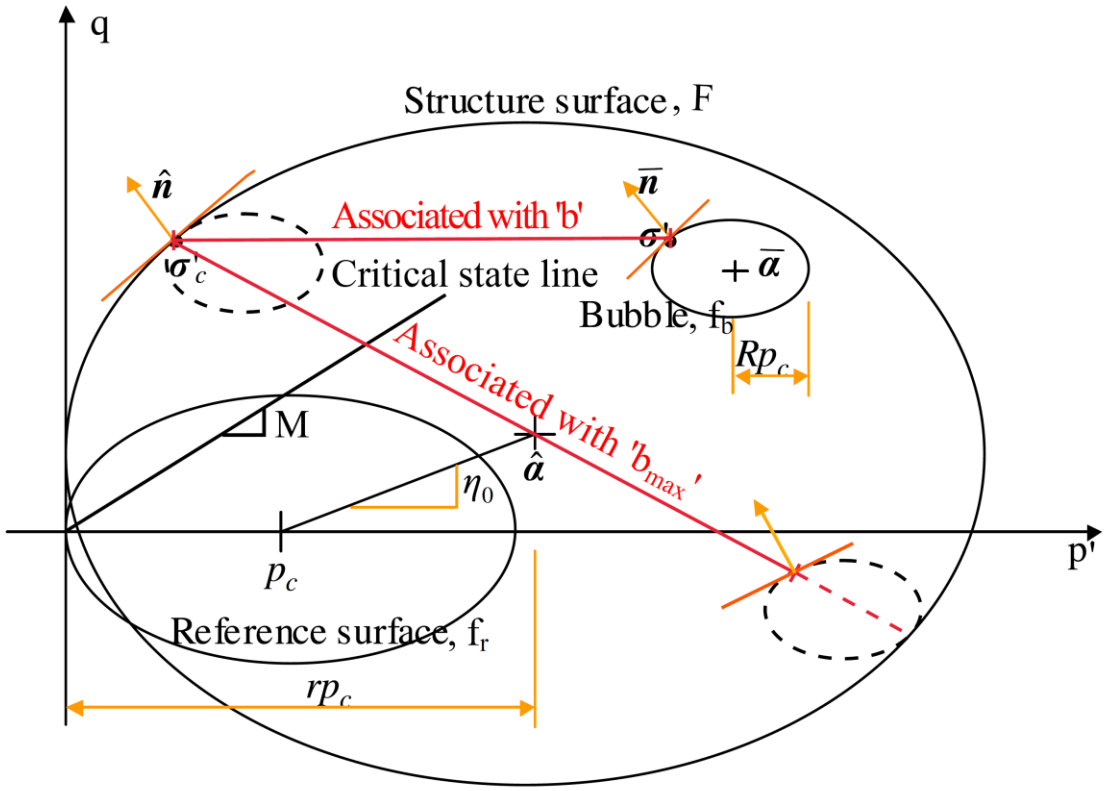

Figure 3.36 Conjugate stresses and vectors of movement of the kinematic surface model [Ni (2007), Panayides (2014)]

The conjugate plastic hardening modulus H_c described numerically below is derived from the consistency condition on the structure surface when the bubble and the structure surface are in contact.

$$H_c = \frac{rp_c\left\{T\left[(p'-p'_{\bar{\alpha}})+\left(\frac{3}{2{M_\theta}^2}\right)(\boldsymbol{s}-\boldsymbol{s}_{\bar{\boldsymbol{\alpha}}}):\eta_0+Rp_c\right]-\left(p'-p'_{\bar{\alpha}}\right)+\left(\frac{3}{2{M_\theta}^2}\right)(\boldsymbol{s}-\boldsymbol{s}_{\bar{\boldsymbol{\alpha}}}):\frac{\eta_0}{r}\right\}}{(\lambda^*-\kappa^*)\left[(p'-p'_{\bar{\alpha}})+\left(\frac{3}{2{M_\theta}^2}\right)(\boldsymbol{s}-\boldsymbol{s}_{\bar{\boldsymbol{\alpha}}}):(\boldsymbol{s}-\boldsymbol{s}_{\bar{\boldsymbol{\alpha}}})\right]} \quad 3.99$$

where the quantity T is expressed as:

$$T=(p'-p'_{\bar{\alpha}})-k\left(\frac{r-1}{r}\right)\left[(1-A)(p'-p'_{\bar{\alpha}})^2+\left(\frac{3A}{2{M_\theta}^4}\right)(\boldsymbol{s}-\boldsymbol{s}_{\bar{\boldsymbol{\alpha}}}):(\boldsymbol{s}-\boldsymbol{s}_{\bar{\boldsymbol{\alpha}}})\right]^{1/2} \quad 3.100$$

The variation of the plastic hardening modulus H within the structure surface, as defined by an interpolation rule along a distance b (shown in Figure 3.36) between the current stress on the yield surface and the conjugate stress on the structure surface, is given in Equation 3.101.

$$H = H_c + \frac{1}{\|\bar{\boldsymbol{n}}\|^2}\frac{B{p_c}^3}{(\lambda^*-\kappa^*)R}\left(\frac{b}{b_{max}}\right)^{\psi} \quad 3.101$$

where ψ and B = the material parameters controlling the rate of decay of stiffness with strain and the magnitude of the contribution of the interpolation term, respectively; b = normalised distance between current stress point σ' on the bubble and the conjugate stress point σ'_c on the structure surface; and b_{max} = the maximum distance of b when the bubble is touching the structure surface at a point diametrically opposite the conjugate stress point σ'_c as illustrated in Figure 3.36. The expressions for b and b_{max} are given below.

$$b = \bar{\boldsymbol{n}}:(\boldsymbol{\sigma}'_c-\boldsymbol{\sigma}') \quad 3.102$$

$$b_{max} = 2\left(\frac{r}{R}-1\right)\bar{\boldsymbol{n}}:\bar{\boldsymbol{\sigma}} \quad 3.103$$

where $\bar{\boldsymbol{\sigma}}=\boldsymbol{\sigma}'-\bar{\boldsymbol{\alpha}}$ is the normalised stress with respect to the centre of the bubble.

In line with the Cam Clay model, the isotropic hardening rule adopted a volumetric hardening rule where the change in size of the reference surface p_c is controlled only by plastic volumetric strain rate $\dot{\varepsilon}_v{}^p$ as shown below.

$$\frac{\dot{p}_c}{p_c} = \frac{\dot{\varepsilon}_v{}^p}{\lambda^* - \kappa^*} \qquad 3.104$$

Following the works of Mróz (1967), Hashiguchi (1988), among others, the kinematic hardening rule was formulated such that the translation of the bubble ensures a smooth transition between the bubble and the structure surface while avoiding the two surfaces to intersect. To achieve this, the centre of the bubble was defined such that it translates relative to the centre of the structure surface in a direction parallel to the line that joins the current stress and the conjugate point, i.e. the line associated with *b* shown in Figure 3.36. The translation rule is summarised through Equation 3.105.

$$\dot{\bar{\boldsymbol{\alpha}}} = \dot{\hat{\boldsymbol{\alpha}}} + (\bar{\boldsymbol{\alpha}} - \hat{\boldsymbol{\alpha}})\left(\frac{\dot{r}}{r} + \frac{\dot{p}_c}{p_c}\right) + \frac{\bar{\boldsymbol{n}}:\left\{\dot{\hat{\boldsymbol{\sigma}}} - \hat{\boldsymbol{\sigma}}\left[\frac{\dot{r}}{r} + \frac{\dot{p}_c}{p_c}\right] + \bar{\boldsymbol{\sigma}}\left(\frac{\dot{r}}{r}\right)\right\}}{\bar{\boldsymbol{n}}:(\boldsymbol{\sigma}'_c - \boldsymbol{\sigma}')}(\boldsymbol{\sigma}'_c - \boldsymbol{\sigma}') \qquad 3.105$$

The above equation includes the shift of the centre of the structure surface, the scaling of the space inside the structure surface in accordance to the change in the values of *r* and p_c and the translation along the line joining common normals.

As plastic deformation progresses, the parameter η_0 ultimately degrades to zero and the initial measure of structure r_0 eventually reduces to unity, thereby degenerating the RMW model to the "bubble" model. In addition, if the bubble surface finally coincides with the reference surface due to continuous yielding, i.e. $R = 1$, then the model reduces further to Cam Clay model.

RMW model requires eleven material parameters, four of which, λ^*, κ^*, M, μ, are common with Modified Cam Clay, three (R, ψ, B) are introduced by the "bubble" model and the additional four parameters (A, k, r_0, η_0) incorporate the anisotropy, the initial structure of the soil and the destructuration rate. In addition, the initial conditions of the soil need to be specified, i.e. p_{c0} = the initial value of p_c in order to define the size of the surfaces and $\bar{\boldsymbol{\alpha}}$ = the location of centre of the bubble yield surface.

The enhanced features gained in the development of RMW model overcame the flaws found in its predecessors, i.e. Modified Cam Clay and "bubble" model. The model not only addresses the soil's non-linear behaviour, hysteretic action, stiffness degradation,

pore pressure build-up (for saturated soils) and material anisotropy but also takes into account the early development of early strains, the response in the small strain region and the effects of damage to structure caused by irrecoverable plastic strains. Nonetheless, Ni (2007) in his thesis listed some observed limitations of the RMW model. Some of those relevant observations are as follows:

1. The model does not allow tensile mean principal stress when used to model a rigid strip foundation in a homogeneous over-consolidated non-structured soil subjected to vertical vibration, thus the steady state response cannot be demonstrated numerically under high level of excitations.
2. The model predicts less dilatancy than laboratory measurements resulting to a predicted small strain behaviour which is less stiff than measured.
3. The model inherits the non-smooth elasto-plastic transition of MCC and "bubble" models, thus an abrupt change in stiffness, when the stress state reaches the kinematic yield surface.

Further improvements on the formulations of the model were carried out by researchers including works by González *et al.* (2011) to provide a smooth transition from elastic to elasto-plastic behaviour to avoid a spurious stiffness degradation response by modifying the plastic hardening modulus. Ni (2007) proposed an alternative form to the plastic modulus function of the model to incorporate better size ratio effects of the yield surface. Ni (2007) also suggested a multiplier to the plastic modulus function to smoothen transition in stiffness from elastic region to yielding based on the concept proposed by Kavvadas and Amorosi (2000). Moreover, Elia and Rouainia (2016) introduced a modification on the Viggiani and Atkinson (1995) equation for the variation of G_0 with current state to account for the influence of structure r_0 on the initial elastic stiffness thereby enhancing further the model's predictive capabilities under static and cyclic loading conditions. It should be noted that the only modification to the original RMW model is in the elasticity part, (i.e. G_0). In this project, the G_0 profile was based from known experimental data of the soil medium and therefore its profile will not be greatly affected by the modified equation. This, in turn, will not alter the rest of the performance of RMW during cyclic loading. In the case of parametric studies, similar value of G_0 has been used in all cases (i.e. the value of r_0 is similar in all cases) and therefore will be cancelled out when comparison

is made between the results (e.g. comparing results from two values of destructuration rate *k*). Also, this version of RMW is not available in Plaxis. Hence, these improvements are not utilised in this project but noted as a recommendation for future research work.

3.6 Numerical methods

There are several numerical methods to obtain solutions to boundary-value or initial-value problems. Numerical methods only provide approximations to the correct or exact mathematical solution. This is due to some simplifications made to solve the system of differential equations either inside the continuum or at the boundaries of the discretisation. Three of the most commonly used methods in geotechnics are the Finite Element Method (FEM), Finite Difference Method (FDM) and Boundary Element Method (BEM). A general definition of these methods including their advantages and disadvantages are given below. Details and procedures of these methods will not be discussed further but can be found in relevant books and literatures.

3.6.1 *Finite element method (FEM)*

The finite element method yields approximate values of the unknowns at discrete number of points over the domain. The method involves subdividing a large complex problem into smaller, simpler parts that are called finite elements. Each finite element is represented by a set of element equations which are then assembled together with the rest of the finite elements into a larger system of equations that models the entire problem. The global system of equations is calculated from the initial values and boundary conditions of the problem to obtain a numerical answer using known solution techniques (https://en.wikipedia.org/wiki/Finite_element_method).

FEM is by far the most used method for the analysis of continuous or quasi-continuous media. The method is based on the principle of virtual displacements. It relies on the assumption that, through appropriately chosen interpolation functions, displacements at any point within the element can be accurately obtained from the displacements of the nodes (Bobet, 2010).

Advantages

- Almost no limitations with respect to modelling complex geometries
- Construction steps can be easily modelled (e.g. embankment layers, excavation sequence, prestressing of anchors, etc.)
- Application of advanced soil constitutive models possible (e.g. anisotropy, time dependent, non-linear behaviour, etc.)
- Change of material properties can be introduced during calculation (e.g. grouting, stiffness and strength increase of shotcrete, etc.)
- Soil-structure interaction can be modelled with interface elements
- Extensively used not only in engineering but also in other fields bringing significant wider experience

Disadvantages

- Volume discretisation required particularly in 3D producing significant pre- and post-processing effort
- Longer calculation times and high disk storage requirements especially for large and complex models
- Matrix operations required for solution
- Non-symmetric equation systems for some constitutive models
- Modelling of post peak behaviour requires special formulations and algorithms
- Highly advanced constitutive models need special solution algorithms
- Not suitable for blocky structures (discontinua)

3.6.2 *Finite difference method (FDM)*

The finite-difference method is the most direct approach to discretising partial differential equations where one considers a point in space taking the continuum representation and replacing it with a set of discrete algebraic equations, called finite-difference equations (Sjodin, 2016). Finite Differences are just algebraic schemes where one can derive approximate solutions. This method is typically defined on a regular grid which can be used for very efficient solution methods. It is therefore not usually used for irregular geometries, but more often for rectangular or block-shaped models.

FDM is used to solve differential equations that have conditions imposed on the boundary rather than at the initial point. The governing equations are substituted by finite differences in space, written in terms of field variables at discrete points specifically at the nodes whereas in the finite element method the equations define variables at discrete elements. Because of that, the algorithms used in FDM require generally less computational power to solve the equations, but the results are less refined and accurate compared to FEM. In FDM, the solution is achieved by time stepping using small intervals of time and the grid values are generated at each time step.

Advantages

- Complex constitutive models easier to implement than in FEM
- For explicit solution algorithms, no equation system required
- Requires less computational power and in most cases provides faster calculation times
- No matrix operations are required

Disadvantages

- Volume discretisation required
- Has a lower order of approximation (accuracy)
- Not the same range of higher order elements available as FEM
- Long calculation times in 3D
- For linear or moderately nonlinear systems less efficient than FEM
- Method is based on Newton's law of motion thus no "converged" solution for static problems exist, i.e. solution can be achieved but it may not be correct. However, this is at the same time an advantage for unstable conditions.

3.6.3 *Boundary element method (BEM)*

The boundary element method, as its name suggests, is a numerical method where only the boundaries of the continuum need to be discretised in contrast with FEM and FDM where the entire medium has to be discretised (Bobet, 2010). Also, if the medium extends to infinity, which is common in problems in geomechanics, no artificial

boundaries are required. Thus, the BEM automatically satisfies far-field conditions unlike in FDM and FEM where artificial boundary conditions are necessary.

In the BEM, the solution is approximated at the boundaries while equilibrium and compatibility are exactly satisfied in the interior of the medium as pointed out by Bobet (2010). This is an exact opposite in FDM and FEM where the approximations are made inside the medium. One advantage of limiting the discretisation to the boundaries is that the problem is reduced by one order, i.e. from 3D to a 2D surface problem at the boundary, and from 2D to a line problem. Thus, the method is very efficient and attractive for those problems where the volume to boundary surface ratio is large.

Advantages

- Only surface discretisation for 3D
- Number of unknowns significantly reduced
- Shorter run times, less storage capacity required
- Multiple region formulation allows modelling of distinct fault zones
- Discretisation error only at surface, i.e. calculation of results in the interior of the domain involves no further approximation
- Results can be obtained anywhere in the domain not only at predefined (e.g. Gauss) points

Disadvantages

- Not well suited for modelling highly nonlinear material behaviour
- Equation system non-symmetric
- So-called fundamental solution must be known
- Modelling of excavation sequence more difficult

3.7 Geotechnical engineering software

Several geotechnical engineering codes/software currently available have been identified and their features and capabilities assessed to select the most appropriate tool which meets the project objectives.

The author examined both open- and closed-source (commercial) codes/software by reviewing information from literature, brochures and websites as well as communicating with suppliers and comparing their individual attributes based on selection criteria developed by the author to suit the project requirements. Seven codes/software have been shortlisted and fully assessed. These codes/software are listed below and briefly described in the succeeding sections.

Open-source codes/software

- SwanDyne + GID (Graphic Interface Device)
- OpenSees + GID
- Tochnog + GID

Closed-source codes/software

- FLAC
- LS-Dyna
- PLAXIS
- MIDAS GTS NX

According to Saltis (2018), open-source codes/software are distributed under a licensing agreement which allows computer code to be shared, viewed and modified by other users and organisations. They are available for the general public and can be modified from its original design free of charge or charged minimally. This piece of software can evolve and entirely change form and shape over time.

On the other hand, closed-source codes/software are proprietary software distributed under a licensing agreement to authorise users with private modification, copying, and republishing restrictions. The source code is not published or shared with the public to view and modify. Only the original authors can access, copy, alter and improve that software. Most importantly, one has to pay for the use of the software. Saltis (2018) listed down the key differentiators between open and closed which come down to a few factors namely:

1. Cost

One of the main advantages of open source software is the cost. The cost for closed-source software can vary between a few thousand to a few hundred thousand dollars, which includes a base fee for software license, integration and services and annual licensing/support fees. Additional cost is also charged for advanced features and functionalities.

2. Service/Support

   While the price of closed-source software is higher, it provides better and customised product with ongoing training and full support. There is also a lower requirement for the user's technical skills. In contrast, open-source software relies on a loyal and engaged online user community to deliver support via forums and blogs, but this support often fails to deliver the high level of response that many consumers expect. Normally no formal manual is available to guide users and a limited number of experts are available to mentor new users.

3. Innovation

   Open-source software provides a huge amount of flexibility and freedom to innovate the software without restriction. This innovation, however, may not be passed on to all users and can thereby limit the future support and growth of the software. Compared to open-source software, the inability for the general public to change the source code in closed-source software can restrict its flexibility to innovate and improve. However, this restriction ensures the security and reliability of proprietary software that is fully tested and offered to all users. Closed-source software instead uses their in-house research and development team to regularly offer new products, innovations, improvements and upgrades. Also, closed-source software has dedicated online communities that share ideas and strategies through forums and surveys, fostering innovation and allowing the product to adapt with changing needs.

4. Usability

   One of the major areas of criticism for open-source software is its usability. Generally, open-source software caters to developers rather than the vast majority of novice users, thus it is not user-friendly. User guides are not required by law and are therefore often ignored. Even if manuals are written, they are often filled with jargon that is difficult to follow.

On the other hand, usability is the highest selling point for closed-source or proprietary software. User manuals are always provided for immediate reference and quick training, while support services help to maximise use of the software. Third party systems and developers are also able to use a variety of mechanisms to enhance or redefine some of the functionalities of closed-source software.

5. Security

   As mentioned earlier, the restrictions imposed by closed-source software ensures a high level of security. The fact that only the proprietor's team can view or edit the source code, the software is heavily audited reducing the risk of infection of virus or bugs. In contrast, security of open-source can breach as the software is developed in an uncontrolled environment. Thus, there is a huge risk for the software to be embedded with viruses without the knowledge of the users. Also, with individual users all around the world developing the software, there is a lack of continuity and common direction that prevents effective communication.

3.7.1 *SwanDyne*

SWANDYNE (SWANsea DYNamic) is a unified general purpose finite element program developed by Chan (1988) at University of Swansea available in both 2D and 3D (DYNE3WAC) versions. The program uses Biot's fully coupled dynamic equation and can simulate static, consolidating and dynamic conditions under drained or undrained conditions. It assumes that the acceleration of the fluid phase is negligible compared with that of the solid skeleton. The time integration scheme used is the GNpj (Generalised Newmark pth order scheme for jth order equations) scheme proposed by Katona and Zienkiewicz (1985). This scheme uses a staggered approach and a single field variable is obtained using the extrapolated value of the other (Haigh *et al.*, 2005). Liu and Song (2005) finds this method simple but unconditionally stable, defining all the quantities at a discrete time station and making the solution of the governing equation easy to handle. It uses the displacement–pore pressure formulation, which reduces the number of variables yet still ensures the accuracy for earthquake analysis. Linear and nonlinear shape functions may be used in the discretisation of the displacement and pore pressure field.

In addition, the program provides a number of material models and element shapes to be chosen for the analyses. User-defined soil models can also be incorporated into the software. The software can be downloaded free of charge. One drawback of the software is that a separate source code has to be created to incorporate structural plate elements. The software also requires tedious work on the source code to simulate tunnel excavation.

SwanDyne and its 3D version Dyne3WAC have been used extensively by several researchers in the field of soil dynamics including Ghosh and Madabhushi (2004), Haigh *et al.* (2005), Liu and Song (2005), Ou and Chan (2006), Chan and Ou (2008), Elia *et al.* (2011), Amorosi *et al.* (2010), Elia *et al.* (2013), Elia and Rouainia (2014), Jin and Chi (2017).

3.7.2 *OpenSees*

OpenSees (Open System for Earthquake Engineering Simulation) is an object-oriented open-source finite element software developed by Pacific Earthquake Engineering Research Centre (PEER) in the US and maintained at the University of California Berkeley. The software was developed by Frank McKenna and Gregory L. Fenves with significant contributions from Michael H. Scott, Terje Haukaas, Armen Der Kiureghian, Remo M. de Souza, Filip C. Filippou, Silvia Mazzoni, and Boris Jeremic.

According to Wikipedia, OpenSees allows users to create finite element applications for simulating the response of structural and geotechnical systems subjected to earthquakes and has both 2D and 3D capabilities. OpenSees is primarily written in C++ and uses several Fortran and C numerical libraries for linear equation solving, and material and element routines (OpenSees Wiki). The software can be downloaded at no cost. There are a number of codes created for different material models which users can use. Due to its flexibility, users can modify and customise or even create their own code according to each individual's needs.

As with the majority of open-source software, the major issue with OpenSees is the lack of support/service/training and easy to follow manuals as well as a friendly user-interface. This makes the software difficult to use particularly for novice users which can lead to a longer amount of time to learn and achieve adequate proficiency.

OpenSees has been used widely for earthquake engineering research. Some of the published works using OpenSees include Chang *et al.* (2008), Wang *et al.* (2016), Liu *et al.* (2015), Gu (2014), Pitilakis *et al.* (2015).

3.7.3 *Tochnog*

Tochnog is an explicit/implicit finite element program offering a wide variety of geotechnical and mechanical options, modern material laws including the most recent rate independent and viscous hypoplasticity models, stress, temperature and groundwater pressure analysis, lagrangian and eulerian mesh in space, quasi-static and dynamic calculations. The program includes a full library of isoparametric elements in 1D, 2D and 3D and also featuring typical structural elements like beams, interfaces, springs, etc. It covers geometry-based boundary conditions, mesh independent postprocessing by selecting physical points, lines and surfaces, 2D and 3D mesh refinement, phased modelling stages and extensive parallelisation. The software allows for the uncoupling of material and nodal displacements which defines a Eulerian approach in the finite element method.

Tochnog is a free open-source program but a professional version is now distributed by Finite Element Application Technology (FEAT) (https://www.feat.nl/). There are a few soil models that have been developed and readily available for use. Similar to OpenSees, users can tailor the program by creating customised codes such as a user-defined soil model. The main drawback just like OpenSees is the user-interface issues, underdeveloped user manuals, limited support and need for high technical skills to create codes. Just like any other open-source software, Tochnog needs a longer time to learn and develop proficiency in writing the codes.

Tochnog has been utilised in the works by Dijkstra *et al.* (2006), Anastasopoulos *et al.* (2008), Murianni *et al.* (2015), Reul and Remmel (2010), among others, but only a few applications in soil earthquake engineering.

3.7.4 *FLAC*

FLAC (Fast Lagrangian Analysis of Continua) is a commercial numerical modeling software for advanced geotechnical analysis of soil, rock, groundwater, and ground support in two and three dimensions. FLAC can be used for analysis, testing, and

design of any kind of geotechnical engineering project that requires continuum analysis. The software utilises an explicit finite difference formulation (FDM) that can model complex behaviours and unstable physical processes, such as problems that consist of several stages, large displacements and strains, non-linear material behaviour, or unstable systems (even cases of yield/failure over large areas, or total collapse).

Use of FLAC requires a base fee for the license which can be purchased from Itasca (https://www.itascacg.com/software/flac). Advanced features and functionalities (e.g. dynamics, creep, etc.) and other services can be purchased at an extra cost. The program has several built-in soil models and element types within the software and includes features such as groundwater flow, coupled mechanical-flow calculation, inclusion of structural elements, plotting statistical distribution of any property, optional automatic remeshing during solution, and a built-in scripting language (FISH) that can customise or automate virtually all aspects of program operation, including user-defined properties and other variables.

The main advantage of using the explicit finite difference formulation is that the numerical scheme stays stable even when the physical system may be unstable. This is particularly advantageous, when modeling nonlinear, large strain behaviour and actual instability. However, the use of a time-marching explicit scheme in FLAC increases calculation times compared to those of implicit formulations although memory requirements are reduced as explicit methods do not need to store matrices for calculations of equilibrium (Vlachopoulos and Diederichs, 2014). Just like any other closed-source software, the major drawback of FLAC is the high cost of license purchase including annual fees and additional purchase of optional features such as dynamics. The cost is counterbalanced though by the continuous technical support and improvements to adapt to changing needs.

FLAC has been used extensively in both research and practice for all types of geotechnical problems in both static and dynamic cases. Some of its applications include works by Vlachopoulos and Diederichs (2014) on tunnels and tunnel support static response, El-Emam *et al.* (2004) on retaining walls subjected to base acceleration, Qiao *et al.* (2008) on liquefaction-induced slope failures and damage to

buried pipelines, Ni (2001) on dynamic compliance of a rigid footing, Mayoral *et al.* (2015) on seismic response of floating tunnel shafts, Sliteen *et al.* (2011) on seismic behaviour of a shallow tunnel and Wang *et al.*) on liquefaction of an artificial fill embankment.

3.7.5 *LS-Dyna*

LS-DYNA, developed by Livermore Software Technology Corporation (LSTC), is a multi-purpose explicit and implicit finite element method (FEM) and multiphysics program used to analyse the nonlinear response of structures. LS-DYNA originated from the 3D FEA program DYNA3D, developed by Dr. John O. Hallquist at Lawrence Livermore National Laboratory (LLNL) in 1976.

The code's origins lie in highly nonlinear, transient dynamic finite element analysis using explicit time integration. Its fully automated contact analysis and large library of material models and element types enable users worldwide to solve complex, real-world problems in the field of civil engineering, seismic engineering, rail engineering, biomedical and crashworthiness, among others. LS-DYNA has a wide range of capabilities including full 2D & 3D capabilities, nonlinear dynamics, rigid body dynamics, linear statics, fluid analysis, crack propagation, FEM-rigid multi-body dynamics coupling, etc. Similar to FLAC, it allows incorporation of user-defined soil models. The software license is commercially distributed by Oasys (https://www.oasys-software.com/dyna/software/ls-dyna/) and can also be purchased from LSTC (http://www.lstc.com/).

A particular advantage of LS-DYNA is its speed of computation (using the explicit integration technique) for very large and complex models, which might contain elements numbered in the millions (Willford *et al.*, 2010). Typically, LS-DYNA runs on multiple processor clusters using the distributed memory method coupled with a Message Passing Interface communications protocol (MPI). This allows efficient use of large numbers of processors working in parallel. Its multi-physics capability enables users to solve tightly coupled problems in one code. Similar to FLAC, the high cost to purchase user license remains to be its major drawback.

LS-DYNA has been used in research in both static and dynamic loading including works by Willford *et al.* (2010), Xu *et al.* (2006), Yu *et al.* (2013b), Peiris (2000), Ellison *et al.* (2015), Lubkowski *et al.* (2000), Yu *et al.* (2009b) and Thomas *et al.* (2013).

3.7.6 *PLAXIS*

PLAXIS is a commercial finite element geotechnical engineering software available in both 2D and 3D versions and in different languages. The program has been developed specifically for the analysis of deformation, stability and flow in geotechnical engineering. Its development started in1987 at Delft University of Technology for the analysis of river embankments on the soft soils of the lowlands of Holland (Brinkgreve *et al.*, 2015). It was extended in subsequent years to cover most other areas of geotechnical engineering. Its application to civil and geotechnical engineering ranges from excavations, embankment and foundations to tunnelling, mining and reservoir geomechanics.

PLAXIS has been recently acquired by Bentley Systems Inc. making Bentley a complete source for geotechnical professionals "going digital". The software user license is available for purchase from PLAXIS bv (https://www.plaxis.com/). The program contains a large built-in library from simple to complex soil models which users can utilise while it can accommodate user-defined models that suit every individual's requirements.

PLAXIS implements a fully coupled effective stress approach and Newmark implicit time integration scheme. Its capabilities include statics (e.g. deformation, stress, strain, stability analysis, consolidation, safety analysis, updated mesh), dynamics (e.g. effects of earthquakes and vibrations, excess pore water pressure, liquefaction), fully coupled flow deformation, steady-state and transient ground water flow, steady-state and transient thermal flow. Its main advantage is its renowned higher degree of accuracy compared to FDM type software, i.e. reliable and reproducible results, ease of use enabling new users to work with the package after only a few hours of training thereby maximising efficiency and dedicated customer support and services. Also, the input procedures enable the enhanced output facilities to provide a detailed presentation of computational results.

Aside from its high cost which is typical with closed-source software, finite element method software including PLAXIS is computationally expensive due to the huge amount of time involved in solving a problem. For some problems, there may be a considerable amount of input and output data, as well as sizeable equation systems requiring large computer memory. Also, due to the implicit time integration approach in PLAXIS, non-linear complex models can lead to unstable or non-convergent solutions.

Similar to FLAC, PLAXIS has been extensively and popularly used in both research and practice for all types of geotechnical problems in both static and dynamic cases. Some of the published works involving use of PLAXIS include Amorosi *et al.* (2010), Amorosi and Boldini (2009), Panayides *et al.* (2012), Cabangon *et al.* (2017), Ertugrul (2010), Charlton *et al.* (2016), Bilotta *et al.* (2014), Bolouri Bazaz and Besharat (2008), Patil *et al.* (2018), Cabangon *et al.* (2019), Kim and Jeong (2011), Huat and Mohammed (2006), Wulandari and Tjandra (2015), Surarak *et al.* (2012), Charlton and Rouainia (2016), Cabangon *et al.* (2018) and Strokova (2009), among others.

3.7.7 *MIDAS GTS NX*

MIDAS GTS NX is a comprehensive finite element analysis software package that is equipped to handle the entire range of geotechnical design applications including deep foundations, excavations, complex tunnel systems, seepage analysis, consolidation analysis, embankment design, dynamic and slope stability analysis. It is commercially available through MIDAS (http://midasgtsnx.com/GTS).

Similar to PLAXIS, GTS NX also has an advanced user-friendly modeling platform including multi-windows graphic user interface that enables unmatched levels of precision, ease and efficiency. The software has 2D and 3D capabilities as well as an optimal mesh generator and can interface with CAD (computer-aided design). It contains a large built-in library for element and material models including advanced soil constitutive models. User-defined soil models can also be accommodated into the program.

One of the main advantages of GTS NX is that it incorporates a hybrid mesh generation function that creates a mesh set that uses an optimal combination of hexahedron and

tetrahedral elements. As such, it produces more accurate stress results while at the same time it can accommodate sharper curves and corners of complex geometry. It also has the ability to consider project complexities such as soil anisotropy, irregular soil stratigraphy, surface waves, irregular topography, and soil-structure interaction.

Cost wise, PLAXIS and GTS NX are highly comparable. Just like any other finite element method software, one of its main drawbacks is the high computational cost due to the huge amount of time involved in solving a problem. For some problems, there may be a considerable amount of input and output data, as well as sizeable equations systems requiring large computer memory. Also, due to the implicit time integration approach implemented in the program, non-linear complex models can lead to unstable or non-convergent solutions.

Research conducted in 2D and 3D cases using MIDAS GTS NX include Acosta (2015) on the dynamic response of vertical sand drains, Szerző and Batali (2017) on piled raft foundations, Watson *et al.* (2018) on a shallow cover SEM tunnel, Cha *et al.* (2016) on a vertical shaft, Cho *et al.* (2014) on TBM tunnel excavation, Sahoo *et al.* (2014) on seismic behaviour of buried pipelines, Goel and Sonthwal (2017) on slope stability and Eid *et al.* (2018) on large diameter bored piles.

3.7.8 *Selection of geotechnical software*

Selection criteria have been developed by the author to suit the project requirements. The author has chosen software attributes necessary to fulfill the project objectives. Each attribute is assigned a percentage mark based on their level of importance for a sum total of 100% for all attributes. The different percentage weightings for each attribute are based on the author's perceived hierarchy of individual contribution for successful implementation on the project. Cost and functionality, which include adaptation to both 2D & 3D and capability to implement a fully-coupled soil-structure system with multi-directional dynamic loading, have been the biggest consideration in choosing a suitable software. A second tier of attributes which are also deemed important to the author but to a lesser degree are the software's features and capabilities, such as automatic mesh generation, simulation speed, post-processors, soil strata generator, ease of use (i.e. user interface capability) and the degree of usage and effectiveness of such software based on reviewed publications (added value).

Other minor attributes of least importance are also included like technical support and availability. These attributes and their corresponding percentage marks are as follows:

Attributes	Percentage Mark
• Availability	5%
• Functionality	25%
• Capability	10%
• Ease of use	10%
• Adaptability	5%
• Technical support	5%
• Added value	10%
• Cost	30%
Total	100%

Each software is then given a mark between 1 and 10 for each attribute. The weighted percentage for each software is obtained by multiplying each attribute mark by the percentage mark and adding up all the products. The software selection table, criteria and summary can be found in Appendix B. The marking results are presented in Figure 3.37.

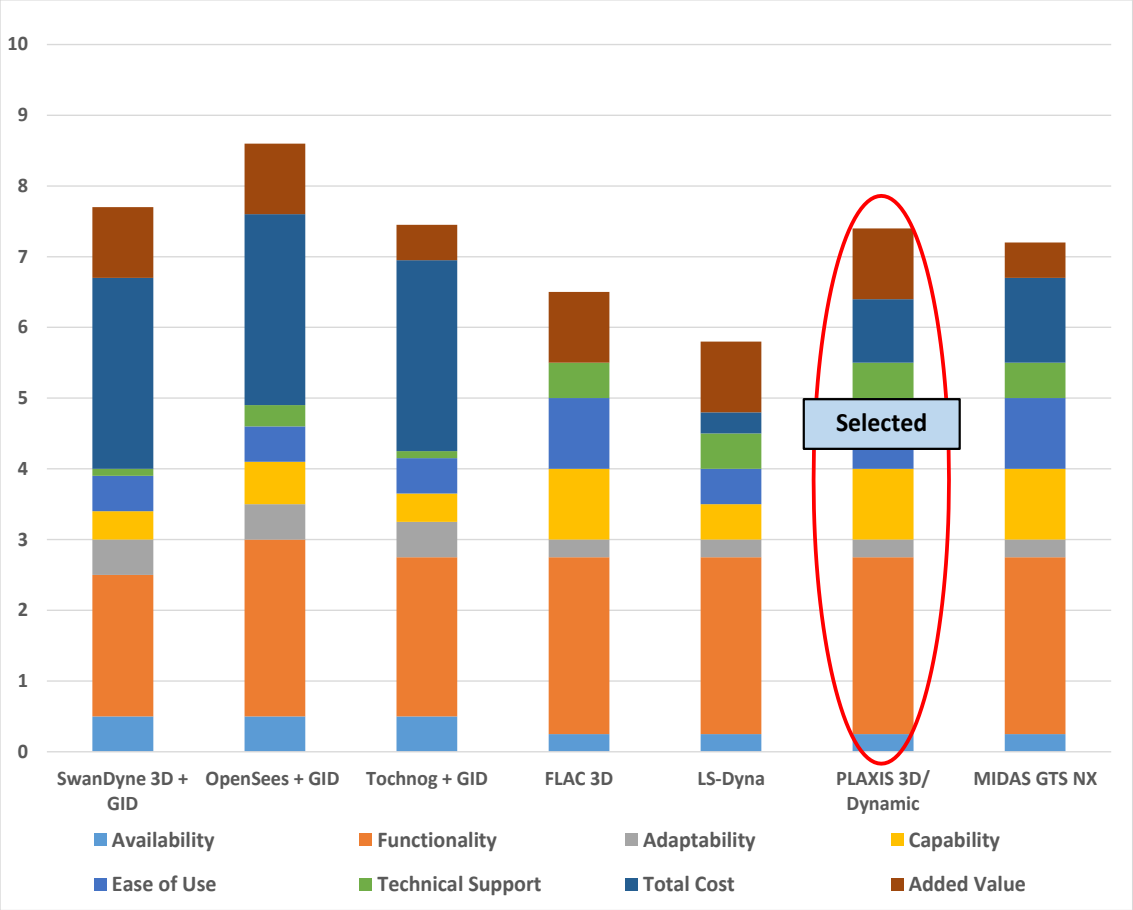

Figure 3.37 Software Selection Summary

The marking summary shows the object-oriented open-source software OpenSees (Open System for Earthquake Engineering Simulation) has the highest mark. It also shows that all open-source software have higher marks than close-source software which is mainly due to its zero cost.

A risk assessment was then conducted for other requirements such as concerns on the project schedule and implementation of the chosen soil constitutive model into the software. It has been concluded that an unsuccessful implementation of the chosen soil model into an unfamiliar software will be a high risk. Implementing and testing a new advanced soil model into an unfamiliar software such as OpenSees will consume a huge amount of time resource, which was deemed unacceptable as per project schedule. It can significantly overshoot the project schedule which can cause the project to slip beyond the completion deadline. Besides, a longer lead time is required to be familiar with such software which will very likely lead to not meeting the project milestones.

The selection list was then reduced to only those software which have successfully implemented the chosen soil constitutive model (RMW model) namely: SWANDYNE, PLAXIS and FLAC. Despite SWANDYNE having the highest score among the three, the following practical considerations have influenced the author's final decision.

- SWANDYNE will need a separate source code to be created to incorporate structural elements. Also, it will require tedious work on the source code to simulate tunnel excavation. These features are already built-in on FLAC and PLAXIS.
- FLAC will cost 31% more than PLAXIS which is beyond the allocated project budget.
- The author is well-familiar and has extensive hands-on experience with PLAXIS.

In the end, PLAXIS garnered the highest rating in terms of practicality and was chosen as the software to use to generate the 2D and 3D numerical models for the project.

PLAXIS has been tested and used extensively in research and in practice. In addition, the code for the RMW model is already available on this software and its implementation has been performed satisfactorily in the past by a number of researchers including Elia *et al.* (2016), Panayides *et al.* (2012), Charlton and Rouainia (2016), González *et al.* (2012), Panayides *et al.* (2010), Charlton and Rouainia (2017) and Rouainia *et al.* (2017). Also, as mentioned earlier, it has an added value because of the author's significant hands-on experience in using the software which reduces the lead time for the project.

Chapter 4. Advanced numerical modelling of the transverse behaviour of circular tunnels in structured clayey soils under seismic loading

4.1 Introduction

The general procedure for seismic design and analysis of tunnel structures is based primarily on the free-field deformation approach where the structures are designed to accommodate the deformations imposed by the ground. This approach ignores the stiffness of the tunnel lining, leading to an overly conservative estimate of the ground deformations especially in soft soils (e.g. alluvial clayey deposits and/or weak rocks). Hashash *et al.* (2001) has recommended that the effect of soil-structure interaction must be taken into consideration in this case.

Soil-structure interaction (SSI) is the process in which the response of the soil influences the motion of the structure and vice versa (Wikipedia). It has the ability to consider relatively complex conditions in terms of heterogeneity of soil strata, nonregularity of tunnel geometry, pre-existence of surface and sub-surface structures and ground water flow. SSI can be efficiently handled using 2D or 3D numerical methods. Although SSI solutions can be approached using pseudo-static analysis (closed-form solution) such as those outlined by Wang (1993) and Penzien (2000), these approaches do not include dynamic or wave propagation effects. In contrast, these effects are inherently considered in a two-dimensional (2D) or three-dimensional (3D) full dynamic numerical analysis using either the Finite Difference Method (FDM), Finite Element Method (FEM) or Boundary Element Method (BEM) (Hashash *et al.*, 2001) as previously discussed in Section 3.6. Also, seismic wave diffraction by underground structures is too complex to be solved accurately, economically and under realistic conditions without the aid of numerical methods (Stamos and Beskos, 1996). All these justify the appropriateness of using numerical methods versus closed-form analytical solutions in simulating seismic effects in tunnels.

In terms of the choice for the type of numerical tool for dynamic analysis, Amorosi and Boldini (2009) recommended FEM or FDM over BEM, despite the great ease and value of BEM in solving problems characterised by infinite or semi-infinite domains. It is mainly due to BEM's lack of ability to account for the highly non-linear soil response,

the accumulation of plastic strains and the build-up of excess pore water pressures during the seismic actions. In this dissertation, FEM has been adopted as the tool for the numerical analysis.

Two-dimensional FEM has grown in popularity over the last two decades and became a norm in analysing the behaviour of tunnels during earthquake as evident from the works by numerous researchers mentioned in Section 3.4. This approach models the tunnel and the surrounding ground in the transverse direction while assuming plane strain conditions in the longitudinal direction. Plane strain conditions are normally used for modelling a cross-section of an (infinitely) long structure, such as tunnels and dams. Under these conditions, the strain and displacement in the long direction are considered zero because of the very large dimension relative to the transverse direction.

In FEM modelling the ground is modelled as a continuum media subdivided into disjoint (non-overlapping) components of simple geometry called *finite elements* while the tunnel lining is modelled as *beam elements* as shown in Figure 4.1 (a). Each element is expressed in terms of a finite number of degrees of freedom at a set of nodal points. An example of which is a simple 3-noded linear triangular element with 2 degrees of freedom per node as shown in Figure 4.1 (b). In general, the number of degrees of freedom associated with an element is equal to the product of the number of nodes and the number of values of the field variable (and possibly its derivatives) that must be computed at each node. The response of the whole model is then considered to be approximated by the assemblage of reactions of all elements and their eventual interactions at the connecting nodes when subjected to external influences. The basic formulations of these actions and reactions are expressed below in matrix forms. Further details of the finite element formulations can be found in numerous books and references including Rao (2018) and will not be discussed exhaustively in this dissertation.

The first step in the finite element method is the discretisation of the domain as outlined in Rao (2018). Typically, the FEM model is discretised into simple geometric shapes. Some of these geometries are shown in Figure 4.2. Based on the shape and number of nodes of each element, the displacement within the element (u) in relation

to the nodal displacements (v) is expressed in Equation 4.1 while the relationship of strain ε to nodal displacements v is shown in Equation 4.2. These nodal displacements are induced by the vector of nodal forces (P) resulting from body forces and tractions applied to the element. Their relationship is represented by Equation 4.3.

$$\{u\} = [N]\{v\} \quad 4.1$$

$$\{\varepsilon\} = [B]\{v\} \quad 4.2$$

$$\{P\} = [K]\{v\} \quad 4.3$$

where N is the matrix of interpolation (shape) functions; B is the strain interpolation matrix; K is the element stiffness matrix.

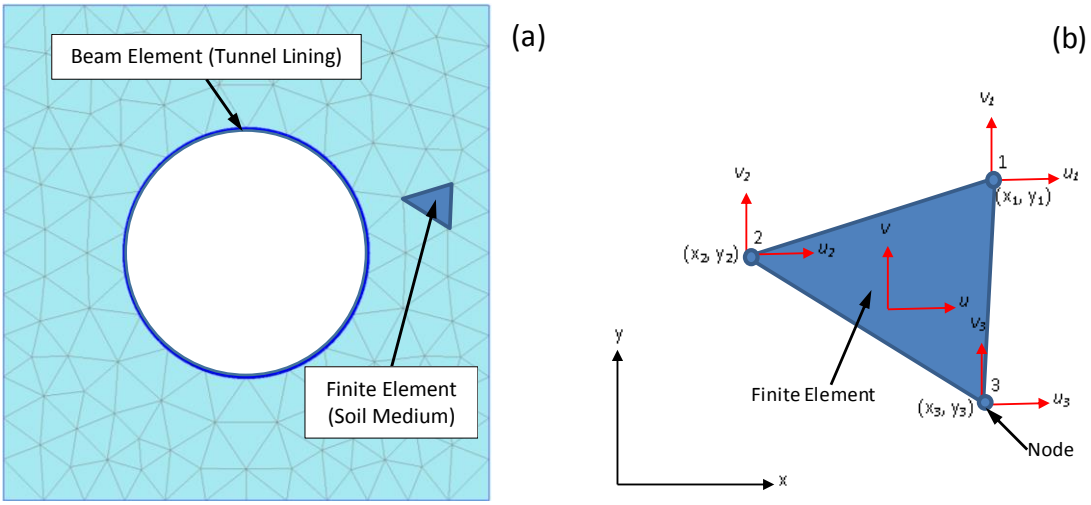

Figure 4.1 Typical finite element model

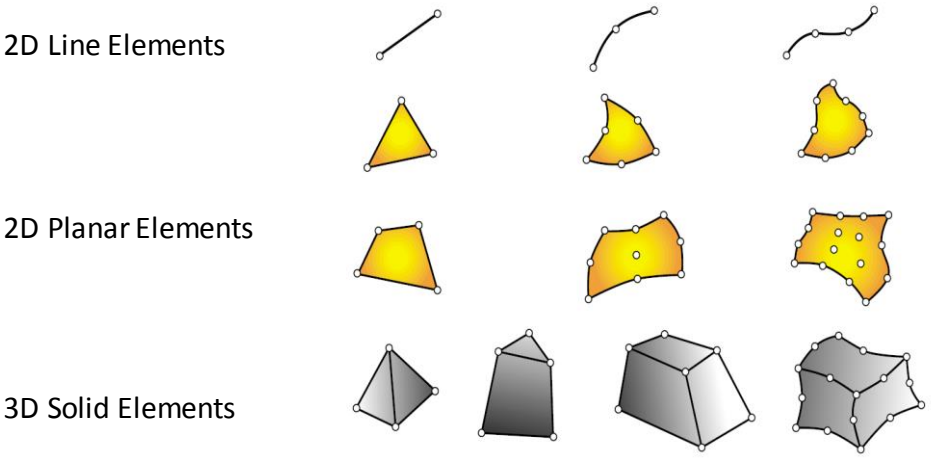

Figure 4.2 Typical finite element geometries (Felippa, 2017)

An element can be represented in simplistic form as a three-dimensional elemental volume in its stress state as shown in Figure 4.3. These stress components induce corresponding strain components such that the stress-strain relationship in Cartesian coordinates is given by Equation 4.4.

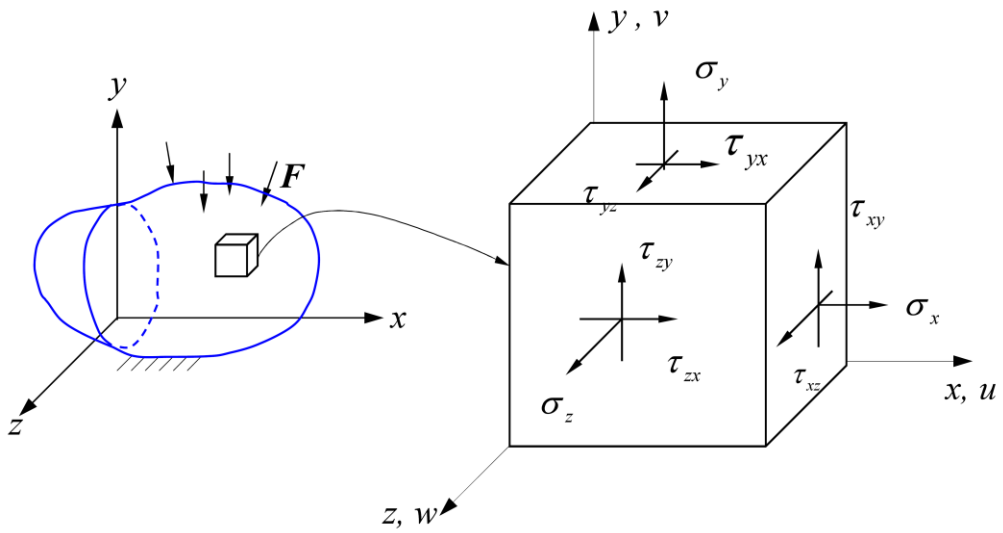

Figure 4.3 Elemental Volume Considered for Internal Equilibrium (Yijun, 2003)

$$\{\sigma\} = [D]\{\varepsilon\} \text{ (general 3-dimensional stress)} \quad 4.4$$

where

$$\{\sigma\} = \{\sigma_x \sigma_y \sigma_z \tau_{xy} \tau_{yz} \tau_{zx}\}^T \text{ (components of stress)} \quad 4.5$$

$$\{\varepsilon\} = \{\varepsilon_x \varepsilon_y \varepsilon_z \varepsilon_{xy} \varepsilon_{yz} \varepsilon_{zx}\}^T \text{ (components of strain)} \quad 4.6$$

$$[D] \text{ (material stiffness matrix)} \quad 4.7$$

In the case of simple elastic-perfectly plastic behaviour such as Mohr-Coulomb, matrix $[D]$ is equal to

$$[D] = \alpha_1 \begin{bmatrix} 1 & \alpha_2 & \alpha_2 & 0 & 0 & 0 \\ & 1 & \alpha_2 & 0 & 0 & 0 \\ & & 1 & 0 & 0 & 0 \\ & & & \alpha_3 & 0 & 0 \\ & & & & \alpha_3 & 0 \\ sym. & & & & & \alpha_3 \end{bmatrix} \quad 4.8$$

where

$$\alpha_1 = \frac{E(1-\nu)}{(1+\nu)(1-2\nu)} \quad 4.9$$

$$\alpha_2 = \frac{\nu}{(1-\nu)} \quad 4.10$$

$$\alpha_3 = \frac{(1-2\nu)}{2(1-\nu)} \quad 4.11$$

for the plane strain case where $\varepsilon_z = 0$, $\sigma_z \neq 0$, $\sigma_z = \nu\,(\sigma_x + \sigma_y)$, matrix [$D$] becomes

$$[D] = \frac{E}{(1+\nu)(1-2\nu)} \begin{bmatrix} 1-\nu & \nu & 0 \\ \nu & 1-\nu & 0 \\ 0 & 0 & \frac{1-2\nu}{2} \end{bmatrix} \quad 4.12$$

where E = Young's modulus of elasticity; ν = Poisson's ratio.

For non-linear soil models such as RMW, the constitutive matrix [D], typically expressed in G (shear modulus) and K (bulk modulus), is not constant and varies with the stresses and the state parameters as discussed in Section 3.5.

4.2 Calibration of the kinematic-hardening model

To predict accurately the behaviour of tunnels during earthquakes through FEM analyses, it is crucial to use a constitutive model that can appropriately capture the soil response to seismic loads. In common engineering practice and design, simple constitutive assumptions (e.g. Linear isotropic elasticity, Ramberg-Osgood, Mohr-Coulomb, Modified Cam Clay, Drucker-Prager) are often employed to model the stress-strain behaviour of the soil deposit. However, these constitutive hypotheses are not adequate to simulate the main characteristics of the mechanical behaviour of soils during cyclic loading such as non-linearity, early irreversibility, anisotropy, decrease of nominal stiffness due to hysteretic energy dissipation, pore pressure build-up in undrained conditions, state dependency and structure degradation. Ignoring these characteristics can lead to an incorrect prediction of the ground deformations, especially in soft soil deposits subjected to dynamic loading, thus resulting in an inappropriate design of tunnel lining.

In this work the kinematic-hardening model (RMW) developed by Rouainia and Wood (2000) (Section 3.5.7) has been employed to simulate the cyclic response of natural clay materials. The model has three surfaces: 1) a reference surface, which controls the state of the soil in its reconstituted, structureless form and describes the intrinsic behaviour of the clay; 2) a structure surface, which controls the process of destructuration and represents the current stress state of the soil; 3) a bubble, which encloses the elastic domain of the soil and moves within the structure surface following a kinematic-hardening rule. The degree of structure, *r*, which describes the relative sizes of the structure and reference surfaces, is a monotonically decreasing function of the plastic strain, thus representing the progressive degradation of the material as plastic straining occurs. The model converges to the Modified Cam Clay model for remoulded structureless soils once the three surfaces are set to be coincident.

This model has been implemented in PLAXIS 2D (Brinkgreve and Broere, 2015) with an explicit stress integration algorithm adopting an automatic sub-stepping and error control scheme (Zhao *et al.*, 2005). PLAXIS 2D is a commercial two-dimensional finite element code discussed in Section 3.7.6.

Despite being a well-established model, published works on the application of RMW to boundary value problems [González *et al.* (2012), Panayides *et al.* (2012), Elia and Rouainia (2014), Elia and Rouainia (2012), Cabangon *et al.* (2019)] are of limited number as similarly observed by González *et al.* (2012). This is mainly due to the difficulties in obtaining and establishing model input parameters from standard laboratory tests as well as calibrating the parameters to suit the model. To measure initial structure, it requires an extensive high quality laboratory regimen and non-conventional procedures or possibly insitu testing.

Two real clay soils of different material properties were used in this work to cover soil samples of different initial structure. One is structureless soil (r_0~1.0), the Marana Capacciotti earth dam material and the other one is of high initial structure (r_0=5.2), the Avezzano clay. The diversity in soil samples will determine the sensitivity of the selected method/approach on this material property and any possible impact on the results. These two clay materials have been collected by undisturbed sampling method

(i.e. samples are collected with precautions without disturbing its structure, texture, density, natural water content and stress condition) and experimentally tested. The results from the laboratory tests were used to calibrate the RMW models.

Calibration of the RMW model has been carried out by conducting oedometer and undrained triaxial compression tests (TRX) on representative samples of the two clay materials. The material parameter λ^* has been derived from the final slope of the 1D compression curve in the ln v : ln p plane, whereas M_θ has been calibrated against the value of the stress ratio at critical state observed during the triaxial compression tests. The parameters A and k, which govern the rate of destructuration with strain, have been obtained from 1D and triaxial compression tests. The other parameters, together with the initial values of the hardening variables, have been established from a trial and error procedure by simulating the tests in single element driver such as SoilTest and SM2D in order to match the experimental results (best-fitting). The details of the RMW calibration steps can be found in (Elia and Rouainia, 2012), (Burghignoli *et al.*, 2003) and (Elia and Rouainia, 2014). In addition, results of resonant column/torsional shear (RC/TS) tests as well as double specimen direct simple shear (DSDSS) performed on samples of the two clay materials have also been used to calibrate the small-strain shear stiffness (G_0) profile and stiffness decay with strain during cyclic/dynamic loads. Numerical simulations of strain-controlled undrained cyclic simple shear tests have been carried out in single element driver to match the experimental results in order to calibrate the model parameters controlling the reduction of shear modulus with cyclic shear strain. These materials including the derived parameters are discussed in detail in the next sections.

4.2.1 *Structureless clay material (r_0~1.0) – Marana Capacciotti earth dam*

The Marana Capacciotti earth dam material is made of sandy silts of low plasticity, characterised by homogeneous granulometry and index properties (Calabresi *et al.*, 2000). The dam is located in Puglia, southeast of Italy, about 13.5 km southwest of the city of Cerignola (Foggia, Italy). The dynamic performance of the earth dam has been studied in the past by several authors [Cascone and Rampello (2003), Rampello *et al.* (2009), Elia *et al.* (2011)]. The geotechnical properties of the dam were obtained from geotechnical investigation that includes three boreholes along the dam crest and the

downstream slope and laboratory testing of 21 undisturbed core samples (Calabresi *et al.*, 2000).

Several tests have been performed on this soil material including undrained triaxial compression tests (TRX) on samples representative of the earth dam clayey material at three different consolidation pressures with minimal disturbance (Elia and Rouainia, 2012). Resonant column (RC) tests, to determine the small-strain shear stiffness profile, were also performed at two different confining pressures on samples representative of the same soil. Following the calibration work performed by Elia and Rouainia (2012), the values of the optimised soil parameters for the earth dam material are listed in Table 4.1.

The RMW model predictions, obtained from the undrained triaxial test in SoilTest (a soil testing program within PLAXIS), are presented in Figure 4.4 (a) & (b), showing a very good agreement with laboratory data in terms of stress-strain (q-ε_a) curves and pore water pressures generated during triaxial shearing up to a maximum axial strain of 12%. In addition, the results generated from the single element driver SM2D, a soil testing software developed by Chan (1993) at the University of Birmingham predicts satisfactorily the normalised secant shear modulus (G/G_0) and damping (D) curves with shear strain (γ) from RC data as shown in Figure 4.4 (c). The use of both SoilTest and SM2D have a distinct advantage where the results are not affected by variables such as the geometry, mesh coarseness or boundary conditions. Due to the low value of the initial structure r_0 (~1.0) of the soil material, it should be noted that the presence of soil structure has not been fully accounted and, actually, degenerates the RMW model employed in the FEM simulations into a two-surface model (with the structure surface almost coincident with the reference surface, i.e. $r_0 = 1$) similar to the "bubble" model (previously discussed in Section 3.5.3).

The reduced single surface version of RMW (with the structure and bubble surfaces coincident with the reference surface, i.e. $r_0 = 1$ and $R = 1$), effectively representing the Modified Cam Clay (MCC) model, has also been calibrated against the same set of laboratory data, as shown in Figure 4.4, to investigate the effect of the constitutive assumptions on dynamic soil-tunnel interaction. The corresponding MCC soil parameters are listed in Table 4.1.

Material	λ^*	κ^*	M	v	R	B	ψ	η_0	r_0	A	k
RMW	0.125	0.015	1.15	0.25	0.10	2.00	2.50	0.0	1.10	1.00	0.50
MCC	0.125	0.015	1.15	0.25	(1.0)	-	-	-	(1.0)	-	-

Table 4.1 RMW and MCC model parameters for earth dam material

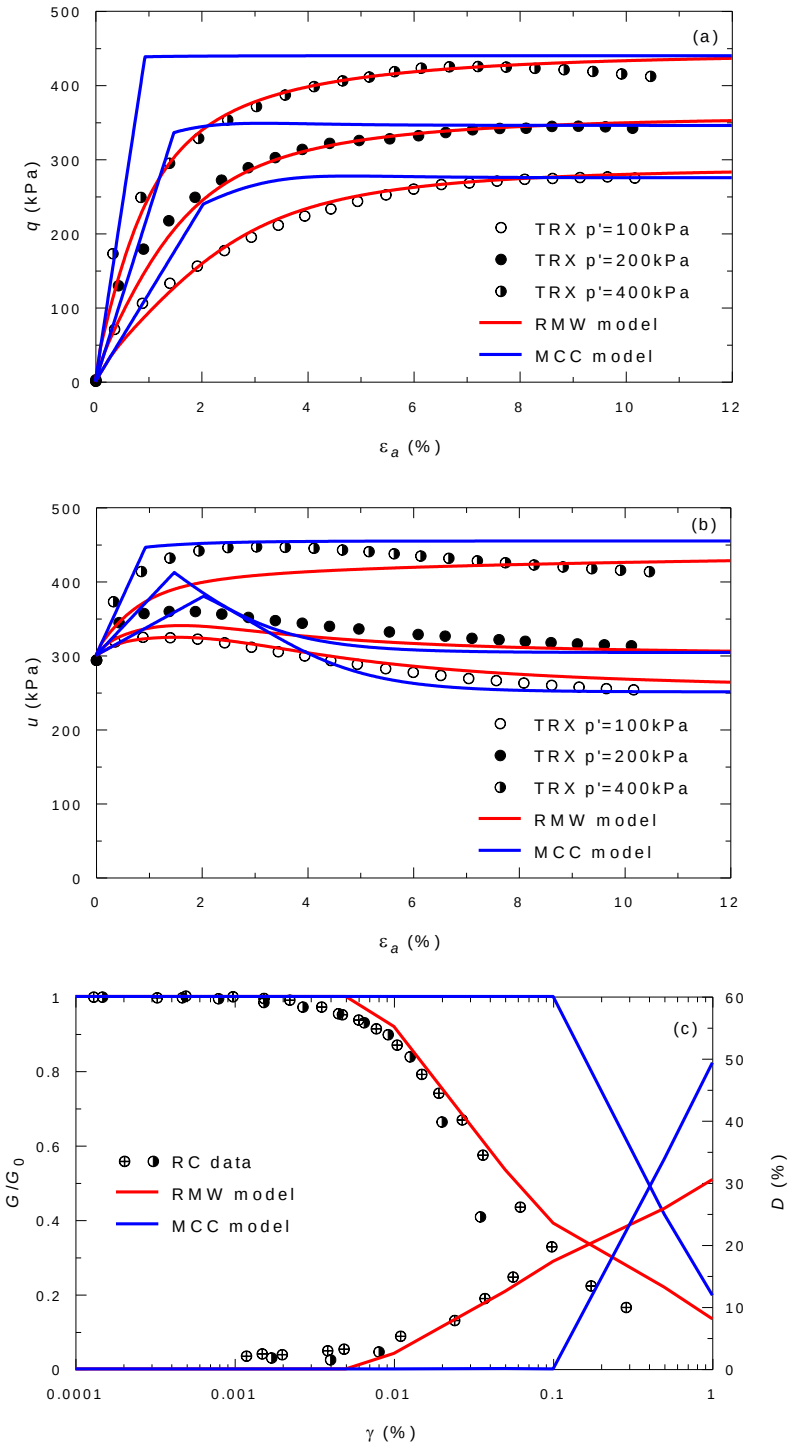

Figure 4.4 Calibration of RMW and MCC models against (a) TRX, (b) pore water pressures and (c) RC data

4.2.2 *Structured clay material (r_0=5.2) – Avezzano clay*

The Avezzano clay is a highly structured clay deposit predominantly found in a highly seismic area of central Italy and could potentially be the location of underground infrastructure and transport links in the future. Specifically, the site considered is in the Fucino basin, a large intra-mountain depression located 80km east of Rome and surrounded by the Apennines. The basin has originated from the sedimentation of fluvio-lacustrine sediments during the Pleistocene period and is composed by top layers of clayey and silty soils, with sand and gravel found underneath. The deposit is geologically normally consolidated and the silty clay layers are characterised by very low plasticity, a PI (Plasticity Index) of about 10% and high values of calcium carbonate content (i.e. $CaCO_3$ content between 60 and 80%). Standard oedometer and undrained triaxial compression tests clearly indicate that the clayey layers are characterised by the typical mechanical behaviour of cemented clays [Burghignoli *et al.* (1999), Burghignoli *et al.* (2010)].

The response of the Avezzano clay deposit to cyclic loads imposed by a silo shallow foundation has been investigated in the past by Burghignoli *et al.* (1999), D'elia *et al.* (1999), Burghignoli *et al.* (2003) and, more recently by Elia and Rouainia (2014) who evaluated the performance of the same footing under seismic loading conditions. In this work, the undrained triaxial compression tests on Avezzano natural samples retrieved at a depth of 21m have been considered. Figure 4.5 shows the comparison in terms of stress paths, stress-strain and pore pressure-strain responses between the laboratory data from Burghignoli *et al.* (2010) and the numerical predictions obtained with RMW. For the same set of experimental data shown in the figure, the constitutive model has been calibrated following the work by Burghignoli *et al.* (2003) and Elia and Rouainia (2014), considering an initial degree of structure r_0 equal to 5.2 and two rates of destructuration with damage strain (i.e. two values of the parameter k). The numerical prediction obtained assuming k equal to 1.5 is in very good agreement with the laboratory data, whereas the strain-softening is more abrupt than in the experiments when a higher rate of destructuration (k=5.0) is adopted. On the other hand, the higher rate of destructuration results in higher pore pressure than those at a lower rate of destructuration. The higher value of k has been used for parametric study presented in Section 4.5.2.

In previous versions of RMW, a classical hypoelastic formulation was employed for the determination of the bulk and initial shear moduli, K and G_0. In this work, the well-known equation as shown below proposed by Viggiani and Atkinson (1995) for the small-strain shear modulus has been implemented to reproduce the dependency of G_0 on the mean effective stress, the plasticity index and overconsolidation ratio. It should be noted that the adopted elastic formulation could not predict the influence of structure on the initial elastic stiffness, as recently proposed by Elia and Rouainia (2016).

$$\frac{G_0}{p_{ref}} = A_g \left(\frac{p'}{p_{ref}}\right)^{n_g} {R_0}^{m_g} \qquad 4.13$$

where A_g, n_g and m_g are dimensionless parameters which depends on the plasticity index, p_{ref} is a reference pressure equal to 1kPa, p' is the mean pressure and R_0 is the overconsolidation ratio in terms of mean effective stress.

Consistently with the Avezzano clay plasticity index of 10%, the dimensionless stiffness parameters A_g, n_g and m_g in the equation have been set equal to 2150, 0.78 and 0.22, respectively. These assumptions have been checked and found to be consistent with the experimental data as shown in the G_0 profile (Figure 4.6) along the depth of the soil deposit compared with RC data on Avezzano presented by Burghignoli *et al.* (2003).

The small-strain stiffness response and the evolution of the shear modulus and damping ratio of Avezzano Clay have been experimentally investigated and reported by D'Elia (2001). In particular, Figure 4.7 shows the normalised modulus decay and damping curves obtained from double specimen direct simple shear (DSDSS) and combined resonant column/torsional shear (RC/TS) tests performed on natural Avezzano clay samples, which were retrieved from the top part of the deposit (i.e. at depths between 8 and 11m). Numerical simulations of strain-controlled undrained cyclic simple shear tests have been carried out using SM2D in order to calibrate the RMW parameters, which control the reduction of shear modulus and the evolution of the damping ratio with cyclic shear strain [e.g. Elia and Rouainia (2016)]. The model predictions, presented in the same figure, are in good agreement with the laboratory data when the lower rate of destructuration is adopted. Consistently with the results

shown in Figure 4.5, the normalised stiffness modulus for *k* equal to 5.0 decays quicker than that obtained assuming a destructuration rate equal to 1.5, over the entire strain range and underestimates the experimental data. In contrast, a very small difference can be observed in terms of hysteretic damping predicted by the model in the two cases.

A summary of the RMW model parameters resulting from the calibration and adopted in the FEM non-linear dynamic simulations undertaken in this work is reported in Table 4.2.

Material	λ^*	κ^*	M	ν	R	B	ψ	η_0	r_0	A	k
Avezzano Clay	0.110	0.016	1.42	0.25	0.40	15.0	1.45	0.0	5.20	0.2	1.5/5.0

Table 4.2 RMW model parameters for Avezzano clay

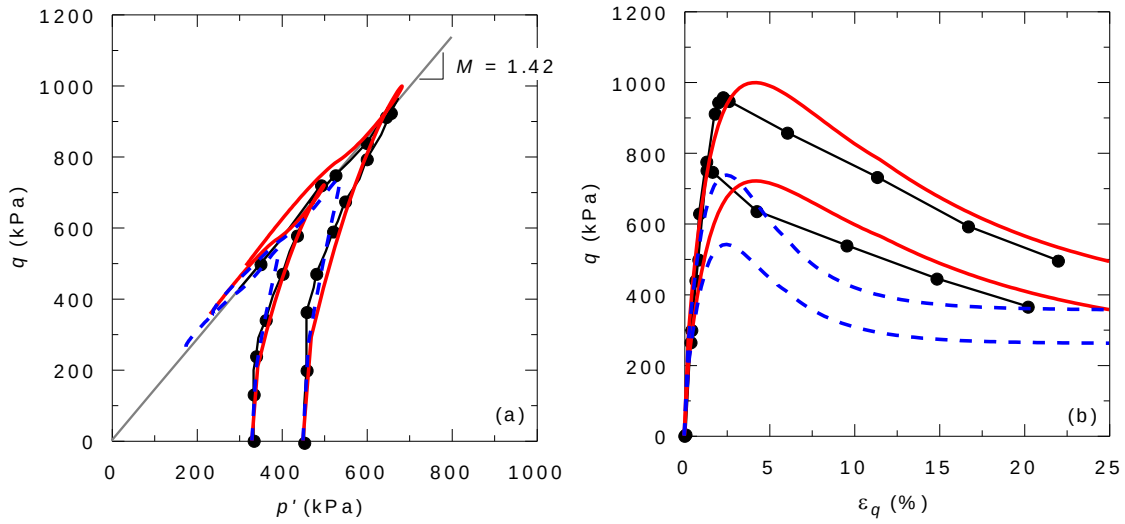

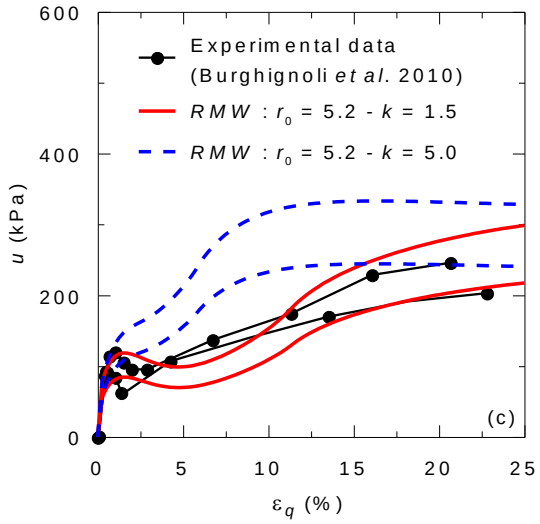

Figure 4.5 Comparison between RMW predictions obtained for two different destructuration rates (i.e. *k* values) and laboratory data on Avezzano Clay: (a) stress path; (b) stress-strain response; (c) pore pressure-strain response

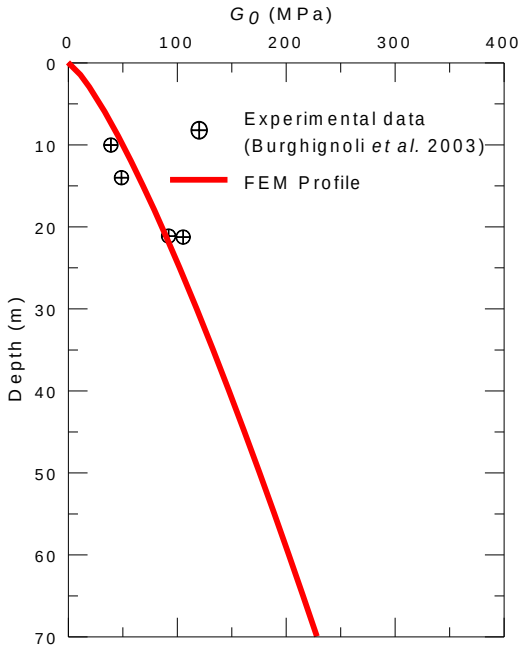

Figure 4.6 G_0 Profile of Avezzano Clay deposit vs Experimental data

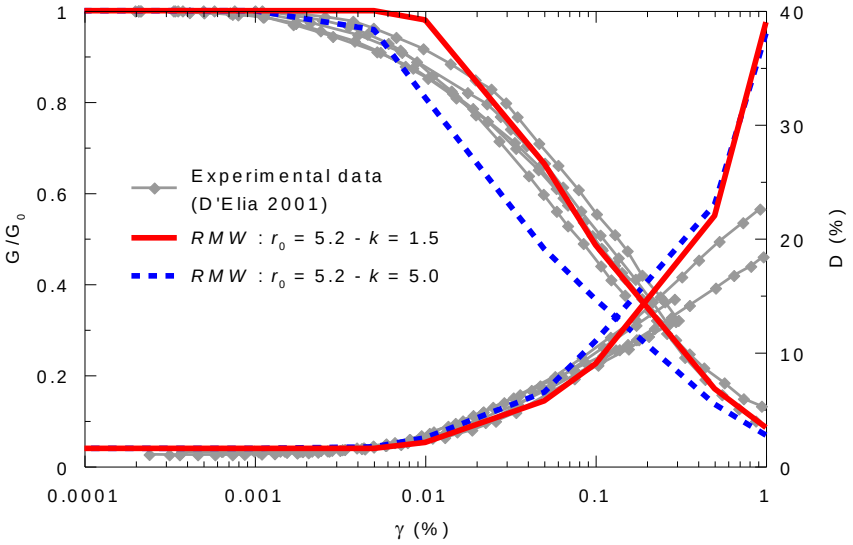

Figure 4.7 Comparison between RMW predictions obtained for two different destructuration rates (i.e. *k* values) and normalised modulus decay and damping curves for Avezzano Clay

4.3 Earthquake selection

Two earthquake signals with different frequency content, both reasonably matching the response spectrum provided by Eurocode 8 (EC8) for soil type A (rock or other rock-like geological formation), have been considered in the dynamic simulations, as illustrated in Figure 4.8. The first signal was recorded at the Assisi-Stallone station during the Umbria-Marche earthquake in September 1997 in Assisi, Italy, while the second was recorded at the Ulcinj-Hotel Albatros station during the Montenegro earthquake in April 1979 in Albania.

The Montenegro earthquake, in particular, has been selected using REXEL version 3.5 [Iervolino *et al.* (2010), Iervolino *et al.* (2012)], a software for computer-aided selection of spectrum matching real records sets, to explicitly match EC8 for the first natural period of the soil deposit T_1. The T_1 values equal to 1.54s and 1.03s for earth dam and Avezzano clay respectively were calculated according to the viscoelasticity theory [e.g. Roesset (1977)]. These values represent only an initial guess of the first oscillation mode of the soil deposits and are used to guide the selection process of the input motion and the interpretation of the non-linear dynamic analyses presented in the succeeding sections. Actually, from Figure 4.8, it is evident that the Montenegro signal is characterised by much higher spectral accelerations at around T_1 with respect to the Umbria-Marche earthquake, thus implying a higher energy content applied to the system at its first oscillation mode.

The relevant characteristics of the selected acceleration time histories are listed in Table 4.3 in terms of magnitude (M_W), Arias Intensity (I_a) as proposed by Arias (1970), epicentral distance, effective duration (T_{90}) as defined by Trifunac and Brady (1975), maximum acceleration (a_{max}) and maximum velocity (v_{max}). Both input motions have been filtered to remove frequencies higher than 10Hz to limit the minimum element dimension adopted in the FEM analyses and scaled up to the same peak ground acceleration (PGA) of 0.30g, according to the seismic hazard analysis of the site presented by Elia and Rouainia (2014). They have been applied at the bedrock base of the 2D models as prescribed horizontal displacement time histories.

Station	Earthquake	Component	M_w	I_a (m/s)	Epicentral Distance (km)	T_{90} (s)	a_{max} (g)	v_{max} (m/s)
Assisi-Stallone	Umbria-Marche (1997)	EW	6.0	0.2793	21.6	5.98	0.188	0.102
Ulcinj-Hotel Albatros	Montenegro (1979)	NS	6.9	0.7289	19.7	12.22	0.181	0.176

Table 4.3 Main characteristics of the selected earthquake signals

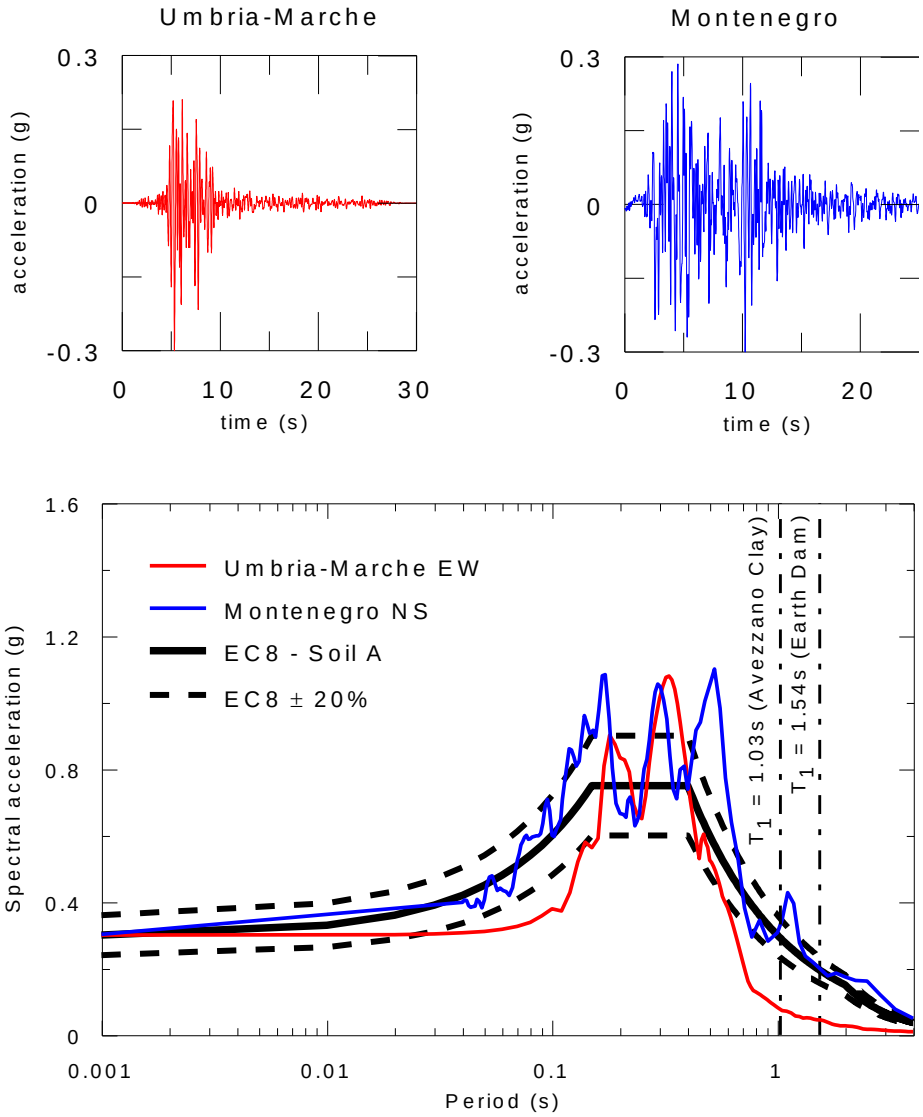

Figure 4.8 Scaled input motion acceleration time histories and comparison between the normalised response spectra of the scaled input (bedrock) records with the Eurocode 8 (EC8) design spectra for Ground type A

4.4 2D finite element numerical model

The dynamic response of deep underground structures is usually considered relatively safe compared to shallow ones as observed by Hashash *et al.* (2001) from case histories of damage to underground facilities; thus, the author has only considered a shallow tunnel for the case study. Chapman *et al.* (2017) classified shallow tunnels as those where C<2D (C is the tunnel crown depth and D is the tunnel diameter), i.e. when the ground above the tunnel crown is assumed to have no bearing capacity, thereby no arching can develop over the crown. It has been observed that as tunnel excavation technology advances, the size of tunnels being built has increased. For the past 10 years, tunnel projects have exceeded the 10m in diameter mark particularly transport tunnels in Australasian and Asian regions such as Airport Link (12.5m) in Brisbane, Australia, Waterview tunnel (13.1m) in Auckland New Zealand and Tuen-Mun Chep Lak Kok Link (13.7m) in Hong Kong. Other tunnels of such massive size found in other continents include Dublin Port tunnel (11.6m) in Ireland, A3 Hindhead tunnel (11.6m) in the United Kingdom and Alaskan Way Viaduct Replacement Tunnel (17.4m) in Seattle, USA.

Tunnels of these sizes make them more vulnerable to earthquake damage. As such, the case of a shallow circular tunnel, 10m in diameter with 15m soil cover, i.e. C/2D=0.75, within a 70m thick soil deposit overlying a rigid bedrock has been considered for the study, using the soil model parameters derived from the calibration procedure in Section 4.2. The lining has been modelled as a linear visco-elastic material assuming an axial stiffness (*EA*) equal to 19GPa, a flexural stiffness (*EI*) equal to 0.4GPa, Poisson's ratio equal to 0.25 and damping ratio equal to 5%. *E* is the Young's Modulus of the lining material whereas *A* and *I* is the cross sectional area and area moment of inertia respectively.

Even with full understanding of the predominant role of the soil-tunnel interface characteristics in the seismic response of tunnel particularly for tunnels enclosed in soft soil, the interface parameters for the studies were assumed and derived from the properties of the soil medium due to the arbitrary nature of the lining material used in the studies. The interface models are normally dictated by the numerical analysis software used. For user-defined soil models in PLAXIS, the interface follows an elastic-

perfectly plastic behaviour and its strength is defined by its shear and normal stiffness which are correlated to the critical state friction angle φ', the apparent cohesion c', the dilatancy angle ψ and the reference oedometer modulus E_{oed}^{ref}. The stress dependency of the interface stiffness is included through Equation 4.14.

$$E_{oed} = E_{oed}^{ref}\left(\frac{\sigma'_n + c'\cot\emptyset'}{p_{ref} + c'\cot\emptyset'}\right)^m \quad 4.14$$

where σ'_n is the effective normal stress, p_{ref} is the reference stress level (set to 100kPa) and m is the rate of stress dependency of the interface stiffness.

For the studies set forth in this dissertation, the interface was assumed rigid, i.e. the strength of the interface is the same as the soil, thus, all interface parameters were derived from the known soil material parameters. The critical state friction angle φ' was approximated from the critical state parameter M as shown in Equation 4.15 (derived from correlation between Mohr-Coulomb yield criterion and definition of the slope of the critical state line M) while conservative values of c' and ψ were used by equating them to zero.

$$M = \frac{6\sin\phi'}{(3-\sin\phi')} \quad 4.15$$

To establish E_{oed}^{ref} and m, correlations were employed between the shear modulus G from the G_0 profile, the Young's modulus E and oedometer modulus E_{oed} of the soil using Equations 4.16 and 4.17.

$$E = 2G(1+v) \quad 4.16$$

$$E_{oed} = \frac{(1-v)}{(1+v)(1-2v)}E \quad 4.17$$

where v is the Poisson's ratio of the soil.

When the values of $\ln\left(\frac{\sigma'_3 + c'\cot\emptyset'}{p_{ref} + c'\cot\emptyset'}\right)$ against $\ln E_{oed}$ of the soil profile are plotted, they form a straight line such that the y-intercept is taken as the E_{oed}^{ref} and the slope of the line is m.

Standard boundary conditions (i.e. lateral boundaries fixed in horizontal direction but free in vertical direction) have been adopted for the static analyses, while the bottom of the model has been assumed rigid and equal displacements have been imposed to the nodes along the vertical sides of the mesh (i.e. tied-nodes lateral boundary conditions) for the dynamic analyses. Tied-nodes have been employed for the dynamic simulations in order to avoid spurious wave reflections at the boundaries of the soil deposit. Their effectiveness in absorbing the energy induced by the seismic action has been proven by Zienkiewicz *et al.* (1999). In addition, a parametric study of the FEM model length discussed fully in Section 4.4.2 has shown that the adopted horizontal dimension (i.e. 350m), equal to 5 times the deposit depth as suggested by Amorosi *et al.* (2010), in conjunction with the tied-node boundaries, is sufficient to properly simulate the free-field conditions at the edges of the model. The water level has been assumed to coincide with the ground surface.

Other types of artificial boundary which can be used include the standard viscous boundary and the free-field boundary. Similar to the tied-node boundary, these boundary types can reproduce the free-field response near the lateral boundaries. However, to be effective in absorbing outgoing wave energy and to eliminate the influence of the lateral boundaries, these boundary types will require bigger model size compared to tied-node boundary (Kontoe, 2006). Also, the analysis run time when using viscous and free-field boundaries is longer compared with tied-node. That, in combination with the larger model size, further increases the computational time. Thus, the use of these boundary types, not only diminish the productivity and computational efficiency but also increases the computational costs. All these boundary types and their comparison are discussed in detail in Chapter 5, Sections 5.1.2 and 5.1.4.

Figure 4.9 shows the geometry of the FEM model adopted in PLAXIS 2D (Brinkgreve and Broere, 2015) along with the dynamic boundary conditions. PLAXIS 2D implements a fully-coupled effective stress approach. In the dynamic analysis, the code adopts an implicit Newmark time integration scheme. To obtain an unconditionally stable solution time step scheme, the Newmark alpha and beta parameters were set to the values of $\alpha_N = 0.3025$ and $\beta_N = 0.60$. This ensures that the dissipation occurs only at high frequency modes (Amorosi and Boldini, 2009).

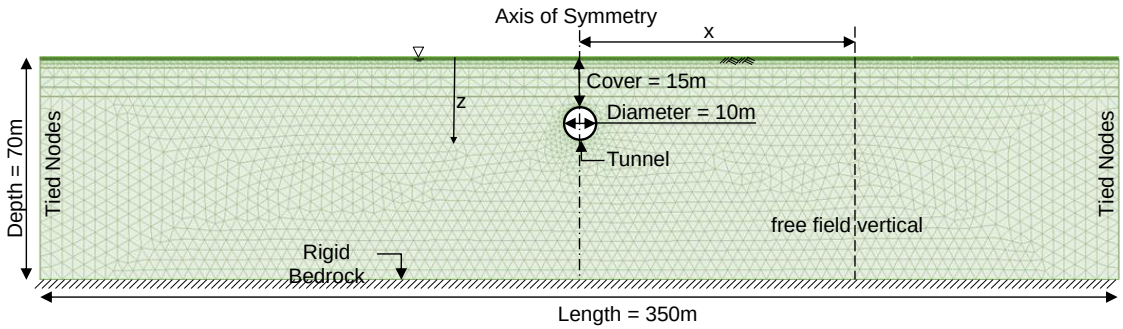

Figure 4.9 Adopted FEM model and boundary conditions for the dynamic simulations

4.4.1 *Initial conditions*

As in previous works of Burghignoli *et al.* (2003) and Elia and Rouainia (2014), a coefficient of earth pressure at rest K_0 equal to 0.5 has been assumed for the normally consolidated Avezzano Clay (i.e. Overconsolidation ratio *OCR* =1.0) in the generation of the geostatic stress state, using a unit weight of 18kN/m^3 for the clay. In the case of the earth dam material, the unit weight is 17kN/m^3 and K_0 has been calculated from the soil material's *OCR* equal to 1.5 and its derived critical state friction angle φ' (from the correlation with critical state parameter *M*, refer to Equation 4.15) equal to 29^o using Equation 4.18 suggested by Mayne and Kulhawy (1982) for overconsolidated soil. In order to account for the non-linearity in small-strain shear stiffness with depth of that same soil, the dimensionless stiffness parameters A_g, n_g and m_g in the Viggiani and Atkinson's equation have been set equal to 600, 0.82 and 0.36, respectively representing a soft soil material as described by (Amorosi and Boldini, 2009). The G_0 profile of which is shown in Figure 4.10.

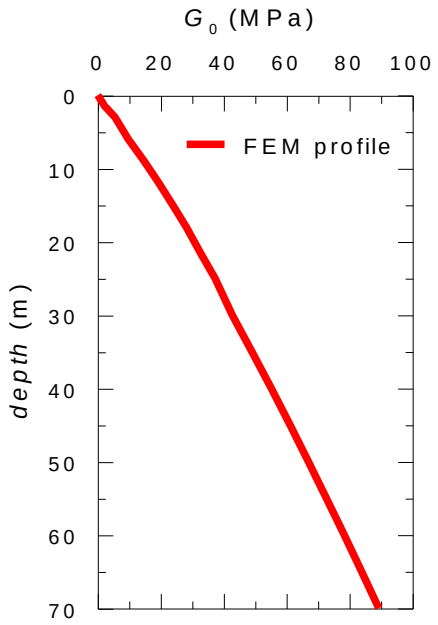

Figure 4.10 G_0 profile of Marana Capacciotti earth dam material

$$K_0 = (1 - \sin\varphi')OCR^{\sin\varphi'} \tag{4.18}$$

The FEM model has been discretised with a total number of 5088 15-noded plane strain triangular elements, with the mesh refined in the region around the tunnel to avoid mesh sensitivity due to the softening behaviour predicted by the RMW model. The 15-noded triangular element as shown in Figure 4.11 has 2 degrees of freedom at each node and 12 integration (Gauss) points. Triangular elements are advantageous compared to other shapes as they fit better with any arbitrary shaped geometries.

The 15-node triangle mesh element provides a fourth-order interpolation for displacements. Such higher order element can increase the accuracy of results compared to those of lower order of the same shape. The shape functions for this type of element are as follows:

$$\begin{aligned}
&N_1 = \zeta(4\zeta-1)(4\zeta-2)(4\zeta-3)/6;\\
&N_2 = \xi(4\xi-1)(4\xi-2)(4\xi-3)/6;\\
&N_3 = \eta(4\eta-1)(4\eta-2)(4\eta-3)/6;\\
&N_4 = 4\zeta\xi(4\zeta-1)(4\xi-1);\ N_5 = 4\xi\eta(4\xi-1)(4\eta-1);\\
&N_6 = 4\eta\zeta(4\eta-1)(4\zeta-1);\ N_7 = \xi\zeta(4\zeta-1)(4\zeta-2)*8/3;\\
&N_8 = \zeta\xi(4\xi-1)(4\xi-2)*8/3;\ N_9 = \eta\xi(4\xi-1)(4\xi-2)*8/3;\\
&N_{10} = \xi\eta(4\eta-1)(4\eta-2)*8/3;\ N_{11} = \zeta\eta(4\eta-1)(4\eta-2)*8/3;
\end{aligned} \tag{4.19}$$

$$N_{12} = \eta\zeta(4\zeta - 1)(4\zeta - 2) * 8/3; N_{13} = 32\eta\xi\zeta(4\zeta - 1);$$
$$N_{14} = 32\eta\xi\zeta(4\xi - 1); N_{15} = 32\eta\xi\zeta(4\eta - 1)$$

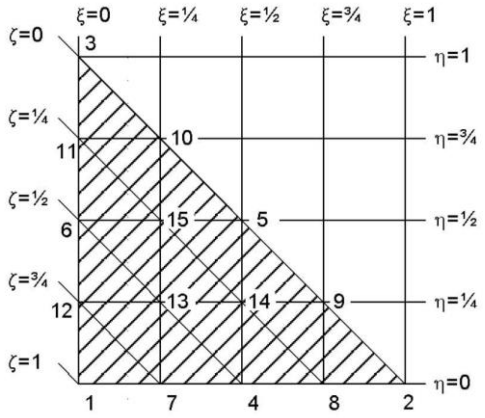

Figure 4.11 15-node triangular element (Brinkgreve and Broere, 2015)

To ensure that the seismic wave transmission is represented accurately through the finite element mesh, the vertical distance between adjacent element nodes *Δh* has been limited to satisfy the condition below recommended by Kuhlemeyer and Lysmer (1973), even when the reduction of the initial shear modulus during the dynamic excitation produces a reduction in the wave length.

$$\Delta h \leq h_{max} = \frac{V_s}{8\, f_{max}} \qquad 4.20$$

where V_s is the shear wave velocity and f_{max} is the maximum frequency of the input seismic wave which has been set to 10 Hz.

To take into account the effects of pre-seismic stress conditions, a static analysis under undrained conditions has been initially performed to simulate the tunnel excavation and installation of the tunnel lining. A contraction equivalent to 0.8% volume loss, deemed to be acceptable for a satisfactory performance of the tunnel excavation [e.g. Mair (1996)], has been imposed. The volume loss is a design parameter and its value is usually chosen on the basis of the excavation method and previous tunnelling experience in similar geotechnical conditions. As reported by (Mair, 1996) for open face tunnelling in stiff clays (e.g. London Clay), the volume loss values are generally between 1% and 2%; for closed face tunnelling, using earth pressure balance or slurry shield, a high degree of settlement control can be achieved by providing a high degree of control on face pressure, particularly in sands where volume loss is often as low as

0.5% and even in soft clays where, excluding consolidation settlements, it is only 0.8–2%. Working on the assumption of a closed face tunneling with high degree of control of the face support, the adopted value of 0.8% sounds reasonable. The dynamic analyses have been carried out under undrained conditions with a time step corresponding to that of the earthquake input signals. All these steps were repeated for each selected earthquake signals for different soil types and constitutive cases.

4.4.2 *Determination of the FEM model length*

Several authors have studied the model length required for shallow tunnels in seismic conditions. According to case study conducted by Torcato (2010), the interaction region where the tunnel influences the vertical propagation of shear waves along the soil medium during earthquakes is 8 to 16 times the diameter of the tunnel depending on the flexibility ratio between the tunnel and the soil medium as defined by Peck *et al.* (1972). Based on the tests presented, it was recommended that 12 times the diameter of the tunnel is the optimal value. Beyond the interaction region, the free-field conditions apply. Amorosi *et al.* (2010), on the other hand, concluded that the model length, with viscous lateral boundaries, equal to eight times the depth of the soil model can clearly reproduce the free-field response near the lateral boundaries. However, it was suggested that four times the depth of the soil model has attained satisfactory results in agreement with one-dimensional 1D soil response (i.e. free-field conditions) and is a good compromise between accuracy and time required to perform the 2D analysis.

In order to determine the appropriate length of the 2D FEM model for the case study, a parametric study of the model length has been conducted to ensure sufficient distance to the lateral boundaries of the mesh that can simulate properly the free-field conditions at the edges of the model. The study is similar to those outlined in the works of Amorosi *et al.* (2010) and Kontoe (2006).

A trial length of 5 times the depth of the soil model (i.e. 350m), shown in Figure 4.9, has been chosen by the author based on the range of 4 to 8 times the depth of the soil suggested by Amorosi *et al.* (2010). Tied nodes have been utilised at the lateral boundaries as their effectiveness in producing free-field response while optimising the size of the model has been proven by Kontoe (2006). Tied degrees of freedom

boundary condition or simply called tied nodes boundary condition was introduced by Zienkiewicz *et al.* (1989). This boundary condition constrains nodes of the same elevations on the lateral boundaries to deform identically by tying them together. It is well-suited for 1D soil response (i.e. soil columns) and in cases where waves radiating away from the structure towards the boundaries of the mesh are negligible or sufficiently damped (Kontoe *et al.*, 2007). If there is no sufficient damping or dynamic wave dissipation occurs in the structure it can cause the wave to become trapped into the mesh resulting in inaccurate results. On that note, tied nodes boundary condition should always be validated to ensure its effectiveness and adequacy.

A 1D FEM model adopting a 5m wide mesh is also created characterised by tied nodes boundaries to represent an ideal free-field response for comparison purposes. The results of the shear strain time history at depths z=5m, 15m (i.e. approximately at tunnel crown), 25m (i.e. approximately at tunnel invert), 35m, 45m and 55m from ground level at a distance x (0m, 20m, 55m, 90m, 125m and 160m) from the axis of symmetry of the 2D FEM model are then matched with those from the 1D FEM model. From Figure 4.12 (a) to (f), it has been noted that at a distance of x=125m (equivalent to 4 times the soil depth), the free-field condition is already attained. Even at a distance of x=90m (equivalent to 3 times the soil depth), a satisfactory agreement is already discernable. These observations are further sustained in Figure 4.13 showing the maximum strain profile along the depth of the soil deposit. It shows that from distances equal or more than x=90m, the plots of maximum strain level approximately coincide and compare well with the free-field condition along the soil depth. This indicates that a shorter FEM model length can be used which essentially reduces the computational time. Although the smaller model has such an advantage, the author has decided to use the original larger model (i.e. 5 times the soil depth) in the succeeding analyses to ensure compatibility as well as comparability with the length of 6 times the soil depth in the 3D FEM model cases in Chapter 5 where viscous boundaries have been adopted.

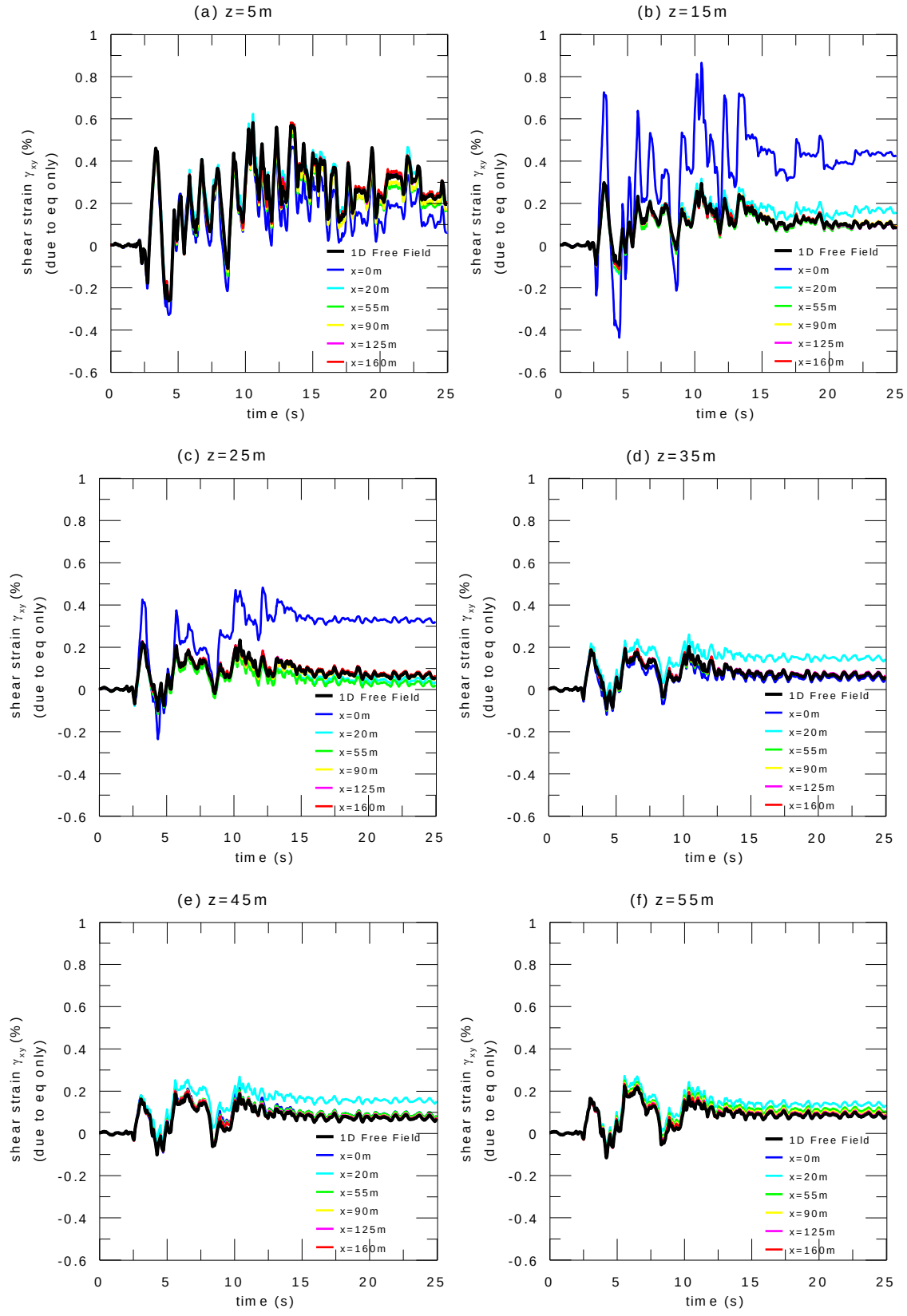

Figure 4.12 Shear strain time history at depths z: (a) 5m; (b) 15m; (c) 25m; (d) 35m; (e) 45m; (f) 55m

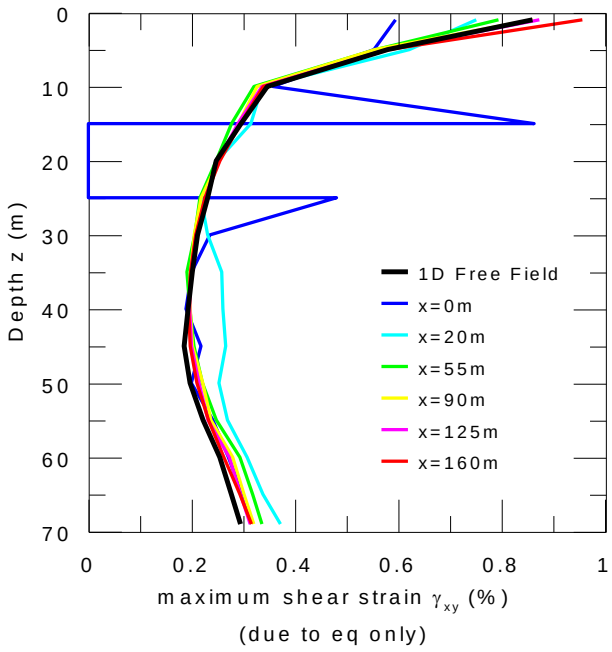

Figure 4.13 Maximum shear strain profile

4.4.3 *Selection of viscous parameters*

A primary limitation of single surface models (e.g. Mohr-Coulomb, Modified Cam Clay, Hardening Soil model) in the context of dynamic analyses is related to their inability to reproduce the observed hysteretic dissipation. This is caused by the unrealistically large extent of their yield surfaces, which leads to limited accumulation of plastic strain during cycles. As a consequence, the use of such simple models in FEM dynamic analyses requires the superposition of an often large, fictitious viscous damping [e.g. Woodward and Griffiths (1996)]. The ability of the RMW soil constitutive model to reproduce such hysteretic damping enables simulation without the introduction of artificial viscous damping, e.g. Rayleigh damping. Rayleigh damping in the form of a *[C]* matrix (Equation 4.21) approximates the material damping which is difficult to quantify a priori and can have a crucial influence on the results of numerical simulations. Nevertheless a small amount of Rayleigh damping (Damping ratio D = 2%) as recommended by Hashash and Park (2002) has been added in the dynamic simulations to avoid the propagation of spurious high frequencies, to compensate for the RMW underestimation of damping in the small-strain range and to prevent unrealistic resonance at small strains during wave propagation which can cause numerical divergence. The additional amount of Rayleigh damping only affects the propagation of the spurious high frequencies by smoothing out the overamplified signal at higher

frequency [(Amorosi *et al.*, 2010), (Bilotta *et al.*, 2014)]. At low frequencies, the range of frequency associated with the larger part of the energy content of the input signal which are the ones that are of more interest, will be damped out by the hysteretic damping provided by RMW, due to plasticity. Based on the studies by (Bilotta *et al.*, 2014), an amount of Rayleigh damping in a range between 0 and 4% does not affect the numerical results.

On the contrary, simulations with single surface models cannot be performed at all without Rayleigh damping, as they will give completely unrealistic results in terms of amplitude of the oscillations/displacements/accelerations. In addition, the FEM model will oscillate forever after the application of the earthquake as there will be no source of dissipation in the small-strain range (Kontoe *et al.*, 2009). Using single surface models require higher values of Rayleigh damping to be introduced in the FEM simulations. This damping will damp out all of the frequencies, not only the higher ones, which can significantly affect the results. This will be fully discussed at the latter part of this chapter. Additionally, even with the introduction of Rayleigh damping, the plasticity introduced by the single surface model will be small and as such, does not allow the prediction of period elongation in nonlinear analyses, thus also affecting the results (Kontoe *et al.*, 2011).

$$[C] = \alpha_R[M] + \beta_R[K] \tag{4.21}$$

where M and K are the mass and the stiffness matrices respectively, and α_R and β_R are the mass-proportional and stiffness-proportional damping coefficients respectively. The damping coefficients are obtained from the following relationships.

$$\begin{Bmatrix} \alpha_R \\ \beta_R \end{Bmatrix} = \frac{2D}{\omega_1 + \omega_2} \begin{Bmatrix} \omega_1 \omega_2 \\ 1 \end{Bmatrix} \tag{4.22}$$

where D is the target damping ratio and ω_1, ω_2 are the two frequencies defining the frequency range over which the damping is equal or lower than D as shown in Figure 4.14 (a).

It is evident from Equations 4.21 and 4.22 that viscous damping is highly dependent on the frequencies. There are different selection procedures proposed in the literature to determine frequencies ω_1 and ω_2. One such procedure was proposed by Hudson *et al.*

(1994) where ω_1 is chosen as the first natural frequency of the soil deposit while ω_2 is assumed to be equal to $n\omega_1$, where n is the closest odd integer larger than the ratio ω_p/ω_1 between the predominant frequency of the input earthquake motion (ω_p) and the fundamental frequency of the soil deposit (ω_1). Amorosi *et al.* (2010), however, found that this condition can lead to a significant under-damped response of the system in the frequency range characterised by an amplification factor larger than one, i.e. in the frequency interval in which the site effects would be more relevant. To avoid this issue, Amorosi *et al.* (2008) has introduced a selection procedure which was adopted in this project whereby the frequencies are selected as the range with the highest energy content predicted by equivalent-linear visco-elastic code EERA (Bardet *et al.*, 2000) at different depths of the soil deposit in free-field condition. This is achieved by matching the G_0 and D profile along the soil depth in the FEM model with the corresponding soil profile in EERA. The Fourier amplitude against the frequency from EERA analysis for different depths of the soil deposit for each earthquake motion are then plotted from which the frequency range where the highest energy content observed is selected. This procedure has been implemented successfully in the works of Amorosi and Boldini (2009) and Amorosi *et al.* (2010). The details of the selection procedure are described in the aforementioned reference and are not reported here but the results of the selection process are shown in Figure 4.14 (b) Umbria-Marche and (c) Montenegro with the corresponding derived values of frequencies ω_1 and ω_2 tabled below.

Earthquake	**ω_1 (Hz)**	**ω_2 (Hz)**
Umbria Marche EW	0.5	6
Montenegro NS	0.2	10

Table 4.4 Values of ω_1 and ω_2 for selected ground motions

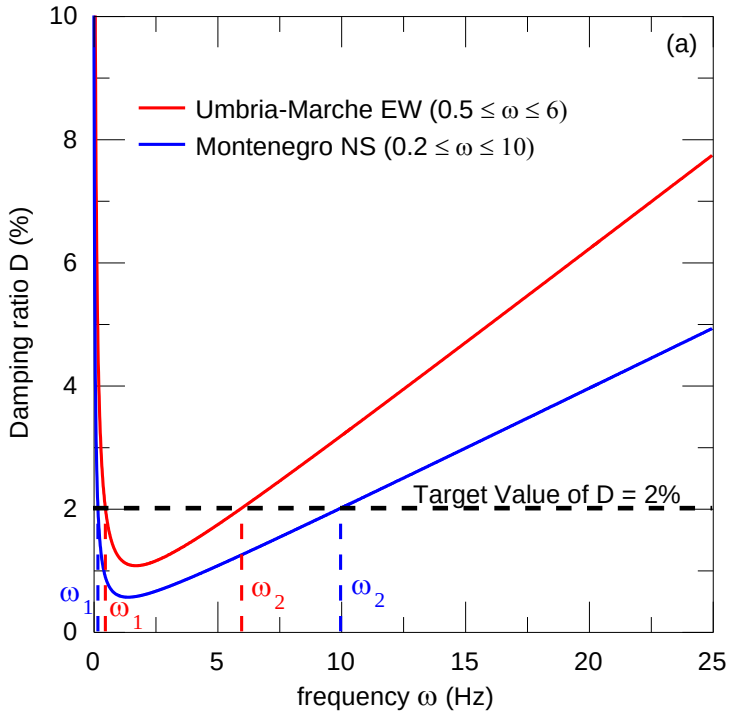
(a)
Umbria-Marche EW (0.5 ≤ ω ≤ 6)
Montenegro NS (0.2 ≤ ω ≤ 10)
Target Value of D = 2%
Damping ratio D (%)
frequency ω (Hz)
ω 1
ω 2
ω 1
ω 2

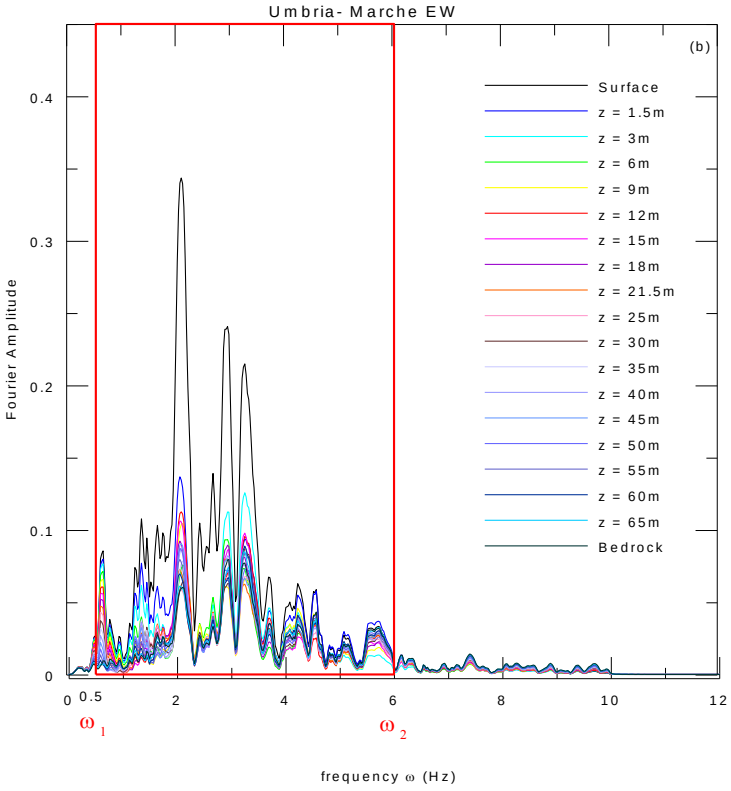
Umbria- Marche EW
(b)
Surface
z = 1.5m
z = 3m
z = 6m
z = 9m
z = 12m
z = 15m
z = 18m
z = 21.5m
z = 25m
z = 30m
z = 35m
z = 40m
z = 45m
z = 50m
z = 55m
z = 60m
z = 65m
Bedrock
Fourier Amplitude
frequency ω (Hz)
ω 1
ω 2

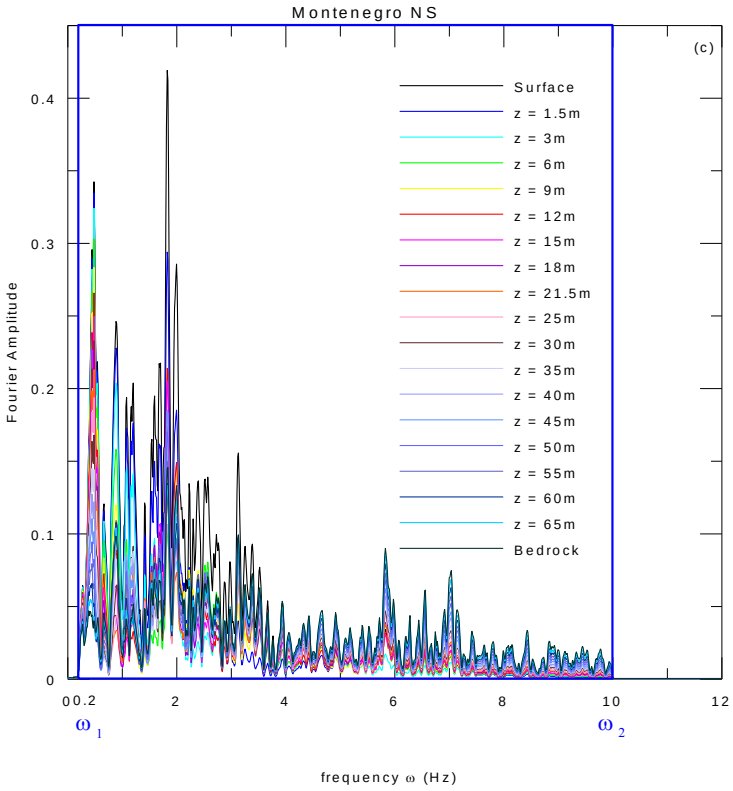

Figure 4.14 (a) Plot of damping ratio with frequency; (b) and (c) Fourier amplitude computed by EERA at different depths of the soil deposit and the selected range of high-energy content frequencies ω_1 and ω_2 for Umbria-Marche and Montenegro earthquakes respectively

4.5 Results and discussion

The case study is intended primarily to highlight for the first time the significance of the effects of soil destructuration induced in natural soil deposits in the assessment of the dynamic response of shallow tunnels constructed in structured clayey deposits. Its impact can significantly control the magnitude of the tunnel lining forces and, in consequence, alter the performance of the tunnel. Soil destructuration can only be simulated using advanced soil constitutive models. Hence, the study will also emphasise the advantage of adopting advanced soil constitutive models over simpler models. These are all taken within the context of evaluating the performance of the tunnel lining during seismic actions using this advanced approach. In order to compare the results systematically and ensure compatibility, the results are grouped into two categories.

1. Influence of soil constitutive model – comparing results between RMW against Modified Cam Clay (MCC). Some of these results and findings have been presented by the author (Cabangon *et al.*, 2017) in the Fourth International

Conference on Computational Methods in Tunneling and Subsurface Engineering (EURO:TUN 2017) held in Innsbruck, Austria on 18-20 April 2017.

2. Effect of initial structure and destructuration rate – comparing results by varying rates of degradation k = 1.5 & 5.0. A paper titled *Modelling the transverse behaviour of circular tunnels in structured clayey soils during earthquakes* (Cabangon *et al.*, 2019) has been published in Acta Geotechnica by the author based on the results and findings from this case study.

4.5.1 *Comparison between RMW and Modified Cam Clay*

In order to assess how much the choice of constitutive model can affect the tunnel response under seismic loading, dynamic simulations have been performed in the 2D FEM model adopting the soil parameters for Marana Capacciotti earth dam material derived in Section 4.2.1 for both RMW and MCC. The MCC parameters have been extracted from the general elastic and plastic parameters of RMW, i.e. λ^*, κ^*, M, v and φ'. Where dynamic analyses involve utilising MCC, a value of 6% Rayleigh damping, obtained from an equivalent linear 1D simulation with EERA (Bardet *et al.*, 2000), has been applied to the bottom 40m of soil to compensate the lack of hysteretic damping provided by the simpler constitutive model for shear strain levels smaller than 0.1%. As stated in Section 4.4.3, for RMW, a small amount of 2% Rayleigh damping has been introduced in the dynamic simulations to avoid the propagation of spurious high frequencies, to compensate for the RMW underestimation of damping in the small-strain range and to prevent unrealistic resonance at small strains during wave propagation which can cause numerical divergence but with no ill-effect on the numerical results.

The profiles of maximum horizontal acceleration recorded along the tunnel location and in free-field conditions during the two selected earthquake events are presented in Figure 4.15 for the RMW and MCC analyses. The simulations performed with the single surface model (MCC) show an overall amplification of the input signals in the top 15m of the soil deposit, while a considerable reduction of the maximum acceleration can be observed above the tunnel during the RMW analyses. This amplification of MCC at T_1 compared to RMW is also quite evident in terms of the response spectra recorded at the surface for both earthquakes (Figure 4.16). However, at a depth from

40m below ground the maximum acceleration for the two soil constitutive models is even for both earthquakes. As a result, the maximum shear strain near the surface level for MCC model under Montenegro earthquake is about twice that of RMW model (15% vs 8%) and about four times under Umbria-Marche earthquake (2% vs 0.5%) as shown in Figure 4.17. From 40m down to the bedrock the maximum shear strains become very much similar though for both soil constitutive models under both earthquakes which agrees with the maximum acceleration profiles. Moreover, the Montenegro event induces shear strain levels in the deposit significantly higher than those induced by the Umbria-Marche seismic motion (about eight times for MCC and sixteen times for RMW at the surface), given its higher energy content at T_1 (Figure 4.17). This is associated with higher accelerations recorded during the Montenegro simulations with respect to those predicted applying the Umbria-Marche input motion (Figure 4.15).

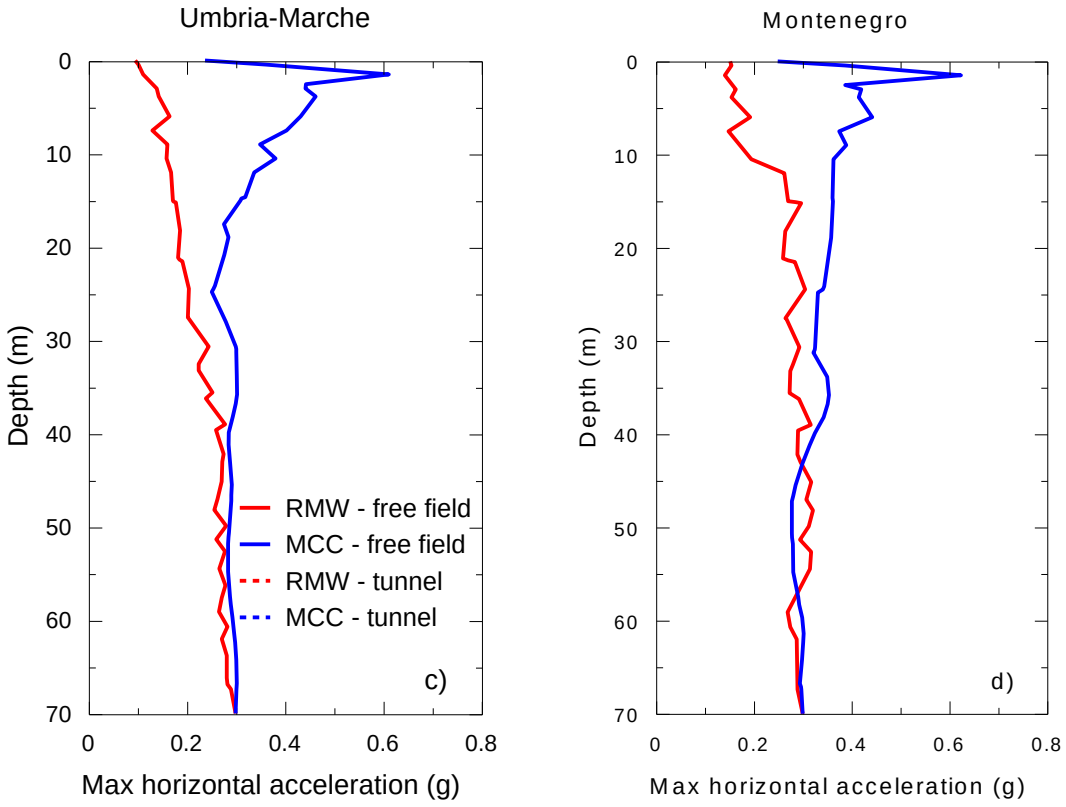

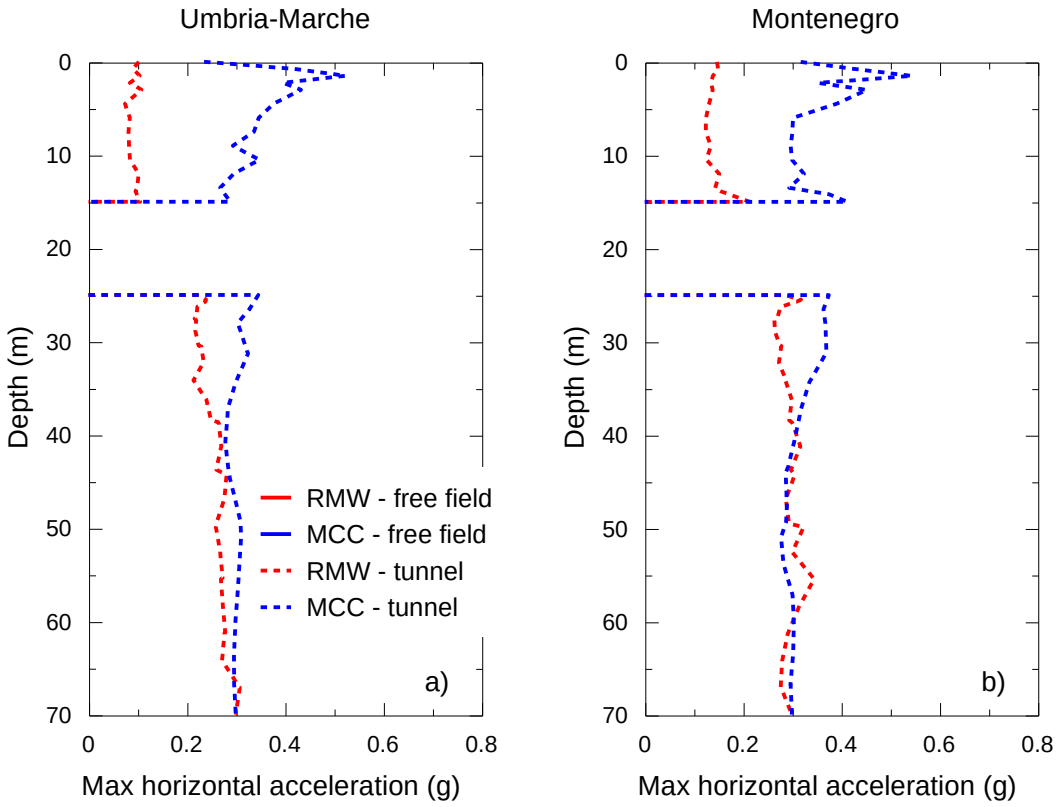

Figure 4.15 Profiles of max accelerations recorded in free-field conditions and along the tunnel location during the (a-c) Umbria-Marche and (b-d) Montenegro simulations for RMW and MCC

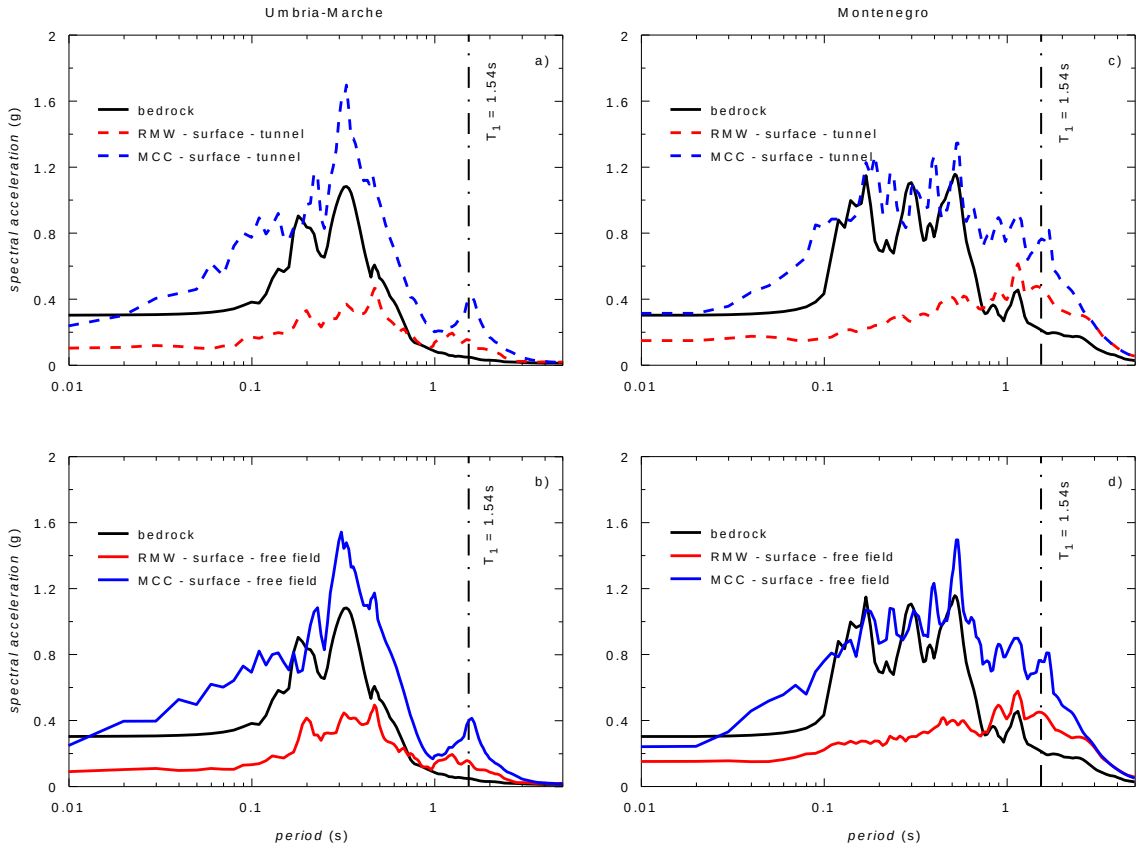

Figure 4.16 Comparison of response spectra recorded at bedrock and at surface during the: (a-b) Umbria-Marche; (c-d) Montenegro event for different soil constitutive models

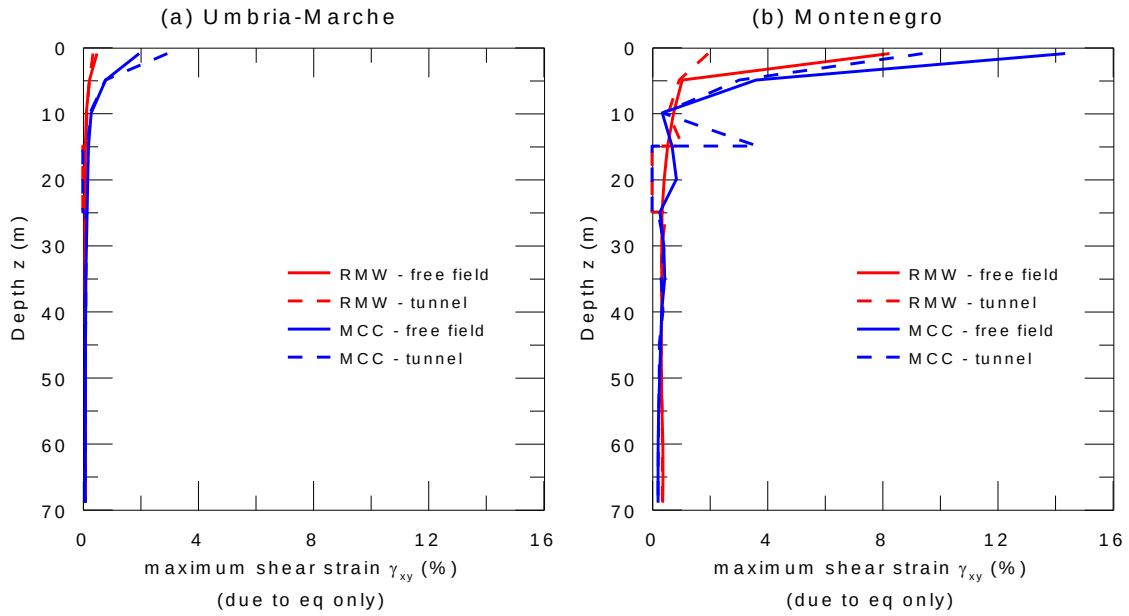

Figure 4.17 Comparison of maximum shear strain profile during the: (a) Umbria-Marche; (b) Montenegro event for different soil constitutive models

The stress-strain curve associated with the two seismic events in free-field conditions at different depths (i.e. at 10, 15, 25 and 50 m from the ground surface) are presented in Figure 4.18. It is observed that the RMW model already exhibits irreversible hysteretic behaviour even at low strain levels less than 0.1% while the MCC model still shows the soil in the elastic phase at the same strain level. The figure also shows a softer behaviour of the RMW model compared to MCC. These are all consistent with the normalised stiffness modulus curve presented in Figure 4.4 (c).

Figure 4.19 shows the distribution of predicted hoop force *N*, bending moment *M* and shear force *Q* before and after the seismic events as function of the angle θ, defined positive in the anti-clockwise direction. For both seismic events, the use of elasto-plastic models allows to predict permanent increments of hoop force, bending moment and shear force at the end of the motions due to the accumulation of plastic deformation in the soil deposit during the earthquakes, consistent with what has been observed by other researchers [Amorosi and Boldini (2009), Shahrour *et al.* (2010), Kontoe *et al.* (2011)]. As for the maximum accelerations, the permanent increments of *N*, *M* and *Q* predicted at the end of the Montenegro analyses are higher than those recorded at the end of the Umbria-Marche simulations.

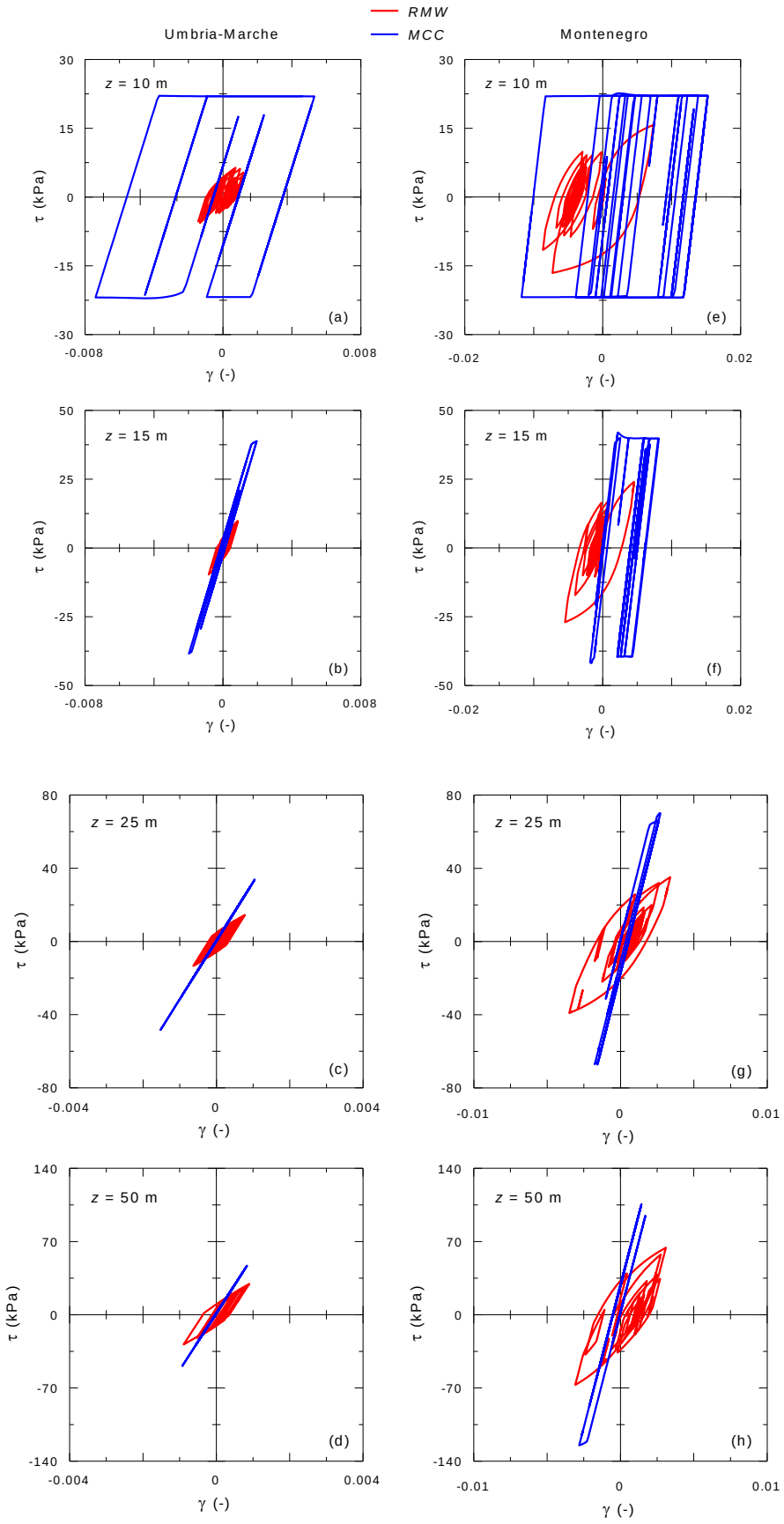

Figure 4.18 Stress–strain curves during the: a–d Umbria-Marche; e–h Montenegro event for different soil constitutive models in free-field conditions

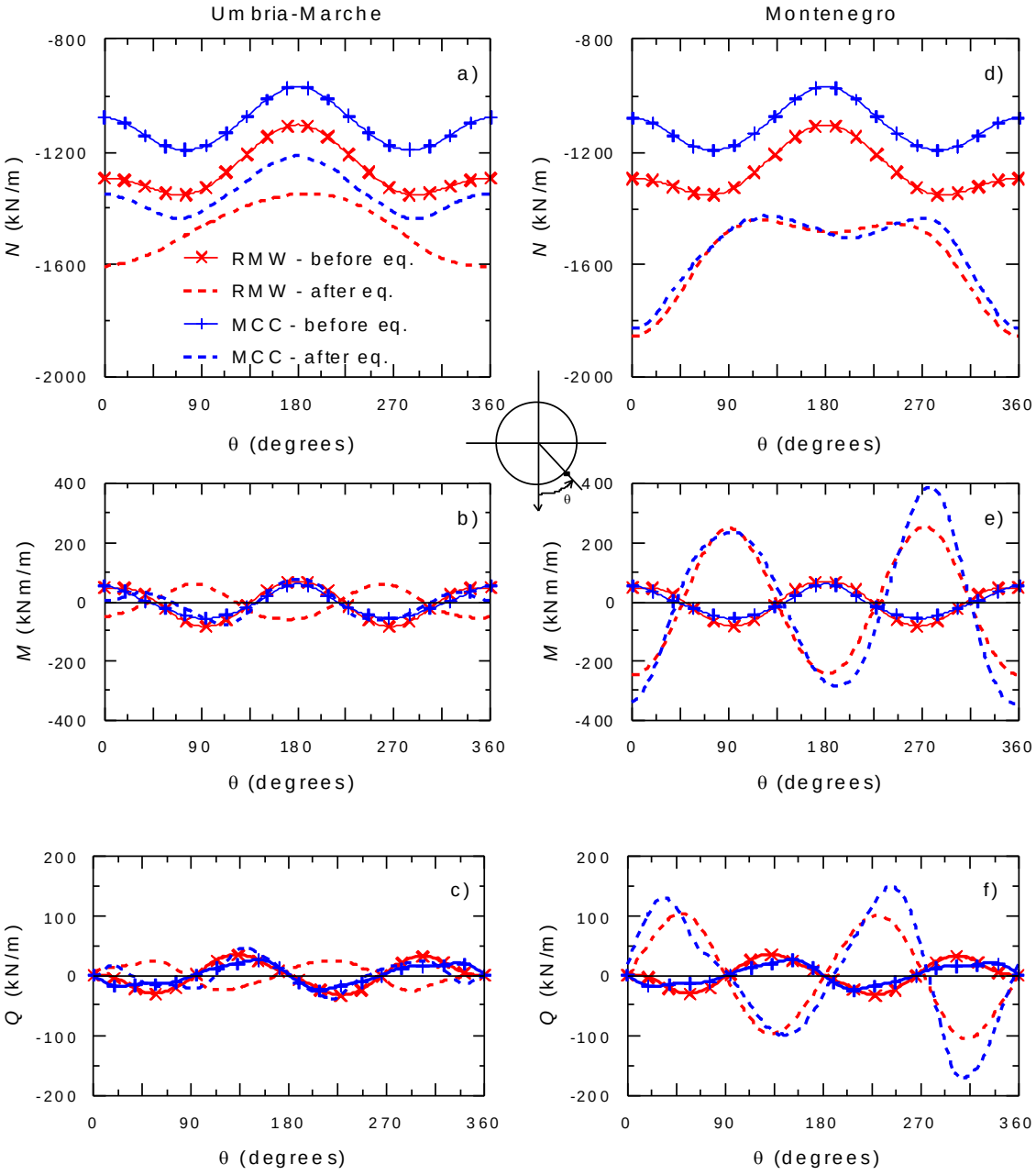

Figure 4.19 Distribution of hoop force, bending moment and shear force before and after the (a-c) Umbria-Marche and (d-f) Montenegro seismic events for different soil constitutive models

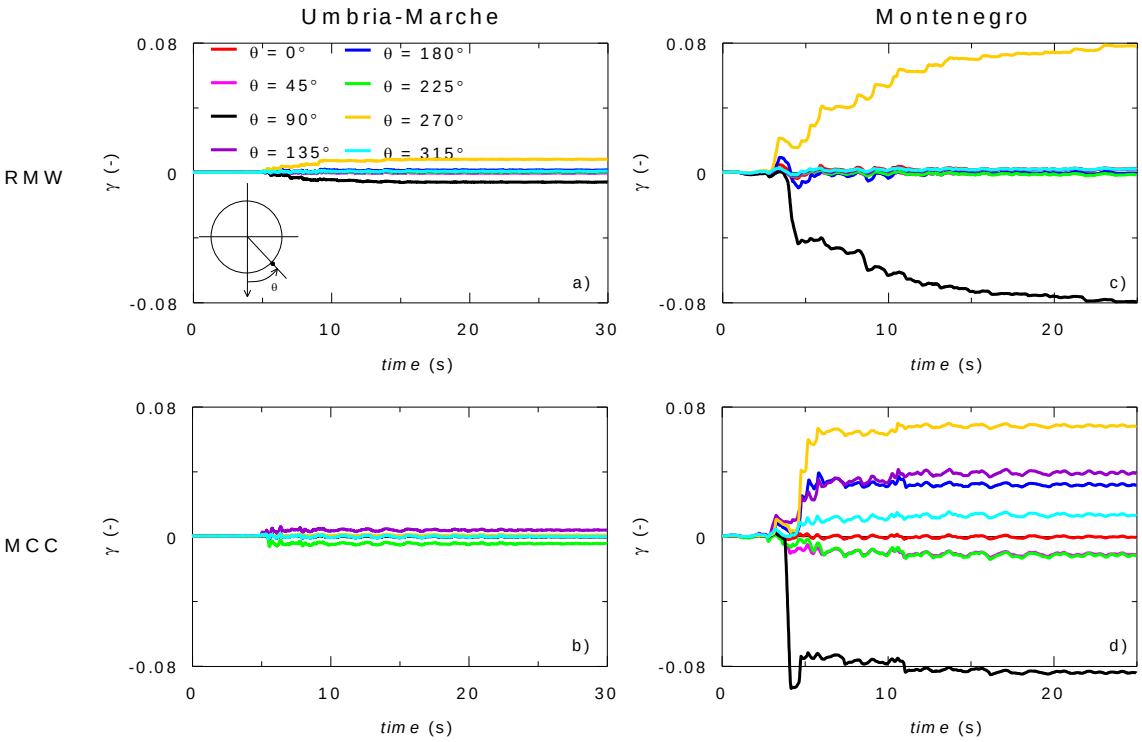

Figure 4.20 Time histories of shear strain around the tunnel during the: a–b Umbria-Marche; c–d Montenegro event for different soil constitutive models

The comparison between the MCC and RMW lining force predictions for the Montenegro event indicates that the single surface model produces permanent increments of hoop forces, bending moments and shear forces that are always higher than those obtained with RMW at the same lining location, as shown in Figure 4.22. This is due to the higher shear strain level (0.2 to 9.4%) induced by the Montenegro earthquake causing the MCC model to produce higher shear strains around the tunnel compared to RMW as shown in Figure 4.20 (c-d), hence, imposing higher loads to the tunnel lining. This is not necessarily happening at every location along the lining when the Umbria-Marche earthquake is applied at bedrock as shown in Figure 4.21. This can be attributed to the lower shear strain level induced by the Assisi earthquake primarily around 0.2% or less as shown in Figure 4.20 (a-b). At such low strain level, the shear strains produced by the MCC model around the tunnel were also low and relatively similar to RMW. As such, the forces imposed by the soil on the lining for both models were not significantly different from one another. Hence, no distinct dominance of one model from the other can be observed.

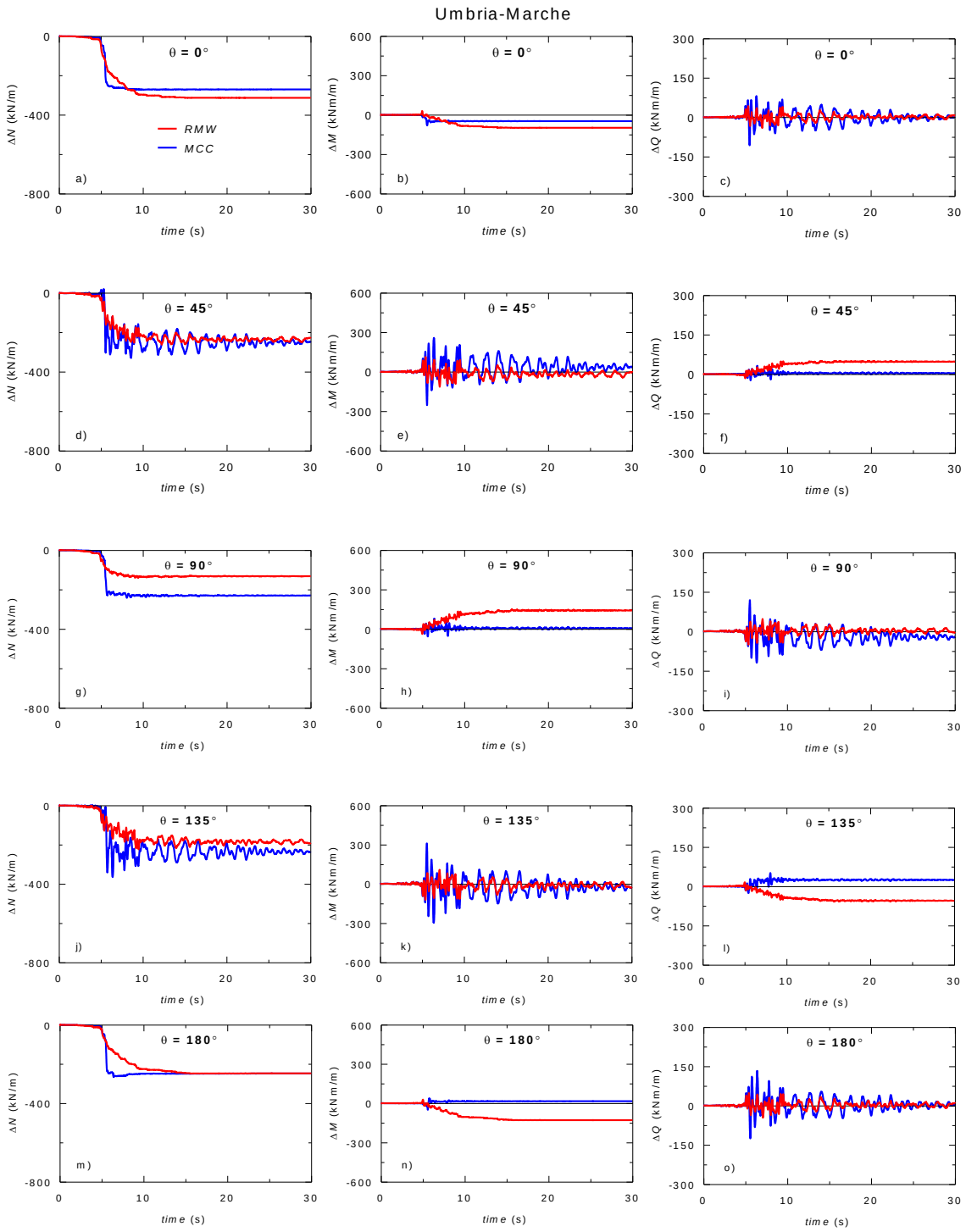

Figure 4.21 Influence of soil constitutive models on time histories of hoop force, bending moment and shear force increments during the Umbria-Marche event for: a-c $\theta = 0^{o}$; d-f $\theta = 45^{o}$; g-i $\theta = 90^{o}$; j-l $\theta = 135^{o}$; m-o $\theta = 180^{o}$

Notwithstanding these observations, it is evident that the MCC model predominantly overestimates the tunnel lining forces as compared to RMW as shown in the envelope of maximum and minimum hoop forces, bending moments and shear forces around the tunnel lining for both earthquakes (Figure 4.23). The results also confirm the conclusion drawn by Kontoe *et al.* (2011) that MCC-type models can significantly over-

predict the permanent increments of lining forces at the end of the seismic action with respect to kinematic hardening based assumptions particularly for earthquakes inducing higher shear strain levels, thus highlighting the benefits of using more advanced constitutive models in tunnel design practice. Consistent with the observations by other researchers, the peak maximum axial force and bending moments occurred around the shoulder and knee regions while the peak maximum shear force occurred at the spring lines, invert and crown of the tunnel.

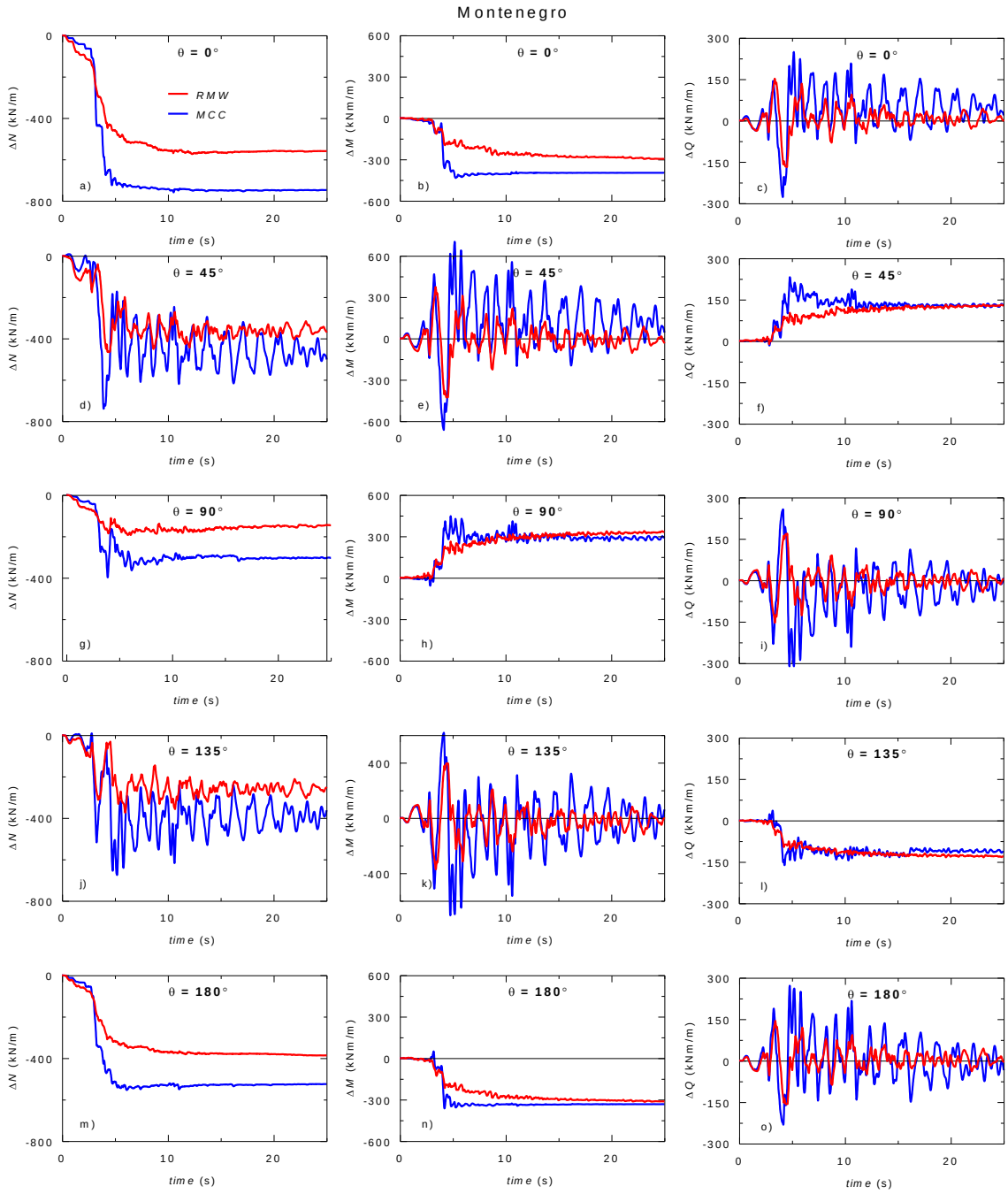

Figure 4.22 Influence of soil constitutive models on time histories of hoop force, bending moment and shear force increments during the Montenegro event for: a-c $\theta = 0^o$; d-f $\theta = 45^o$; g-i $\theta = 90^o$; j-l $\theta = 135^o$; m-o $\theta = 180^o$

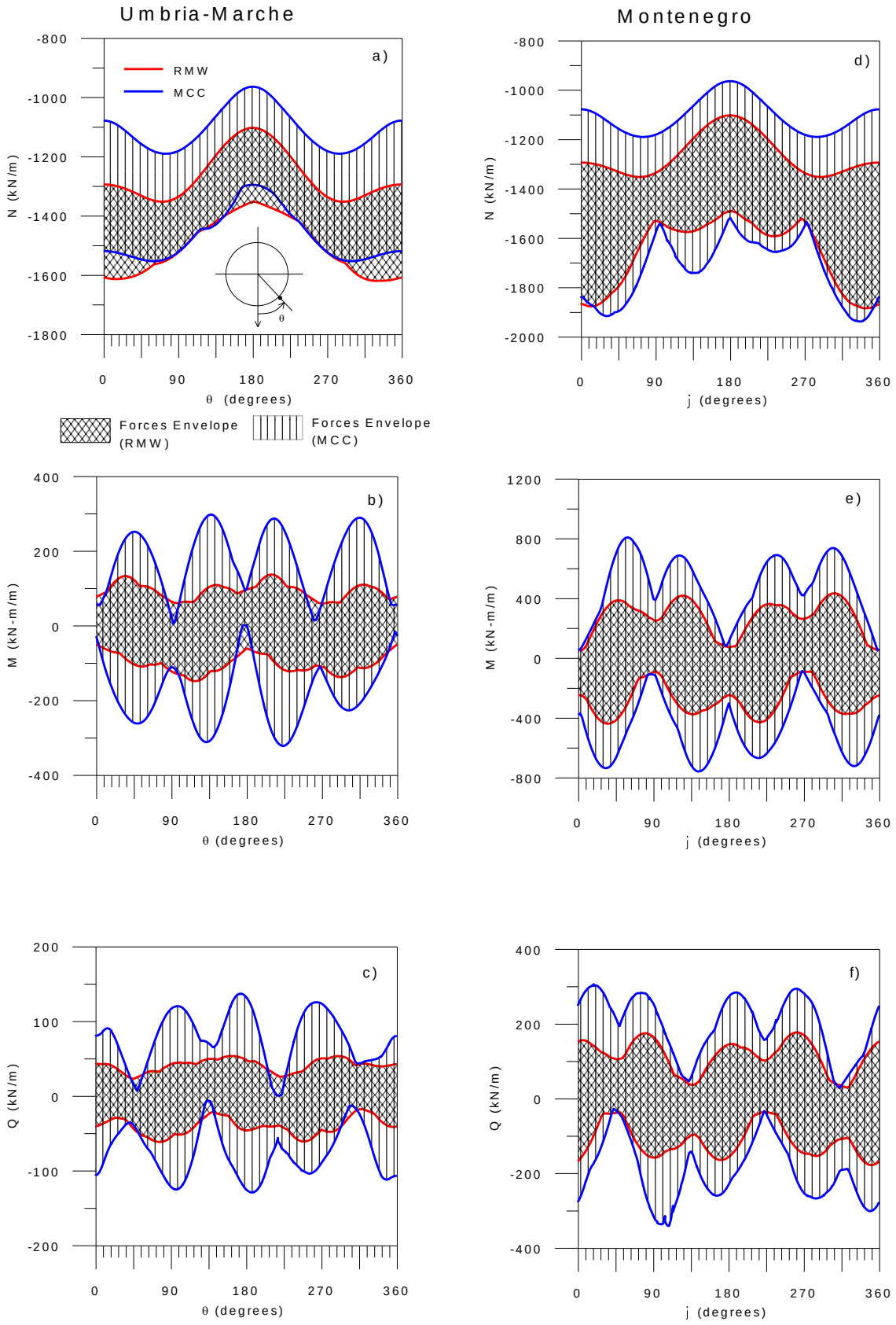

Figure 4.23 Maximum and minimum forces envelope in the tunnel lining during the: a–c Umbria-Marche; d–f Montenegro event for different soil constitutive models

4.5.2 *Effect of initial structure and destructuration rate*

In this section, the soil-tunnel interaction response during the selected earthquake events has been systematically investigated to highlight the influence of the initial degree structure and its subsequent degradation induced by the seismic loads. Specifically, two sets of simulations have been considered and compared: the ones performed applying the two input motions and using a rate of destructuration k equal to 1.5 and those in which the RMW parameter k has been set equal to 5.0. To ensure comparability, the initial conditions, i.e. the initial stress level and the initial soil structure r_0 = 5.2 were kept similar for both parametric cases. In the following, the results of the dynamic analyses are presented in terms of propagation of the seismic waves within the deposit, mechanical response of the soil surrounding the tunnel and distribution and time histories of the lining forces induced in the tunnel by the earthquake actions.

The profiles of maximum horizontal acceleration recorded in free-field conditions (with location shown in Figure 4.9) and along the tunnel vertical during the two selected earthquake events are presented in Figure 4.24. For both seismic events and along both verticals, the FEM analyses predict an overall deamplification of the bedrock motion at surface. It also seems that the degradation rate does not particularly influence the wave propagation in the deposit. Moreover, it appears that the Montenegro input motion induces higher accelerations, especially in the bottom part of the deposit and below the tunnel, but the PGA at the surface is similar to the one recorded during the Umbria-Marche event. These findings are confirmed by the response spectra of the accelerations recorded at ground surface along the tunnel vertical and in free-field conditions shown in Figure 4.25 and compared with the response spectra of the input motions applied at bedrock. In general, given the higher energy content of the Montenegro event at T_1 (see Figure 4.8) significantly higher shear strain levels are induced in the deposit than those by the Umbria-Marche seismic motion.

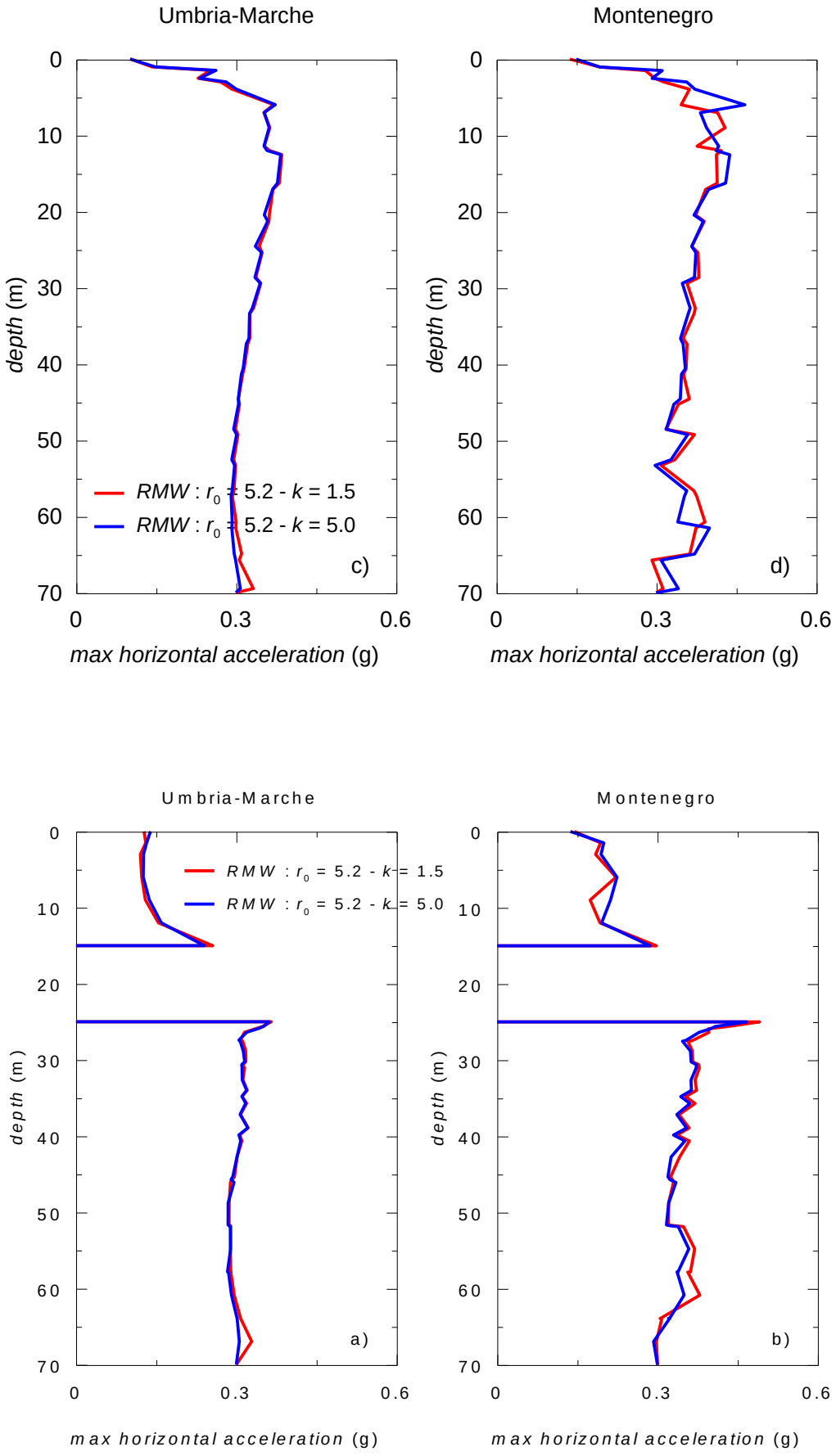

Figure 4.24 Influence of structure degradation rate on the profiles of maximum accelerations recorded along the tunnel vertical and in free-field conditions during the: a–c Umbria-Marche; b–d Montenegro event

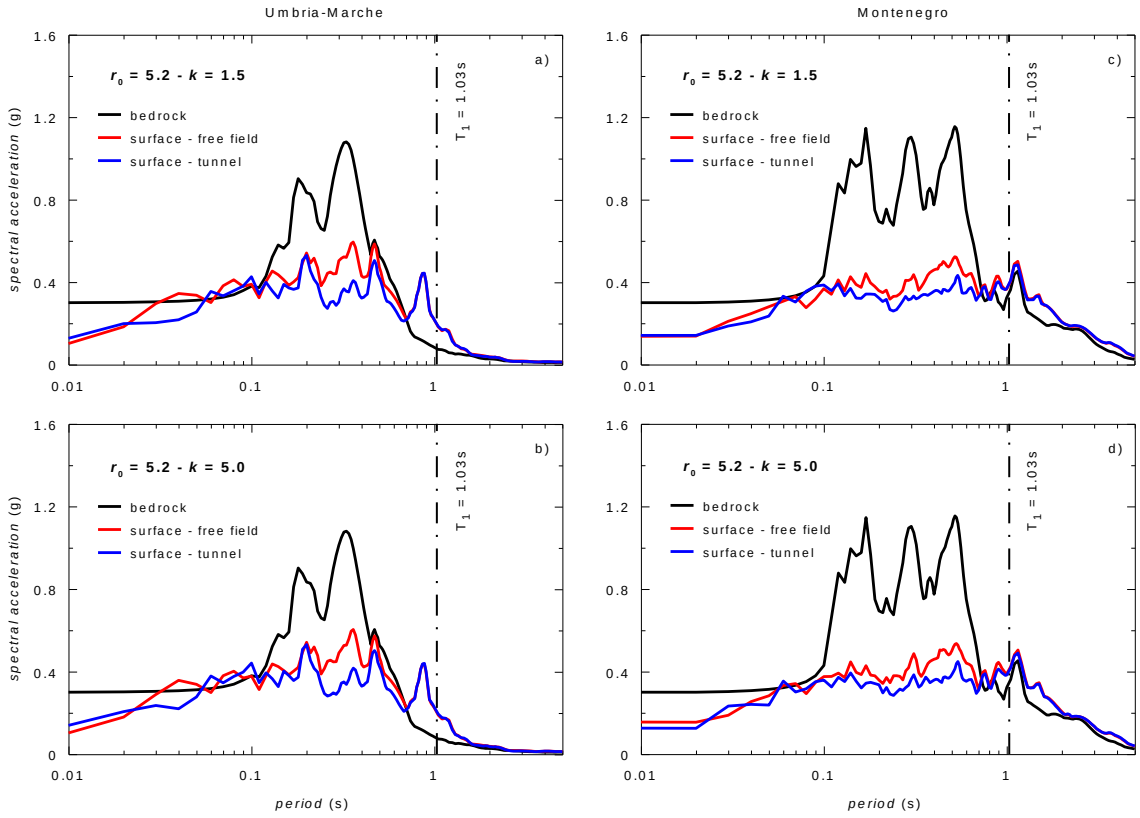

Figure 4.25 Comparison of response spectra recorded at bedrock and at surface during the: a-b Umbria-Marche; c-d Montenegro event for different destructuration rates

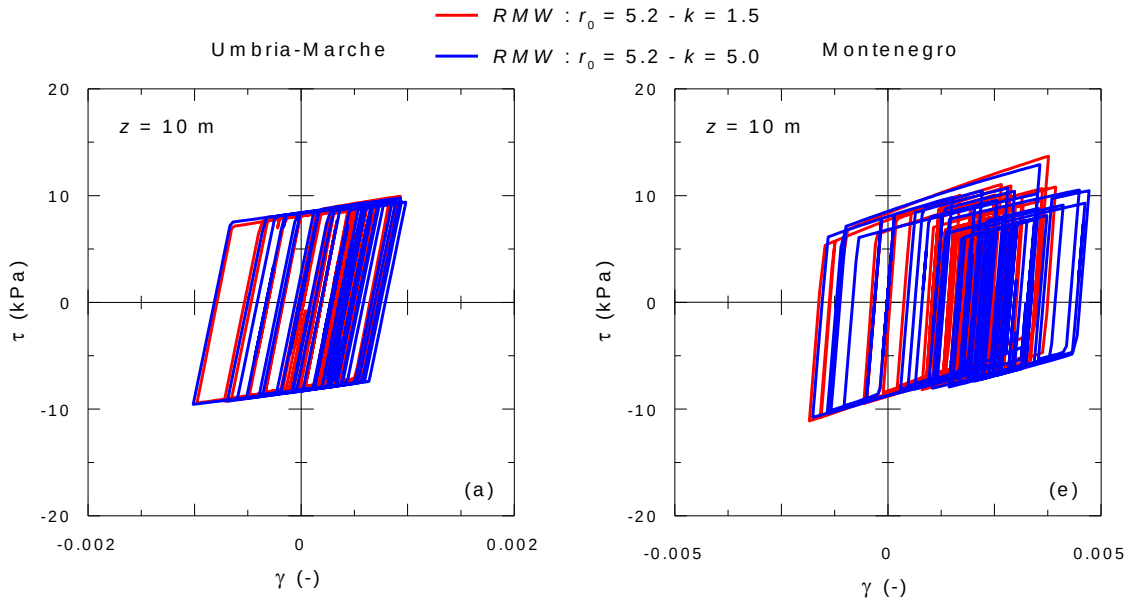

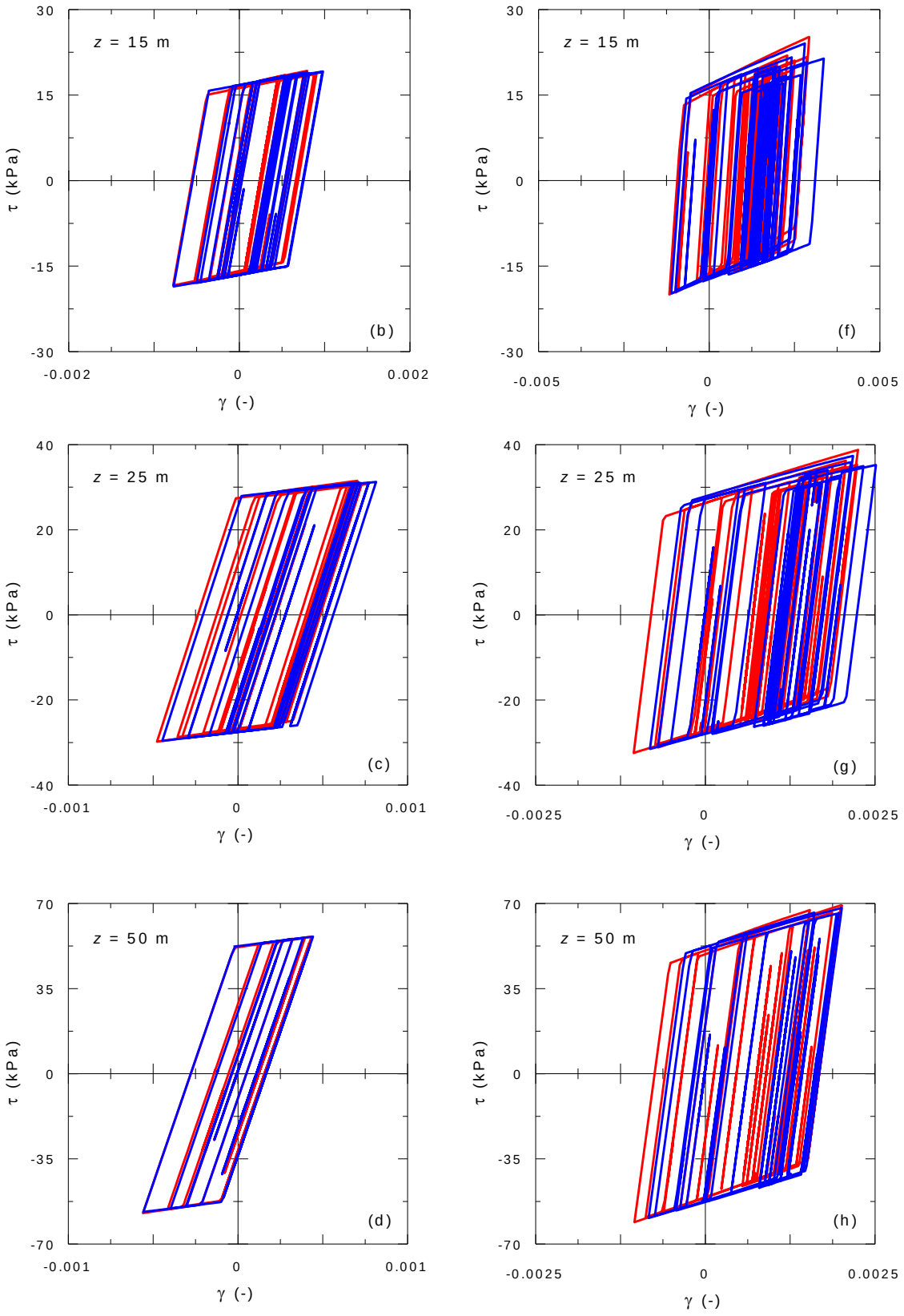

Figure 4.26 Stress–strain curves during the: a–d Umbria-Marche; e–h Montenegro event for different destructuration rates

The stress-strain curves recorded in free-field conditions during the two seismic events at different depths (i.e. at 10, 15, 25 and 50 m from the ground surface) and assuming two rates of destructuration are presented in Figure 4.26. The shear strains induced by

the Montenegro earthquake, ranging between about 0.5% at the surface and 0.25% at depth, are at least double the corresponding strains associated to the Umbria-Marche event. The figure also shows a softer behaviour of the soil when the rate of destructuration assumed in the simulations is higher (i.e. for k = 5.0), consistent with the normalised stiffness modulus curves presented in Figure 4.7.

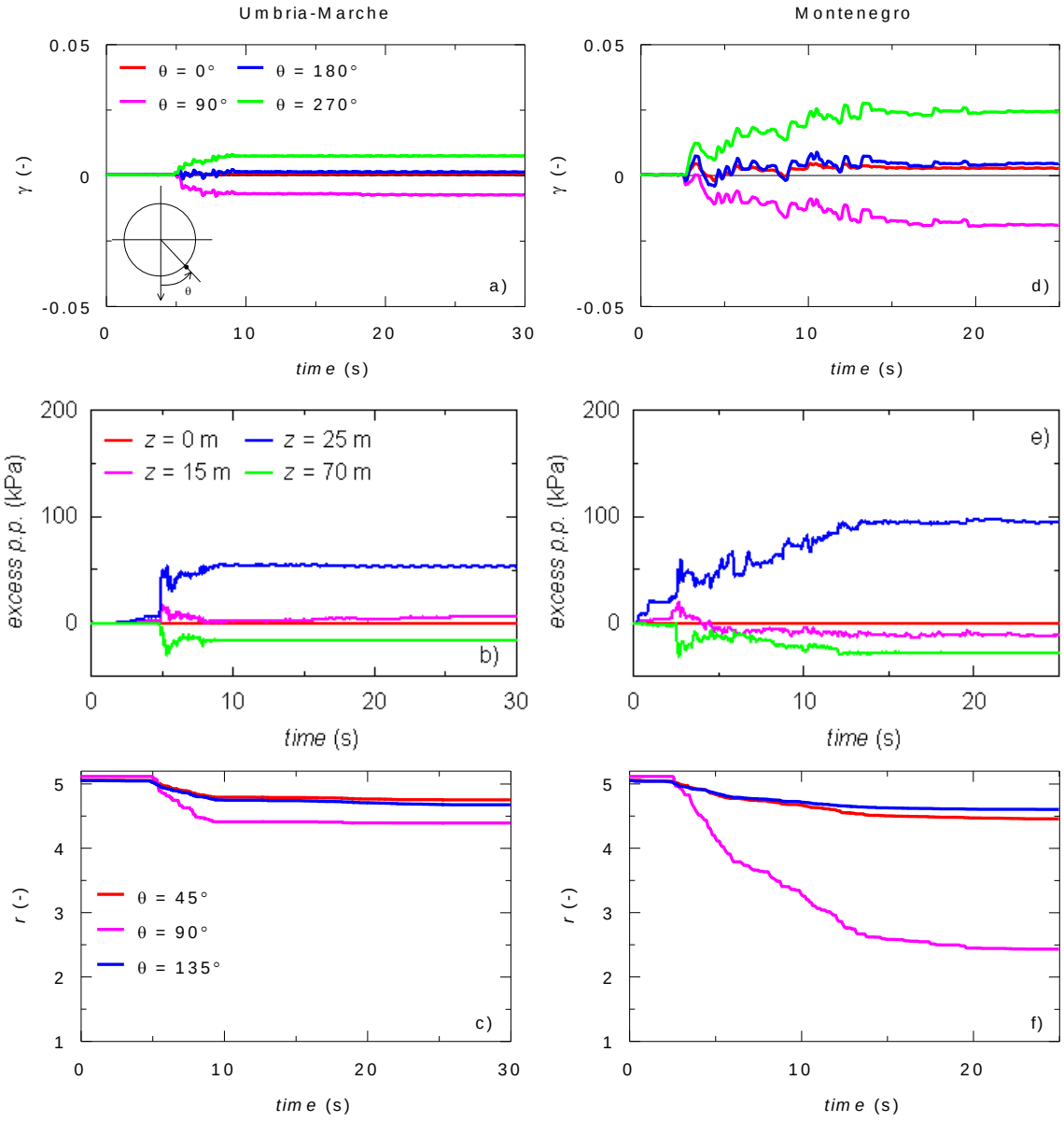

Figure 4.27 Time histories of shear strain, excess pore pressure and RMW soil structure parameter r during the: a–c Umbria-Marche; d–f Montenegro event for a destructuration rate k = 1.5

For the case of k = 1.5, the evolution with time of the shear strains recorded during the two seismic events around the tunnel is shown in Figure 4.27 (a & d) as a function of the angle θ. The non-symmetric response observed in terms of shear strains is the counterpart of an elasto-plastic behaviour induced in the soil deposit by the dynamic

excitation. In addition, Figure 4.27 (b & e) show the time histories of excess pore water pressures predicted along the tunnel vertical for the Umbria-Marche and Montenegro events, respectively. The FEM non-linear analyses predict the build-up of positive pore pressures above the tunnel and negative pore pressures below it, associated with the accumulation of permanent soil deformations and structure degradation throughout the two earthquake motions. Higher excess pore pressures are recorded during the Montenegro event, ranging between 100kPa at 25m depth and -27kPa at the bottom of the mesh.

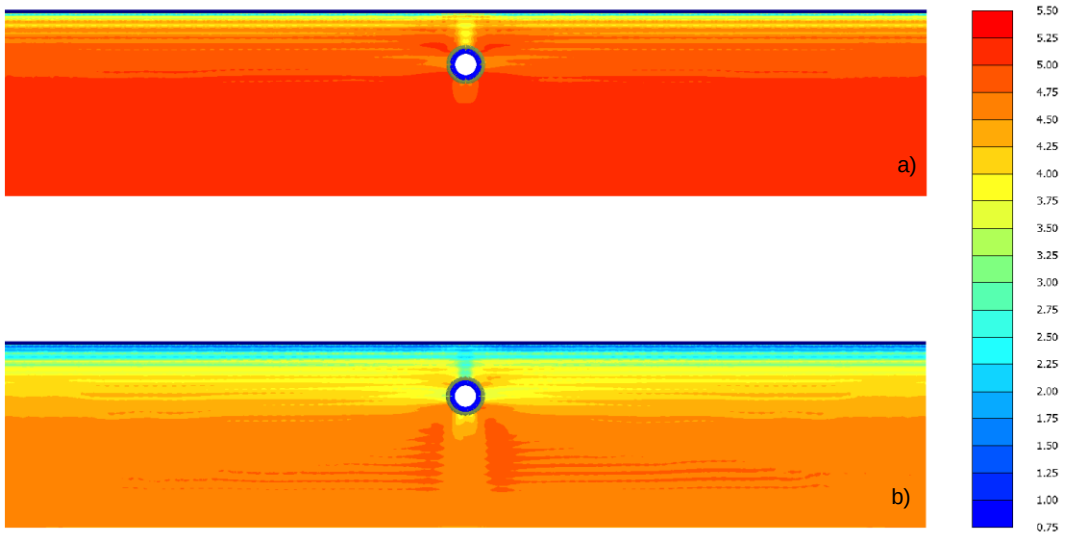

Figure 4.28 Contours of the RMW parameter r at the end of the: a Umbria-Marche; b Montenegro event for a destructuration rate $k = 1.5$ (note that r_0 is equal to 5.2 in both cases)

The evolution with time of the RMW parameter r, describing the degree of soil structure, during the two seismic motions is shown in Figure 4.27 (c & f) for three different locations around the tunnel. More pronounced structure degradation is induced in the soil surrounding the tunnel by the Montenegro seismic event, consistent with the higher shear strain levels and excess pore pressures recorded during this earthquake in the same locations. Figure 4.28 shows the contours of r obtained at the end of the two seismic events, indicating a more diffused destructuration occurred in the soil deposit during the Montenegro analysis compared to the Umbria-Marche case. Moreover, in both cases higher destructuration is observed in the top part of the model, between the tunnel and ground surface, where the deamplification of the input signal occurs (see Figure 4.24).

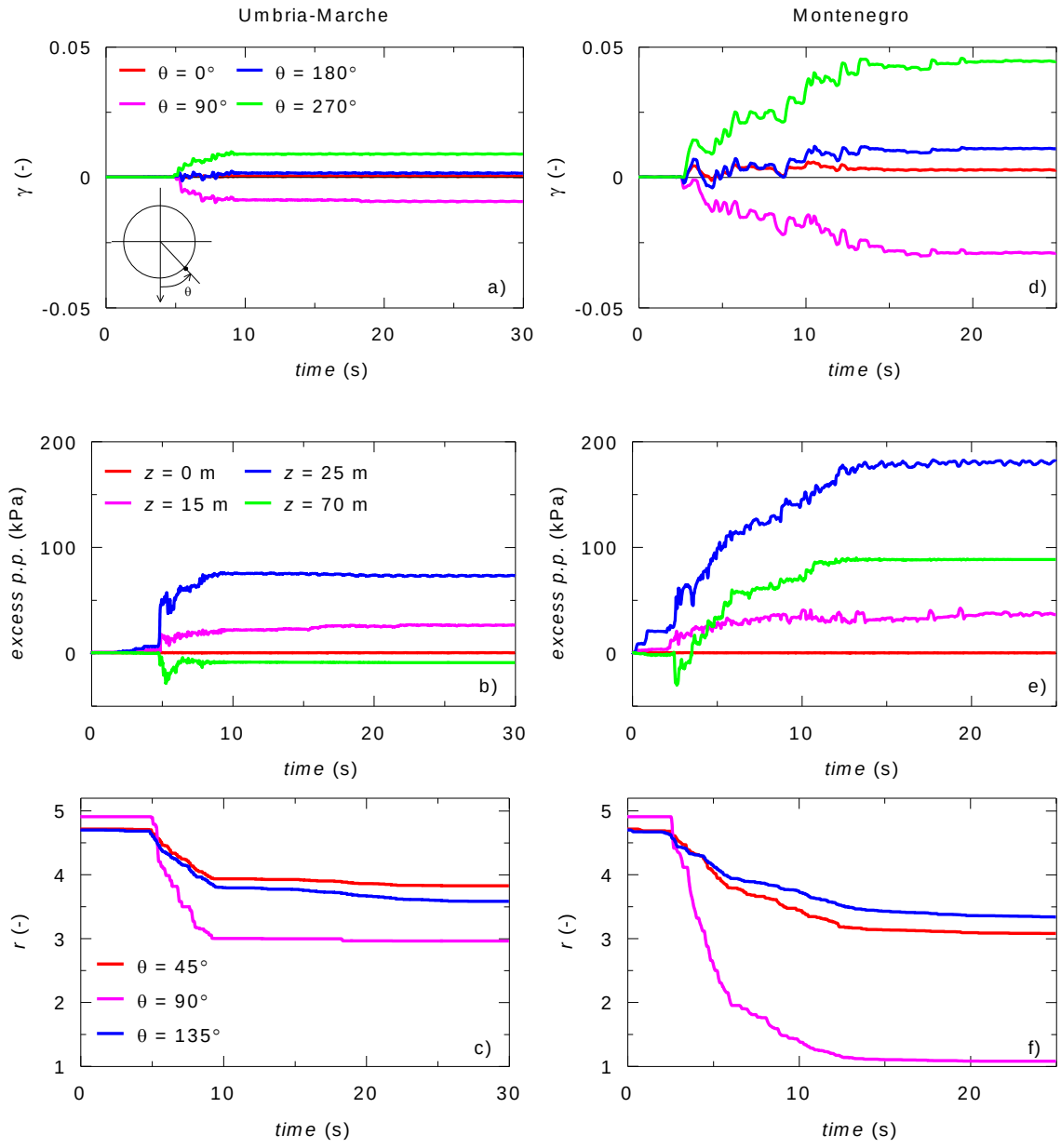

Figure 4.29 Time histories of shear strain, excess pore pressure and RMW soil structure parameter r during the: a–c Umbria-Marche; d–f Montenegro event for a destructuration rate $k = 5.0$

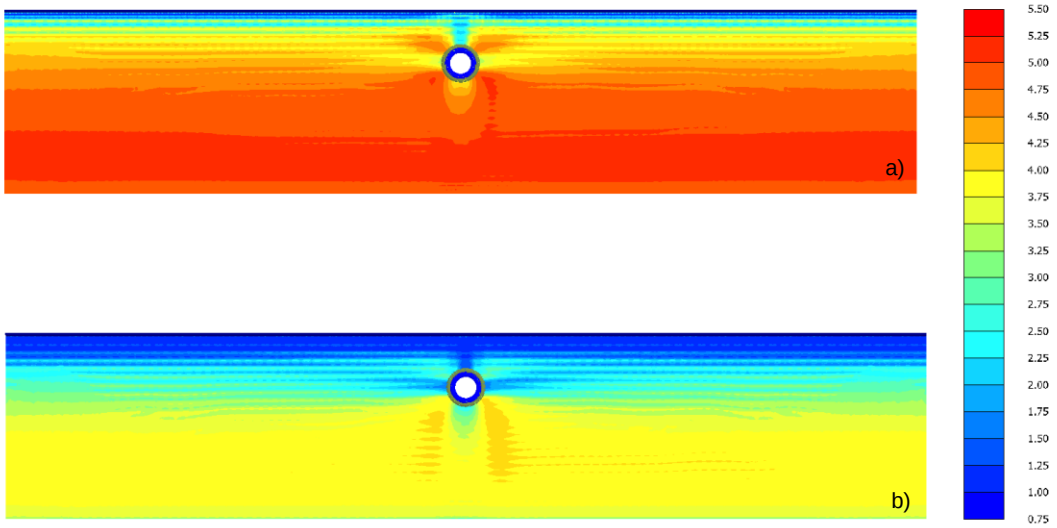

Figure 4.30 Contours of the RMW parameter r at the end of the: a Umbria-Marche; b Montenegro event for a destructuration rate $k = 5.0$ (note that r_0 is equal to 5.2 in both cases)

Figure 4.29 presents the time histories of shear strain, excess pore pressure and RMW structure parameter r during the two earthquake events when a destructuration rate k of 5.0 is adopted in the simulations. The higher degree of destructuration allowed in the simulations leads to the development of higher shear strains around the tunnel (Figure 4.29 a & d) and the consistent accumulation of positive pore water pressures in the soil deposit (Figure 4.29 b & e), reaching a maximum value of excess pressure almost equal to 200kPa in the Montenegro analysis. Almost a full structure degradation (i.e. the soil is almost fully remoulded) is observed at $\theta = 90^o$ when the Montenegro input motion is applied at bedrock (i.e. r approaches a final value of 1.0), as indicated by Figure 4.29 (f). This is confirmed by the contours of r obtained at the end of the two seismic events, shown in Figure 4.30, where full destructuration of the top 5m of the soil deposit can be observed in the Montenegro case.

Comparing the shear strains recorded around the tunnel between the two rates of destructuration for the two earthquake motions [Figure 4.27(a) vs Figure 4.29(a) & Figure 4.27(d) vs Figure 4.29(d)], the shear strains for the soil with faster destructuration rate $k = 5.0$ were higher than those for the soil with $k = 1.5$. This is due to the higher degree of structure degradation (i.e. smaller r) induced when $k = 5.0$ [Figure 4.27(c) vs Figure 4.29(c) & Figure 4.27(f) vs Figure 4.29(f)] resulting to a softer behaviour of the soil, thus increasing the shear strain level, even for a weak ground

motion, more so for a strong earthquake. As much as 23% increase from 0.0078 to 0.0096 in the maximum shear strain increment between rates k = 1.5 and k =5.0 were recorded at the tunnel spring line (i.e. θ = 270°) for Umbria-Marche earthquake and 66% increase from 0.0274 to 0.0455 for Montenegro earthquake. Consistent with the increase in shear strain level, the excess pore water pressures have also increased with the increased rate of destructuration [Figure 4.27(b) vs Figure 4.29(b) & Figure 4.27(e) vs Figure 4.29(e)].

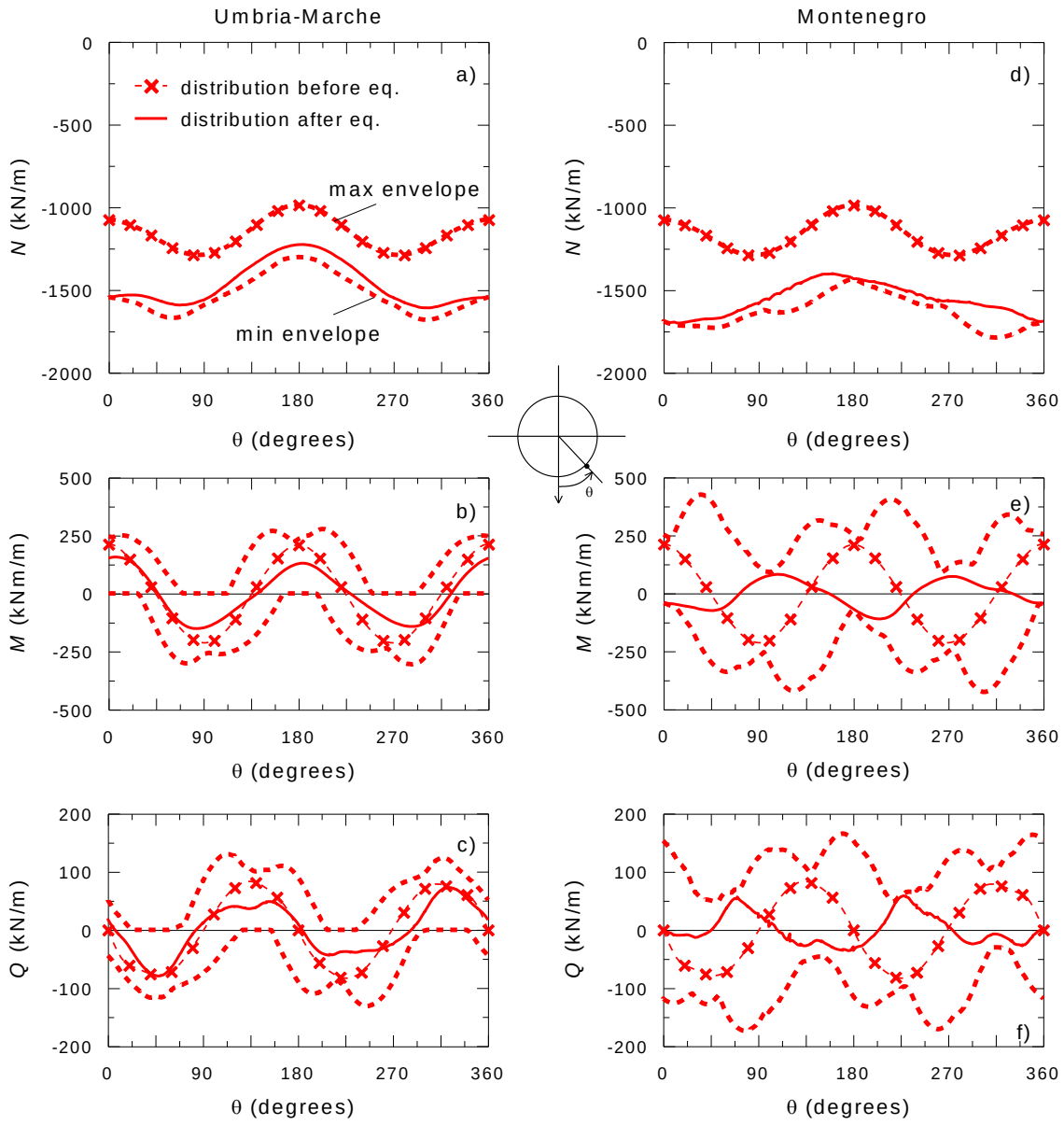

Figure 4.31 Distribution of hoop force (N), bending moment (M) and shear force (Q) before and after the: a–c Umbria-Marche; d–f Montenegro event for a destructuration rate k = 1.5

Moving to the dynamic behaviour of the tunnel, Figure 4.31 shows the distribution of hoop force N, bending moment M and shear force Q before and after the seismic

events as a function of the angle θ for a destructuration rate k = 1.5. The standard convention of structural analysis (i.e. compression is negative) is adopted here when presenting the results in terms of lining forces. The envelopes of maximum and minimum values of N, M and Q during the earthquake events are also shown in the same figure with dashed lines. For both input motions, the use of elasto-plastic models allows the prediction of permanent increments of hoop force (ΔN), bending moment (ΔM) and shear force (ΔQ) at the end of the motions due to the accumulation of plastic deformation in the soil deposit during the earthquakes, as already observed by other researchers Amorosi and Boldini (2009), Shahrour *et al.* (2010), Kontoe *et al.* (2011).

The lining forces predicted at the end of the Montenegro analyses (Figure 4.31 d-f) are larger than those recorded at the end of the Umbria-Marche simulations (Figure 4.31 a-c). This can be attributed to the higher accelerations induced by the Montenegro signal at tunnel location (see Figure 4.24 a & b). The corresponding distribution of lining forces obtained for a destructuration rate k equal to 5.0 are reported in Figure 4.32. With respect to the case of k = 1.5, higher hoop forces, bending moments and shear forces are induced in the tunnel, especially by the Montenegro earthquake, when a higher degree of destructuration is allowed to occur in the dynamic analyses.

Figure 4.33 shows, for the two destructuration rates assumed, the time histories of hoop force, bending moment and shear force increments during the Umbria-Marche event at θ equal to 0º, 45º, 90º, 135º and 180º, whereas the evolution with time of ΔN, ΔM and ΔQ predicted at the same lining locations throughout the Montenegro event is reported in Figure 4.34. The sensitivity analysis indicates that the assumption of a higher destructuration rate can alter the lining forces, causing a consistent increase of hoop force and bending moment increments accumulated in the tunnel lining during both earthquake scenarios. This rise is due to the softer response of the soil characterised by a higher rate of destructuration (Figure 4.7), which, in turn, causes the transmission of higher loads to the tunnel lining. The increase in the internal forces due to the higher destructuration, seems to be insignificant for Umbria-Marche earthquake, but were more apparent for the stronger Montenegro earthquake as evident from Figure 4.35 which shows the envelope of maximum and minimum hoop forces , bending moments and shear forces around the tunnel lining between the two destructuration rates for both earthquakes. The maximum increase in the lining forces

between k = 1.5 and k = 5.0 at any location point around the tunnel lining for Umbria-Marche earthquake are 44kN for the hoop force, 37kN-m for the bending moment and 17kN for the shear force while for Montenegro earthquake, the maximum increase in the lining forces are 93kN for the hoop force, 102kN-m for the bending moment and 56kN for the shear force. It shows a marked difference when the tunnel is subjected to a strong earthquake and illustrates the impact of destructuration in controlling the magnitude of the lining forces. In terms of peak values in the lining forces, the difference between the peaks of the two destructuration rates for Umbria-Marche earthquake are 29kN for the hoop force, 5kN-m for the bending moment and 10kN for the shear force while for Montenegro earthquake, the difference between peaks in the lining forces are 68kN for the hoop force, 20kN-m for the bending moment and 4kN for the shear force. In this case, these differences may not be substantial in terms of designing based on the peak values but nevertheless show the effect of destructuration in altering the magnitude of the lining forces. These differences may become more significant though in the case of a natural clay with a very high value of initial soil structure subjected to a very much stronger earthquake, i.e. earthquake with a very high energy content.

Simply scaling the ground motion records at the same peak acceleration can induce very different levels of shear strain in the deposit, thus affecting the propagation of the accelerations in the soil and, consequently, the forces in the tunnel lining. This is due to the importance of the spectral shape of the input motion in non-linear soil response, as PGA is not a good indicator of the strength and frequency content of the seismic motion as similarly observed by Patil *et al.* (2018). Instead the energy content of earthquake is a better gauge of the levels of shear strain in the deposit. Thus, the higher the energy content of earthquake, the higher the acceleration and associated shear strain induced in the soil and consequently higher forces in the tunnel lining.

Overall, the simulation results highlight the importance of the input motion frequency content in controlling the magnitude of shear strains induced by the earthquake in the tunnel and surrounding deposit. The parametric analysis points out a consistent increase in the hoop force, bending moments and shear force increments accumulated in the tunnel lining when a higher degree of destructuration is allowed to occur in the dynamic simulations.

4.6 Key point summary

Selection of an appropriate soil constitutive model is highly important for accurately predicting the seismic induced loads in the tunnel lining particularly for shallow tunnels in soft soil. The first study highlights the benefits of using an advanced kinematic hardening two-surface model as opposed to simple single-surface elasto-plastic model. The advanced model not only simulates correctly the hysteretic behaviour of the soil but also predicts reasonably the internal forces in the tunnel lining. Single surface models predominantly overestimate the tunnel lining forces with respect to two-surface models and can significantly overpredict the permanent increments of the lining forces at the end of the seismic action. This is due to the limited ability of single surface models to accumulate plastic strain during cycles, even with the introduction of Rayleigh damping, while advanced two-surface kinematic hardening models have an inherent plasticity which allows the accumulation of plastic deformation during the unloading stage in every cycle. Consequently, the use of advanced soil models for dynamic analysis, particularly for soft soils, can lead to smaller transverse forces in the tunnel lining resulting in more economic design. Thus, highlighting the benefits of using more advanced constitutive models in tunnel design practice.

The second study demonstrates the effect of destructuration in the seismic performance of the tunnel. The results show that the energy content of the earthquake highly influences the degree of structure degradation. The higher the energy content, the more pronounced the structure degradation induced in the soil. It also shows that the higher degree of destructuration allowed during a seismic event results to a softer behaviour of the soil leading to the development of higher shear strains around the tunnel and the consistent accumulation of excess pore water pressures in the soil deposit. These, in turn, cause the transmission of higher loads to the tunnel lining. Thus, it highlights the importance of the input motion frequency content in controlling the magnitude of shear strains induced by the earthquake in the tunnel and surrounding deposit. The parametric study has also proven the assumption that a higher destructuration rate can alter the lining forces, causing a consistent increase of hoop force, bending moment and shear force increments accumulated in the tunnel lining during earthquake. The increase in the tunnel lining forces were found to be more significant when the tunnel is subjected to an earthquake with a

higher energy content. All these highlight for the first time the importance of considering structure degradation in the assessment of the dynamic response of shallow tunnels constructed in structured clayey deposits as it can increase the magnitude of the tunnel lining forces. However, the increase caused by destructuration may not be substantial enough to alter the overall tunnel design, as demonstrated by the case study, but nevertheless show its potential in altering the magnitude of the lining forces.

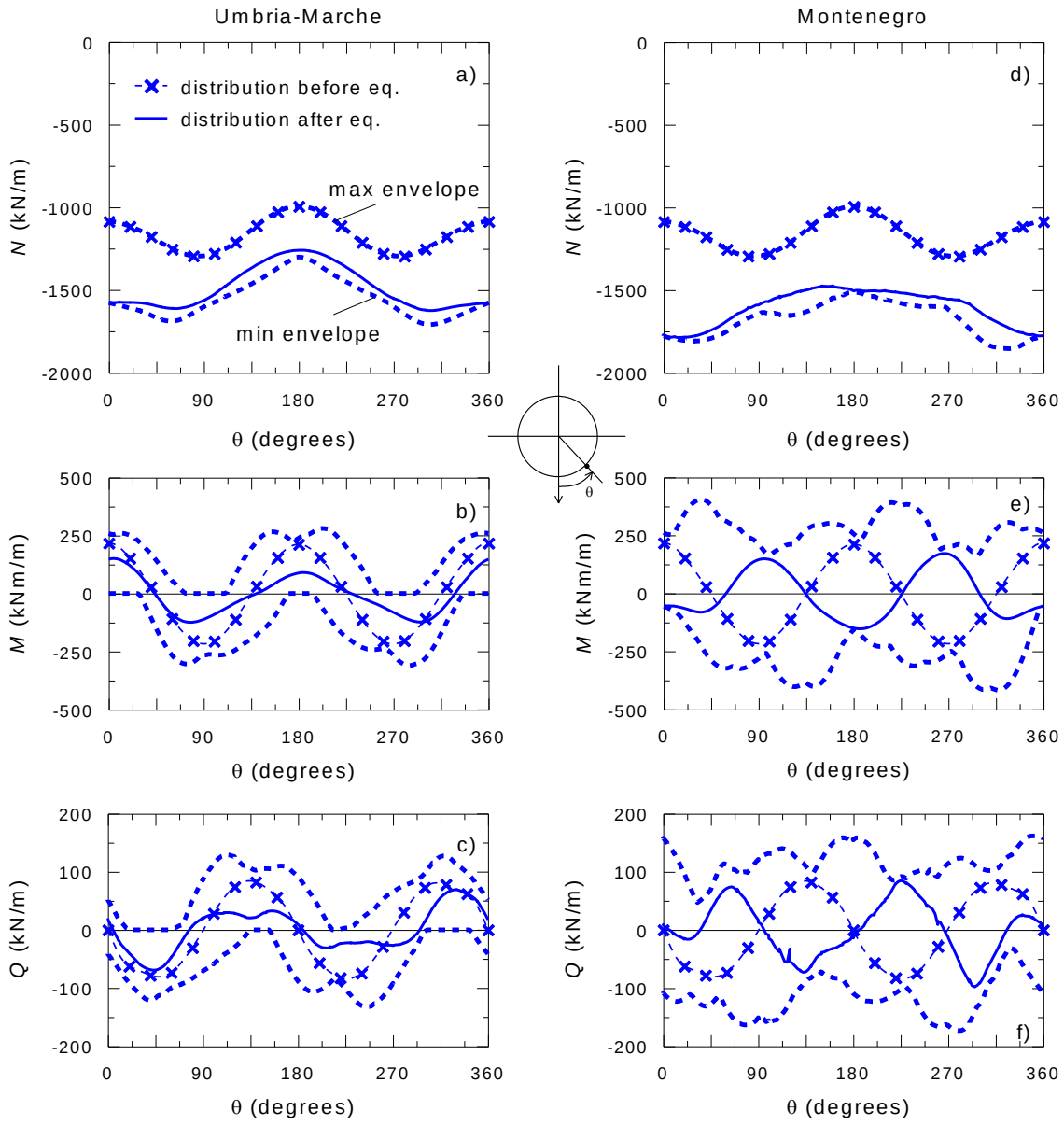

Figure 4.32 Distribution of hoop force (*N*), bending moment (*M*) and shear force (*Q*) before and after the: a–c Umbria-Marche; d–f Montenegro event for a destructuration rate k = 5.0

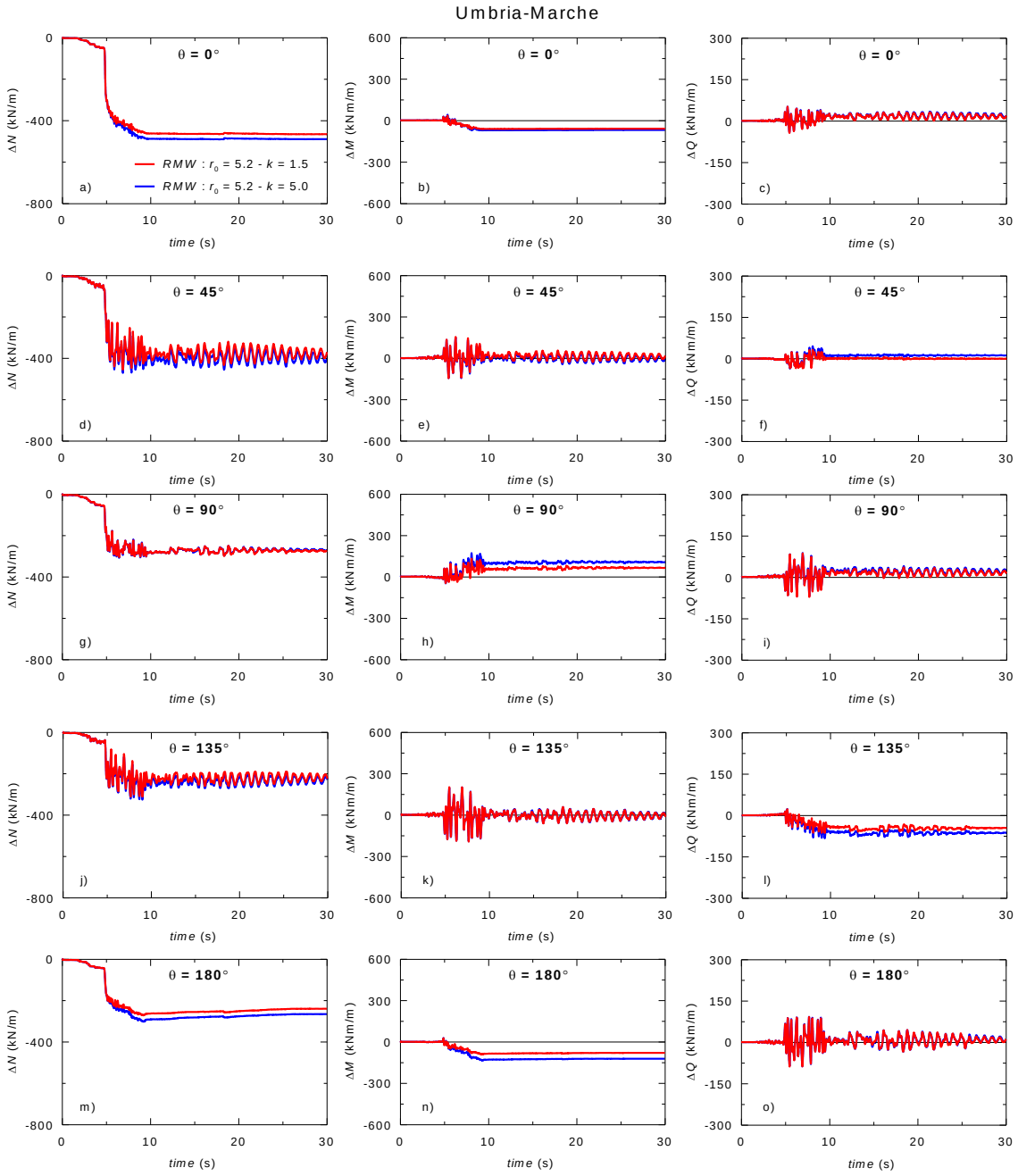

Figure 4.33 Influence of structure degradation rate on the time histories of hoop force, bending moment and shear force increments during the Umbria-Marche event for: a-c $\theta = 0^{o}$; d-f $\theta = 45^{o}$; g-i $\theta = 90^{o}$; j-l $\theta = 135^{o}$; m-o $\theta = 180^{o}$

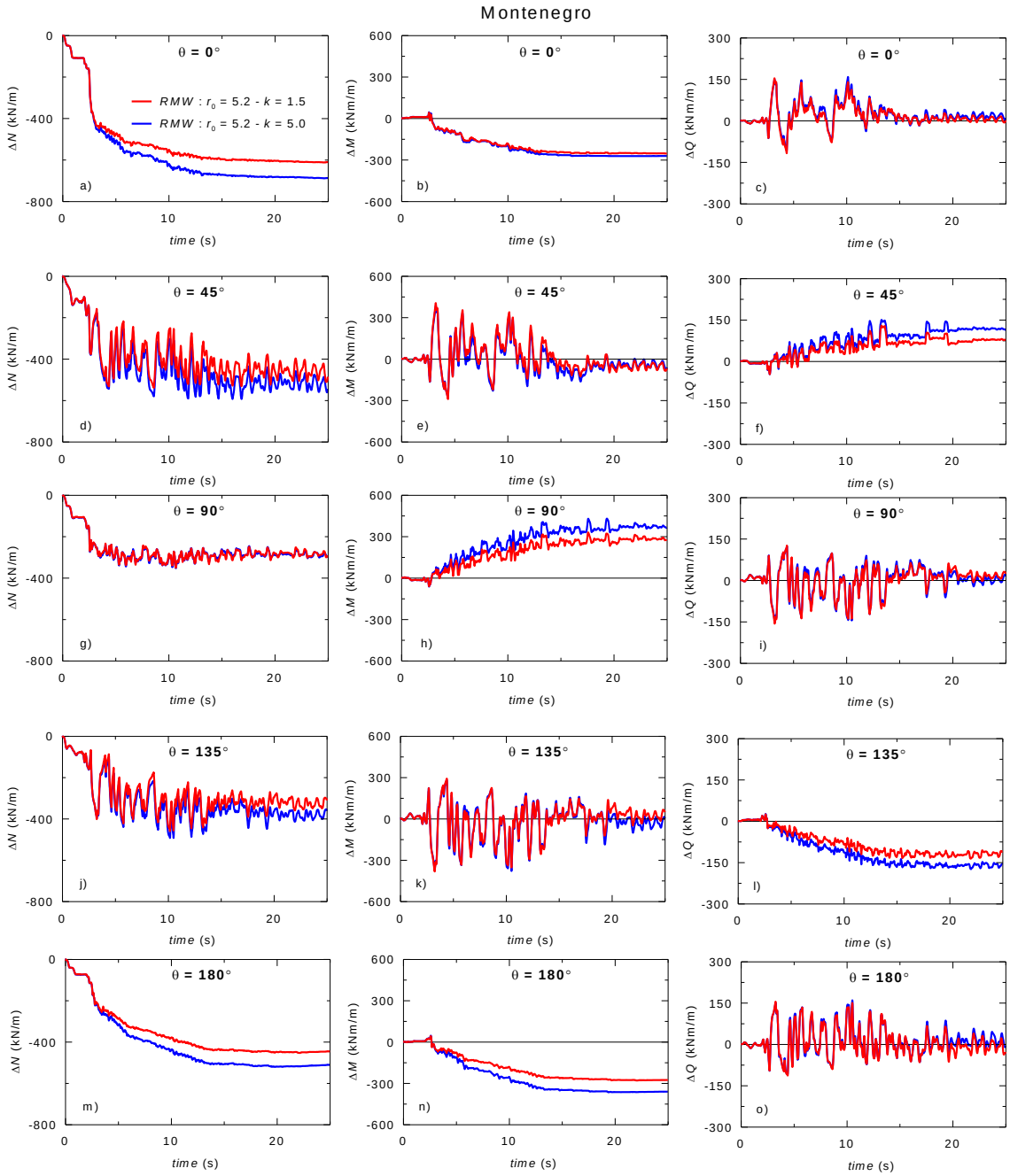

Figure 4.34 Influence of structure degradation rate on the time histories of hoop force, bending moment and shear force increments during the Montenegro event for: a-c $\theta = 0^{o}$; d-f $\theta = 45^{o}$; g-i $\theta = 90^{o}$; j-l $\theta = 135^{o}$; m-o $\theta = 180$

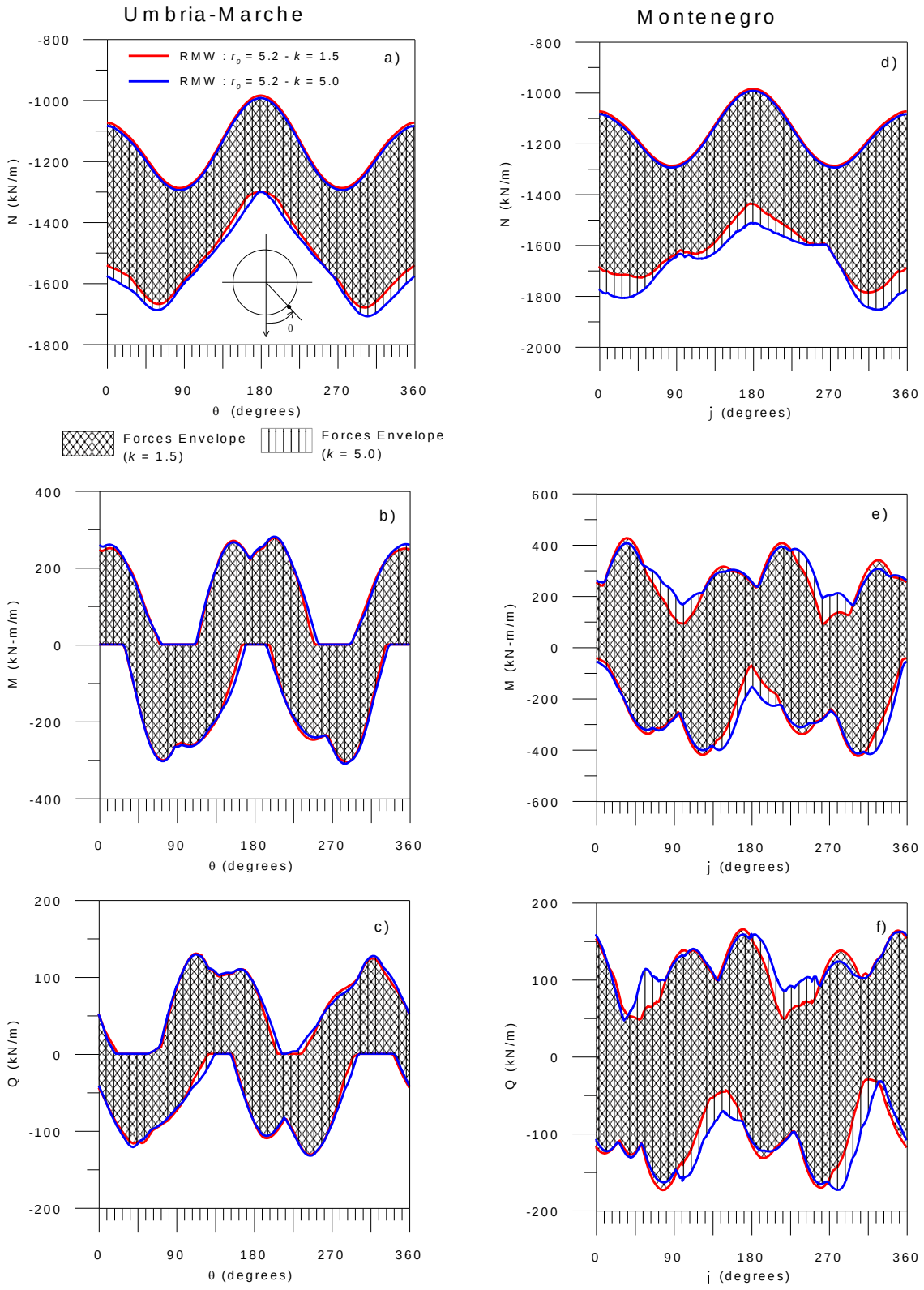

Figure 4.35 Maximum and minimum forces envelope in the tunnel lining during the: a–c Umbria-Marche; d–f Montenegro event for two different rates of soil destructuration

Chapter 5. 3D numerical analysis of seismic behaviour of circular tunnels in structured clay

5.1 Introduction

Current research extensively uses 2D modelling to simulate tunnels under seismic loading to predict their response. However, 2D approaches require simplifications in order to capture 3D effects, such as longitudinal axial and bending responses as well as construction sequence, which may underestimate tunnel lining forces. Furthermore, seismic wave propagation has an arbitrary direction with respect to the axis of the structure that causes multi-directional loading for the soil deposit and the tunnel lining. With the availability of high-performance computing, 3D modelling is considered nowadays to be a better approach in predicting the spatial behaviour of tunnels during seismic actions. In addition, traditional constitutive models developed within the framework of linear-visco-elasticity and elasto-plasticity are not able to capture the complex mechanical behaviours exhibited by clayey soils subjected to earthquake loading, particularly structure degradation, thus the need to adopt advanced soil constitutive models such as RMW.

In this chapter the dynamic performance of a shallow circular tunnel in a natural clay deposit subjected to multi-directional earthquake loading is analysed by means of a 3D non-linear FEM approach. The 3D FEM model is firstly validated against a simplified 2D numerical model to determine the optimal dimensions to the viscous lateral boundaries. To account for the effect of soil structure degradation, the kinematic hardening model developed for natural clays by Rouainia and Wood (2000) has been employed for the rest of the numerical simulations. The results from the numerical simulations are compared between 2D vs 3D. Most importantly, the effects of multi-directional earthquake loading are investigated by comparing the results of the 3D FEM simulations when the N-S component of the input motion is imposed at bedrock level either by just itself or simultaneously with the E-W component.

5.1.1 *3D numerical model*

For ease of comparison, the 2D FEM model developed in Chapter 4 has been adopted in this chapter. To extend the 2D model into a 3D model, a longitudinal axis orthogonal

to both axes of the 2D plane has been created. In this case, the orthogonal axis is parallel with the tunnel axis in the longitudinal direction as shown in Figure 5.1. The numerical model was simulated in PLAXIS 3D (Brinkgreve *et al.*, 2015) which is the 3D version of PLAXIS 2D.

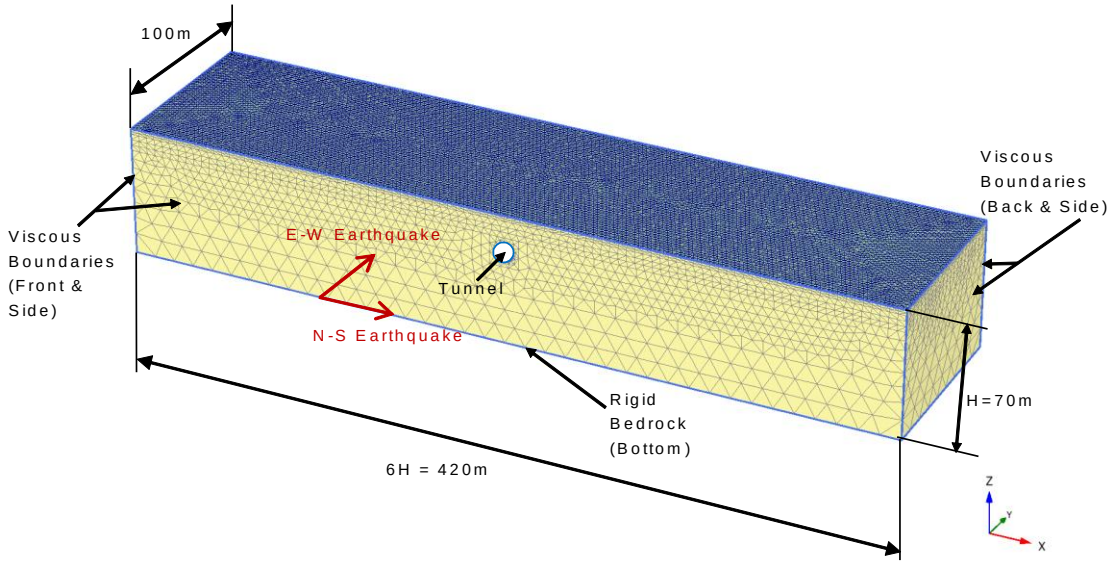

Figure 5.1 3D FEM model and lateral boundary conditions for the dynamic simulations

The FEM model has been discretised with a total number of 128374 linear strain tetrahedral elements. The tetrahedral element has 10 nodes, 3 translational degrees of freedom at each node and 4 integration (Gauss) points designated by x in Figure 5.2.

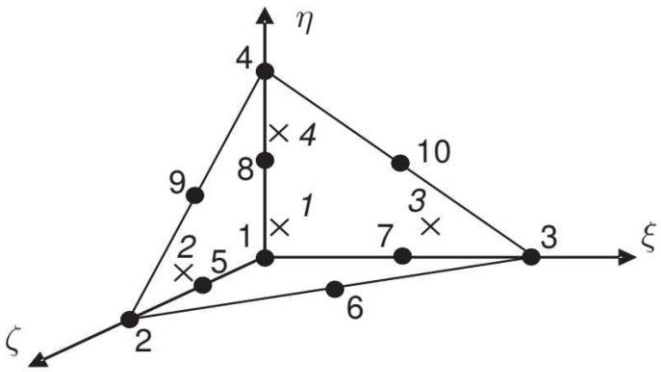

Figure 5.2 10-node tetrahedral element (Brinkgreve *et al.*, 2015)

This type of element provides a second-order interpolation of displacements. It is the best shape to model complex geometry domain and fits very well with arbitrary shaped geometries with little distortion of the mesh. Moreover, the computational cost for assembling the global stiffness matrix for tetrahedral elements is lower

because tetrahedra use exact formulations without any integration to get the same characteristics of a hexahedral element. The general equations presented in Section 4.1 to calculate the displacement within the element (u) in relation to the nodal displacements (v) expressed in Equation 4.1, the relationship of strain ε to nodal displacements v shown in Equation 4.2 and nodal displacements induced by the vector of nodal forces (P) expressed in Equation 4.3, also apply in this case. The shape functions of these 10-node volume elements are as follows:

$$N_1 = (1-\xi-\eta-\zeta)(1-2\xi-2\eta-2\zeta);\ N_2 = \zeta(2\zeta-1);\ N_3 = \xi(2\xi-1);$$
$$N_4 = \eta(2\eta-1);\ N_5 = 4\zeta(1-\xi-\eta-\zeta);\ N_6 = 4\xi\zeta;\ N_7 = 4\xi(1-\xi-\eta-\zeta);$$
$$N_8 = 4\eta(1-\xi-\eta-\zeta);\ N_9 = 4\eta\zeta;\ N_{10} = 4\xi\eta \qquad 5.1$$

To ensure that the seismic wave is transmitted accurately through the finite element mesh, the vertical distance between adjacent element nodes has been limited to satisfy the condition recommended by Kuhlemeyer and Lysmer (1973) similar to the 2D model. Standard boundary conditions (i.e. all lateral boundaries fixed in horizontal direction but free in vertical direction) are adopted for the static analyses, while the bottom of the model is assumed rigid. The ground water level is assumed coincident with the ground surface.

Whereas in the 2D model, tied-nodes lateral boundary conditions were employed for the dynamic simulations, the 3D model utilised standard viscous boundaries (see Figure 5.1) to absorb outgoing wave energy and prevent reflections at all the lateral boundaries during the dynamic simulations. This change in boundary conditions is due to unavailability of tied-nodes condition in PLAXIS 3D software. Using the viscous boundaries though has been found to satisfactorily absorb most of the incident energy, reproduce the free-field response near the lateral boundaries and achieve reasonable response of the tunnel compared to free and fixed boundaries through works by Fattah *et al.* (2015), Amorosi and Boldini (2009), Sliteen *et al.* (2011) and Gu *et al.* (2007). The standard viscous boundary developed by Lysmer and Kuhlemeyer (1969) is the most versatile boundary condition for seismic analysis (Nielsen, 2008) and remains the most widely used one. It can be applied at the base and at the lateral

boundaries of the model. The fundamental principle behind this method is the application of a traction condition at a free artificial boundary which dictates any reflected stresses to be zero. The viscous boundary is implemented as series of discrete dashpots oriented normal and tangential to the boundary (Figure 5.3) in finite element codes. In essence, the viscous boundary effectively absorbs body waves approaching the boundary at normal incidence. Thus, this boundary type is perfect for 1D propagation of body waves, however, for oblique angles of incidence, or for surface waves, total absorption cannot be achieved. For this reason, Kontoe (2006) suggested to keep the boundary significantly placed farther away from the source of excitation or area of interest (e.g. around a tunnel) to improve the accuracy of the results. Generally, at such large distance the direction of body waves as they approach the boundary propagate one-dimensionally normal to the artificial boundary (Wolf, 1989). As a result, a significantly wider mesh might be needed to obtain due accuracy. Use of viscous boundaries is very popular as it gives acceptable accuracy for low computational cost but it is more suitable for problems where the dynamic source is inside the mesh. The application of viscous boundaries at all lateral boundaries in a similar 3D tunnel model to simulate effects of the asynchronism of ground motion on the longitudinal behaviour of a continuous circular tunnel has been successfully implemented in PLAXIS 3D by Fabozzi *et al.* (2018).

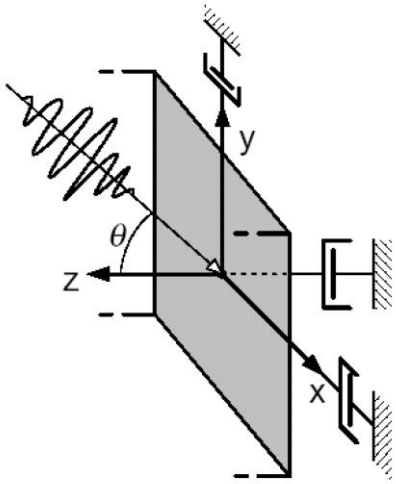

Figure 5.3 Viscous damping boundary concept (Ross, 2004)

The 3D model utilised a normally consolidated (i.e. *OCR* = 1.0) Avezzano clay material, a highly structured Italian clay, as the soil medium which has been calibrated and

discussed in Section 4.2.2. This soil material has a coefficient of earth pressure at rest K_0 equal to 0.5 and a unit weight of 18kN/m^3. Consistently with the Avezzano clay plasticity index of 10%, the dimensionless stiffness parameters A_g, n_g and m_g used to calculate the initial shear modulus G_0 by Viggiani and Atkinson's equation have been set equal to 2150, 0.78 and 0.22, respectively. The kinematic hardening model RMW developed by Rouainia and Wood (2000) has been employed to simulate the cyclic response of natural clay materials subjected to structure degradation. The soil parameters resulting from the calibration and adopted in the FEM non-linear dynamic simulations is presented in Section 4.2.2 and reproduced below.

Material	λ^*	κ^*	M	v	R	B	ψ	η_0	r_0	A^*	K
Avezzano Clay	0.110	0.016	1.42	0.25	0.40	15.0	1.45	0.0	5.20	0.2	1.5

Table 5.1 RMW model parameters for Avezzano clay

Similar to 2D, the tunnel lining has been modelled as a linear visco-elastic plate material assuming an axial stiffness (EA) equal to 19GPa, a flexural stiffness (EI) equal to 0.4GPa, Poisson's ratio equal to 0.25 and damping ratio equal to 5%. The soil-tunnel interface was assumed rigid, i.e. the strength of the interface is the same as the soil. The interface parameters were derived from the properties of the soil medium due to the arbitrary nature of the lining material used in the studies. The derivations of those parameters were discussed in detail in Chapter 4 Section 4.4.

The signals recorded at the Ulcinj-Hotel Albatros station during the Montenegro earthquake in April 1979 which reasonably matches the response spectrum provided by Eurocode 8 (EC8) for soil type A (rock or other rock-like geological formation) are adopted in the analysis. The time histories of the N-S and E-W components of the earthquake and their response spectra are illustrated in Figure 5.4. The two components of the event are filtered to prevent frequencies higher than 10Hz and scaled up to 0.30g to simulate a strong motion occurring at the site. Table 5.2 gives general information about the two input motions.

Earthquake	Component	Magnitude (M_w)	Arias intensity I_a (m/s)	Epicentral distance (km)	Duration T_{90} (s)	a_{max} (g)	v_{max} (m/s)
Montenegro (1979)	N-S	6.9	0.7289	19.7	12.22	0.181	0.176
	E-W	6.9	0.7289	19.7	12.22	0.224	0.263

Table 5.2 Main characteristics of the selected earthquakes

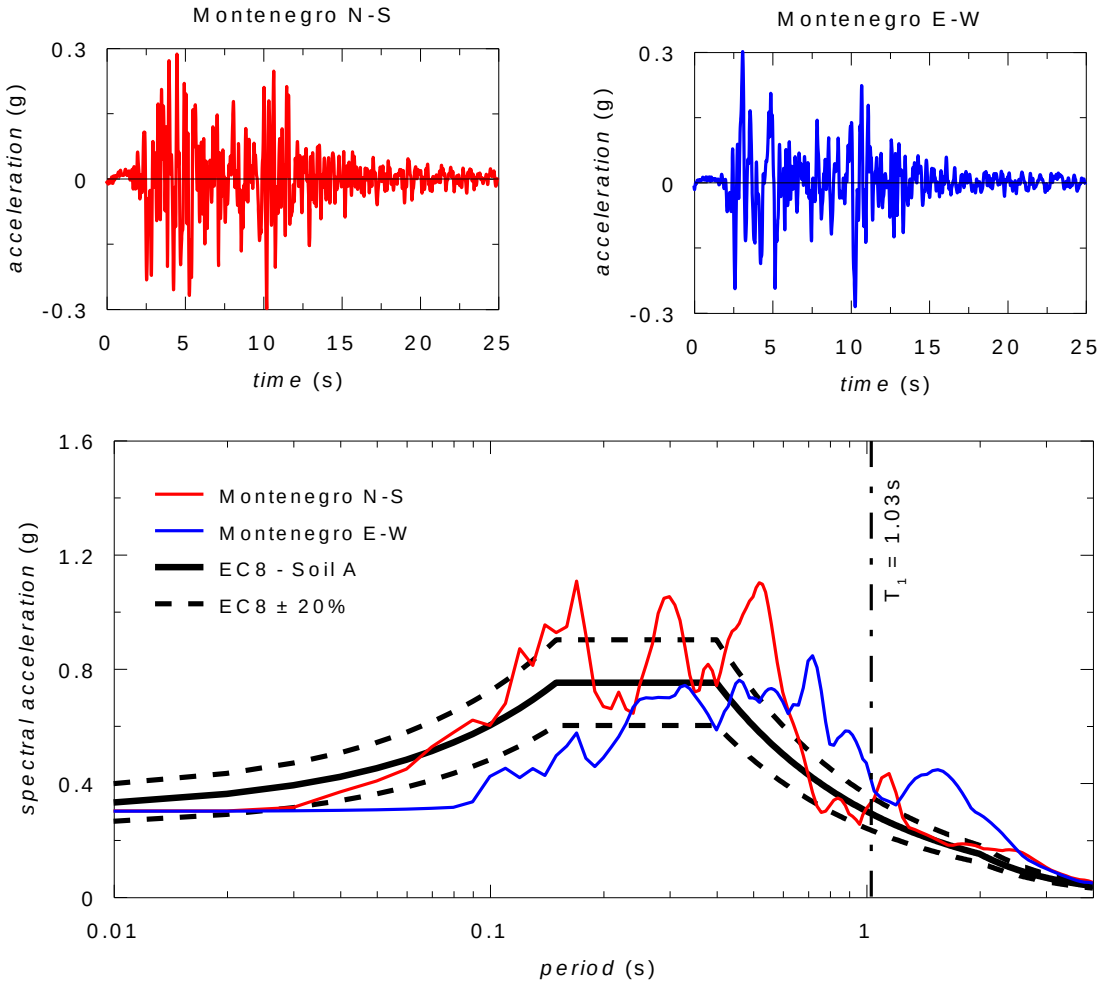

Figure 5.4 Scaled input motion acceleration time histories and comparison between the normalised response spectra of the scaled input (bedrock) records with the Eurocode 8 (EC8) design spectra for Ground type A

To take into account the effects of pre-seismic stress conditions, a static analysis in an undrained condition is initially performed to simulate the tunnel excavation and the installation of the tunnel lining. Similar to the 2D model and as explained in Chapter 4 Section 4.4.1, a contraction equivalent to 0.8% volume loss, deemed to be acceptable for a satisfactory performance of the tunnel excavation [e.g. Mair (1996)], is imposed. The dynamic analyses are then carried out under undrained conditions adopting a time step corresponding to that of the earthquake input signals. The scaled acceleration time histories are imposed at the rigid bedrock level, i.e. at the base of the model. The

N-S component of the earthquake acceleration is imposed in the transverse x-direction of the model, while the E-W component is applied in the longitudinal y-direction. 3D FEM simulations are carried out by applying only the N-S component of the input motion and then the results are compared with those obtained by imposing the two horizontal components simultaneously.

5.1.2 *Determination of FEM model dimensions*

To ensure that the boundary is significantly far enough from the tunnel to simulate properly the free-field conditions at the edges of the model and avoid the problem of the fictitious reflection of the outgoing waves on the boundaries, parametric studies of the FEM model's size have been conducted by the author to optimise both the lateral transverse and longitudinal dimensions as discussed below. For these parametric studies, an equivalent single surface MCC model of Avezzano clay has been used to speed up the computer simulation process and thus reduce the amount of time spent in the simulations of the FEM models particularly those in 3D. To compensate for the lack of hysteretic damping provided by the simpler constitutive model, Rayleigh damping equal to 5%, associated with the frequencies of 0.2 and 10Hz, previously discussed in Section 4.4.3, has been introduced to the soil model during the MCC dynamic analyses.

Optimisation of distance between transverse lateral boundaries

To determine the optimal transverse lateral distance of the 3D FEM model between viscous vertical boundaries, 2D FEM models were simulated in the dynamic condition using the MCC model by varying lateral distances to the boundaries from 2H to 8H, where H is the depth of the soil model. A 1D soil column FEM model adopting 5m wide mesh is also created characterised by tied-nodes boundaries to represent an ideal free-field response for comparison purposes. The free-field maximum acceleration vs depth results were compared with the results from 1D free-field soil column as shown in Figure 5.5 (a). The graph shows that at lateral distance of 6H, the acceleration-depth curve satisfactorily agrees with the 1D soil column. Increasing it further to 8H does not give much advantage. 6H is then considered as a good compromise between accuracy and optimal computational time and was used for the 3D FEM simulations. The choice of 6H is further justified by the plots of the shear strain time history at depths z=5m,

15m (i.e. approximately at tunnel crown), 25m (i.e. approximately at tunnel invert), 35m, 45m and 55m from ground level (Figure 5.6) and the maximum shear strain level along the soil depth in free-field conditions [Figure 5.8 (a)] which show that 6H conforms closest to 1D soil column. These findings validate the results of the parametric study on the optimal transverse width of the 2D FEM model in Section 4.4.2 and sustain the recommendations suggested by Amorosi *et al.* (2010).

Optimisation of distance between longitudinal lateral boundaries

Adopting 6H as the width of the transverse lateral boundaries and utilising the same MCC model, a similar approach was undertaken on the longitudinal lateral boundaries of 3D FEM models, in order to reproduce free-field conditions at the longitudinal edges, by varying the distance between the viscous vertical boundaries from 50m to 150m. The results of the free-field maximum acceleration vs depth were compared with the results from the 2D FEM model as shown in Figure 5.5 (b). The graph shows that the 3D results obtained for a length of 100m is closer and in better agreement with the 2D output. These results have been substantiated by the plots of the shear strain time history at depths z=5m, 15m, 25m, 35m, 45m and 55m from ground level (Figure 5.7) and the maximum shear strain level along the soil depth in free-field conditions [Figure 5.8 (b)] which show conformance of 100m length to 2D outcome. Thus, a 100m long 3D FEM model is adopted. At first, the longer model (i.e. 150m long model) was expected to better match the 2D results as the distance between the lateral boundaries are farther and therefore, the lateral boundaries have lesser influence on the numerical results. However, 3D models have very high demand on the memory requirements of the software and the computer particularly for large models. In order to keep within the limitations of the computing capacity, the software limits the number of generated elements. As a consequence, the generated element meshes become coarser for longer models, thus, compromising the accuracy of the results leading to lesser agreement with the 2D output. Hence, the shorter model (i.e. 100m), in this case, provided a good balance between size and accuracy while achieving free-field conditions near the longitudinal boundaries.

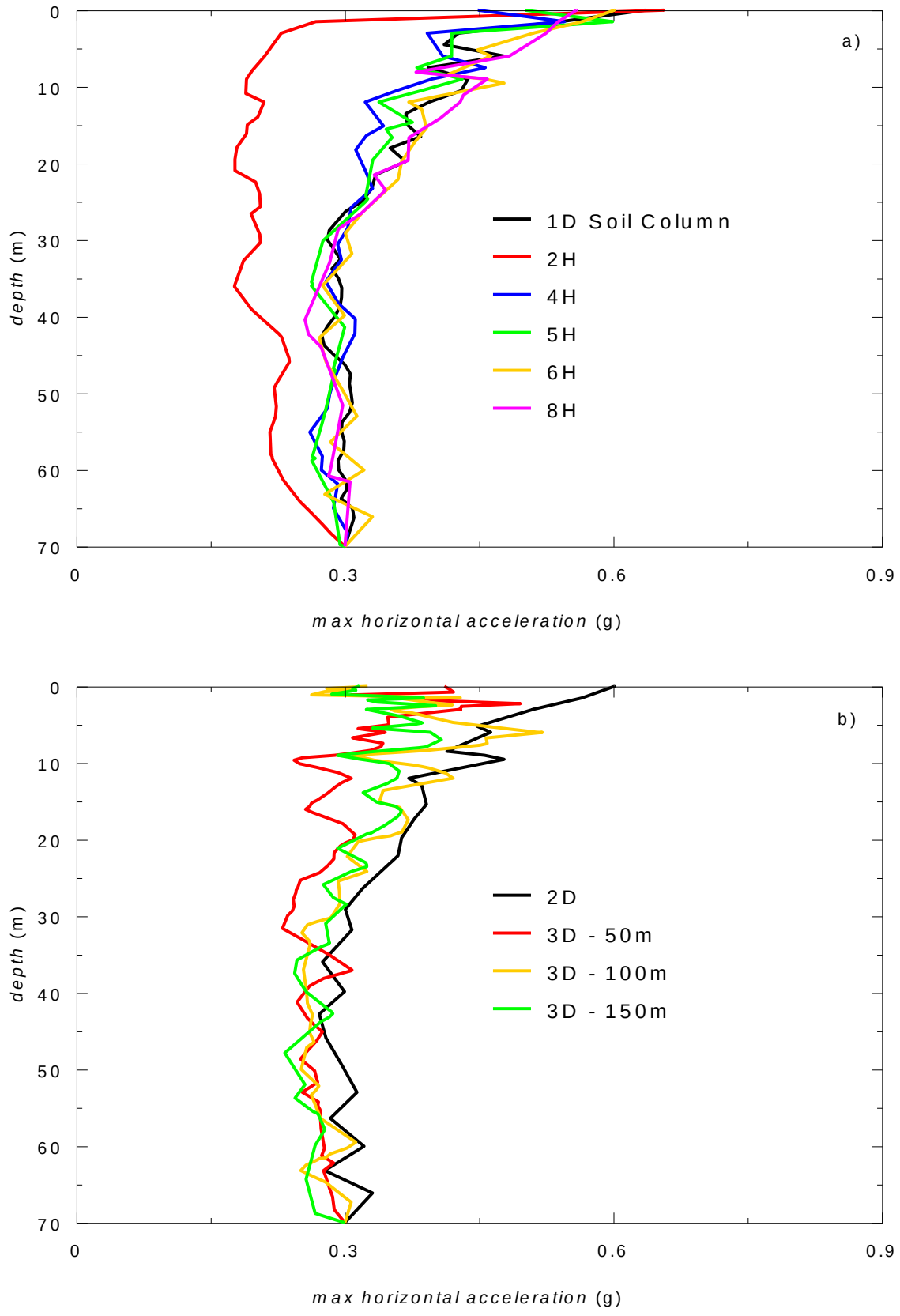

Figure 5.5 Profiles of max accelerations recorded in free-field conditions of the FEM model for (a) different lateral dimensions and (b) different longitudinal dimensions

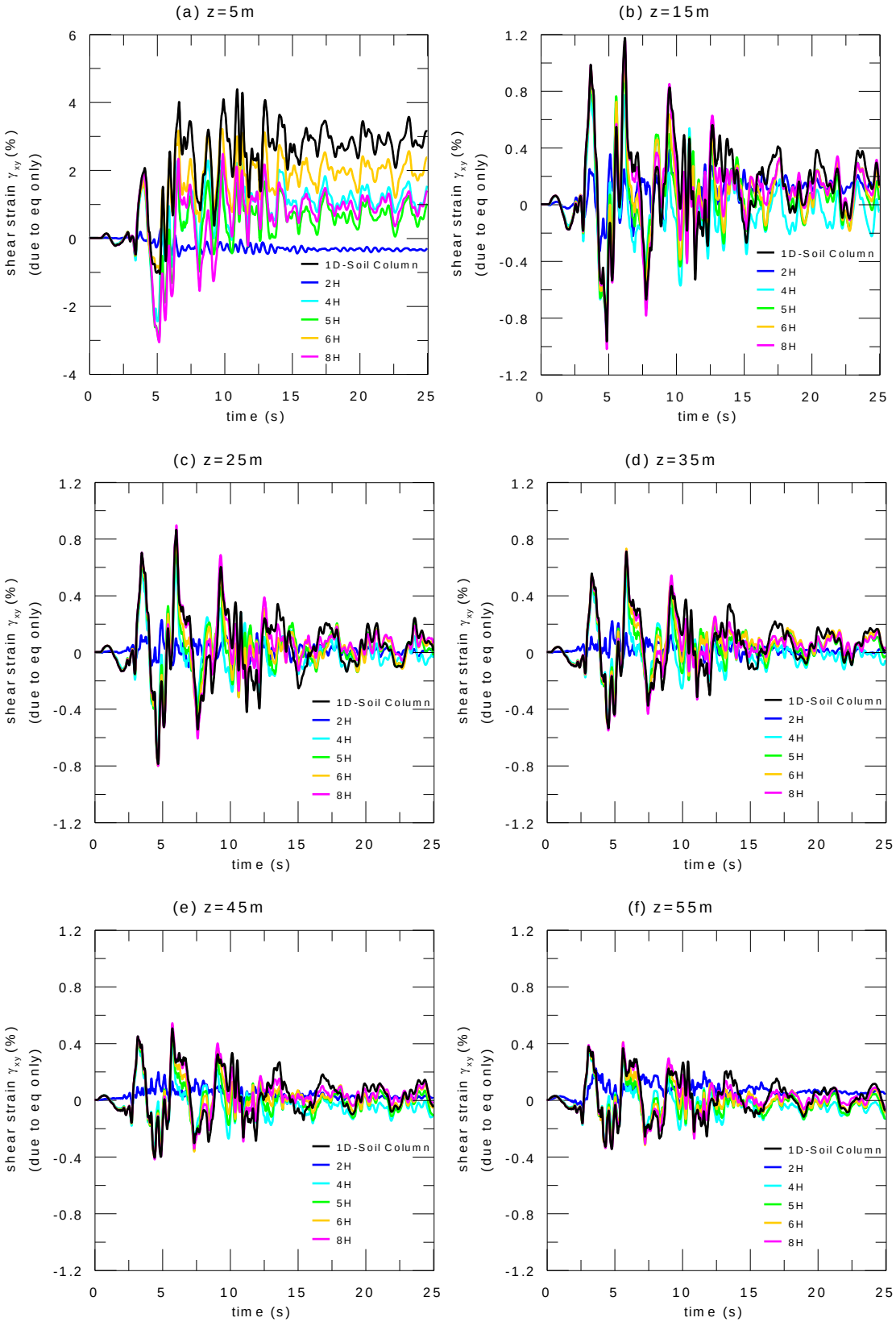

Figure 5.6 Shear strain time history at depths z in free-field conditions: (a) 5m; (b) 15m; (c) 25m; (d) 35m; (e) 45m; (f) 55m for different lateral dimensions

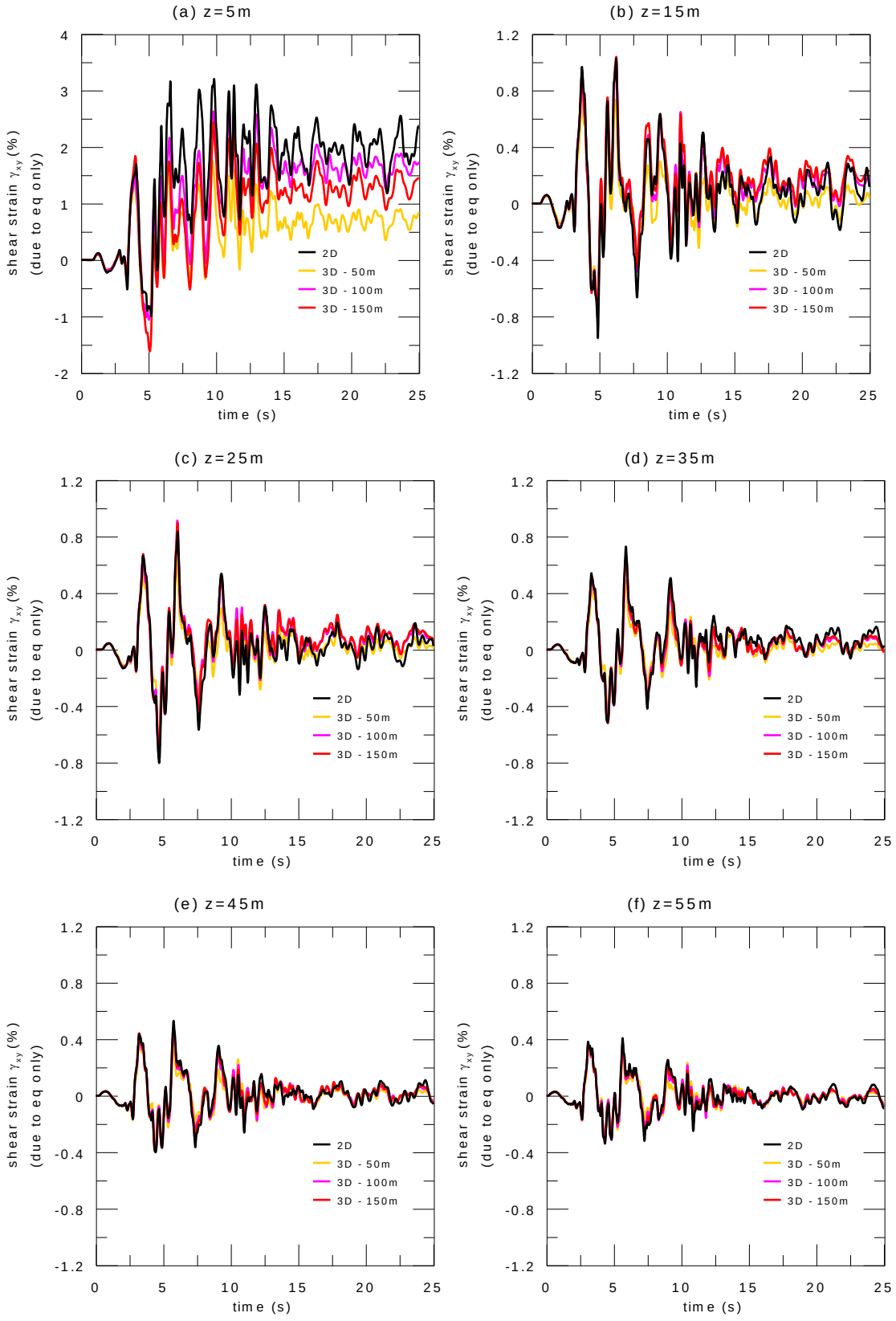

Figure 5.7 Shear strain time history at depths z in free-field conditions: (a) 5m; (b) 15m; (c) 25m; (d) 35m; (e) 45m; (f) 55m for different longitudinal dimensions

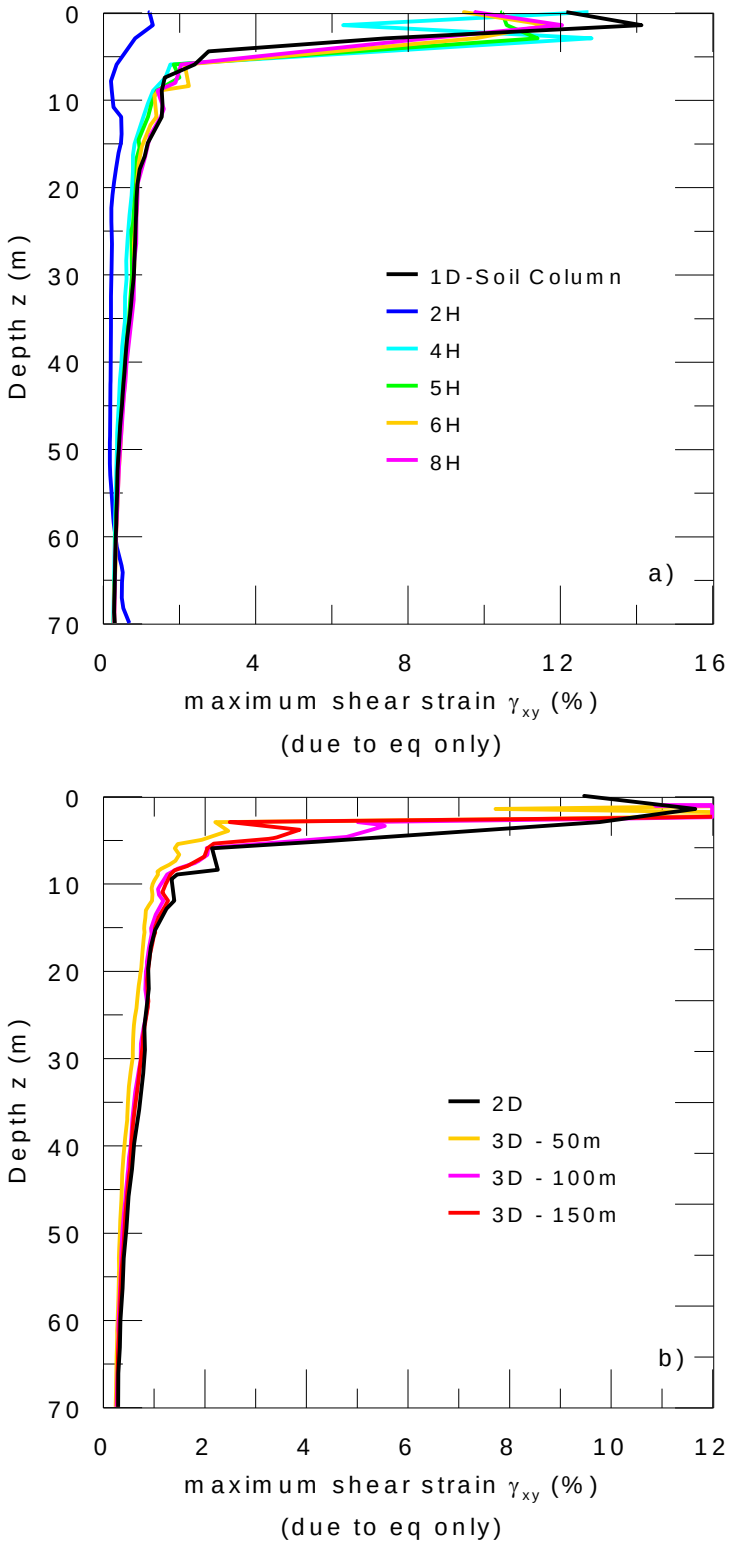

Figure 5.8 Maximum shear strain profile in free-field conditions for (a) different lateral dimensions and (b) different longitudinal dimensions

5.1.3 *Validation of the 2D and 3D FEM models with standard viscous boundaries using the advanced soil model RMW*

In Kontoe (2006), the standard viscous boundary failed to reproduce the free-field response which led to a serious underestimation of the response in the near field. The

failure was attributed either to the proximity of dashpots to the seismic excitations, especially at the bottom corners of the mesh or proximity of the boundaries from the area of interest (e.g. tunnel). The consequence is more apparent when using advanced non-linear kinematic hardening soil constitutive model (e.g. RMW) than using a simpler elasto-plastic soil model (e.g. MCC). This can significantly affect the results of the tunnel lining forces. It was found that the performance of viscous boundaries significantly improved when the source of excitation or the area of interest was placed farther away from the boundaries.

To ensure that the assumed lateral distance of the viscous boundaries from the tunnel is far enough and no influence from the boundaries has been achieved, the results of the tunnel lining forces from the 2D RMW model with tied-nodes boundary conditions at a lateral distance 5H in Chapter 4 which successfully reproduced the free-field response have been compared with those results from a 2D RMW model with viscous boundary conditions at a lateral distance 6H. For guidance, the sign convention (+ for positive direction) of all the tunnel lining forces is shown in Figure 5.9. Figure 5.10 shows the distribution of the predicted hoop force, transverse bending moment and transverse shear force in the tunnel lining for both models at the end of the seismic event including the minimum and maximum force envelope as a function of the angle θ, defined positive in the anti-clockwise direction. The plots of the tunnel lining forces indicate satisfactory agreement between the results of the two boundary conditions. Thus, the lateral distance of 6H satisfies the condition at which the viscous boundaries are sufficiently far enough from the tunnel to cause any unwanted influence on the results of the tunnel lining forces.

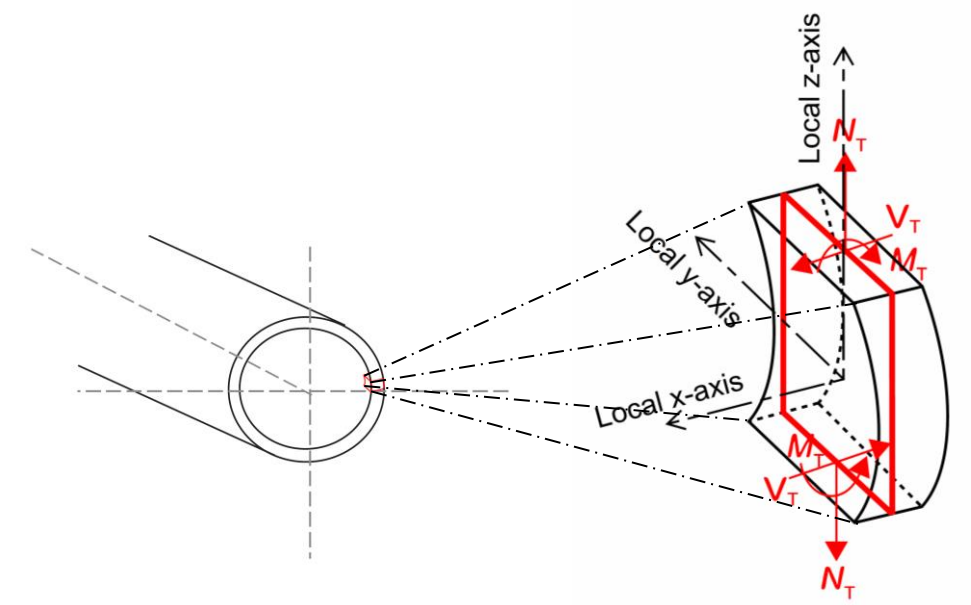

c) Positive Hoop Force N_T, Bending M_T & Shear V_T

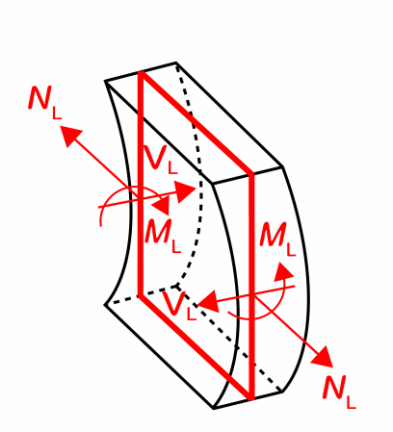

b) Positive Longitudinal Axial N_L, Bending M_L & Shear V_L

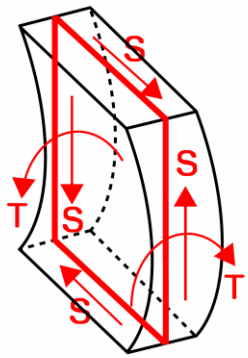

a) Positive Torsion T & In-plane Shear S

Figure 5.9 Sign Convention (+ for positive direction) of (a) transverse forces; (b) longitudinal forces and (c) torsion & in-plane shear in the tunnel lining

Further to the discussion above, a 1m strip of the 3D FEM model with viscous boundaries has been compared to the 2D FEM with viscous boundaries to ensure compatibility between the 2D and 3D models. The results of the predicted hoop force, transverse bending moment and transverse shear force in the tunnel lining at the end of the seismic event including the minimum and maximum force envelope as a function of the angle θ between the two models as shown in Figure 5.10 are in satisfactory agreement, thereby validating the 3D FEM model.

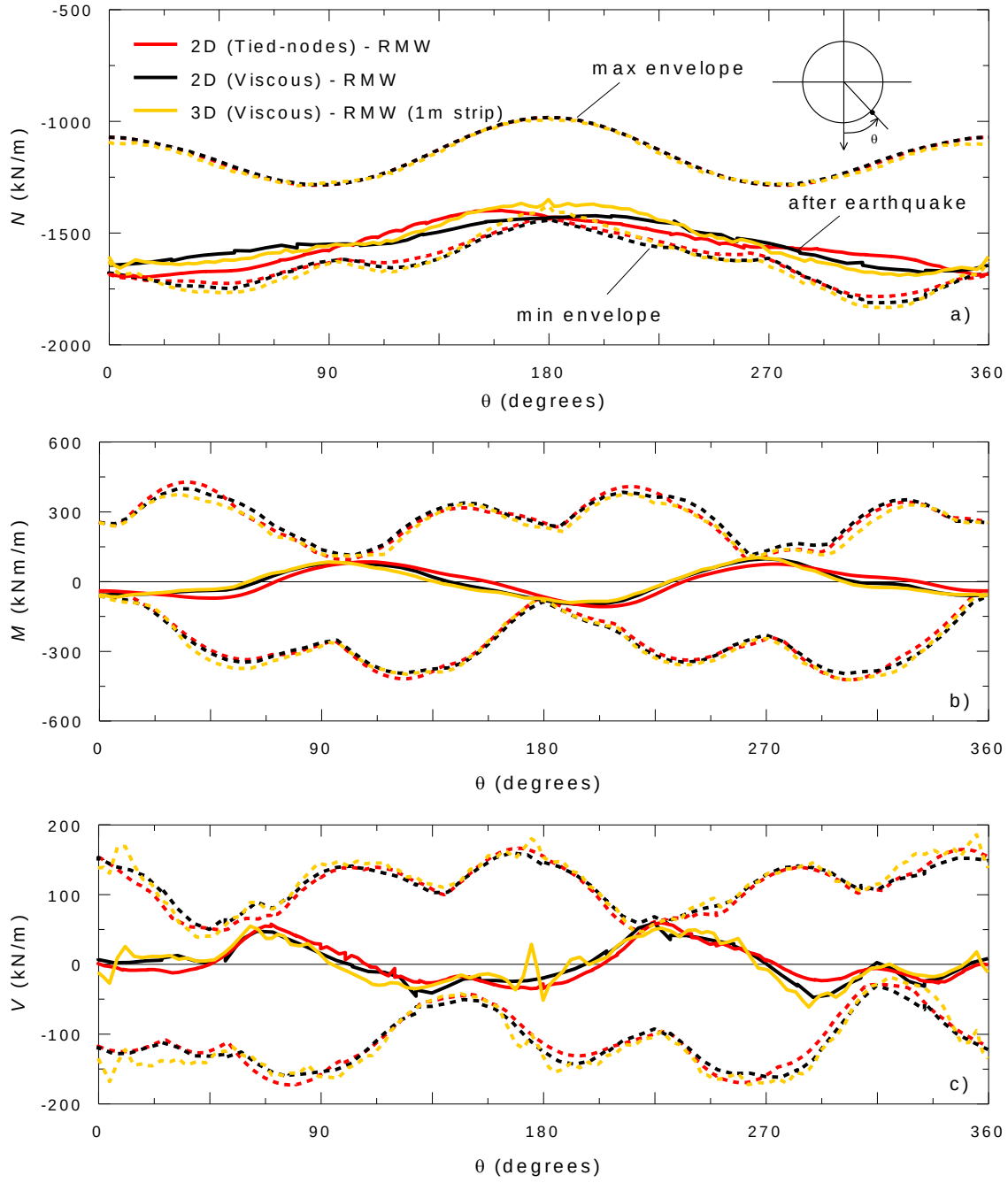

Figure 5.10 Distribution of maximum and minimum (a) hoop force; (b) transverse bending moment and (c) transverse shear force between tied-nodes and viscous boundary conditions

5.1.4 *Influence of the boundary conditions*

The effect of the boundaries is illustrated in Figure 5.11 on the section profiles of the effective mean stress *p'*. With tied-nodes boundaries shown in Figure 5.11 (a), the free-field response is readily apparent and almost constant from about midway between the tunnel and the lateral boundary to the boundary. Whereas, with standard viscous boundaries shown in Figure 5.11 (b), the free-field response occurred about halfway from the tunnel to the lateral boundary, but the profile starts to vary as it

draws nearer to the boundary. In this case, a disturbance is significantly visible around the bottom corners of the mesh as similarly observed by Kontoe (2006). This is due to the close proximity of the dashpots to the seismic source (i.e. bottom of the mesh model) causing spurious waves to reflect back from these locations. It is known that viscous boundaries can only achieve perfect absorption for angles of incidence greater than 30° (when the angle is measured from the direction parallel to the boundary). It implies that at these locations, the wave approaches the boundary at a sharper angle of incidence preventing full absorption of outgoing wave energy. The disturbance is also visibly more significant when using advanced non-linear kinematic hardening soil constitutive model (e.g. RMW) than using simpler elasto-plastic soil model (e.g. MCC) as shown in Figure 5.11 (c).

This highlights one of the common pitfalls in using viscous boundaries and reinforced the need to move the boundary as far as possible from the tunnel to eliminate the influence of the viscous boundary conditions on the response of the tunnel. It also demonstrates in this case study that the use of tied-nodes boundaries are generally more effective in absorbing outgoing wave energy during the dynamic simulations. It means that a smaller model can already reproduce the free-field response using this type of boundary conditions thereby saving computational time. However the option to choose tied-nodes boundary is only available in PLAXIS 2D. Having nodes in the corners of the model tied together and kept exactly on the same elevation level has been found to be difficult to achieve in PLAXIS 3D. For these reasons, it has not been implemented in PLAXIS 3D at all.

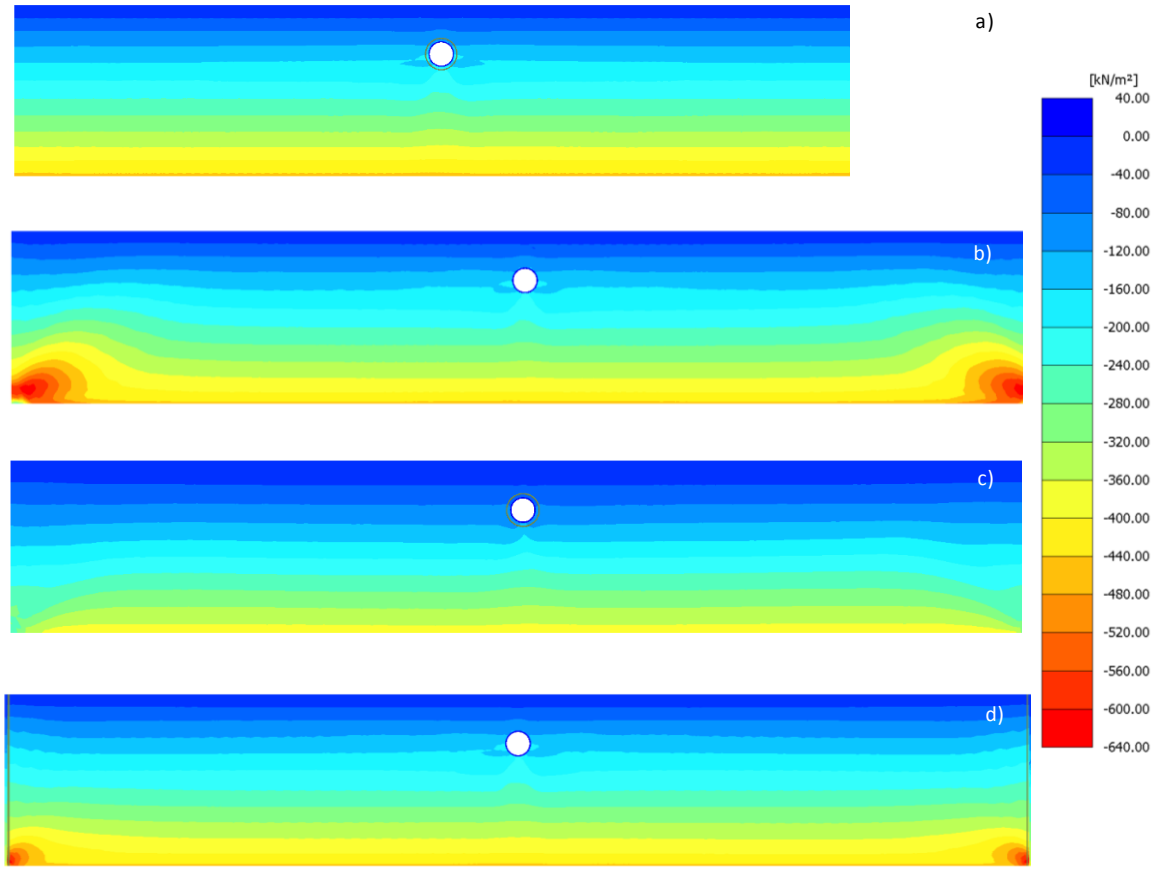

Figure 5.11 Profiles of effective mean stress *p'* after the seismic event using (a) tied-nodes boundaries with RMW; (b) viscous boundaries with RMW; (c) viscous boundaries with MCC and (d) free-field boundaries with RMW

The use of free-field boundaries has also been considered in this project. A free-field boundary is another type of boundary condition commonly used in dynamic FEM models. It simulates the propagation of seismic waves into the far-field with minimum reflection at the boundary. The free-field motion is transferred to the main domain from the free-field elements by applying equivalent normal and shear forces (Brinkgreve *et al.*, 2015) as illustrated in Figure 5.12. It is implemented as two dashpots, in the normal and shear direction, at each node of the vertical boundary. It effectively absorbs the waves reflected from the internal structures similar to a viscous boundary. This boundary condition is preferred when the dynamic input is applied along the model bottom boundary. Figure 5.11 (d) shows the effect of this type of boundary conditions in this case study. Since this boundary condition also implements a viscous-type wave absorbing principle, it prevents full absorption of outgoing wave energy at sharper angle of incidence as indicated by the occurrence of a disturbance at the bottom corners of the mesh. The introduction of the free-field elements however significantly reduces the disturbance and the results agree better with the case with

tied-nodes boundary conditions but still needs a bigger model than the tied-nodes case to ensure that the disturbance is far from the tunnel to cause any influence on the tunnel response.

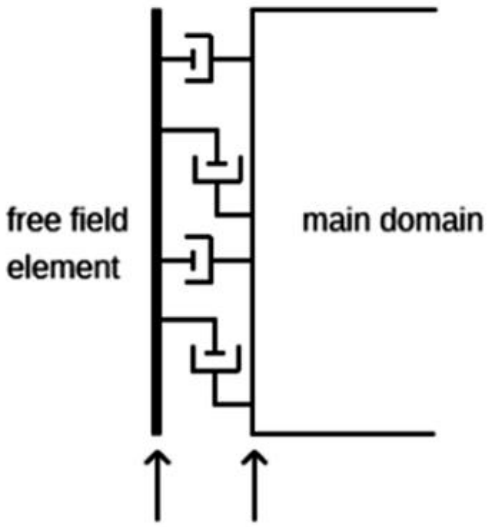

Figure 5.12 Free-field boundary condition (Brinkgreve *et al.*, 2015)

Although the use of a free-field boundary in PLAXIS 2D has been validated and verified, it turned out that the results in PLAXIS 3D as per current advice from PLAXIS do not perform as expected when compared with results from plane strain PLAXIS 2D model. This flaw has not been resolved by PLAXIS at the time of writing this dissertation. PLAXIS recommends using viscous boundaries instead over the free-field boundaries to perform dynamic analysis in PLAXIS 3D until this issue is resolved. Thus, only viscous boundaries have been applied in all 3D FEM models.

5.2 Results and discussion

Three case studies were investigated as outlined below. These case studies are intended to highlight the significance of the 3D approach in capturing the effect of the direction of seismic wave propagation which is arbitrary with respect to the axis of the structure in conjunction with using an advanced kinematic hardening soil constitutive model taking into account the effects of damage to structure (RMW). These are all taken within the context of evaluating the performance of the tunnel lining during seismic actions using this advanced approach.

1. 2D vs 3D – comparing results between the 2D FEM model and 3D FEM model with transverse earthquake component (N-S) only.
2. Multidirectional seismic loading effects – comparing results between 3D (transverse earthquake component only) and 3D (both earthquake components applied simultaneously) taken at the centre plane of the 3D model.
3. Effects of multidirectional seismic loading along the tunnel length – comparing 3D results along the tunnel length with transverse earthquake component only and with both earthquake components applied simultaneously.

The author has conducted a similar study in London Clay using MCC soil constitutive model (Cabangon *et al.*, 2018). The results and findings from that study have been presented in the 16th European Conference on Earthquake Engineering (16ECEE) held in Thessaloniki, Greece on 18-21 June 2018. A variation of that study utilising Avezzano clay as the soil medium has also been carried out by the author for comparison purposes. Some of the succeeding discussions include a certain degree of comparison between the results from RMW and the results from those MCC studies. It should be noted that the author has avoided making direct comparison on the actual values of the results between RMW and MCC but instead focused on the trend of the output results. This is due to incompatibility between the 3D RMW and 3D MCC models. Even though they have relatively similar parameters, these models have used different assumptions. 3D MCC has utilised linear-elastic shear modulus (Equation 3.28) along the soil depth which is built-in in PLAXIS while 3D RMW, a user-defined model, utilised non-linear shear modulus based on Viggiani and Atkinson's formulation (Equation 3.55). This was done to reduce immensely the amount of computing hours as running the MCC as a user-defined model in PLAXIS 3D will take weeks or even months to complete as opposed to days with the use of the built-in MCC model. A more comprehensive comparison between RMW and MCC has already been performed in 2D and presented in Chapter 4 Section 4.5.1. In the case of the 2D comparison, the Viggiani and Atkinson's formulation for initial shear modulus G_0 was employed in both models to ensure compatibility as the demand for computing hours was way lesser in simulating 2D models.

5.2.1 *Comparison between 2D and 3D results*

In order to assess the differences between 2D and 3D in seismic conditions while ensuring compatibility, both 2D and 3D FEM models adopt similar input data and boundary conditions including similar earthquake input signals, i.e. N-S component only. The 3D results have been extracted along the centre plane of the 3D FEM model (i.e. at 50m along the tunnel length).

The profiles of the minimum and maximum horizontal accelerations (a_x, a_y) and maximum vertical acceleration (a_z) recorded along the soil depth and obtained in free-field conditions with a 2D and a 3D model (denoted as 3D – x in the graphs) when the N-S component of the earthquake event is applied in the transverse x-direction are presented in Figure 5.13. The same accelerations recorded along the tunnel vertical are shown in Figure 5.14.

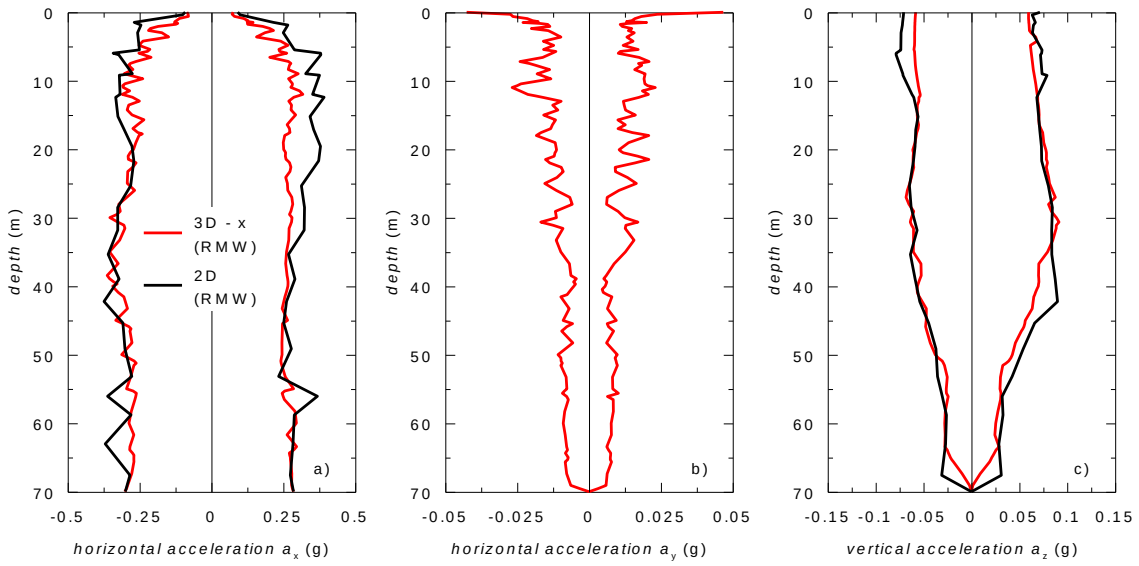

Figure 5.13 Profiles of max and min (a) horizontal acceleration a_x, (b) horizontal acceleration a_y and (c) vertical acceleration a_z recorded in free-field conditions when the N-S component is applied transversely using RMW

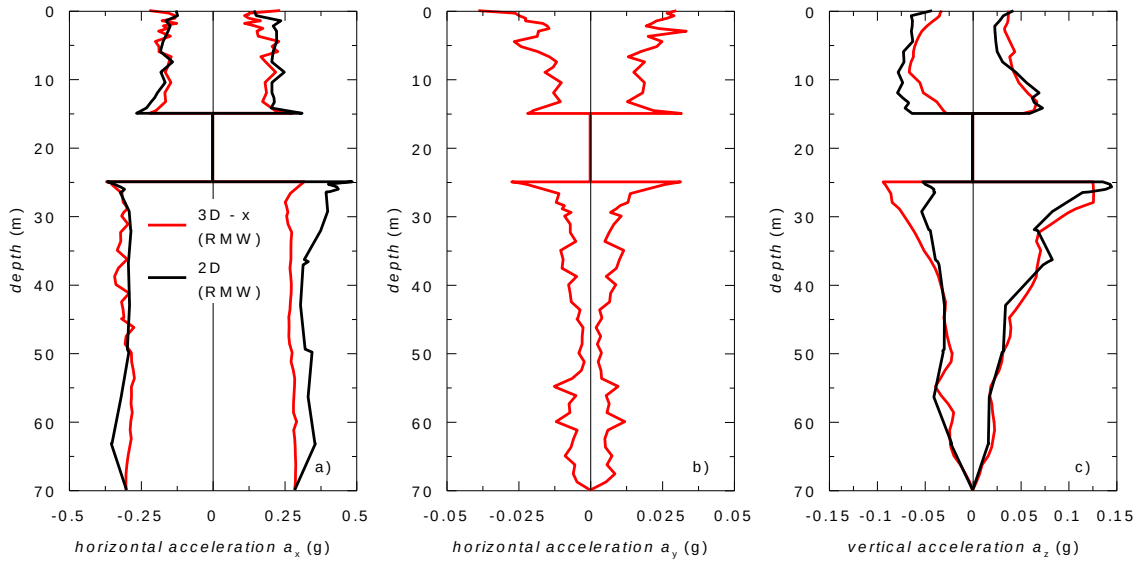

Figure 5.14 Profiles of max and min (a) horizontal acceleration a_x, (b) horizontal acceleration a_y and (c) vertical acceleration a_z recorded along the tunnel vertical when the N-S component is applied transversely using RMW

The 2D and 3D results are in satisfactory agreement, although the 3D accelerations are generally smaller than the 2D ones, especially on the transverse horizontal acceleration a_x both in free-field conditions and along the tunnel vertical. The same trend was observed in the paper by Cabangon *et al.* (2018) which adopted the same FEM model and earthquake data but instead used the MCC soil constitutive model in London clay. Similar observations were recorded by Brown *et al.* (2001) and Maheshwari *et al.* (2004) while studying the 3D response of a pile group to seismic excitation. By applying an earthquake acceleration time history at the bottom of the mesh on both 3D and 1D models, it was shown that the free-field response of 3D is considerably lower than 1D. To explain the disparity in their results, it was suggested that the 3D model has higher total damping, as the 3D allows wave propagation and thus energy dissipation in all directions. It implies that 3D results will be similarly lower than 2D due to more space for the seismic wave to propagate. This rationally explains the differences in the outcomes of the transverse accelerations between 2D and 3D models.

As a consequence of the wave dispersion, a horizontal acceleration a_y propagating in the longitudinal y-direction is generated by the 3D model as presented in Figure 5.13 (b) and Figure 5.14 (b), where a maximum a_y value of about 0.05g and 0.04g can be observed at the surface in free-field conditions and along the tunnel vertical respectively. In addition, in both the 2D and 3D simulations spurious vertical

accelerations a_z, reaching up to 0.07g and 0.04g at surface in free-field conditions and along the tunnel vertical respectively, are recorded [Figure 5.13 (c) and Figure 5.14 (c)]. It has been noted that the presence of the tunnel structure has heightened the acceleration at the tunnel crown and invert location. It can also be observed that at a depth from 40m below ground the maximum acceleration for both 2D and 3D becomes quite even.

The dissipation of the seismic wave in the longitudinal direction has also resulted in the disparity in the transverse shear strain γ_{zx} between 2D and 3D along the soil depth in free-field conditions and along the tunnel vertical as shown in Figure 5.15 (a) and Figure 5.16 (a). Consequently, it produces longitudinal shear strains γ_{xy} and γ_{yz} in 3D as shown in Figure 5.15 (b & c) and Figure 5.16 (b & c) which cannot be predicted by the 2D model. However, in this case, these longitudinal shear strains are almost insignificant except near the surface in free-field conditions and around the tunnel invert to the ground surface at the tunnel location.

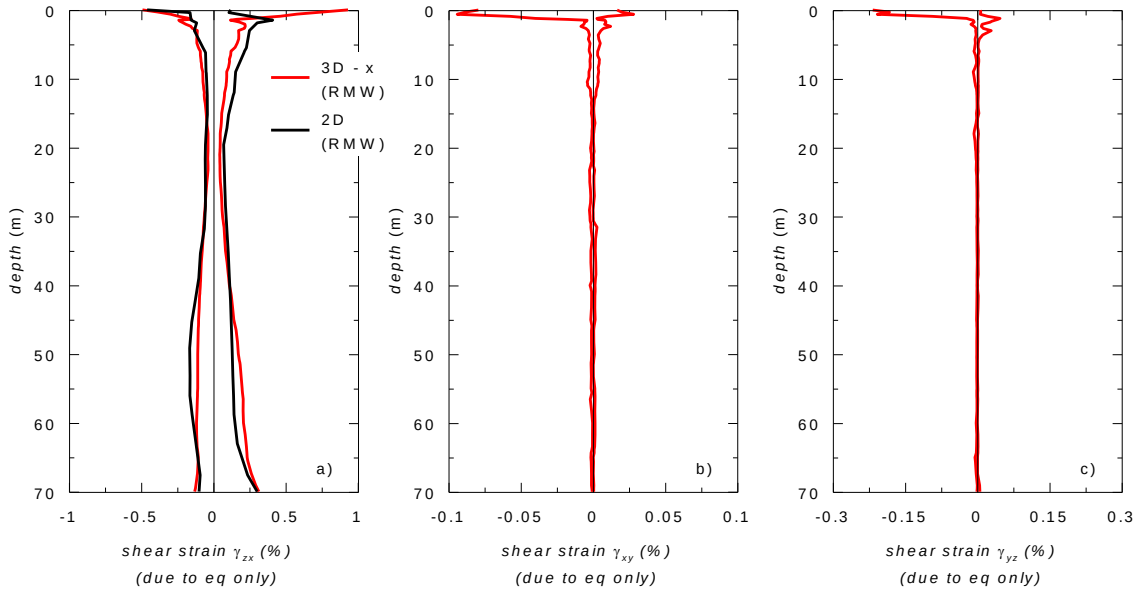

Figure 5.15 Profiles of max and min (a) transverse shear strain γ_{zx}, (b) longitudinal shear strain γ_{xy} and (c) longitudinal shear strain γ_{yz} recorded in free-field conditions when the N-S component is applied transversely using RMW

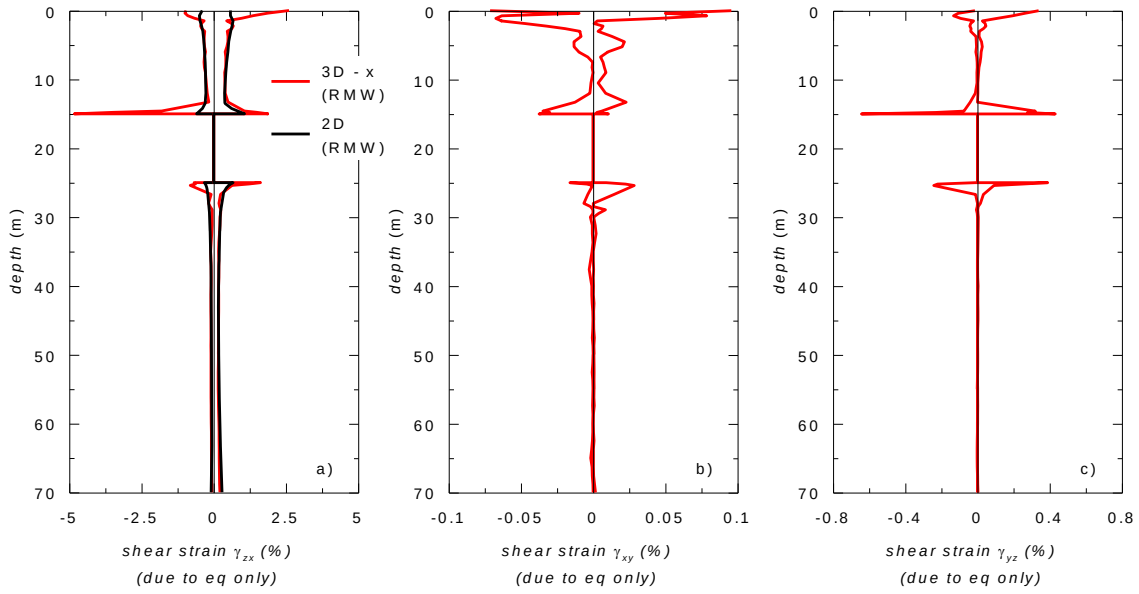

Figure 5.16 Profiles of max and min (a) transverse shear strain γ_{zx}, (b) longitudinal shear strain γ_{xy} and (c) longitudinal shear strain γ_{yz} recorded along the tunnel vertical when the N-S component is applied transversely using RMW

Figure 5.17 shows the distribution of the predicted hoop force, transverse bending moment and transverse shear force at the end of the seismic event as a function of the angle θ, defined positive in the anti-clockwise direction as well as the maximum and minimum force envelopes. The 3D results (denoted as 3D – x in the graphs) are more scattered than the smooth 2D output due to a smaller number of nodes in the 3D tunnel model which is driven by the modelling limitations imposed by the software (e.g. 10-noded tetrahedral element in 3D compared to 15-noded triangular element in 2D), but they follow the same trend of the 2D simulations.

The hoop forces at the central tunnel section of the 3D model (i.e. at 50m along the tunnel length) are comparable with the corresponding 2D results but relatively smaller ranging from 985kN/m to 1820kN/m in compression. A similar trend has been observed in the 3D transverse bending moments and transverse shear forces relative to their 2D counterparts whereby the 3D forces are comparable, but generally lower than the 2D ones due to the dissipation of the earthquake accelerations in the longitudinal direction as previously mentioned. The transverse bending moment reaches a maximum of 397kNm/m (positive bending) and a minimum of 552kNm/m (negative bending) while the transverse shear force reaches a maximum value of 168kN/m. The same trend is also observed from the tunnel lining results of a similar study by Cabangon *et al.* (2018) using the MCC soil constitutive model in London Clay

and a variation of that study using Avezzano clay, shown in Figure 5.18. The dissipation of the earthquake accelerations in the longitudinal direction is also evident in the results of the tunnel lining transverse forces when the size of the model increases longitudinally as shown in Figure 5.19 (1m strip of 3D FEM vs. 100m of 3D FEM) allowing more space for the seismic wave to propagate in that direction thereby reducing the transverse lining forces. However, the residual (i.e. after earthquake) bending moments and shear forces between 2D and 3D results [Figure 5.17 (b-c) and Figure 5.18 (b-c)] did not match well and the locations of the peak residual bending moments and shear forces around the lining did not line up. These observations can also be seen between the results of the residual bending moments and shear forces between the 3D full model (100m long) and the same model with only 1m length [see Figure 5.19 (b-c)]. Whereas, the residual bending moment results of this same 1m long 3D model is in satisfactory agreement with the 2D model results [Figure 5.10 (b-c)], these results, on the other hand, did not matched very well with the longer full 3D model. These disparities can be attributed to the dissipation of the earthquake accelerations in the longitudinal direction together with the 3D interaction effects of the soil and the tunnel structure which cannot be observed in a 2D model or even a 3D model with a very short length as this amount of length is not sufficient to observe full dissipation of earthquake waves and well-distinct 3D soil-structure interactions in the longitudinal direction. Despite these disparities, the results of the residual bending moments and shear forces did not affect the maximum bending moment and shear force envelopes for the 2D and 3D (both 1m and 100m long) which are then comparable and are more important for design and detailing of the tunnel lining. The residual forces, however, are important when assessing the effects of the locked-in forces from a previous earthquake when subjected to another later earthquake/s or aftershocks, which is outside the scope of this dissertation.

In general, the 2D transverse seismic behaviour is very similar to the 3D ones but more conservative in magnitude because it lacks the ability to disperse the seismic wave longitudinally as similarly observed by other researchers. Thus, the level of results achieved from 2D is considered adequate and a conservative approach when designing the tunnel lining just based on its transverse seismic behaviour. However, the propagation of a horizontal acceleration in the y-direction generates longitudinal

forces in the lining (i.e. longitudinal axial force, longitudinal bending moment, longitudinal shear force, torsional moment and in-plane shear force), which cannot be captured by the 2D model. The longitudinal axial force is quite substantial and can reach maximum values of 1433kN/m in compression and 674kN/m in tension [Figure 5.20 (a)]. The longitudinal bending moment can also be as large as 142kNm/m [Figure 5.20 (b)]. Ignoring these forces may lead to under-design of the tunnel lining, thus potentially compromising the integrity of the underground structure in the longitudinal direction. Other longitudinal effects including longitudinal shear, torsional moment and in-plane shear are shown in Figure 5.20 (c), (d) & (e). Nonetheless, these forces can be considered insignificant due to its small load size.

Figure 5.21 shows the time histories of shear strain and excess pore water pressure predicted along the tunnel vertical for the 2D and 3D models. The transverse shear strains between the two models at chosen points are relatively similar indicating their compatibility. The FEM non-linear analyses for both models predict the build-up of positive pore pressures above the tunnel invert and negative pore pressures below it, associated with the accumulation of permanent soil deformations and structure degradation throughout the earthquake motions. However, an increase in excess pore pressures were recorded in 3D, ranging between 110kPa at 15m depth (tunnel crown level) and –123kPa also at the tunnel crown compared to 2D which only ranges between 62kPa to -30kPa. Nevertheless, the increase in excess pore water pressure such as those observed at the tunnel crown and invert as shown in Figure 5.21 (b & d) and Figure 5.22, were in line with the higher maximum shear strain levels in the same locations [Figure 5.16 (a)]. It can also be seen from Figure 5.21 (d) that the pore water pressure at 15m depth (i.e. tunnel crown) in 3D started as negative pore pressures up to around 9 seconds approximately at the peak of the input excitation and gradually built up to positive pressures until it stabilised while the 2D results has been kept as positive pressures during the whole period of the applied earthquake motion. As previously stated, these disparities can be attributed to the higher shear strain levels induced at those locations such as at the tunnel crown and invert by the 3D interaction effects of the soil and the tunnel structure which cannot be simulated in a 2D model.

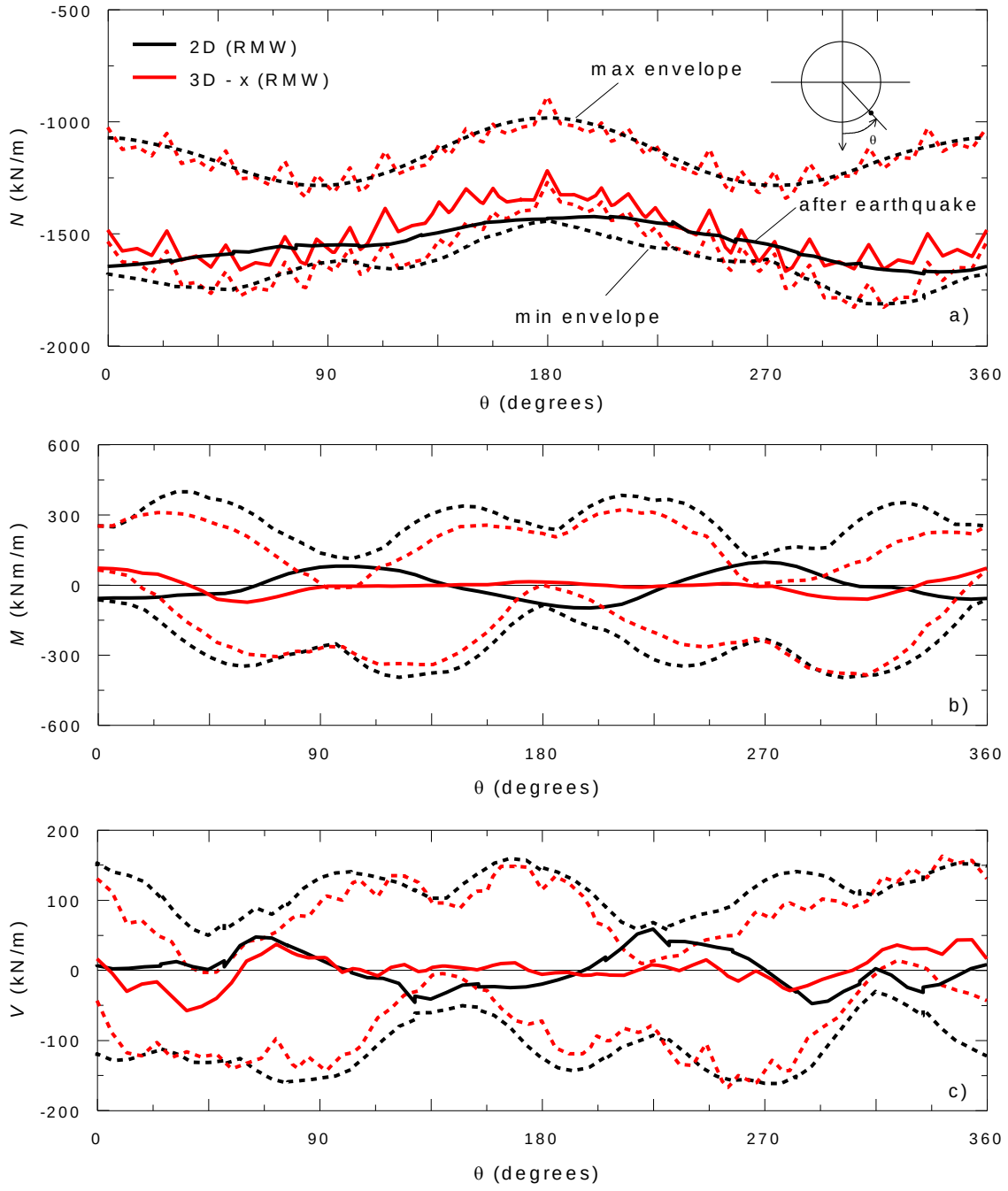

Figure 5.17 Distribution of maximum and minimum (a) hoop force; (b) transverse bending moment and (c) transverse shear force when the N-S component is applied transversely using RMW

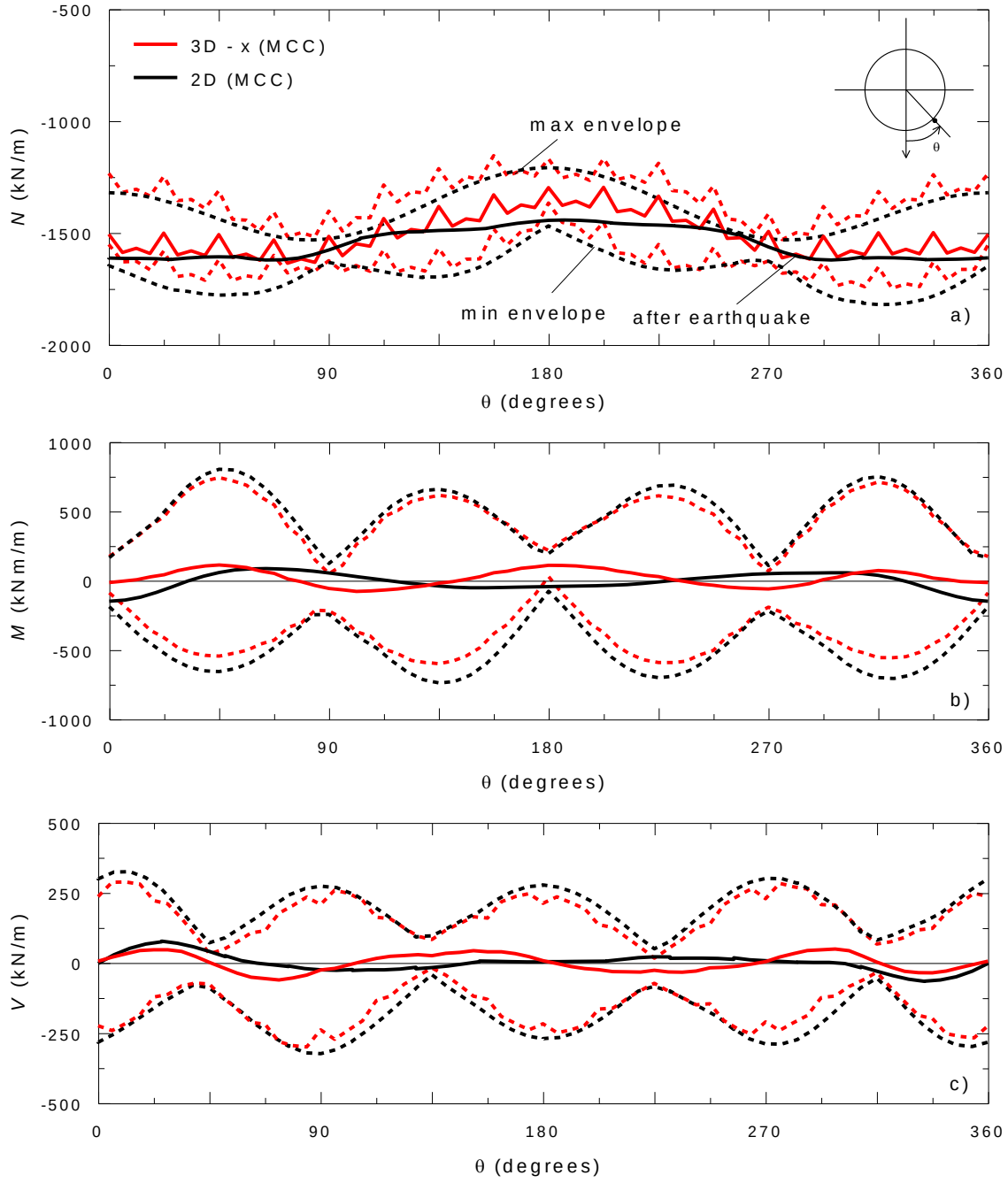

Figure 5.18 Distribution of maximum and minimum (a) hoop force; (b) transverse bending moment and (c) transverse shear force when the N-S component is applied transversely using MCC

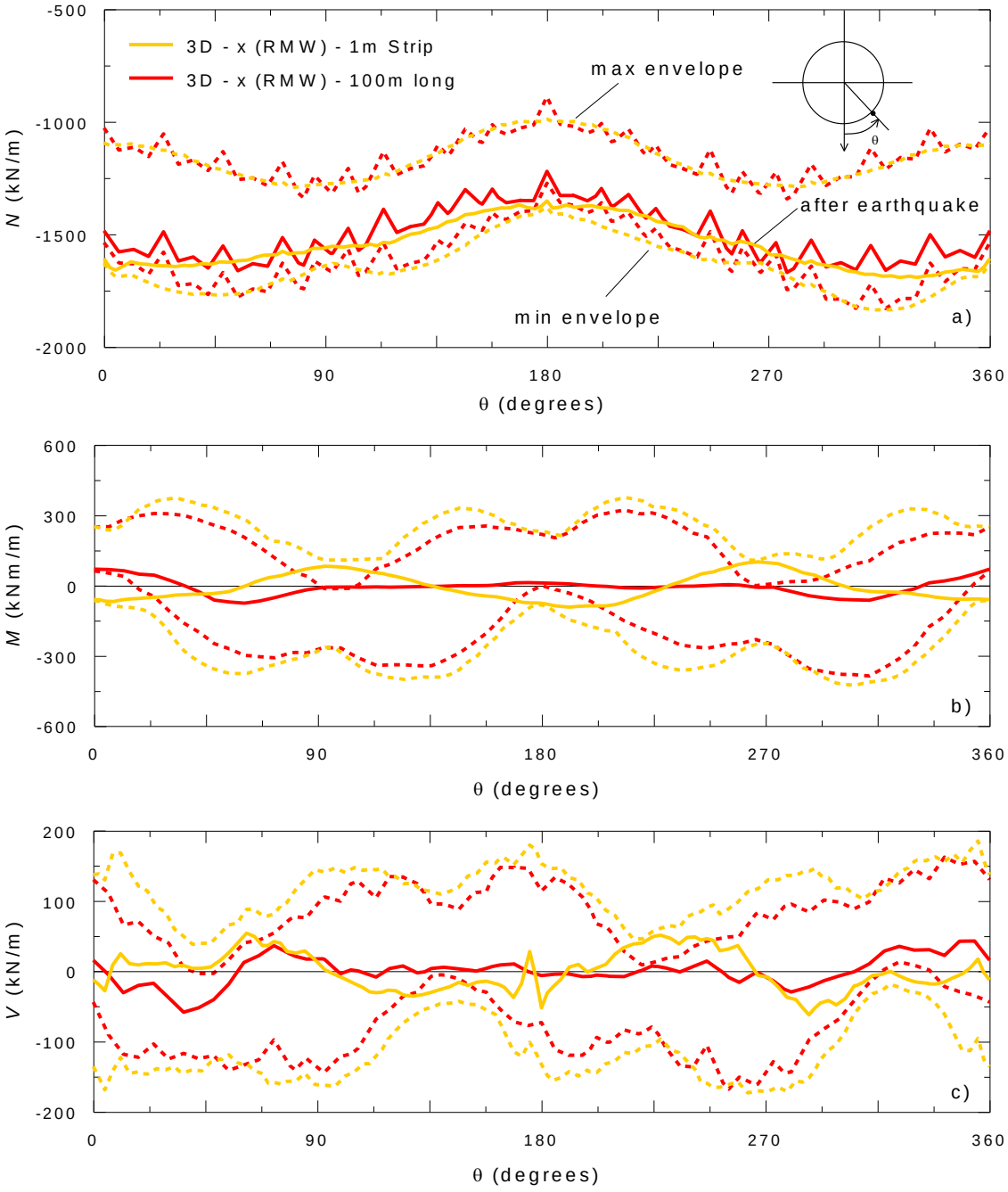

Figure 5.19 Distribution of maximum and minimum (a) hoop force; (b) transverse bending moment and (c) transverse shear force when the N-S component is applied transversely in 1m and 100m long 3D FEM using RMW

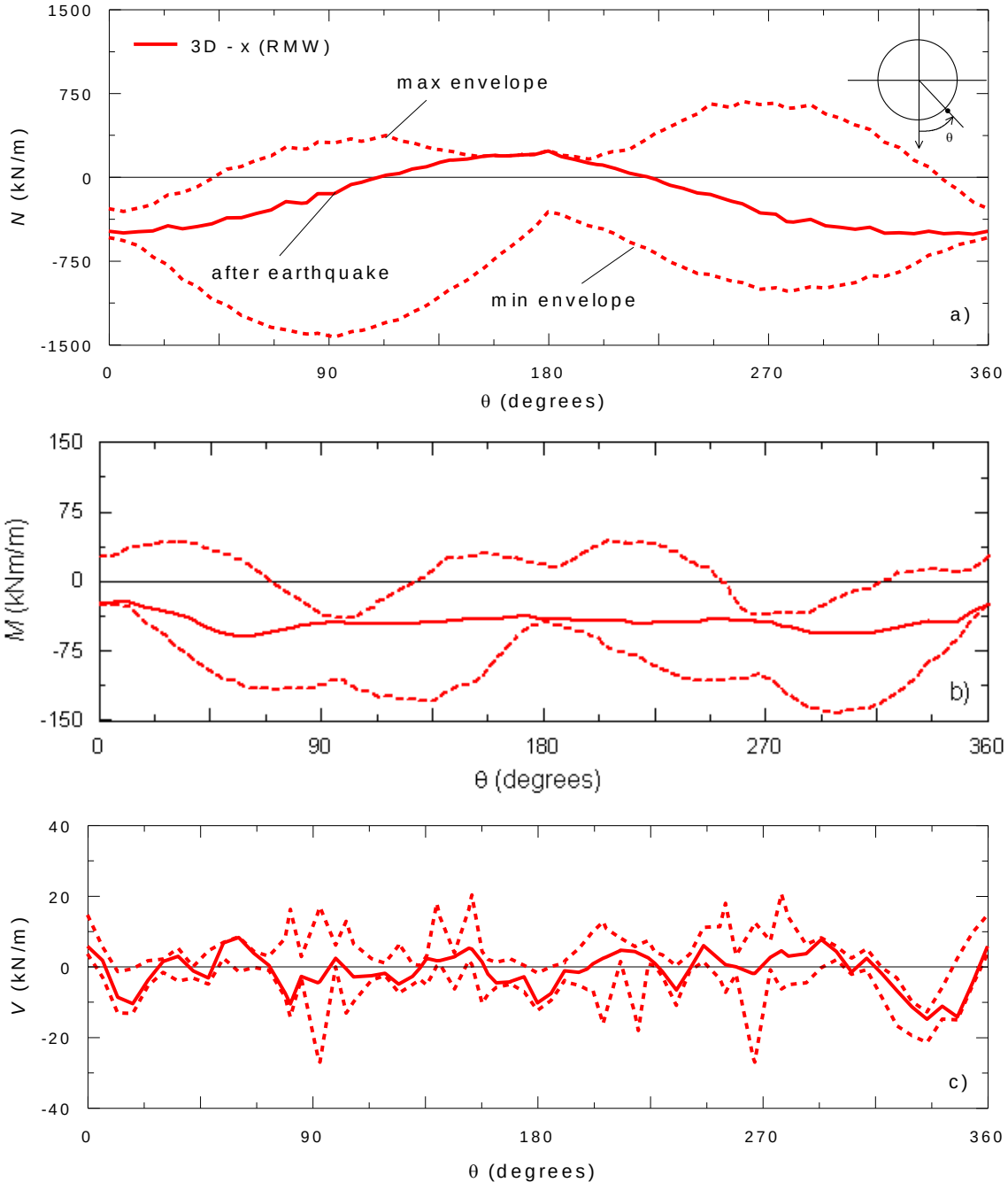
3D - x (RMW)
max envelope
after earthquake
min envelope
θ
N (kN/m)
1500
750
0
-750
-1500
0
90
180
270
360
θ (degrees)
a)

M (kNm/m)
150
75
0
-75
-150
0
90
180
270
360
θ (degrees)
b)

V (kN/m)
40
20
0
-20
-40
0
90
180
270
360
θ (degrees)
c)

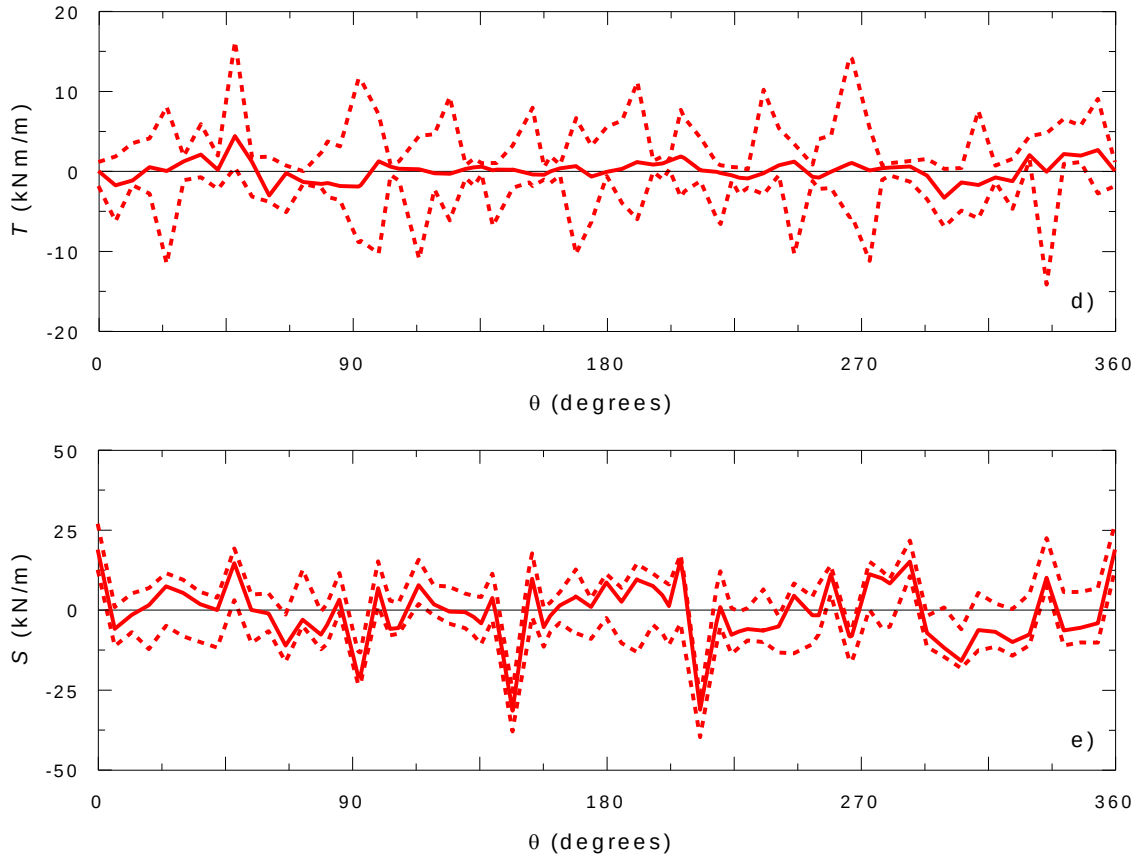

Figure 5.20 Distribution of maximum and minimum (a) longitudinal axial force; (b) longitudinal bending moment; (c) longitudinal shear force; (d) torsional moment and (e) in-plane shear when the N-S component is applied transversely using RMW

Figure 5.23 (a & b) shows the contours of RMW parameter *r*, describing the degree of soil structure, obtained at the end of the seismic event for both 2D and 3D. The contours indicate very similar destructuration occurred in the soil deposit for both cases but generally more pronounced structure degradation is induced in the soil around the tunnel springline in 2D than in 3D [Figure 5.24 (a & b)], while 3D structure degradation around the tunnel invert and crown is higher which is consistent with the higher shear strain levels and higher excess pore water pressures in the same locations.

As pointed out in Section 5.1.4, disturbance has been observed propagating from the bottom corners of the mesh when using viscous boundaries which is due to the close proximity of the dashpots from the seismic source (i.e. bottom of the mesh model) causing spurious waves to reflect back from this location. This is similarly observed in the contours of RMW parameter *r* at the end of the seismic event for both 2D and 3D as indicated in Figure 5.23 (a & b). As recommended in Section 5.1.4, in order to minimise the effect of this disturbance on the lining response, the tunnel has to be

placed as far as possible from the viscous boundaries, thus maintaining the reliability of the tunnel lining results.

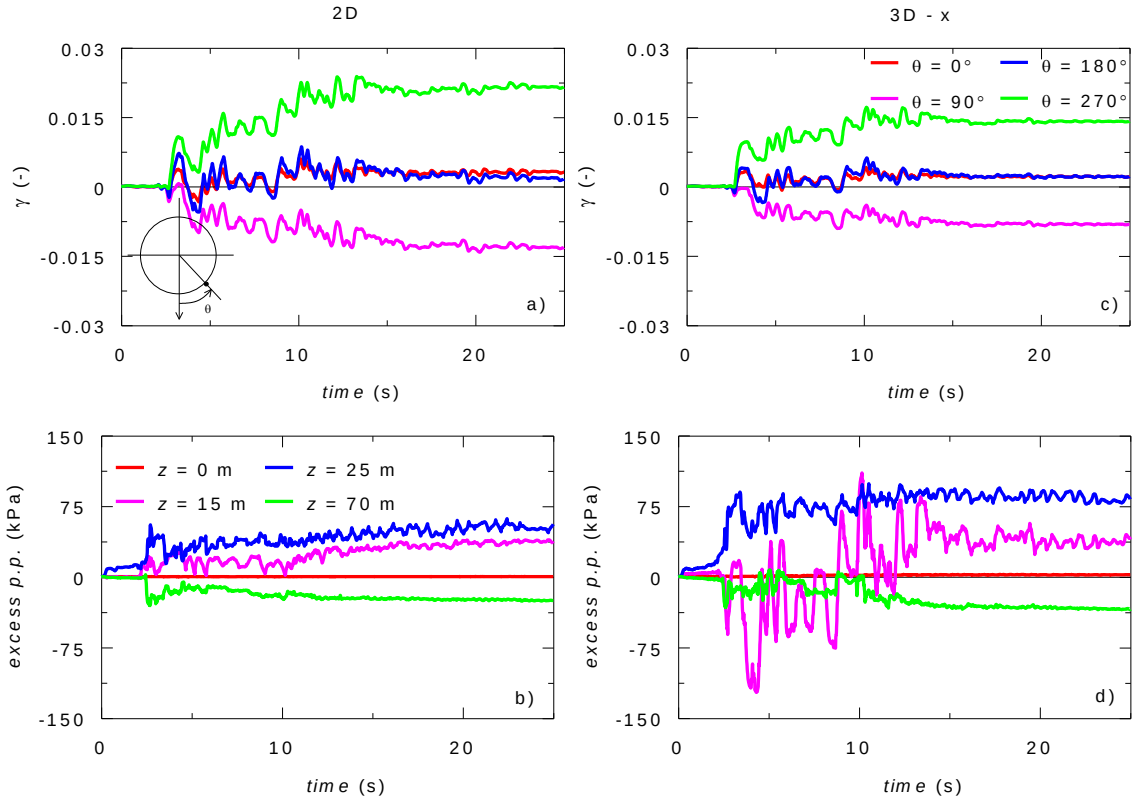

Figure 5.21 Time histories of shear strain and excess pore pressure of RMW model for (a–b) 2D and (c–d) 3D when the N-S component is applied transversely

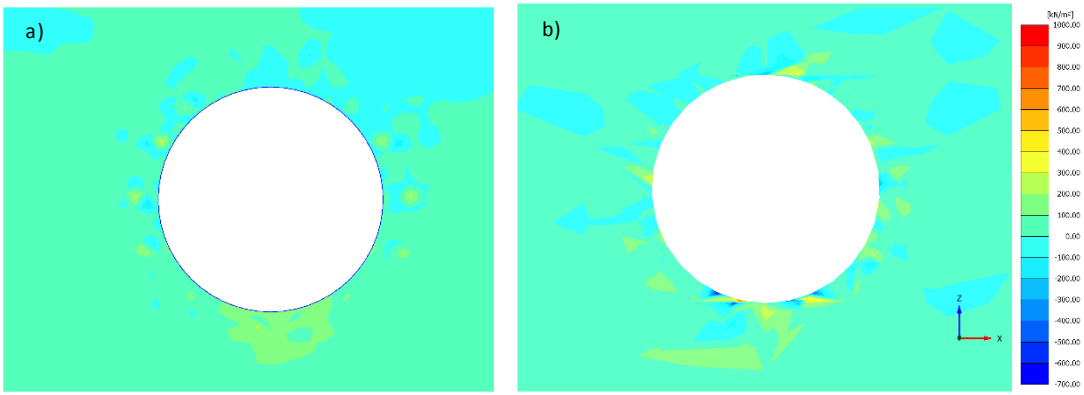

Figure 5.22 Contours of the excess pore water pressure at the end of the seismic event around the tunnel for (a) 2D and (b) 3D when the N-S component is applied transversely using RMW

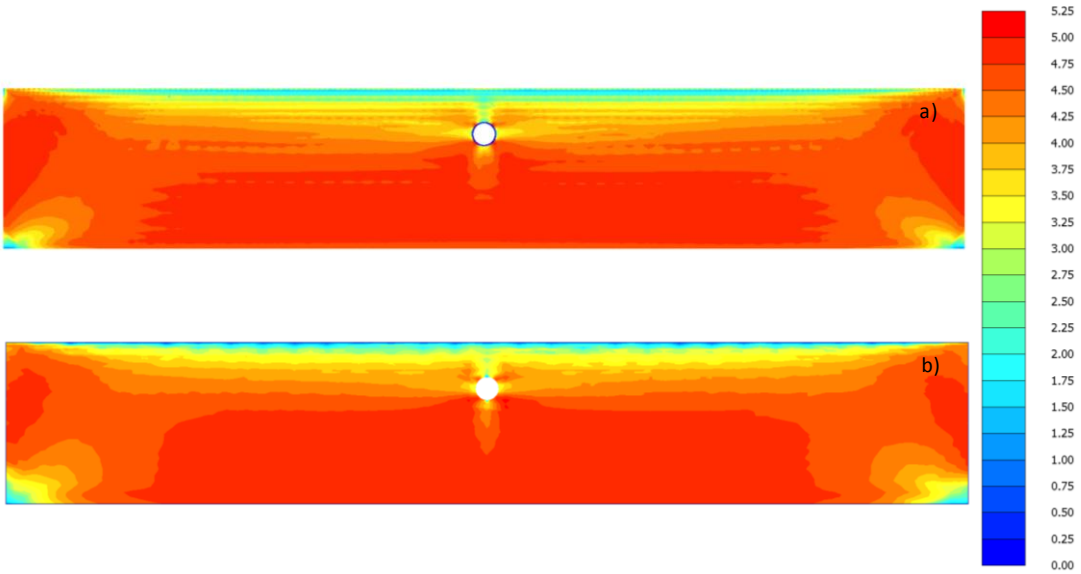

Figure 5.23 Contours of the RMW parameter *r* at the end of the seismic event for (a) 2D and (b) 3D when the N-S component is applied transversely

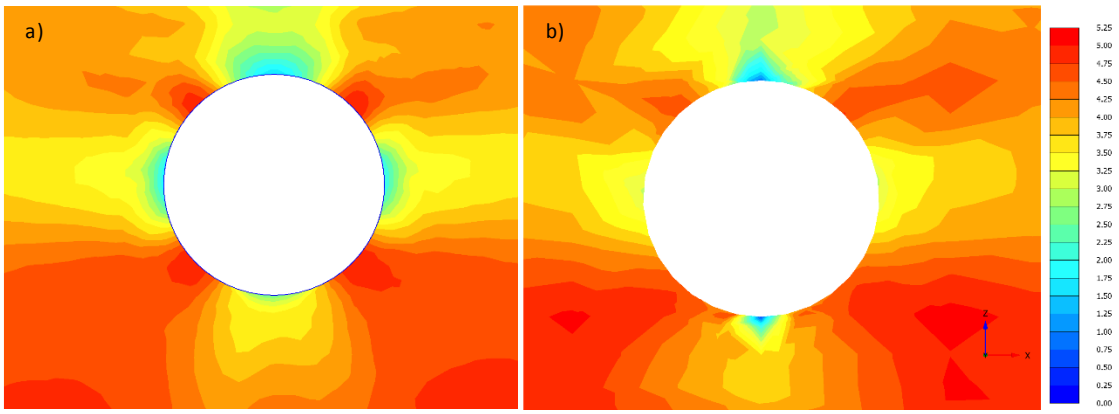

Figure 5.24 Contours of the RMW parameter *r* at the end of the seismic event around the tunnel for (a) 2D and (b) 3D when the N-S component is applied transversely

5.2.2 *Multidirectional seismic loading effects*

To assess the effects of multidirectional seismic loading, the 3D results have been compared between the cases when only the transverse earthquake component is applied at bedrock and with both earthquake components applied simultaneously. The results were extracted along the centre plane of the 3D FEM model (i.e. at 50m along the tunnel length).

Figure 5.25 shows a comparison of the minimum and maximum transverse (a_x) horizontal accelerations, longitudinal (a_y) horizontal accelerations and vertical accelerations a_z recorded along the soil depth and obtained in free-field conditions with the 3D model in cases when only N-S earthquake component is applied transversely at bedrock (denoted as 3D – x) and with both N-S and E-W components

applied simultaneously (denoted as 3D – xy). Figure 5.26 shows the same accelerations taken at the tunnel vertical. As observed by Cabangon *et al.* (2018) in his paper, whenever an input motion is imposed in the 3D model in transverse direction, an acceleration will be generated in the orthogonal directions due to dissipation of seismic waves in all directions. Similarly, in this case study, the application of the N-S earthquake component generates accelerations in the longitudinal direction from 0g at bedrock and up to 0.05g at the ground surface in free-field conditions.

When both N-S and E-W components are applied simultaneously at bedrock, the transverse accelerations a_x are comparable but generally smaller to those obtained when a single event is imposed in transverse direction only as shown in Figure 5.25 (a). Similar observations are recorded in vertical accelerations a_z in those two simulations as illustrated in Figure 5.25 (c). The same conclusions can be drawn at the tunnel vertical [Figure 5.26 (a & c)] where a_x and a_z for the 3D – xy case are in satisfactory agreement but smaller than 3D – x case. This is not the case though for a similar study performed by Cabangon *et al.* (2018) using MCC model whereby a_x and a_z in both simulations are almost coinciding (Refer to Figure 5.27). Since the MCC model is fully remoulded (i.e. degree of soil structure r = 1, thus no structure), while the RMW model considers the soil structure (i.e. r >1) and includes a small inner yield surface (i.e. bubble) which allows accumulation of permanent strains during cyclic loading, the difference in the trend between RMW and MCC can be attributed to the steady fall of stiffness with the shear strain resulting to the collapse of the "bubble" surface towards the reference surface (i.e. Cam clay yield surface) in conjunction with destructuration of the soil structure (i.e. collapse of the structure surface towards the reference surface). The imposition of the longitudinal component of the earthquake in conjunction with the transverse component generates a higher degree of destructuration particularly at the bottom part of the mesh which will be further discussed later in the chapter. Hence it reduces further the soil's shear stiffness while increasing the shear strain, which in turn causes further dissipation of the transverse earthquake accelerations in the longitudinal direction, thus the reduction in a_x. As a consequence, it increases the longitudinal acceleration a_y as shown in Figure 5.25 (b) and Figure 5.26 (b).

In free-field conditions, the longitudinal acceleration a_y has increased from 0g to 0.3g at bedrock and from 0.04g to 0.07g at the ground surface due to the contribution from the E-W earthquake component and the ensuing soil structure degradation. While at the tunnel vertical, a_y has increased from 0g to 0.3g at bedrock and from 0.04g to 0.12g at ground surface. It demonstrates that the evolution of the soil structure can influence the dissipation of the seismic wave within the soil thereby affecting not only the longitudinal acceleration but also the transverse and vertical accelerations when considered in the dynamic simulation. In contrast, only the longitudinal acceleration will be affected if the soil has no structure and has limited ability to accumulate plastic strains. Thus, the soil structure plays a big role in influencing the results of the soil-tunnel interaction in a 3D space during a seismic event.

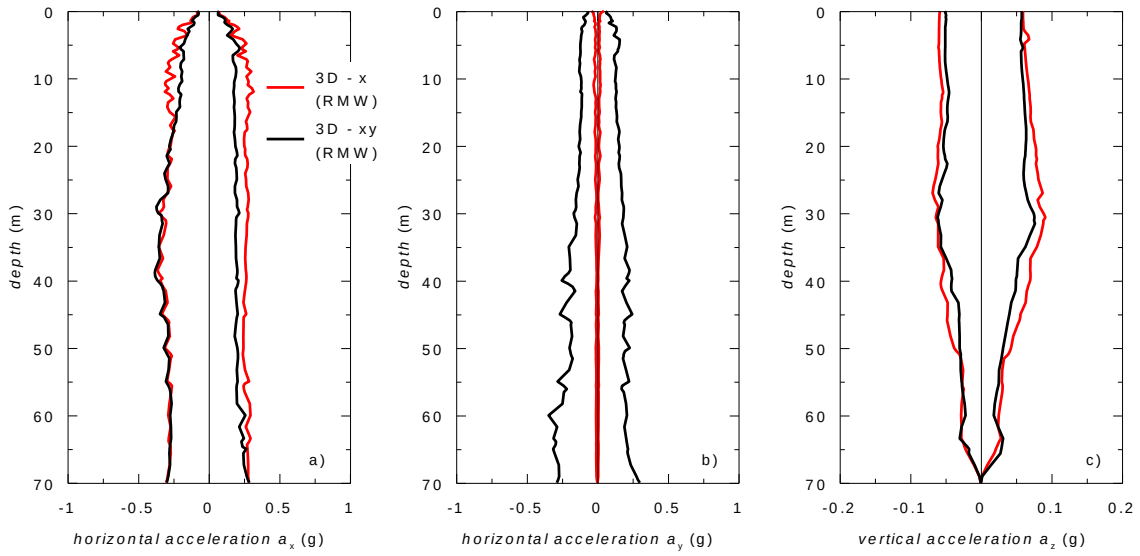

Figure 5.25 Profiles of max and min (a) horizontal acceleration a_x, (b) horizontal acceleration a_y and (c) vertical acceleration a_z recorded in free-field conditions when only N-S earthquake component is applied transversely at bedrock and with both N-S and E-W components applied simultaneously using RMW

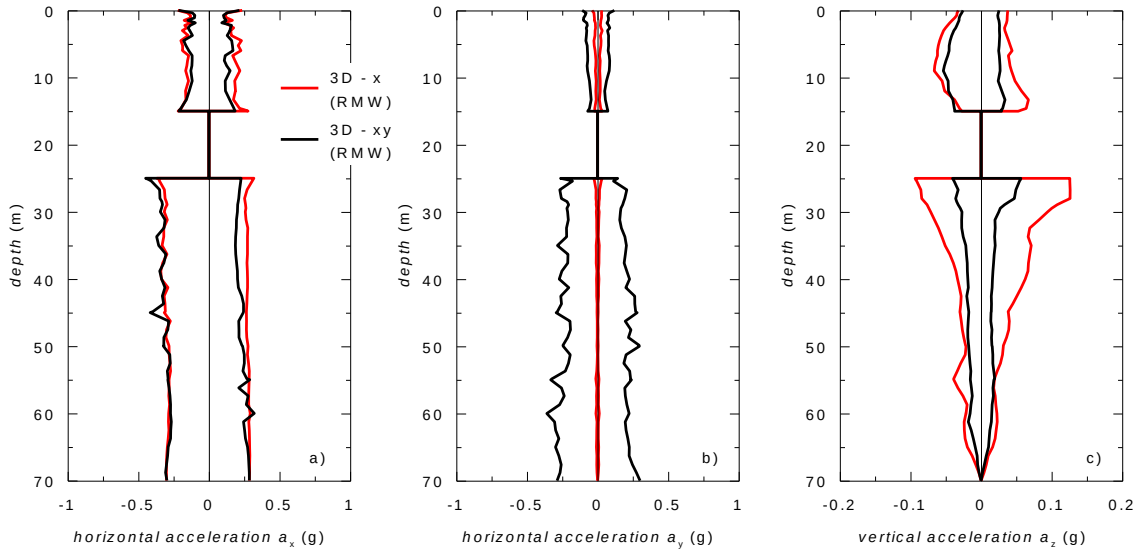

Figure 5.26 Profiles of max and min (a) horizontal acceleration a_x, (b) horizontal acceleration a_y and (c) vertical acceleration a_z recorded at tunnel vertical when only N-S earthquake component is applied transversely at bedrock and with both N-S and E-W components applied simultaneously using RMW

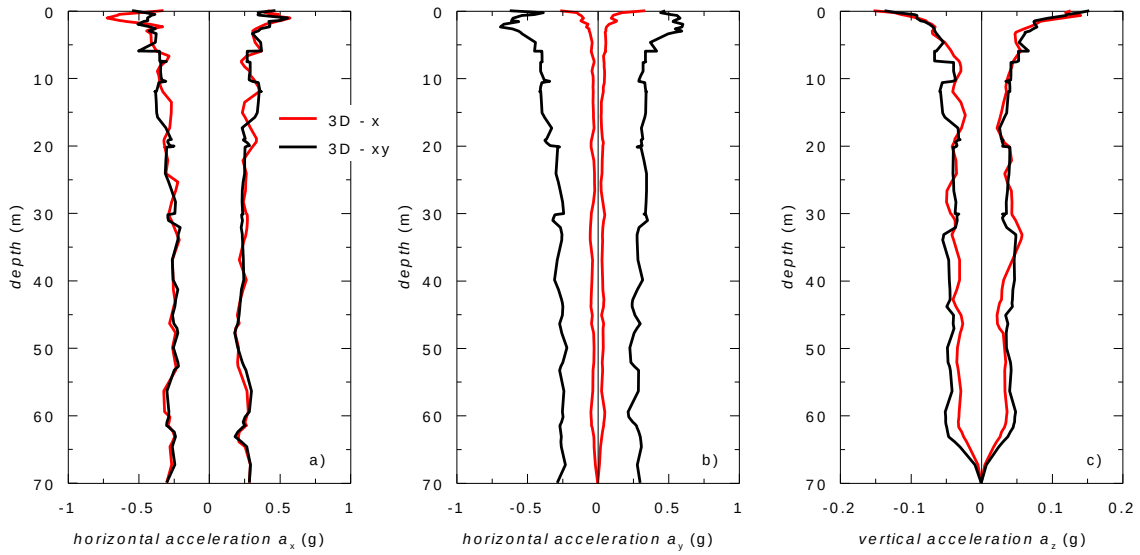

Figure 5.27 Profiles of max and min (a) horizontal acceleration a_x, (b) horizontal acceleration a_y and (c) vertical acceleration a_z recorded in free-field conditions when only N-S earthquake component is applied transversely at bedrock and with both N-S and E-W components applied simultaneously using MCC (Cabangon *et al.*, 2018)

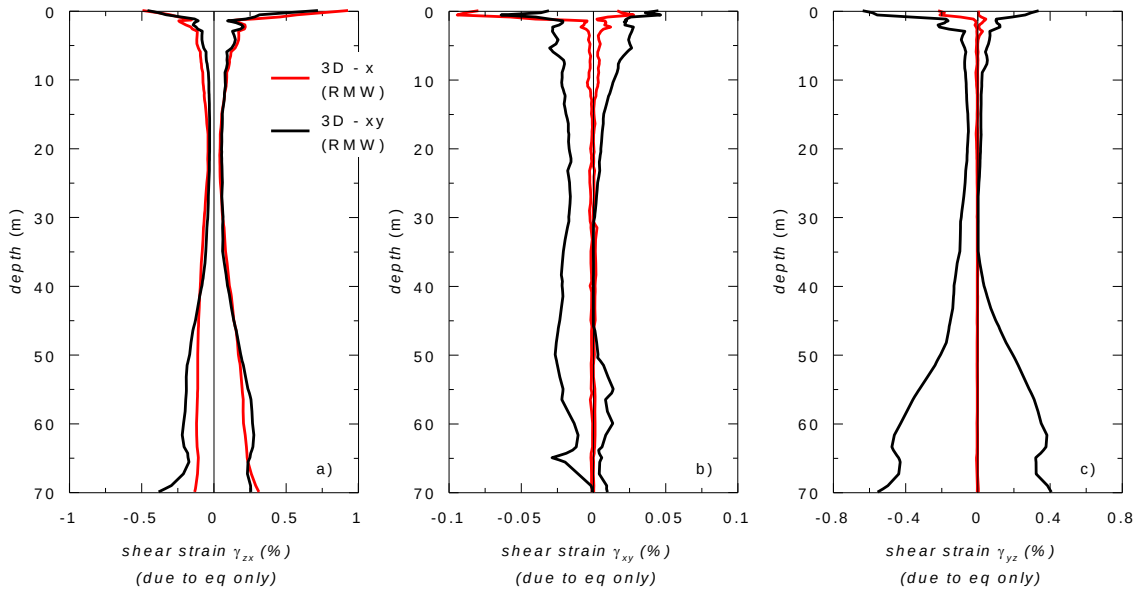

Figure 5.28 Profiles of max and min (a) transverse shear strain γ_{zx}, (b) longitudinal shear strain γ_{xy} and (c) longitudinal shear strain γ_{yz} recorded in free-field conditions when the N-S component is applied transversely at bedrock and with both N-S and E-W components applied simultaneously using RMW

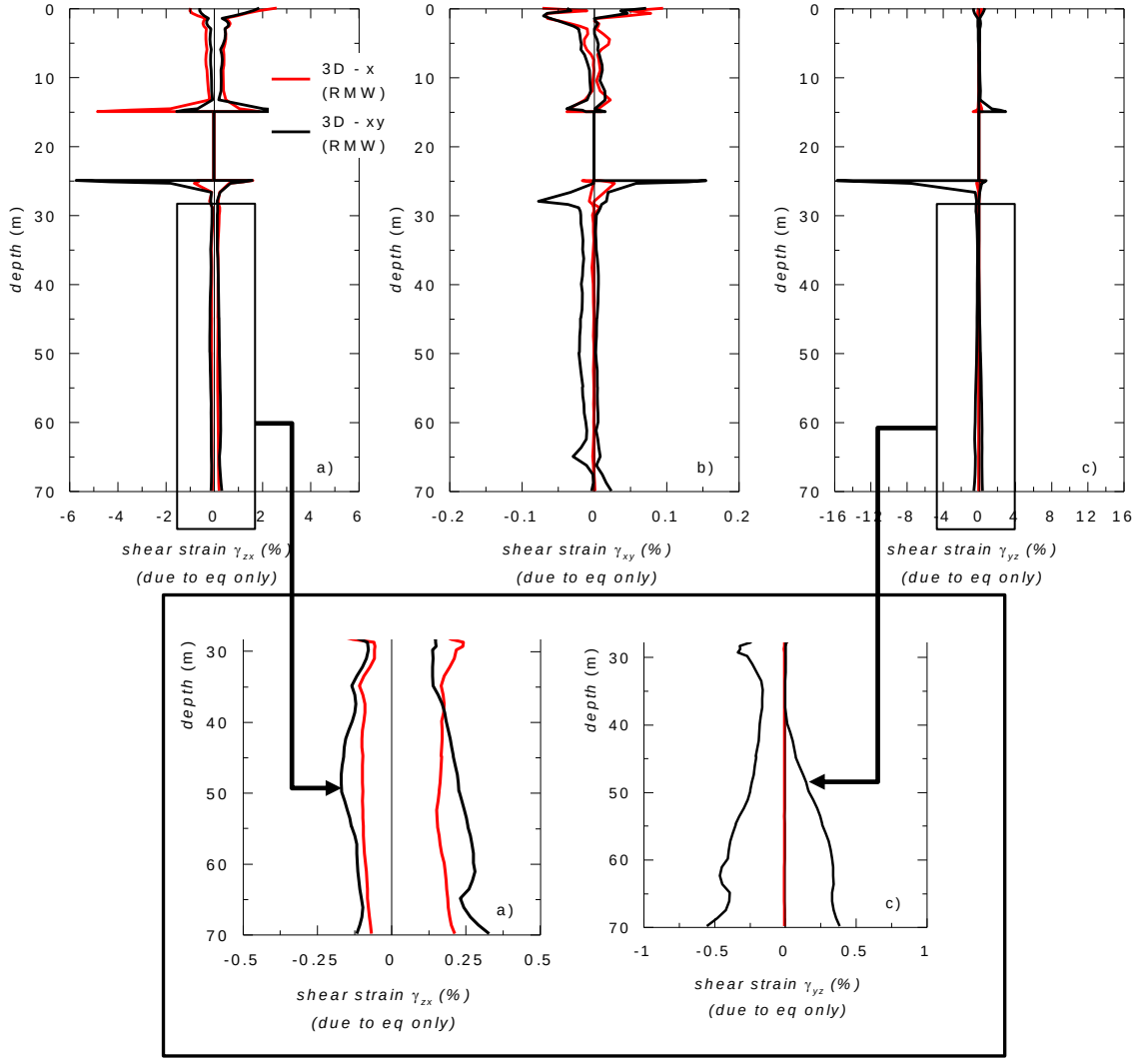

Figure 5.29 Profiles of max and min (a) transverse shear strain γ_{zx}, (b) longitudinal shear strain γ_{xy} and (c) longitudinal shear strain γ_{yz} recorded at tunnel vertical when the N-S component is applied transversely at bedrock and with both N-S and E-W components applied simultaneously using RMW

The corresponding shear strains are shown in Figure 5.28 in free-field conditions and Figure 5.29 along the tunnel vertical. Similar to the acceleration profiles, the transverse shear strains γ_{zx} between 3D – xy and 3D – x simulations are comparable. However, with higher degree of soil destructuration induced at the bottom section of the model to be discussed later in the chapter caused by the concurrent application of the E-W and N-S earthquake components, the shear stiffness of the soil medium decreases, thereby increasing the transverse shear strains γ_{zx} at that bottom section in the free-field conditions [Figure 5.28 (a)] and at the tunnel vertical [Figure 5.29 (a)]. Similarly, longitudinal shear strains γ_{xy} and γ_{yz} for 3D – xy case have generally increased compared to 3D – x case due to the influence of the combined effect of the imposed E-W component and soil destructuration as illustrated in Figure 5.28 (b & c) and Figure 5.29 (b & c).

Consistent with the response observed in the acceleration and shear strain profiles, the maximum and minimum values of the hoop force, transverse bending moment and transverse shear force in the central section of the tunnel lining as a function of the angle θ, defined positive in the anti-clockwise direction resulting from the simultaneous application of the two horizontal components of the earthquake are generally smaller than the case when only the transverse earthquake component is applied at bedrock as shown in Figure 5.30. Comparison with the MCC results in the paper by Cabangon *et al.* (2018) in London clay and a variation of that study using Avezzano clay (Figure 5.31) shows that in contrast the transverse lining forces for both simulations are generally similar except for very slight differences due to spatial effects. This, as mentioned previously, is due to the lack of soil structure and the absence of the small inner yield surface (i.e. bubble) which limits the accumulation of permanent strains during cyclic loading in the MCC model thereby preventing further dissipation of the transverse acceleration in the longitudinal direction. Thus, the design of the tunnel lining in the transverse direction can be based conservatively on the results of imposing singly the transverse earthquake component which is considered adequate.

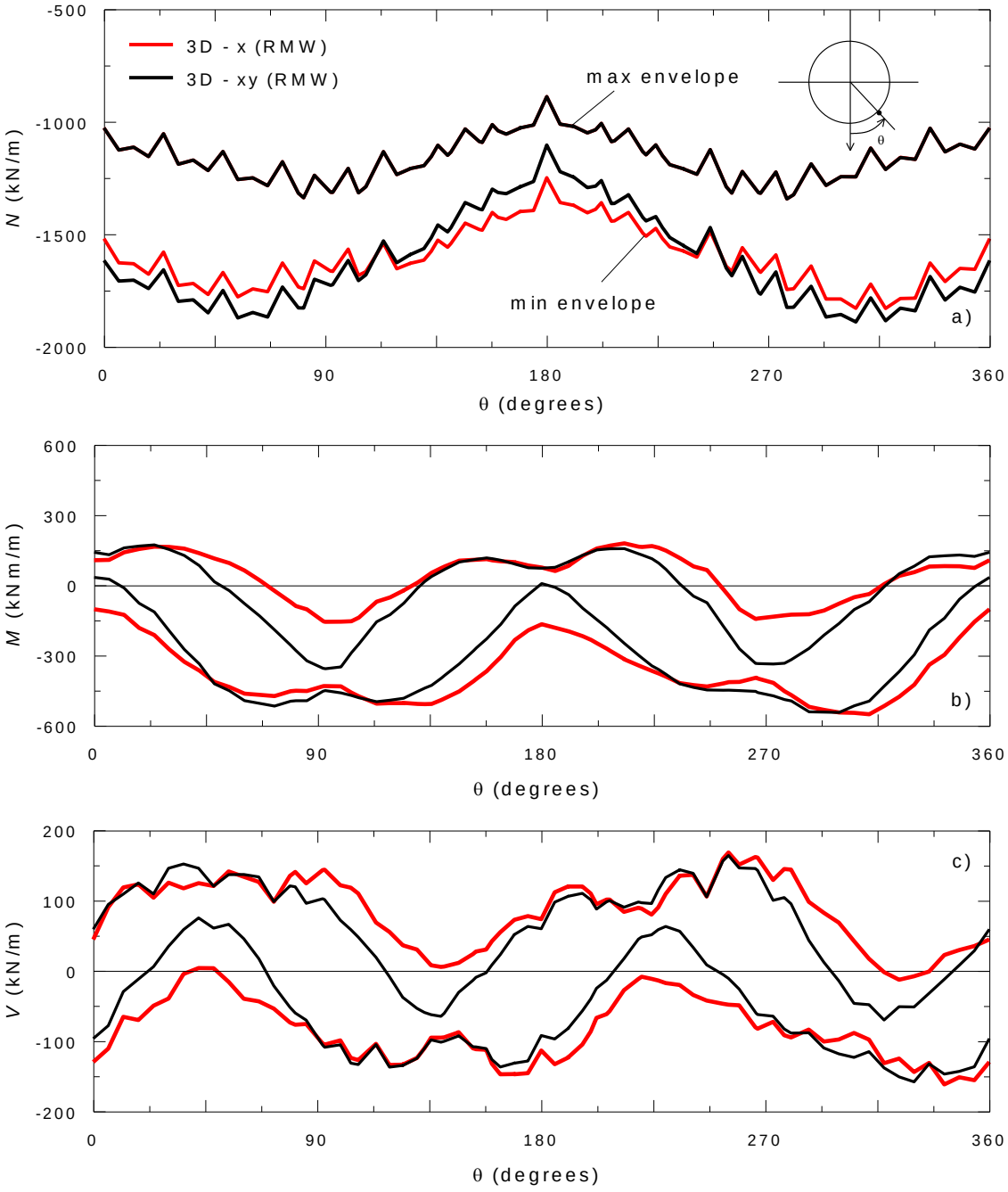

Figure 5.30 Distribution of maximum and minimum (a) hoop force; (b) transverse bending moment and (c) transverse shear force when the N-S component is applied transversely at bedrock and with both N-S and E-W components applied simultaneously using RMW

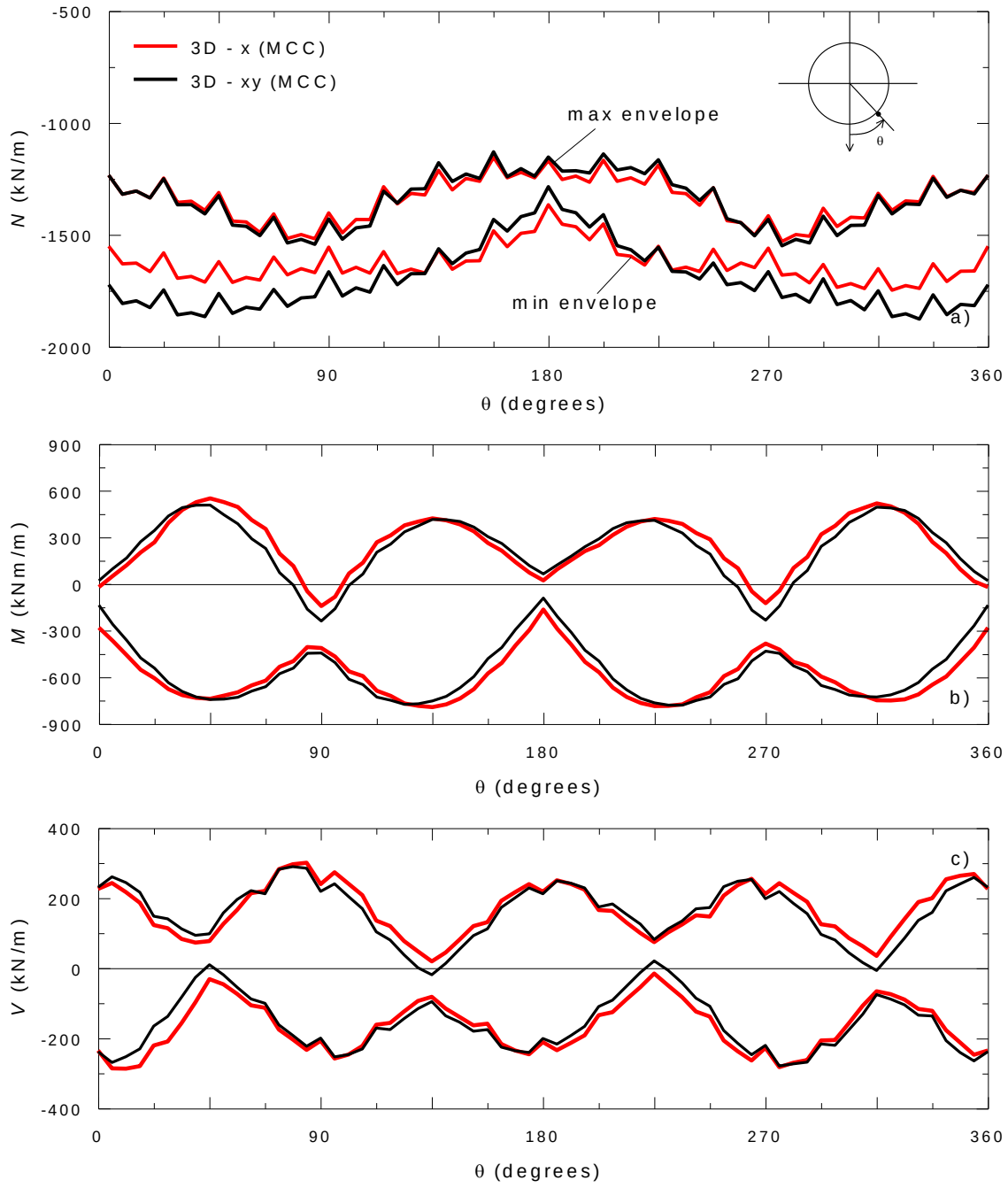

Figure 5.31 Distribution of maximum and minimum (a) hoop force; (b) transverse bending moment and (c) transverse shear force when the N-S component is applied transversely at bedrock and with both N-S and E-W components applied simultaneously using MCC

As a consequence of increased destructuration which further increases dissipation of the transverse earthquake accelerations in the longitudinal direction and thereby the longitudinal and shear strains in the tunnel, the maximum longitudinal compressive force in the lining has increased by as much as 805kN/m between θ = 0° to 90° and θ = 270° to 360° while the maximum longitudinal tensile force in the lining increases by about 743kN/m between θ = 90° to 270°, as indicated in Figure 5.32 (a). In addition, the shear force in the longitudinal direction (Figure 5.32 (c)) and in-plane shear [Figure

5.32 (e)] have increased to around 40kN/m and 625kN/m respectively. Unlike the longitudinal shear and torsional moment which remain insignificant, the in-plane shear has substantially increased in magnitude from 40kN/m to 625kN/m and has now become significant when the two earthquake components are applied simultaneously. The in-plane shear is crucial for the design of the bolted joint connections in segmental lining particularly in the circumferential joint and for the design of shear key joints for axial stresses relief in a continuous lining during a fault seismic rupture event (Young *et al.*, 2010). This internal force is also critical for designing shear keys to provide stability to TBM tunnels segmental lining during cross passages construction (Della Valle *et al.*, 2014). The in-plane shear which contributes to the total shear cannot be determined from a 2D model and therefore neglected in the design. Even in a 3D model, where only the transverse earthquake component is applied to the model as widely adopted by engineers in seismic design practice, the magnitude of the in-plane shear force, taken at the centre plane of the 3D model, only accounts for a very small percentage of the transverse shear force [refer to Figure 5.17 (c) and Figure 5.20 (e)] and is often disregarded. For the case study presented in this section, the in-plane shear contribution to the resultant shear is only 2.8% of the transverse shear when only the transverse earthquake component was applied to the model, whereas its contribution to the resultant shear has jumped to 285% of the transverse shear [refer to Figure 5.30 (c) and Figure 5.32 (e)] when the two earthquake components were applied simultaneously. Thus, it shows that the in-plane shear force can highly influence the design of the tunnel lining including the joints for multi-directional earthquake motion, hence highlighting the importance of considering the multi-directional effects of the seismic loading in designing tunnels.

As the simultaneous application of the two earthquake components corresponds to an equivalent resultant wave propagating at an angle with the tunnel axis, these numerical results agree well with the solutions developed by St John and Zahrah (1987), who observed the occurrence of maximum longitudinal and shear strains (and hence maximum longitudinal and shear force) when the direction of the wave propagation is at an angle with the axis of the tunnel. Nevertheless, the distribution of maximum and minimum longitudinal bending moment and torsional moment for 3D – xy remain relatively unchanged or lower than 3D – x [Figure 5.32 (b & d)] as these

forces are predominantly affected by the earthquake components perpendicular to the axis of the tunnel.

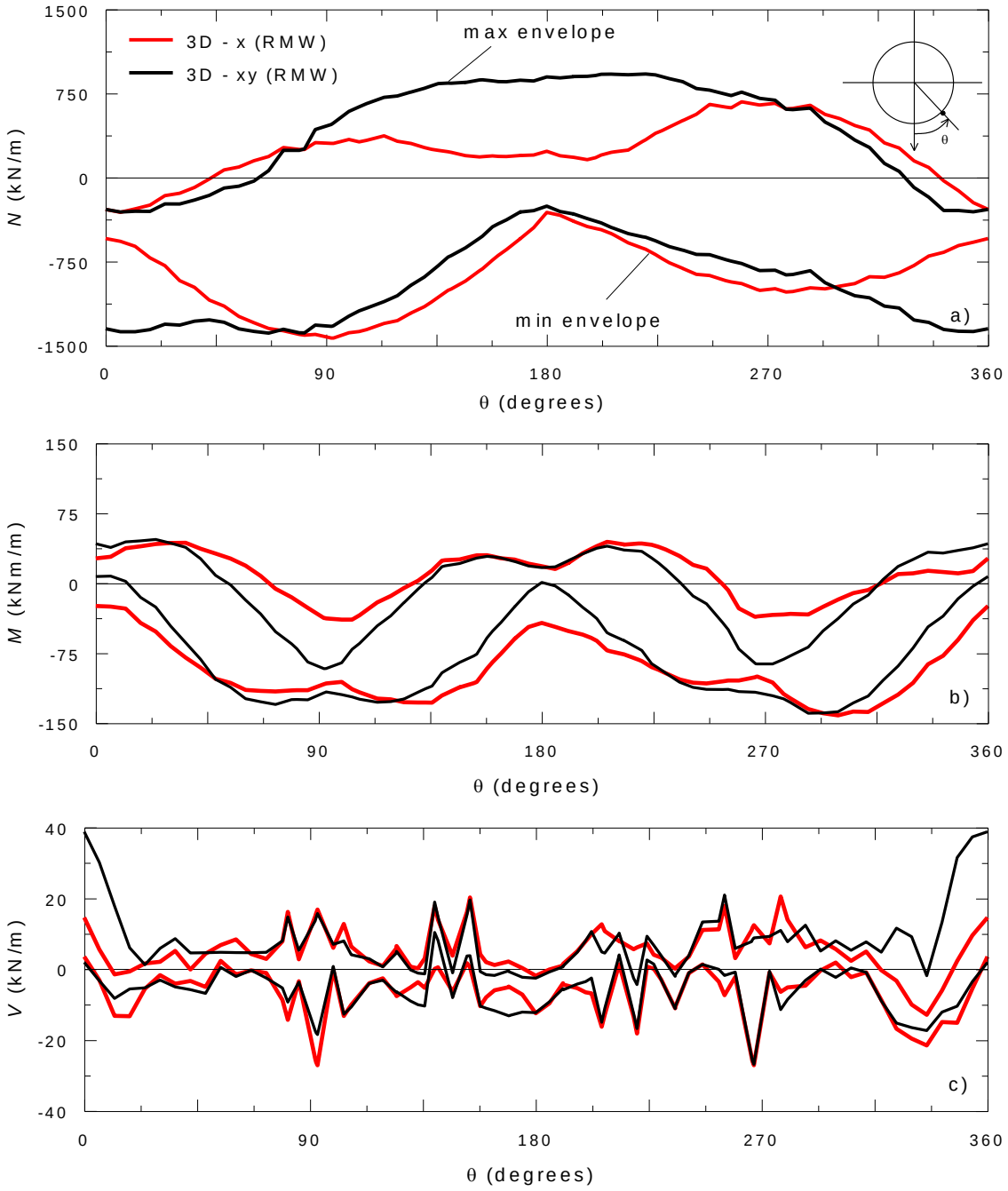

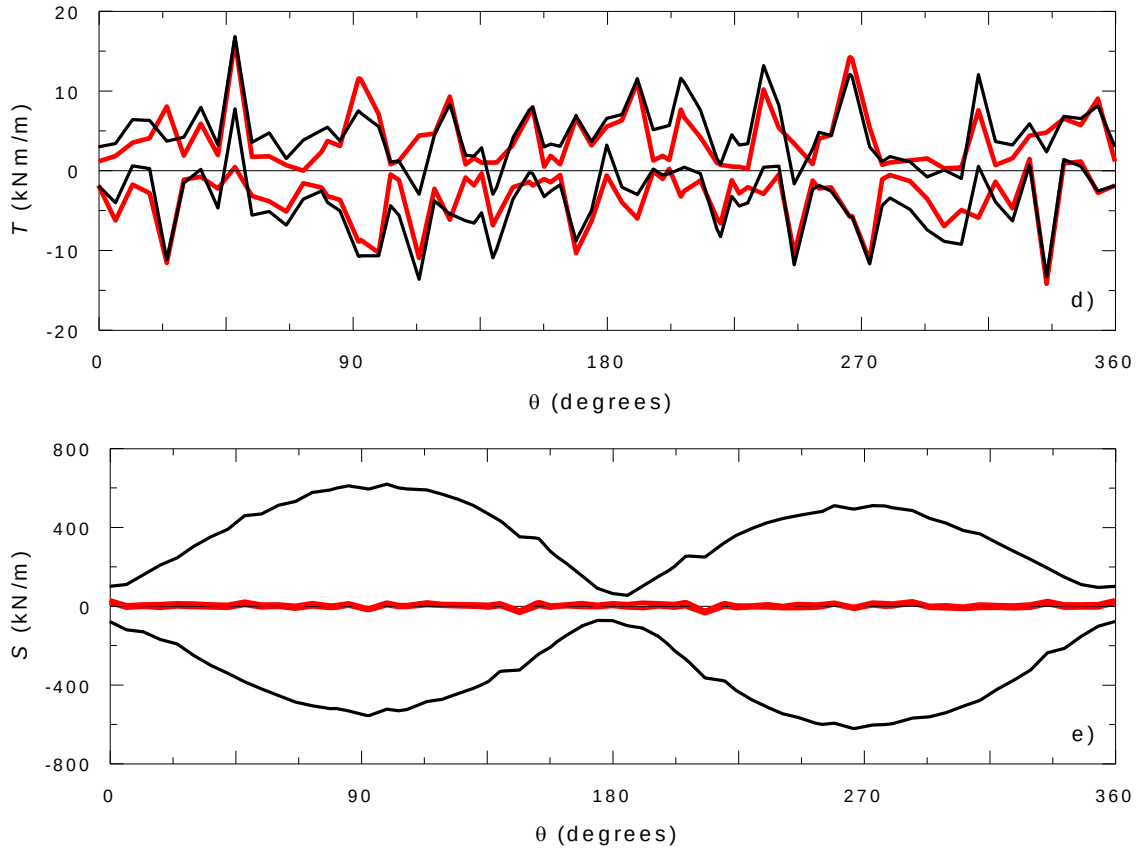

Figure 5.32 Distribution of maximum and minimum (a) longitudinal axial force; (b) longitudinal bending moment; (c) longitudinal shear force; (d) torsional moment and (e) in-plane shear when the N-S component is applied transversely at bedrock and with both N-S and E-W components applied simultaneously using RMW

The time histories of transverse shear strain at chosen points between the case of imposing simultaneously both transverse and longitudinal earthquake components (3D – xy) and that with only the transverse component applied (3D – x) as shown in Figure 5.33 (a & c) are relatively comparable indicating very similar behaviour in the transverse direction. The coupled effective stress simulations predict the build-up of positive pore pressures above the tunnel invert and negative pore pressures below it, associated with the accumulation of permanent soil deformations and structure degradation throughout the earthquake motions. Figure 5.33 (b & d) show the time histories of excess pore water pressures predicted along the tunnel vertical for the 3D – xy and 3D – x models, respectively. The plots indicate an increase in excess pore pressure at the tunnel invert (25m from ground surface) from 99kPa when only the transverse earthquake component was applied at the bedrock to 233kPa when both earthquake components were applied simultaneously. Also, the excess pore water pressure at the tunnel crown (15m from ground surface) was predominantly negative pore pressure during the whole period of seismic event for 3D – xy while it jumped to

positive pore pressure at around 9 seconds at approximate peak of the input excitation for 3D – x. It can also be seen from the figures that the pore water pressures near the bedrock (70m from ground surface) for 3D – xy have also increased when compared to the pore pressures for 3D – x case. The results demonstrate the strong influence of imposing the longitudinal component of the earthquake motion in addition to the transverse component resulting to higher strains in the longitudinal direction and higher degree of soil destructuration causing disparities in the magnitude of the pore water pressures.

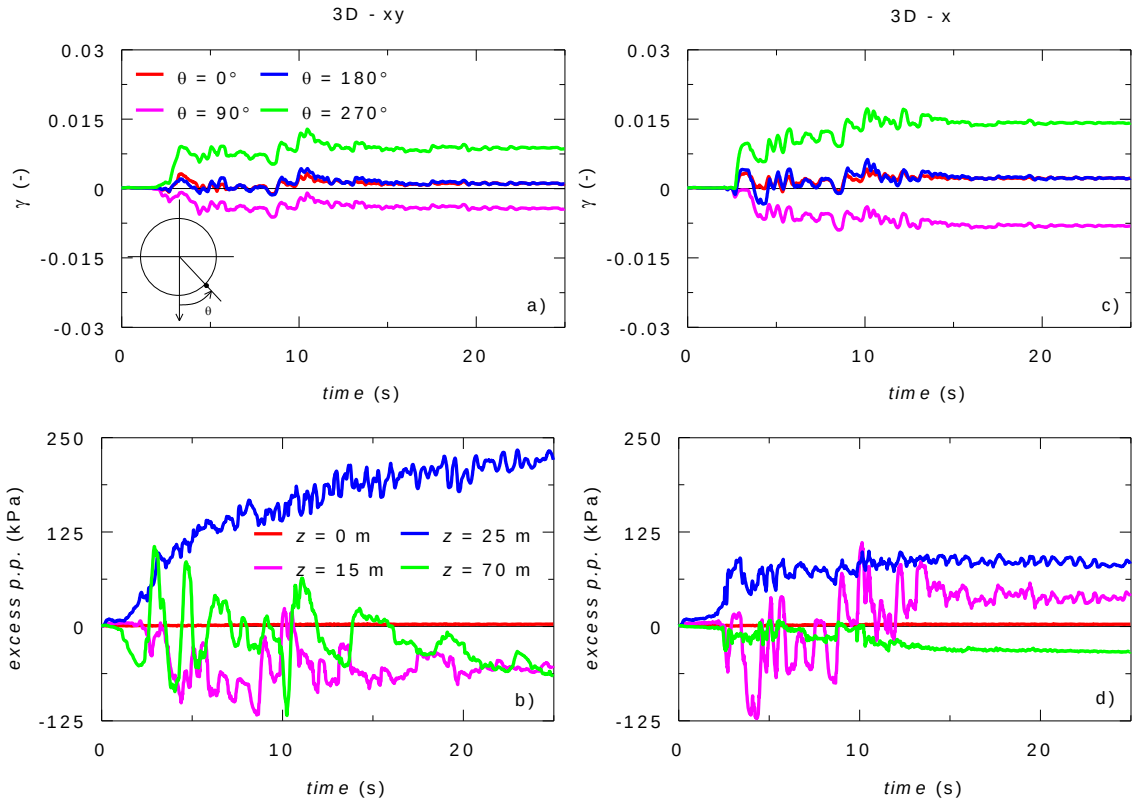

Figure 5.33 Time histories of shear strain and excess pore pressure of RMW model for (a–b) 3D when the N-S and E-W components are applied simultaneously and (c–d) 3D when the N-S component is applied transversely

Figure 5.34 shows the contours of the RMW parameter *r*, describing the degree of soil structure, obtained at the end of the seismic event for both 3D - x and 3D – xy cases. The contours indicate increased structure degradation induced in the soil deposit resulting from the imposition of the longitudinal earthquake component in addition to the transverse component. It also shows that a higher degree of destructuration occurred at the bottom section of the model as a result of the simultaneous application of both earthquake components [Figure 5.34 (b)]. This is due to a significant increase in the longitudinal shear strains particularly γ_{yz} as evident in Figure

5.28 (c) and Figure 5.29 (c). As expected, the structure degradation also increased in the soil surrounding the tunnel when both earthquake components were applied concurrently (Figure 5.35) which is consistent with the higher longitudinal shear strain levels in the same locations.

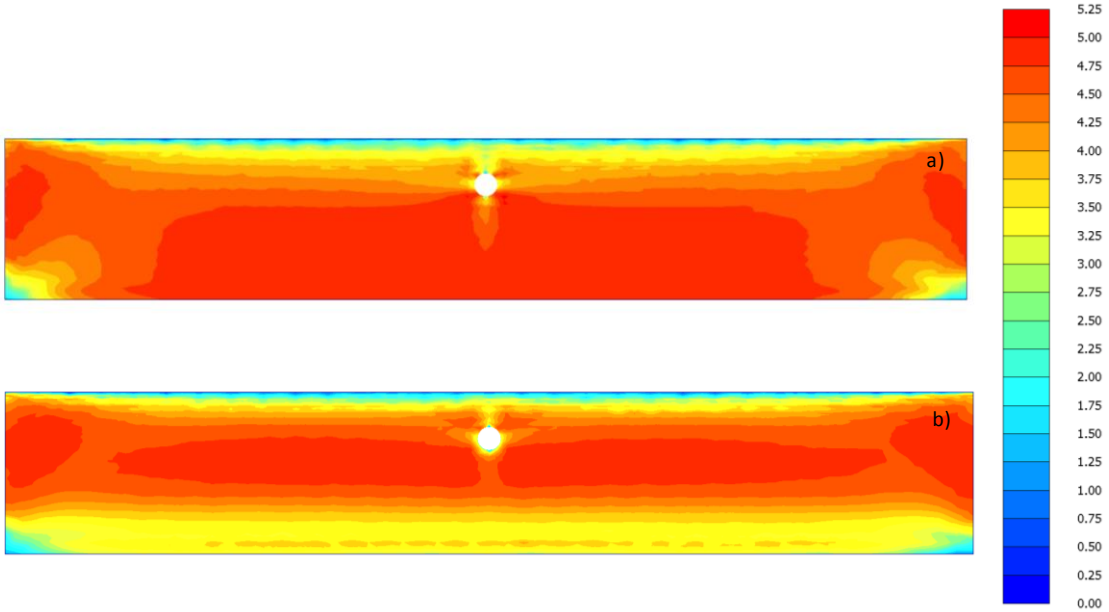

Figure 5.34 Contours of the RMW parameter *r* at the end of the seismic event for (a) 3D when the N-S component is applied transversely and (b) when both N-S and E-W components are applied simultaneously

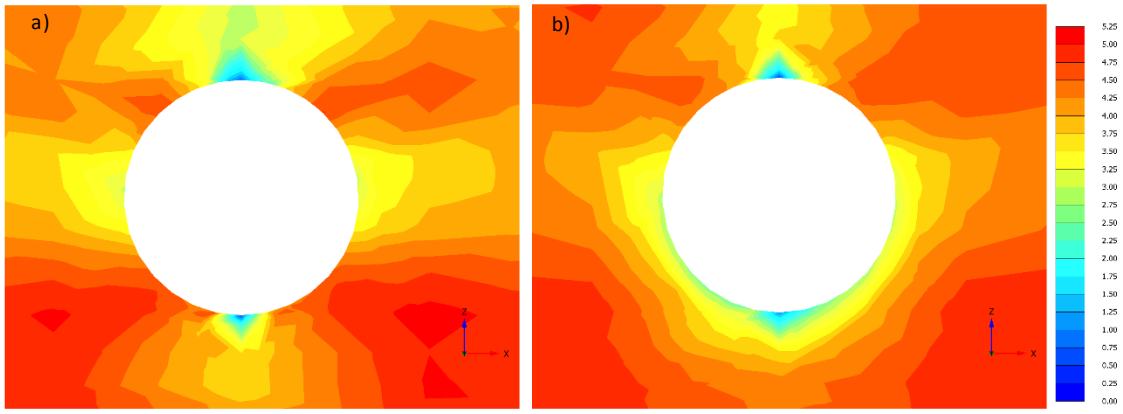

Figure 5.35 Contours of the RMW parameter *r* at the end of the seismic event around the tunnel for (a) 3D when the N-S component is applied transversely and (b) when both N-S and E-W components are applied simultaneously

5.2.3 *Effects of multidirectional seismic loading along the tunnel length*

In addition to the effects of the three-dimensional geometry of the numerical model on the propagation of the seismic waves and of the multi-directionality of the seismic load on the tunnel lining forces, the 3D model has also been assessed on its ability to predict the variation of lining forces along the length of the tunnel. The results were

extracted along the centre plane of the 3D FEM model (i.e. at 50m along the tunnel length) and compared with those at 25m and 75m along the tunnel length. Both cases of only N-S earthquake component applied transversely at bedrock (3D – x) and with both N-S and E-W components applied simultaneously (3D – xy) are considered.

N-S earthquake component applied transversely at bedrock (3D – x)

Figure 5.36 shows the profiles of the minimum and maximum transverse horizontal (a_x), longitudinal horizontal (a_y) and vertical (a_z) accelerations recorded along the soil depth and obtained in free-field conditions at different sections along the tunnel length (i.e. 25m, 50m and 75m) when only N-S earthquake component is applied transversely at the bedrock (denoted as 3D – x). Similar acceleration profiles at tunnel vertical locations are presented in Figure 5.37. As expected, the transverse horizontal acceleration a_x and vertical acceleration a_z remains typically similar in the free-field condition and at tunnel vertical along the longitudinal length of the tunnel as shown in Figure 5.36 (a & c) and Figure 5.37 (a & c) respectively. However, it can be observed that a_x and a_z at the center plane (i.e. at 50m along the tunnel length) are slightly higher than at 25m and 75m sections which is due to the dissipation of the seismic wave in the longitudinal direction as previously established in Section 5.2.1. As a consequence, the longitudinal horizontal acceleration a_y at soil depth changes along the tunnel length as seen in Figure 5.36 (b) and Figure 5.37 (b). The plots show that the acceleration is lowest at the centre plane and increases as the distance moves away from the centre plane.

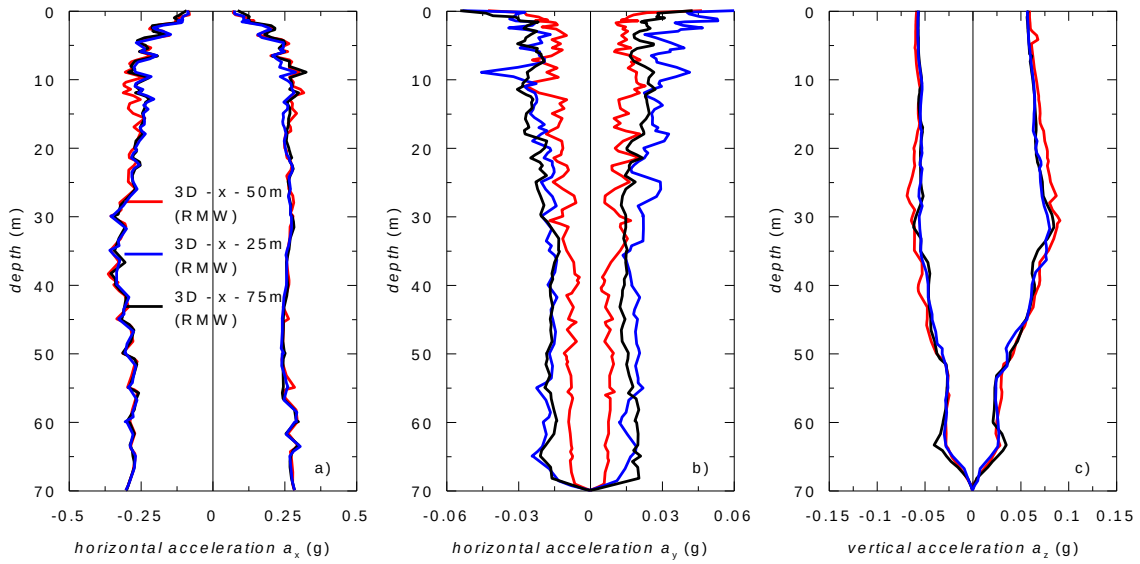

Figure 5.36 Profiles of max and min (a) horizontal acceleration a_x, (b) horizontal acceleration a_y and (c) vertical acceleration a_z recorded in free-field conditions at a distance of 25m, 50m and 75m along the tunnel length when the N-S component is applied transversely using RMW

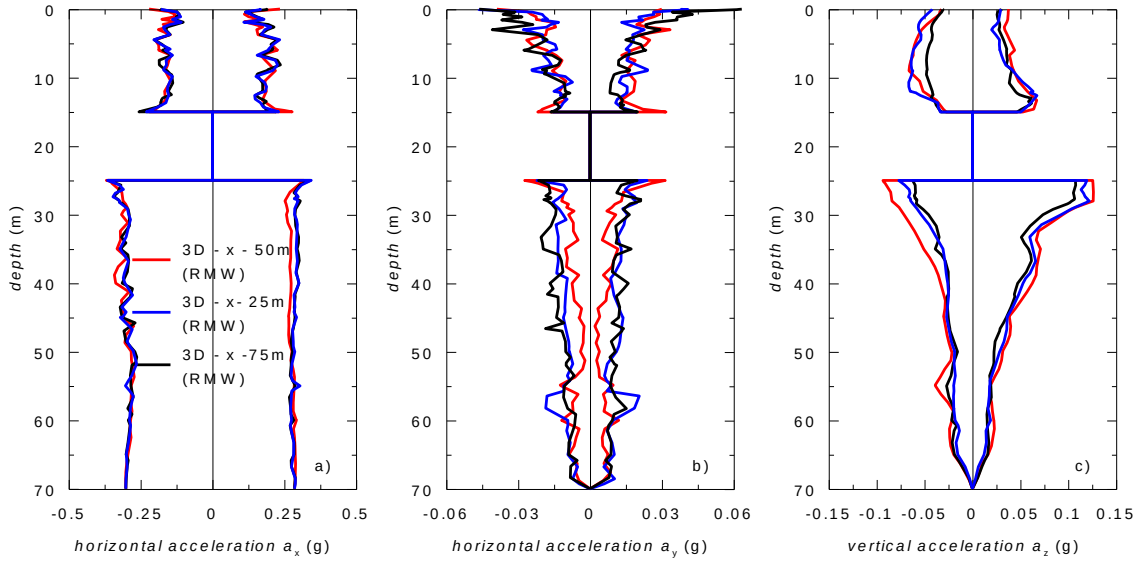

Figure 5.37 Profiles of max and min (a) horizontal acceleration a_x, (b) horizontal acceleration a_y and (c) vertical acceleration a_z recorded at tunnel vertical at a distance of 25m, 50m and 75m along the tunnel length when the N-S component is applied transversely using RMW

Following the same trend as the acceleration profiles, the corresponding transverse shear strains γ_{zx} in free-field conditions [Figure 5.38 (a)] and at tunnel vertical [Figure 5.39 (a)] are very similar at sections along the tunnel length while the longitudinal shear strains γ_{xy} [Figure 5.38 (b) and Figure 5.39 (b)] and γ_{yz} [Figure 5.38 (c) and Figure 5.39 (c)] increase as the distance moves away from the centre plane.

The observations above illustrate that the transverse behaviour of the 3D model is almost similar at every section along the longitudinal direction when only the

transverse earthquake component is applied on the model. The deformed shape of the tunnel at the end of the earthquake [Figure 5.40 (a) and Figure 5.41 (a, b & c)] shows that the relative displacement is almost constant throughout the whole length such that the tunnel moved as one unit. It can be deduced from the deformed shape and relative displacement of the tunnel as well as in the contours of transverse displacements u_x and u_z [Figure 5.42 (a & c)] that the whole length of the tunnel moved almost uniformly in the *x* and *z* directions during earthquake, thus, the transverse behaviour of the tunnel will be constant along the tunnel length. However, the longitudinal displacement u_y of the tunnel varies as shown in Figure 5.42 (b) which indicates the longitudinal compression-extension behaviour due to the longitudinal acceleration and longitudinal shear strains brought about by the 3D spatial effects. Those figures also show that at the tunnel ends, the viscous boundaries employed in the model do not restrict movement of the tunnel in any direction, thus, properly simulating free field conditions at the boundaries. Contours of the degree of soil structure *r* obtained at the end of the seismic event across those three sections along the tunnel length (Figure 5.43) indicate very similar structure degradation in all three sections. Therefore, in this case, the transverse results are mainly affected by the spatial effects and have insignificant influence from the soil destructuration.

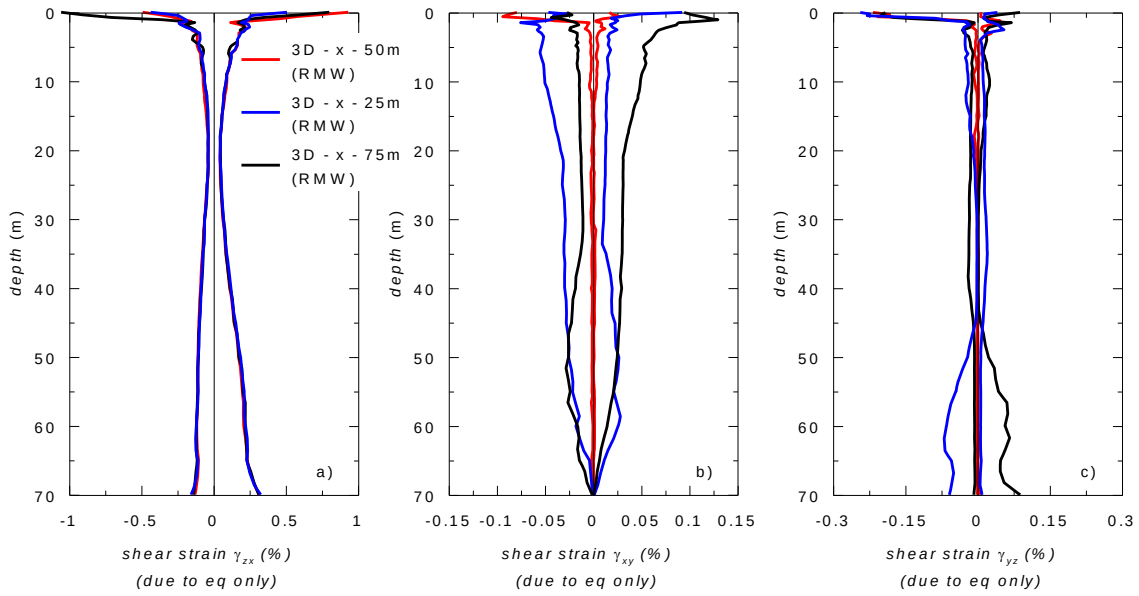

Figure 5.38 Profiles of max and min (a) transverse shear strain γ_{zx}, (b) longitudinal shear strain γ_{xy} and (c) longitudinal shear strain γ_{yz} recorded in free-field conditions at a distance of 25m, 50m and 75m along the tunnel length when the N-S component is applied transversely using RMW

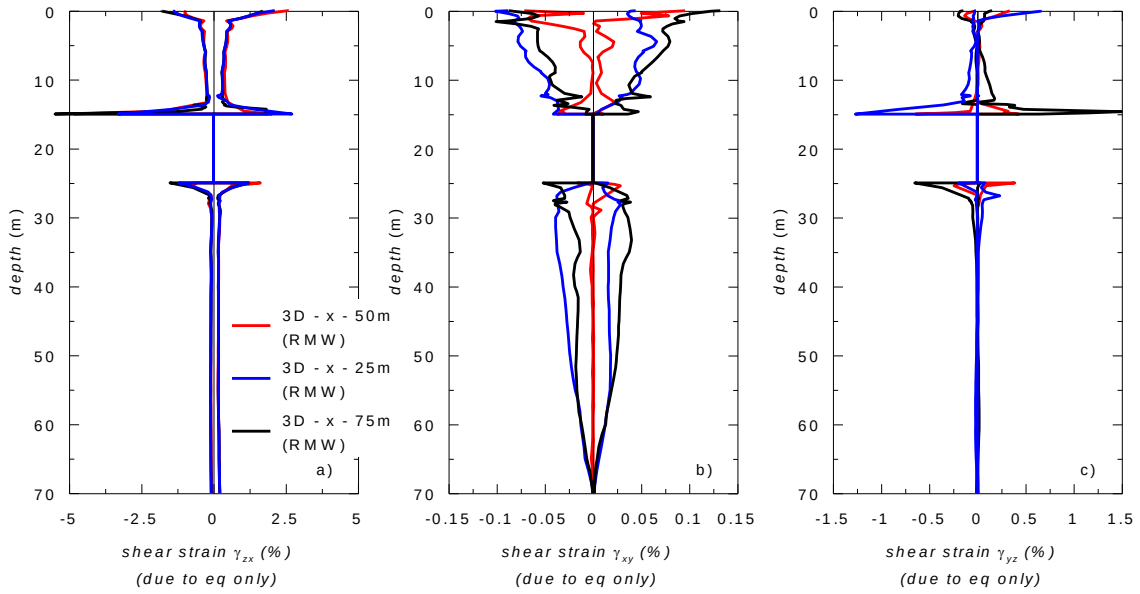

Figure 5.39 Profiles of max and min (a) transverse shear strain γ_{zx}, (b) longitudinal shear strain γ_{xy} and (c) longitudinal shear strain γ_{yz} recorded at tunnel vertical at a distance of 25m, 50m and 75m along the tunnel length when the N-S component is applied transversely using RMW

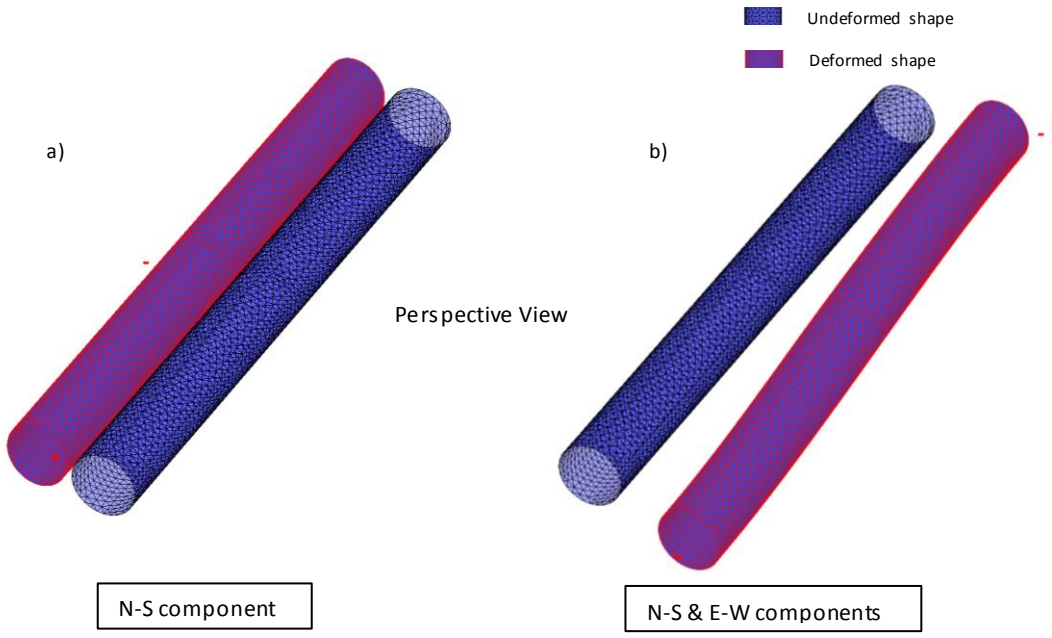

Figure 5.40 3D deformed shape of the tunnel at the end of the seismic action using RMW (a) when the N-S component is applied transversely and (b) when both N-S and E-W components applied simultaneously

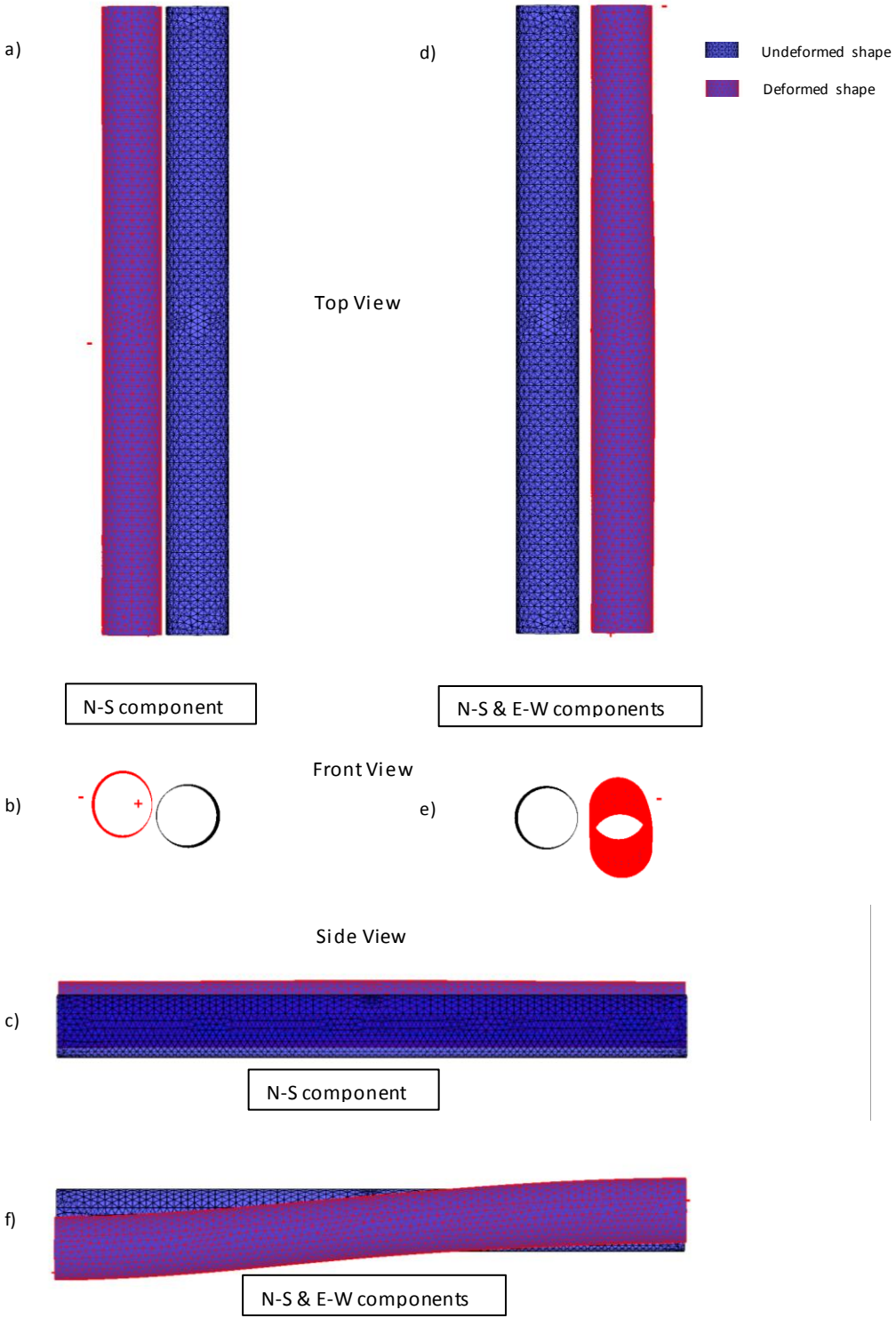

Figure 5.41 3D deformed shape of the tunnel and relative displacement at the end of the seismic action using RMW when the N-S component is applied transversely: (a) top view; (b) front view & (c) side view and when both N-S and E-W components applied simultaneously: (d) top view; (e) front view & (f) side view

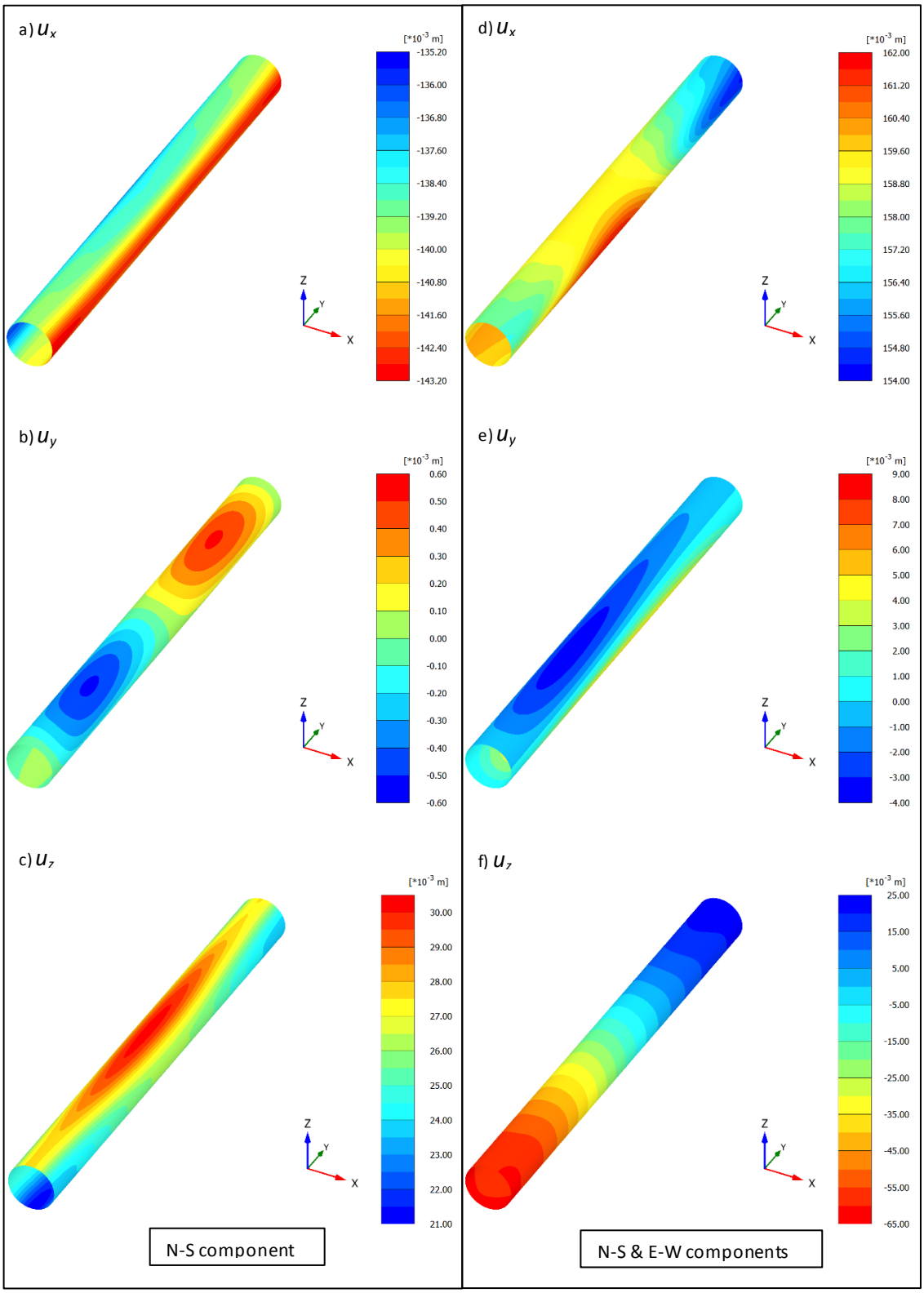

Figure 5.42 3D displacement of the tunnel at the end of the seismic action: (a) & (d) u_x; (b) & (e) u_y and (c) & (f) u_z when the N-S component is applied transversely using RMW and when both N-S and E-W components applied simultaneously using RMW

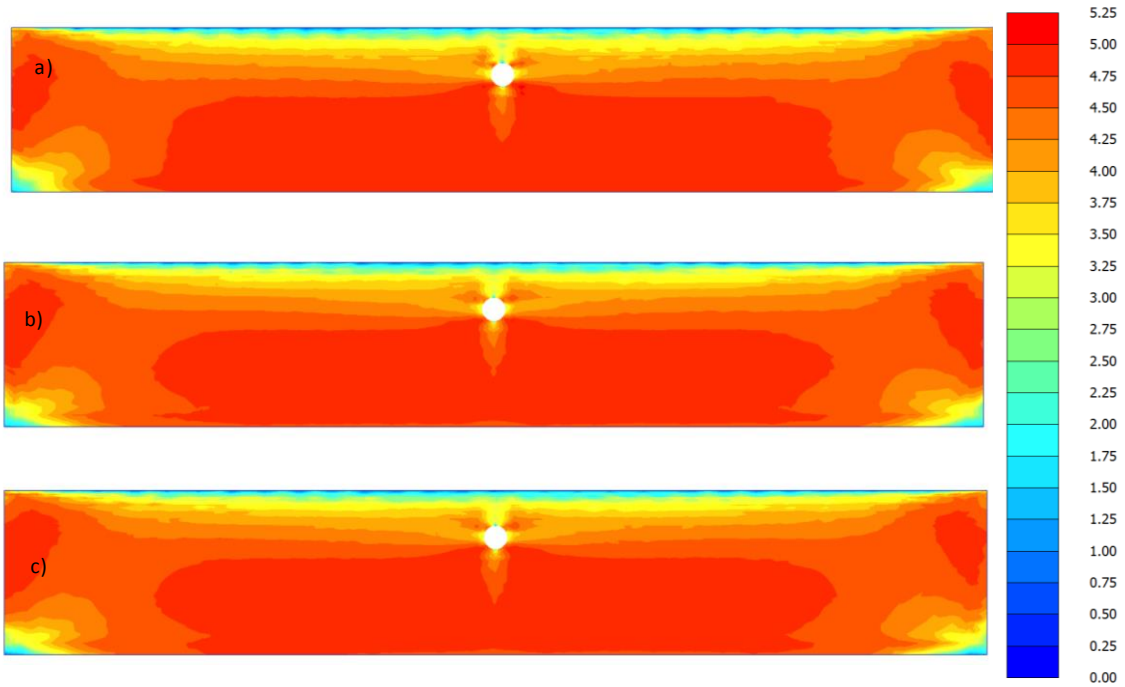

Figure 5.43 Contours of the RMW parameter *r* at the end of the seismic event at a distance of (a) 50m; (b) 25m; and (c) 75m along the tunnel length when the N-S component is applied transversely

In terms of seismic influence on the tunnel lining forces, the predicted hoop force, transverse bending moment and transverse shear force results at the end of seismic action are comparable across all sections along the tunnel length [Figure 5.44 (a, b & c)], when only the transverse earthquake component is considered which agree with the acceleration and strain profiles as well as the deformed shape. These findings are validated by plotting the minimum and maximum transverse forces at 25m, 50m and 75m along the tunnel length as shown Figure 5.45 indicating an almost similar magnitude at different sections of the tunnel. The MCC results in the study by Cabangon *et al.* (2018) in London clay and a variation of that study in Avezzano clay (Figure 5.46) show a similar trend. This further demonstrates that the transverse behaviour of the tunnel throughout the length, when only the transverse earthquake component is applied, remains typically similar in every section, with very slight differences due to the spatial effects, when the degree of destructuration is constant along the length or the soil structure is not considered. In addition, the longitudinal bending moments and torsional moments are also similar along the tunnel length as shown in Figure 5.47 (b & d) and Figure 5.48 (b & d) as these forces are predominantly affected by the transverse earthquake component.

On the other hand, the wave scattering and dissipation of the seismic wave longitudinally and corresponding 3D soil-structure interaction responses cause the longitudinal axial forces, longitudinal shear forces and in-plane shear forces to vary along the tunnel length as illustrated in Figure 5.47 (a, c & e) and Figure 5.48 (a, c & e). Some of these variations are quite substantial particularly in the longitudinal axial force where the maximum tensile force of 674kN/m at 50m along the tunnel length becomes a compressive force of 307kN/m at 25m and 75m sections along the tunnel length due to the longitudinal compression-extension as observed by other researchers [e.g. (Owen and Scholl, 1981)]. Also, the maximum compressive force of 1433kN/m at 50m has decreased to 733kN/m at 25m and 75m. Likewise the in-plane shear has significantly increased in its magnitude from 40kN/m at 50m along the tunnel length to 474kN/m at 25m and 75m sections along the tunnel length. Even though it is only the transverse earthquake that has been applied to the model, the magnitude of the longitudinal forces which are deemed to be crucial in tunnel lining design as previously mentioned in Section 5.2.2 particularly the longitudinal axial force and in-plane shear have changed dramatically along the tunnel length. From these results, it signifies that it is not just the multidirectional seismic loading as observed in Section 5.2.2 which can affect heavily the longitudinal forces but also the 3D soil-tunnel interaction effects along the tunnel length (e.g. longitudinal compression-extension). Ignoring these variations in the magnitude of longitudinal forces can lead to unsafe design and therefore these 3D effects should need be considered in every aspect of the seismic design of the tunnels.

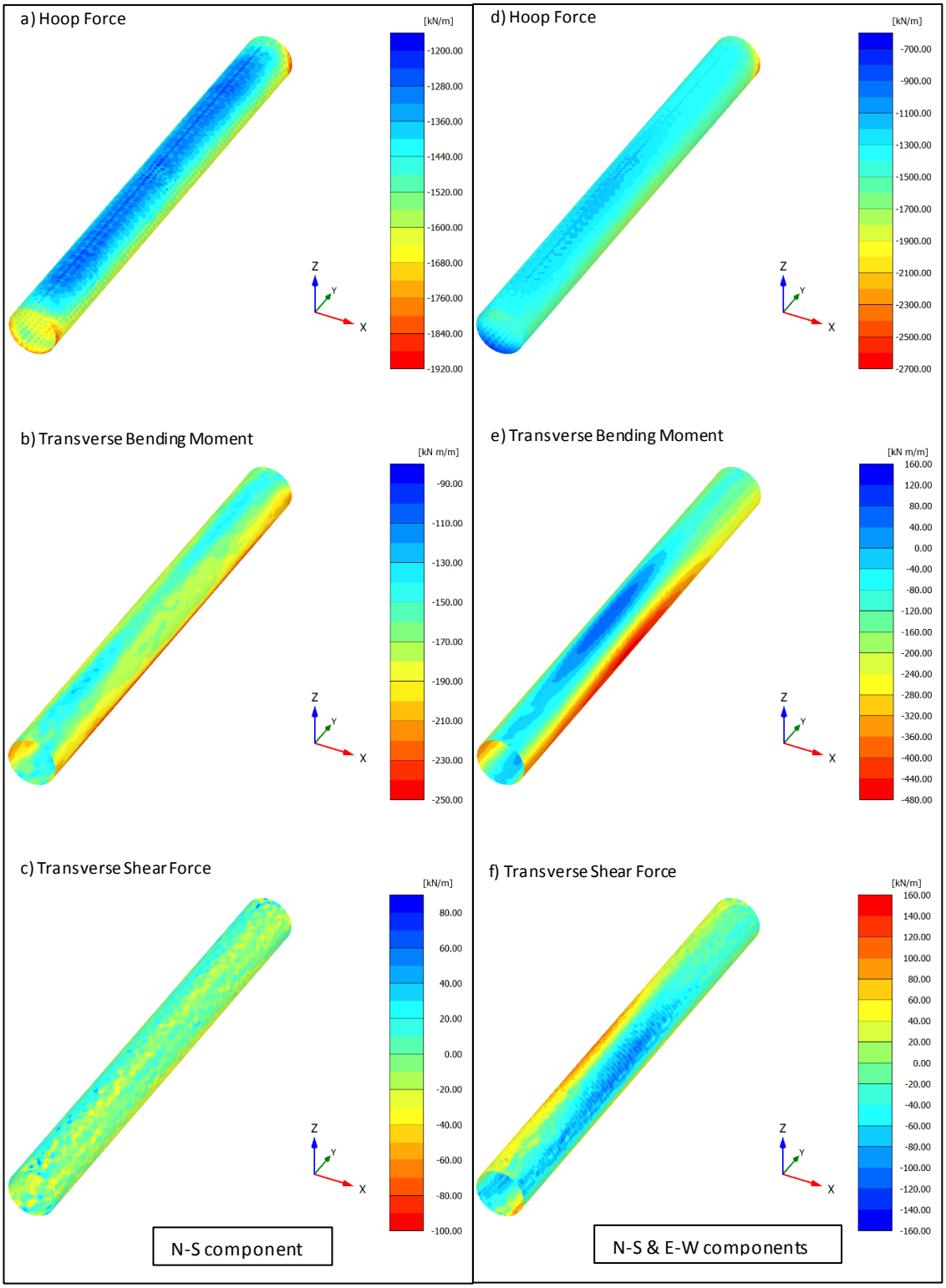

Figure 5.44 Contours of (a) & (d) hoop force; (b) & (e) transverse bending moments; and (c) & (f) transverse shear forces at the end of the seismic action along the tunnel when the N-S component is applied transversely and when both N-S and E-W components applied simultaneously using RMW

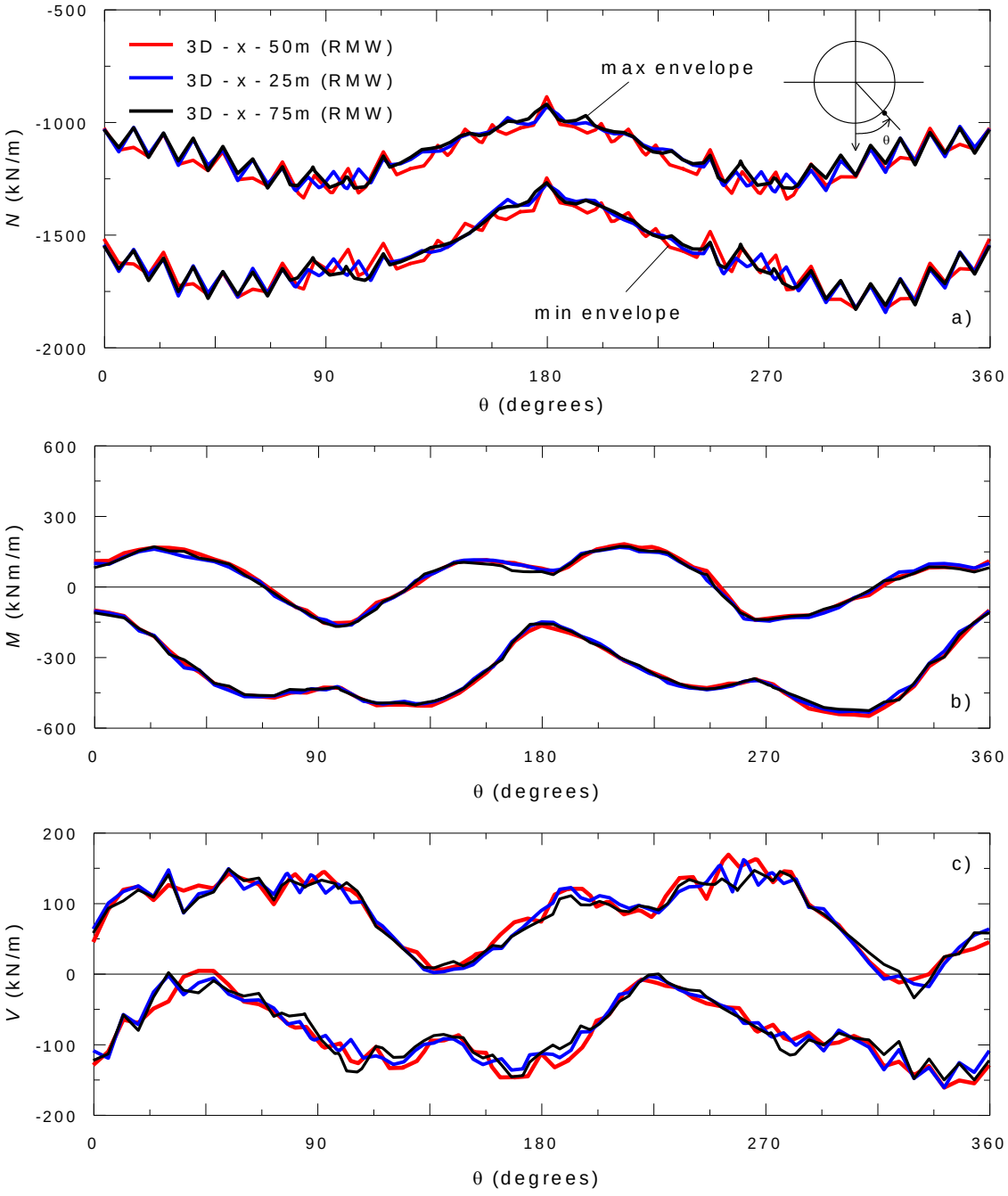

Figure 5.45 Comparison at a distance of 25m, 50m and 75m along the tunnel length of minimum and maximum (a) hoop force; (b) transverse bending moment and (c) transverse shear force when the N-S component is applied transversely using RMW

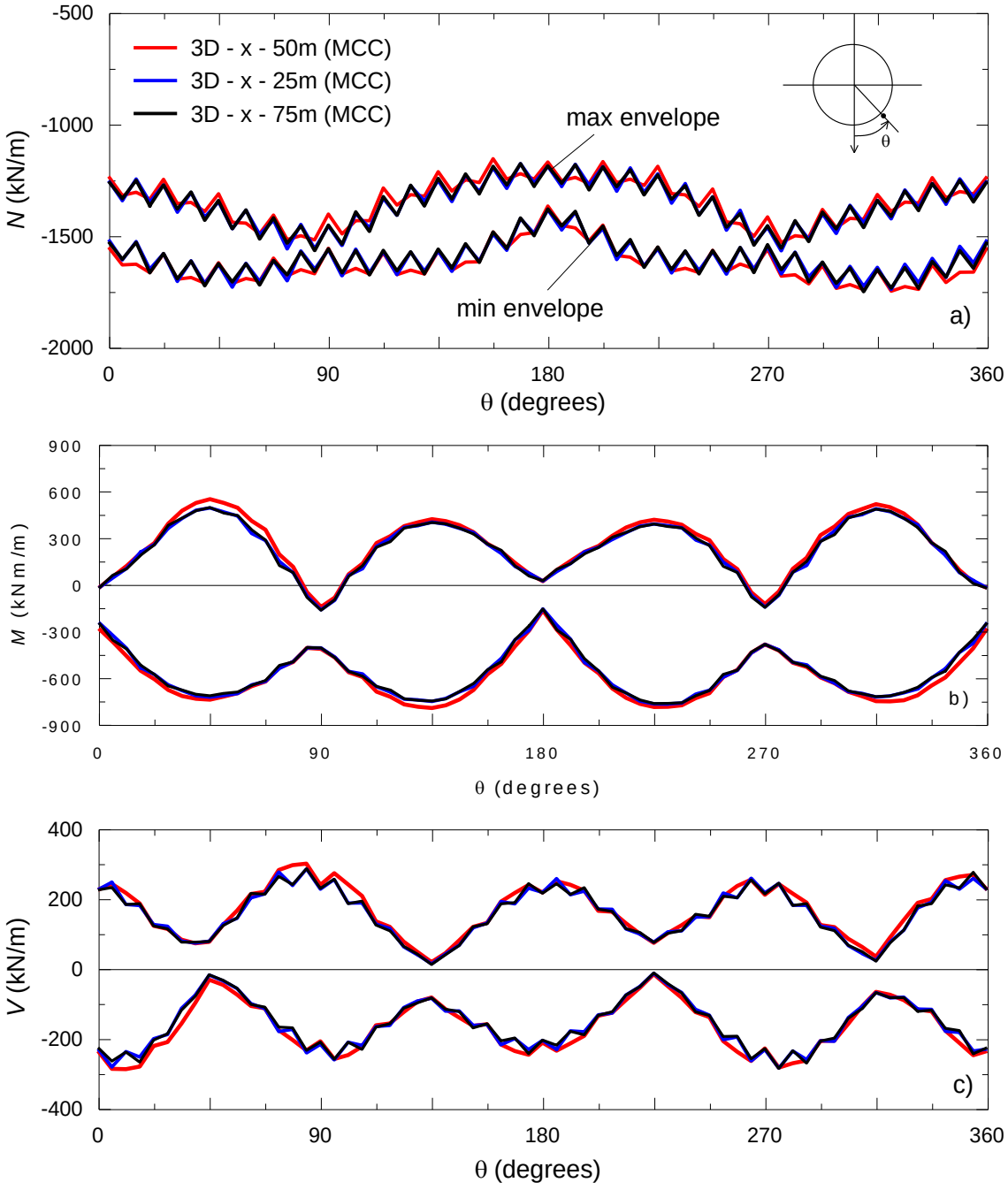

Figure 5.46 Comparison at a distance of 25m, 50m and 75m along the tunnel length of minimum and maximum (a) hoop force; (b) transverse bending moment and (c) transverse shear force when the N-S component is applied transversely using MCC

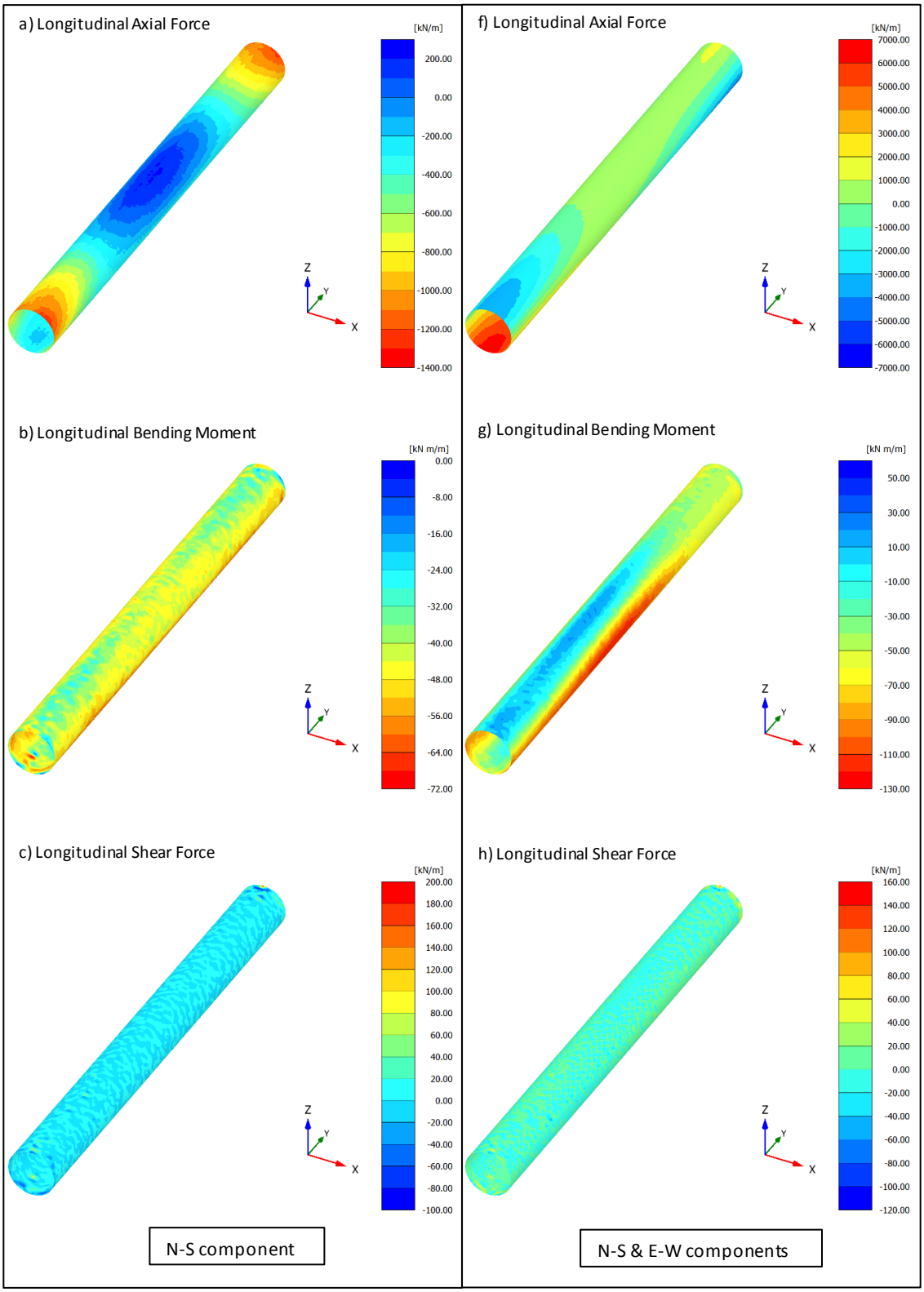
a) Longitudinal Axial Force
[kN/m]
200.00
0.00
-200.00
-400.00
-600.00
-800.00
-1000.00
-1200.00
-1400.00
Z
Y
X
b) Longitudinal Bending Moment
[kN m/m]
0.00
-8.00
-16.00
-24.00
-32.00
-40.00
-48.00
-56.00
-64.00
-72.00
Z
Y
X
c) Longitudinal Shear Force
[kN/m]
200.00
180.00
160.00
140.00
120.00
100.00
80.00
60.00
40.00
20.00
0.00
-20.00
-40.00
-60.00
-80.00
-100.00
Z
Y
X
N-S component
f) Longitudinal Axial Force
[kN/m]
7000.00
6000.00
5000.00
4000.00
3000.00
2000.00
1000.00
0.00
-1000.00
-2000.00
-3000.00
-4000.00
-5000.00
-6000.00
-7000.00
Z
Y
X
g) Longitudinal Bending Moment
[kN m/m]
50.00
30.00
10.00
-10.00
-30.00
-50.00
-70.00
-90.00
-110.00
-130.00
Z
Y
X
h) Longitudinal Shear Force
[kN/m]
160.00
140.00
120.00
100.00
80.00
60.00
40.00
20.00
0.00
-20.00
-40.00
-60.00
-80.00
-100.00
-120.00
Z
Y
X
N-S & E-W components

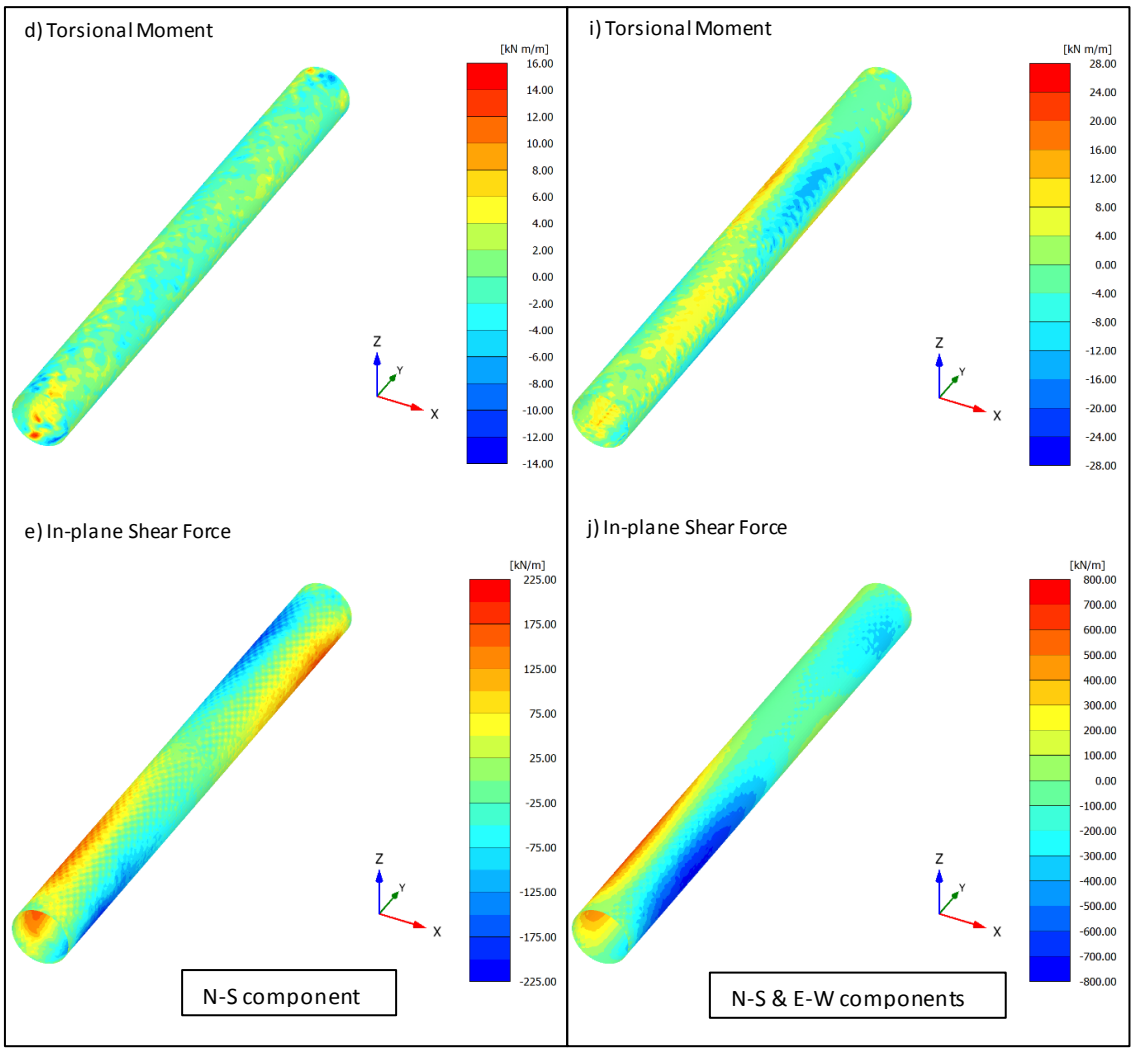

Figure 5.47 Contours of (a) & (f) longitudinal axial forces; (b) & (g) longitudinal bending moments; (c) & (h) longitudinal shear forces; (d) & (i) torsional moment; and (e) & (j) in-plane shear force at the end of the seismic action along the tunnel when the N-S component is applied transversely and when both N-S and E-W components applied simultaneously using RMW

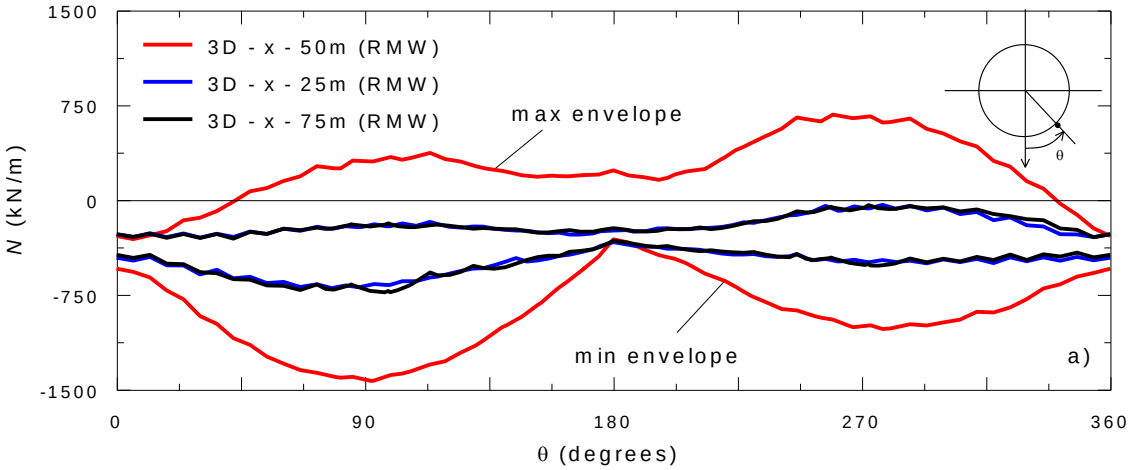
3D - x - 50m (RMW)
3D - x - 25m (RMW)
3D - x - 75m (RMW)
max envelope
min envelope
θ
a)
N (kN/m)
1500
750
0
-750
-1500
0
90
180
270
360
θ (degrees)

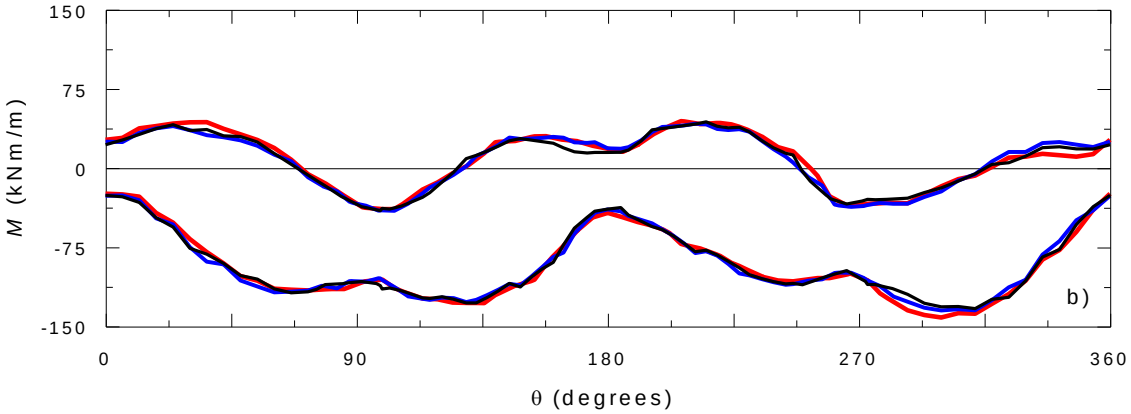
b)
M (kNm/m)
150
75
0
-75
-150
0
90
180
270
360
θ (degrees)

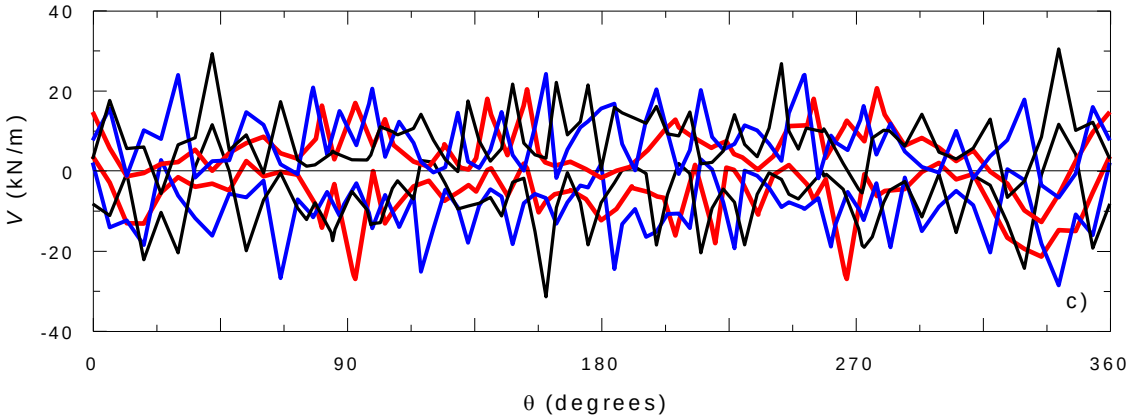
c)
V (kN/m)
40
20
0
-20
-40
0
90
180
270
360
θ (degrees)

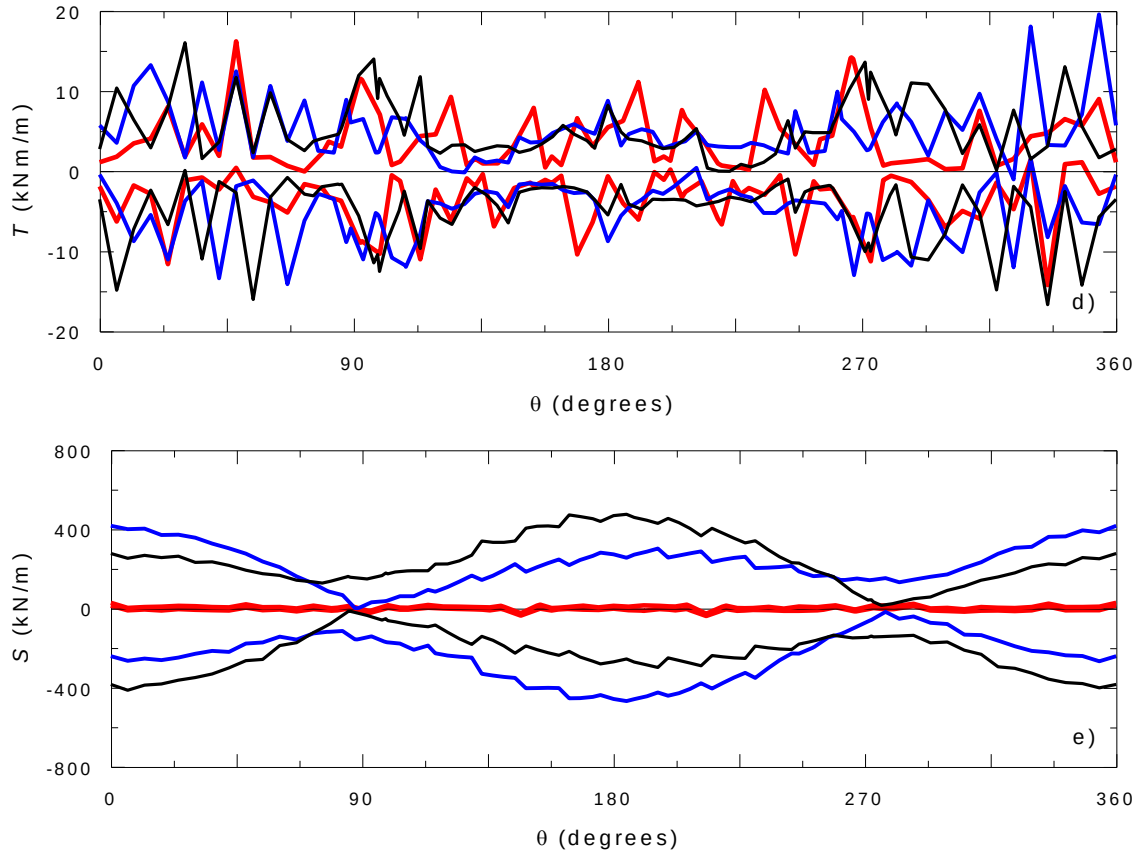

Figure 5.48 Comparison at a distance of 25m, 50m and 75m along the tunnel length of minimum and maximum (a) longitudinal axial force; (b) longitudinal bending moment; (c) longitudinal shear force; (d) torsional moment and (e) in-plane shear when the N-S component is applied transversely using RMW

Figure 5.49 shows the time histories of shear strain and excess pore water pressures at tunnel vertical recorded at 25m, 50m and 75m along the tunnel length when the N-S component is applied transversely. The transverse shear strain at chosen points at different sections along the tunnel length with only the transverse component applied as shown in Figure 5.49 (a-c) are relatively comparable but just slightly less as the section moves away from the centre plane indicating very similar behaviour in the transverse direction. On the other hand, the variation in pore water pressure response is evident with slight changes along the tunnel length [Figure 5.49 (d-f)]. The disparity can be attributed to approximating the stress point locations of the points being compared which might not be exactly compatible or in line with each other due to the difference in the mesh arrangement at every section. Nevertheless, it predicts similar trend where build-up of positive pore pressures occurs above the tunnel invert and negative pore pressures below it. Figure 5.43 shows the contours of RMW parameter *r*, describing the degree of soil structure, obtained at the end of the seismic event at different sections along the longitudinal length. The contours indicate very similar

structure degradation induced in the soil deposit along the length of the tunnel when only the N-S component is applied transversely which is of similar response to a 2D plane strain model. As expected, the structure degradation in the soil surrounding the tunnel is also very similar along the tunnel length as illustrated in Figure 5.50. Therefore, the structure degradation of the soil remains unchanged throughout the length of the tunnel. A more pronounced structure degradation though can be observed in the soil at the tunnel crown and invert as well as at the tunnel spring line which is consistent with the higher shear strain levels in the same locations.

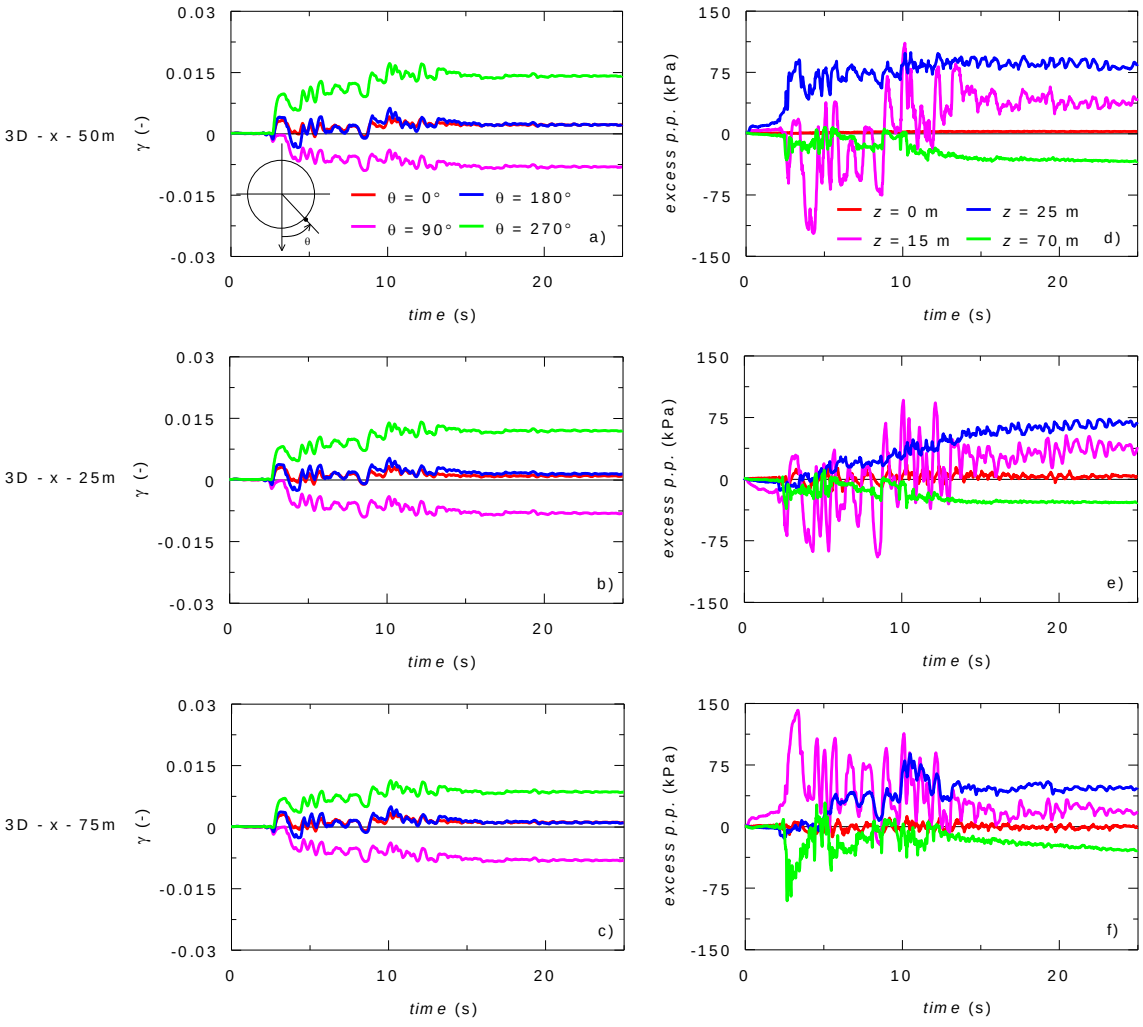

Figure 5.49 Time histories of (a-c) shear strain and (d-f) excess pore pressure of RMW model at 50m, 25m, and 75m along the tunnel length when the N-S component is applied transversely

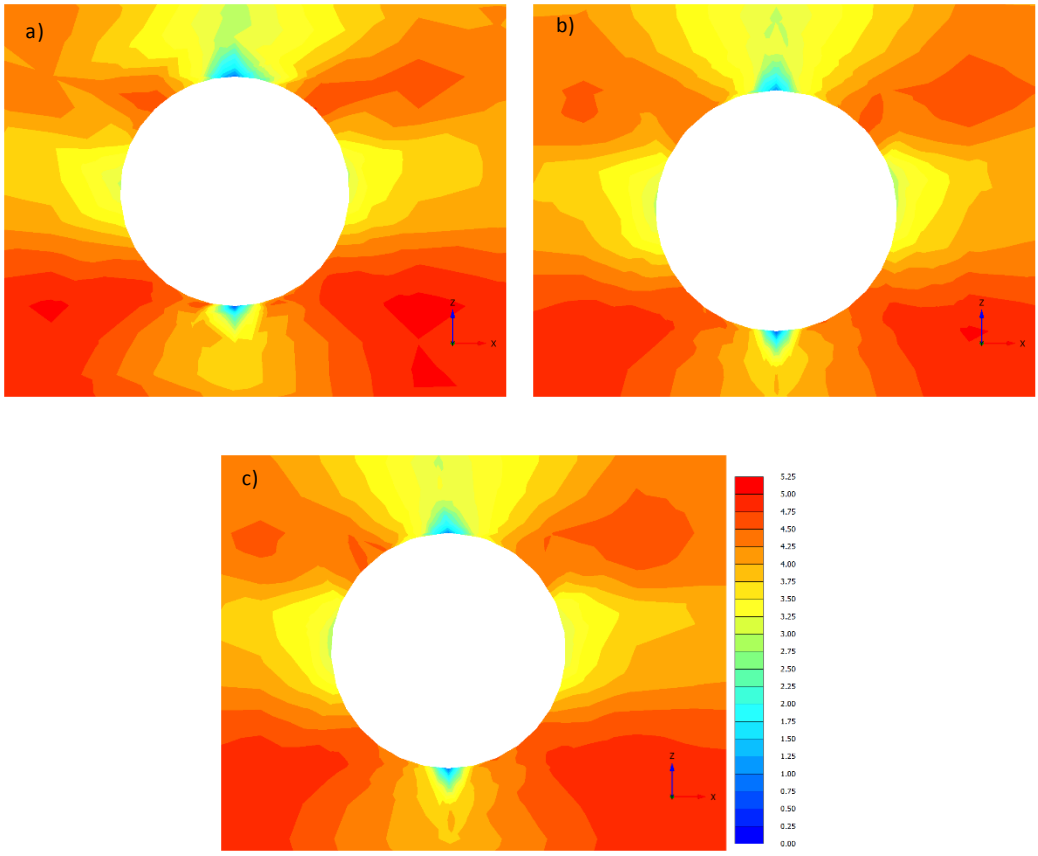

Figure 5.50 Contours of the RMW parameter *r* at the end of the seismic event around the tunnel at a distance of (a) 50m; (b) 25m; and (c) 75m along the tunnel length when the N-S component is applied transversely

N-S and E-W earthquake components applied simultaneously at bedrock (3D – xy)

Figure 5.51 shows the profiles of the minimum and maximum transverse horizontal (a_x), longitudinal horizontal (a_y) and vertical (a_z) accelerations recorded along the soil depth and obtained in free-field conditions at different sections along the tunnel length (i.e. 25m, 50m and 75m) of the 3D model when both N-S and E-W earthquake components are applied simultaneously at bedrock (denoted as 3D – xy). Similar acceleration profiles at tunnel vertical location are presented in Figure 5.52. It has been observed that the transverse horizontal accelerations a_x and longitudinal horizontal acceleration a_y along soil depth are generally lower at 25m and 75m along the tunnel length than those at the centre plane (50m mark) in both free-field conditions and at tunnel vertical as shown in Figure 5.51 (a & b) and Figure 5.52 (a & b) when both earthquake components are applied simultaneously. On the contrary, the vertical acceleration a_z at soil depth at 25m and 75m along the tunnel length are generally higher than those at 50m mark as shown in Figure 5.51 (c) and Figure 5.52

(c). These variations can be attributed to the wave scattering and continuously changing inclined direction of the seismic wave resulting from the concurrent application of the two horizontal components of the event.

The influence of the multi-directional earthquake loading is more evident in the longitudinal shear strain profiles (γ_{xy} & γ_{yz}) which varies in magnitude at different sections along the longitudinal direction as shown in Figure 5.53 and Figure 5.54. The transverse shear strains γ_{zx} in both the free-field conditions (Figure 5.53 (a)) and at tunnel vertical (Figure 5.54 (a)) also deviate but only slightly. These differences along the tunnel length may be caused by further dissipation of the wave into the longitudinal direction as a result of increased soil destructuration due to the imposition of the longitudinal earthquake component and the complex 3D interaction.

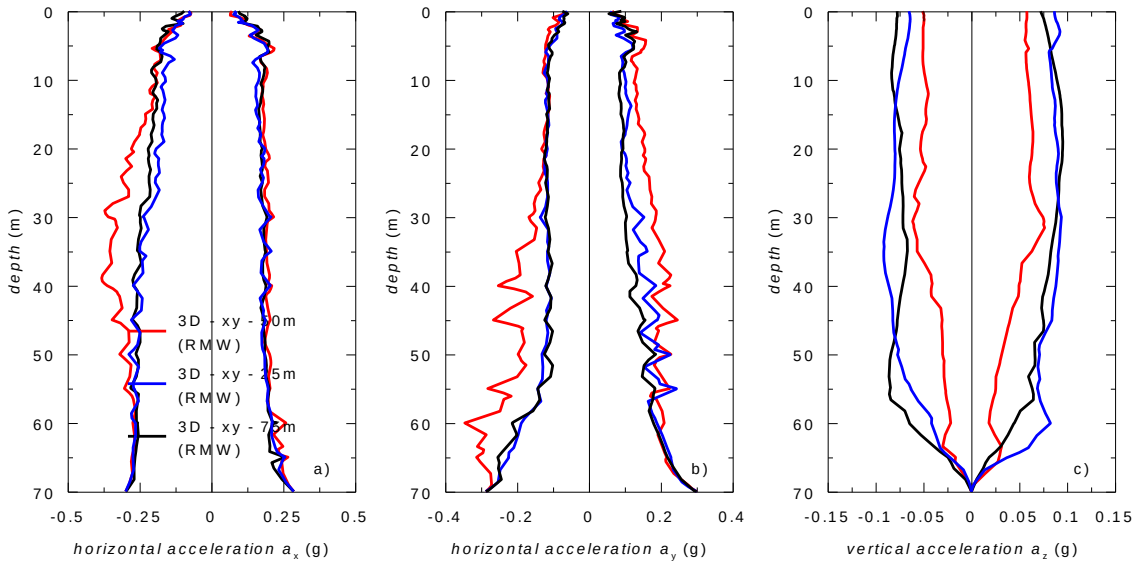

Figure 5.51 Profiles of max and min (a) horizontal acceleration a_x, (b) horizontal acceleration a_y and (c) vertical acceleration a_z recorded in free-field conditions at a distance of 25m, 50m and 75m along the tunnel length at bedrock when both N-S and E-W components applied simultaneously using RMW

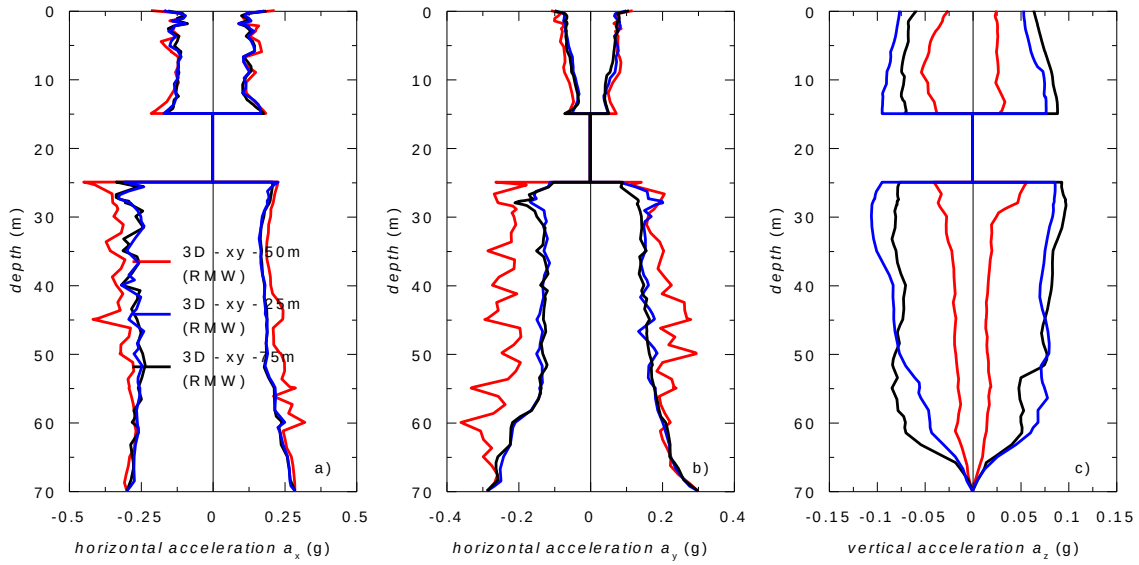

Figure 5.52 Profiles of max and min (a) horizontal acceleration a_x, (b) horizontal acceleration a_y and (c) vertical acceleration a_z recorded at tunnel vertical at a distance of 25m, 50m and 75m along the tunnel length at bedrock when both N-S and E-W components applied simultaneously using RMW

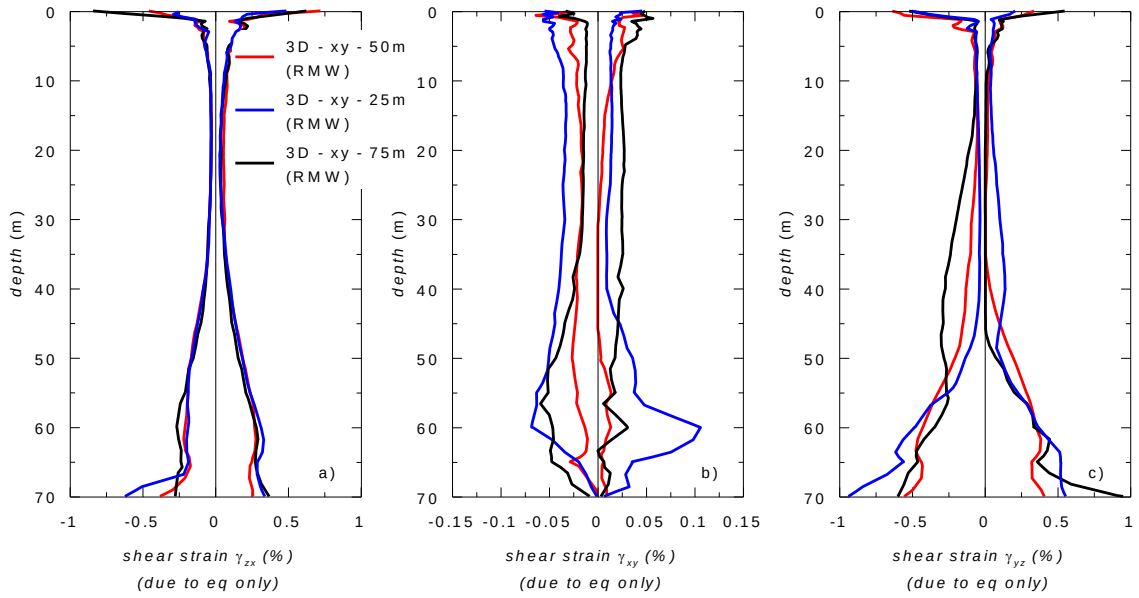

Figure 5.53 Profiles of max and min (a) transverse shear strain γ_{zx}, (b) longitudinal shear strain γ_{xy} and (c) longitudinal shear strain γ_{yz} recorded in free-field conditions at a distance of 25m, 50m and 75m along the tunnel length when both N-S and E-W components applied simultaneously using RMW

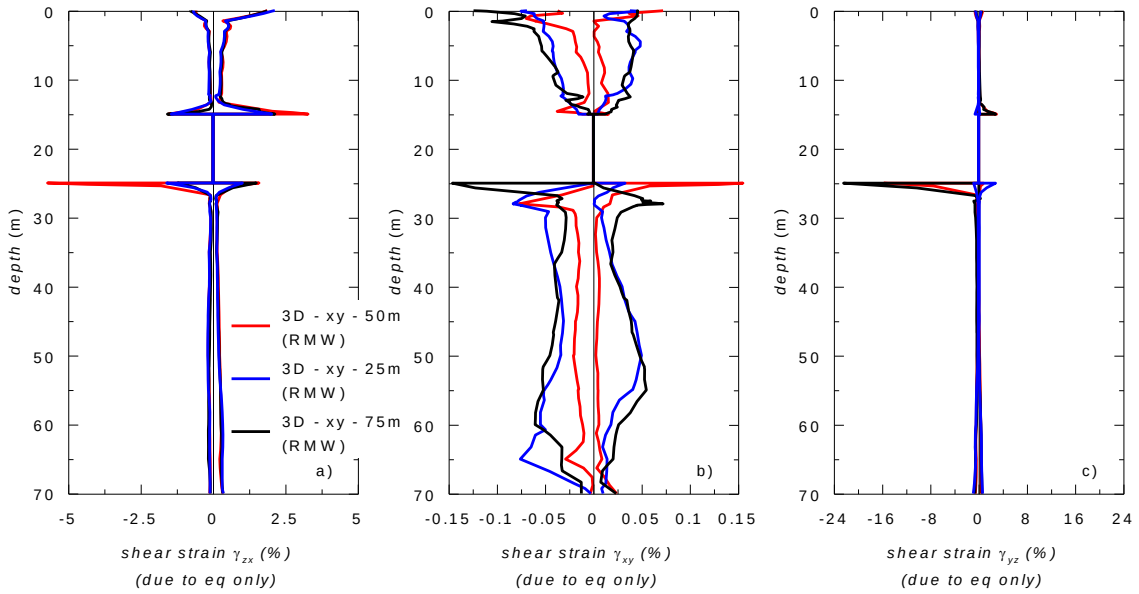

Figure 5.54 Profiles of max and min (a) transverse shear strain γ_{zx}, (b) longitudinal shear strain γ_{xy} and (c) longitudinal shear strain γ_{yz} recorded at tunnel vertical at a distance of 25m, 50m and 75m along the tunnel length when both N-S and E-W components applied simultaneously using RMW

The observations above prove that the inclusion of the E-W earthquake component can influence both the transverse and longitudinal behaviour of the tunnel to a certain degree. These spatial effects were further demonstrated in terms of the lining transverse displacement u_x [Figure 5.42 (d)] at the end of the seismic event which varies along the tunnel length (in contrast with the case of only the N-S component is applied transversely where the contours are uniform along the tunnel length). Likewise, the longitudinal displacement u_y along the tunnel length also slightly varies as shown in Figure 5.42 (e) wherein the tunnel crown moved in one direction while the tunnel invert moved in the opposite direction. On the other hand, the vertical displacement u_z [Figure 5.42 (e)] shows significant movement between one end to the other end of the tunnel at the end of the earthquake. This relative movement can be clearly identified in the deformed shape of the tunnel at the end of the earthquake [Figure 5.40 (b) and Figure 5.41 (f)] where one end of the tunnel moved downward while the other end moved upward. It can be deduced from the deformed shape and in the contours of displacements that both the transverse and longitudinal behaviour of the tunnel will vary along the tunnel length.

To investigate the effects of multi-directional earthquake loading on the tunnel lining along the tunnel length, the contours of the tunnel lining forces at the end of the seismic event are plotted as shown in Figure 5.44 (d-f) and Figure 5.47 (f-j). It can be

observed from the contours of the transverse lining forces [Figure 5.44 (d-f)] that the inclusion of the E-W earthquake component has an impact on the hoop force, transverse bending moment and transverse shear forces particularly around the tunnel crown and the spring line along the tunnel length. By comparing further the minimum and maximum transverse lining forces at 25m, 50m and 75m along the longitudinal direction during the concurrent application of two horizontal motions, it can be seen from Figure 5.55 that the inclusion of the E-W earthquake component has certain influence on the transverse forces along the different sections but only very slight. The same trend can be observed with the MCC results as shown in Figure 5.56. Similarly, the longitudinal bending moment and torsional moments along the tunnel length also varies very slightly as shown in Figure 5.47 (g & i) as these forces are predominantly affected by the transverse earthquake component. This indicates that the degree of destructuration does not influence significantly the transverse results as they are closely similar around the tunnel in all sections even though some degree of variation can be observed as shown in Figure 5.60. These results may also suggest that for the case study presented, the magnitude of destructuration is not large enough to alter significantly the transverse response. Thus, the transverse forces at the centre plane of the 3D model can be adequate enough and can be used conservatively in the transverse seismic design of the tunnel lining. In contrast, significant differences in magnitude of the longitudinal forces have been recorded particularly in the longitudinal axial force [Figure 5.47 (f) & Figure 5.57 (a)] and the in-plane shear force [Figure 5.47(j) & Figure 5.57 (e)] due to the wave scattering and complex wave propagation in the longitudinal direction together with the 3D interaction effects of the soil and the tunnel structure along the tunnel length including contribution from the soil destructuration. The maximum longitudinal tensile force has seen to increase from 923kN/m at 50m along the tunnel length to 2815kN/m at 25m along the tunnel length while the maximum longitudinal compressive force has increased from 1390kN/m at 50m along the tunnel length to 3436kN/m at 75m along the tunnel length. Likewise, the maximum in-plane shear has increased from 624kN/m at 50m along the tunnel length to 775kN/m at 25m along the tunnel length. There are also slight changes in the longitudinal shear force but not significant enough to alter the design. As mentioned earlier, these variations can be attributed to the wave scattering and continuously changing inclined direction of the seismic load with respect to the

longitudinal axis of the tunnel in conjunction with the 3D soil-structure interaction responses and soil destructuration resulting from the concurrent application of the two horizontal components of the event. As pointed out in the previous section, ignoring these variations in the magnitude of longitudinal forces may lead to unsafe design and therefore need be considered in every aspect of the seismic design of the tunnels.

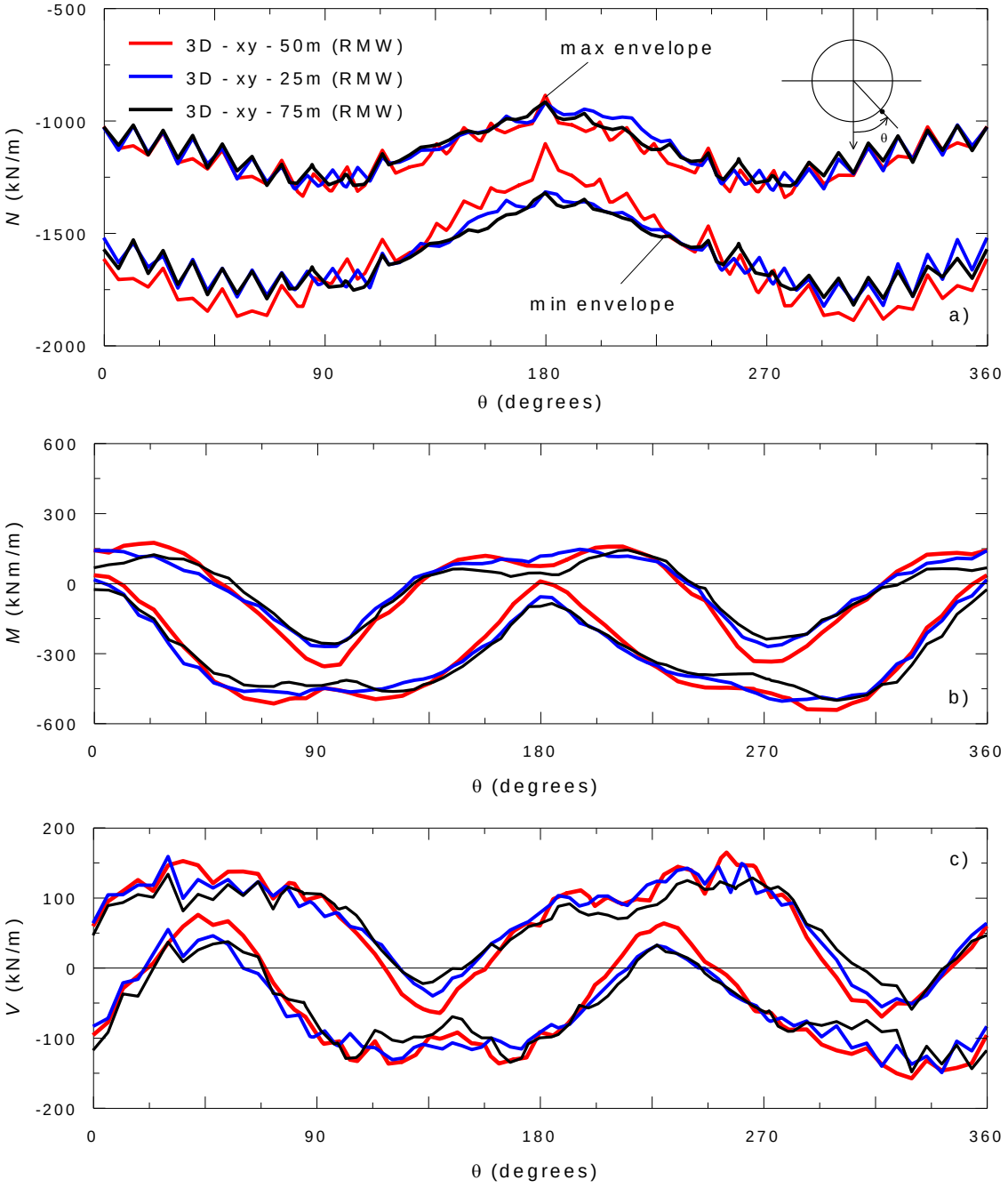

Figure 5.55 Comparison at a distance of 25m, 50m and 75m along the tunnel length of minimum and maximum (a) hoop force; (b) transverse bending moment and (c) transverse shear force when both N-S and E-W components applied simultaneously using RMW

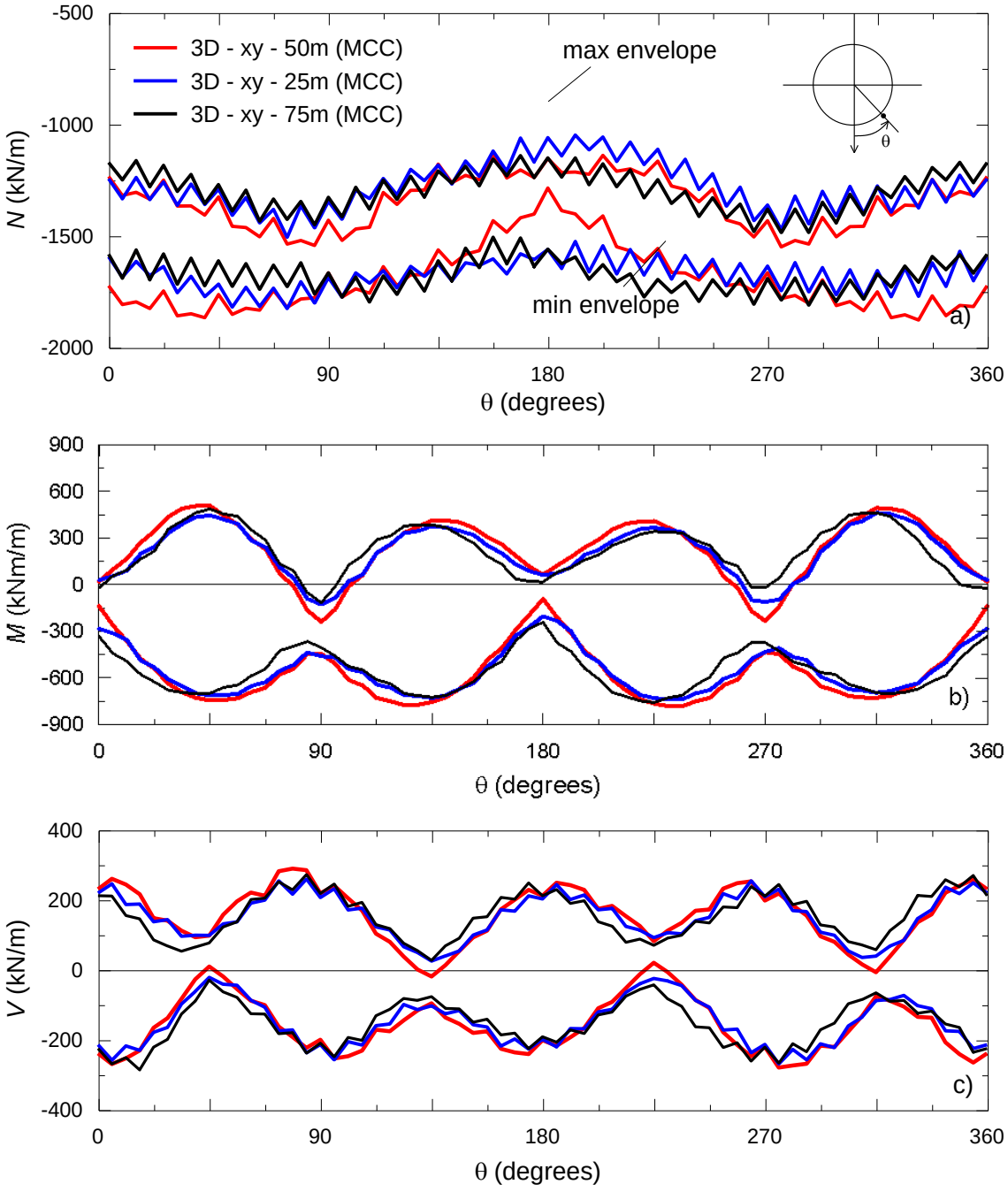

Figure 5.56 Comparison at a distance of 25m, 50m and 75m along the tunnel length of minimum and maximum (a) hoop force; (b) transverse bending moment and (c) transverse shear force when both N-S and E-W components applied simultaneously using MCC

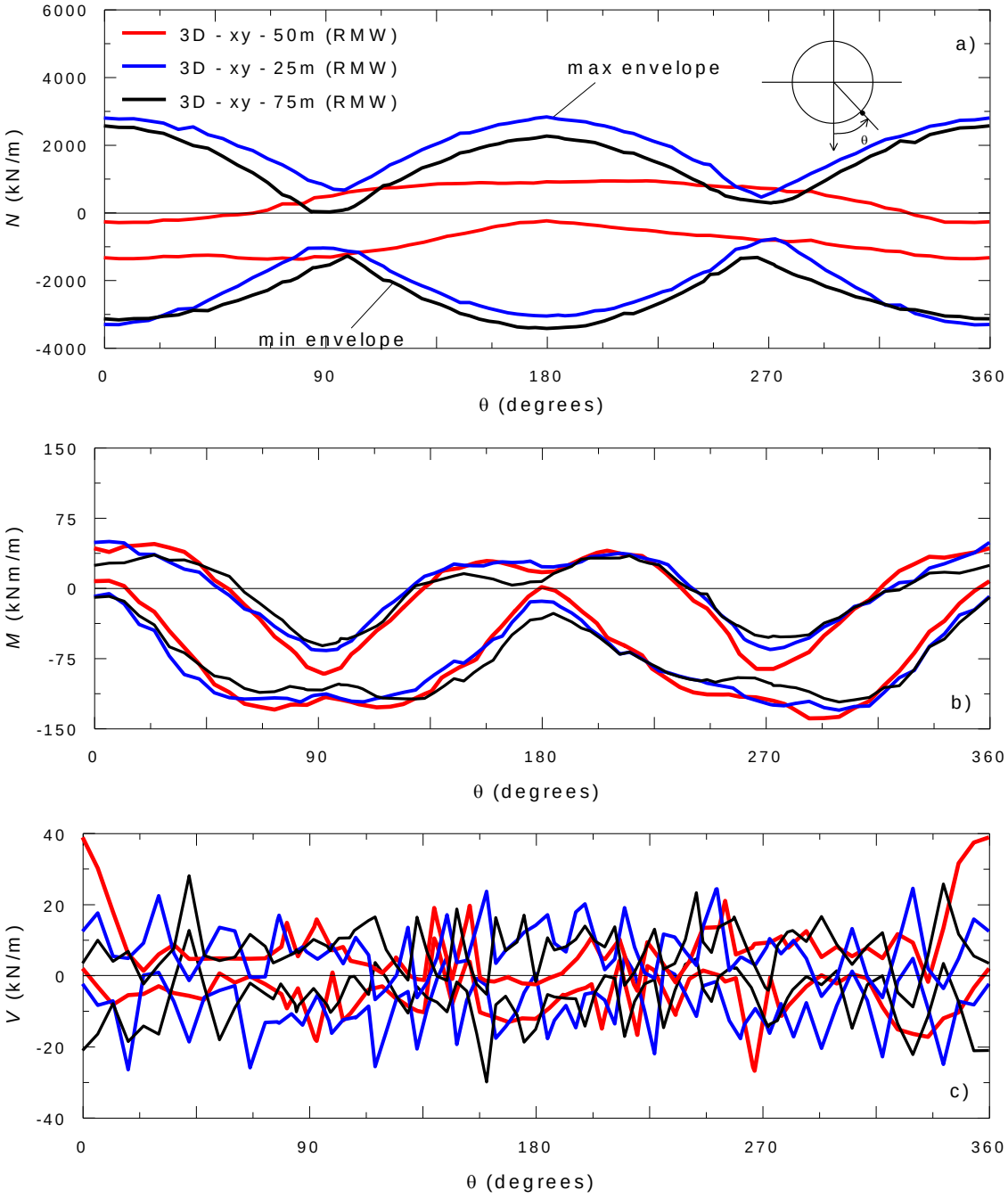
3D - xy - 50m (RMW)
3D - xy - 25m (RMW)
3D - xy - 75m (RMW)
max envelope
min envelope
a)
θ
N (kN/m)
6000
4000
2000
0
-2000
-4000
0
90
180
270
360
θ (degrees)

M (kNm/m)
150
75
0
-75
-150
b)
0
90
180
270
360
θ (degrees)

V (kN/m)
40
20
0
-20
-40
c)
0
90
180
270
360
θ (degrees)

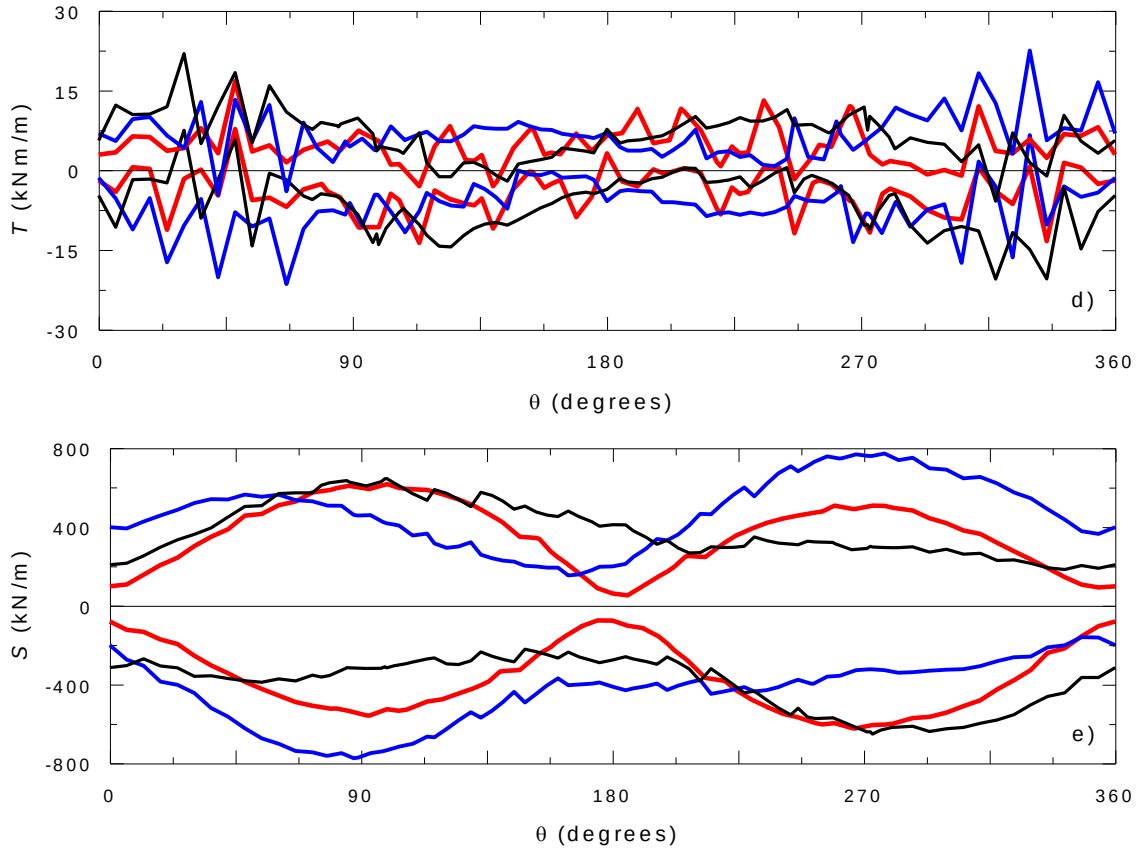

Figure 5.57 Comparison at a distance of 25m, 50m and 75m along the tunnel length of minimum and maximum (a) longitudinal axial force; (b) longitudinal bending moment; (c) longitudinal shear force; (d) torsional moment and (e) in-plane shear when both N-S and E-W components applied simultaneously using RMW

Figure 5.58 shows the time histories of shear strain and pore pressures at tunnel vertical recorded at 25m, 50m and 75m along the tunnel length when the N-S and E-W components are applied concurrently. The transverse shear strain at chosen points at different sections along the tunnel length as shown in Figure 5.58 (a-c) have similar trend but slightly higher in magnitude as the section moves away from the centre plane which indicates very similar behaviour in the transverse direction. In contrast, the pore water pressure varies dramatically along the tunnel length of the model as shown in Figure 5.58 (d-f). Compared to the case of only the N-S earthquake component applied transversely, the variation in the excess pore water pressure along the tunnel length is very much pronounced. This can be attributed to the wave scattering and dissipation of the seismic wave longitudinally in conjunction with the 3D soil-structure interaction responses. Also, as similarly observed in the case of the transverse only earthquake, approximating comparative stress point locations at different sections is difficult due to differences in the mesh arrangement at every section which can lead to incompatibility, thus contributing to the huge variations of

the pore water pressure along the length. Nevertheless, it still predicts similar trend where build-up of positive pore pressures occurs above the tunnel invert and negative pore pressures below it.

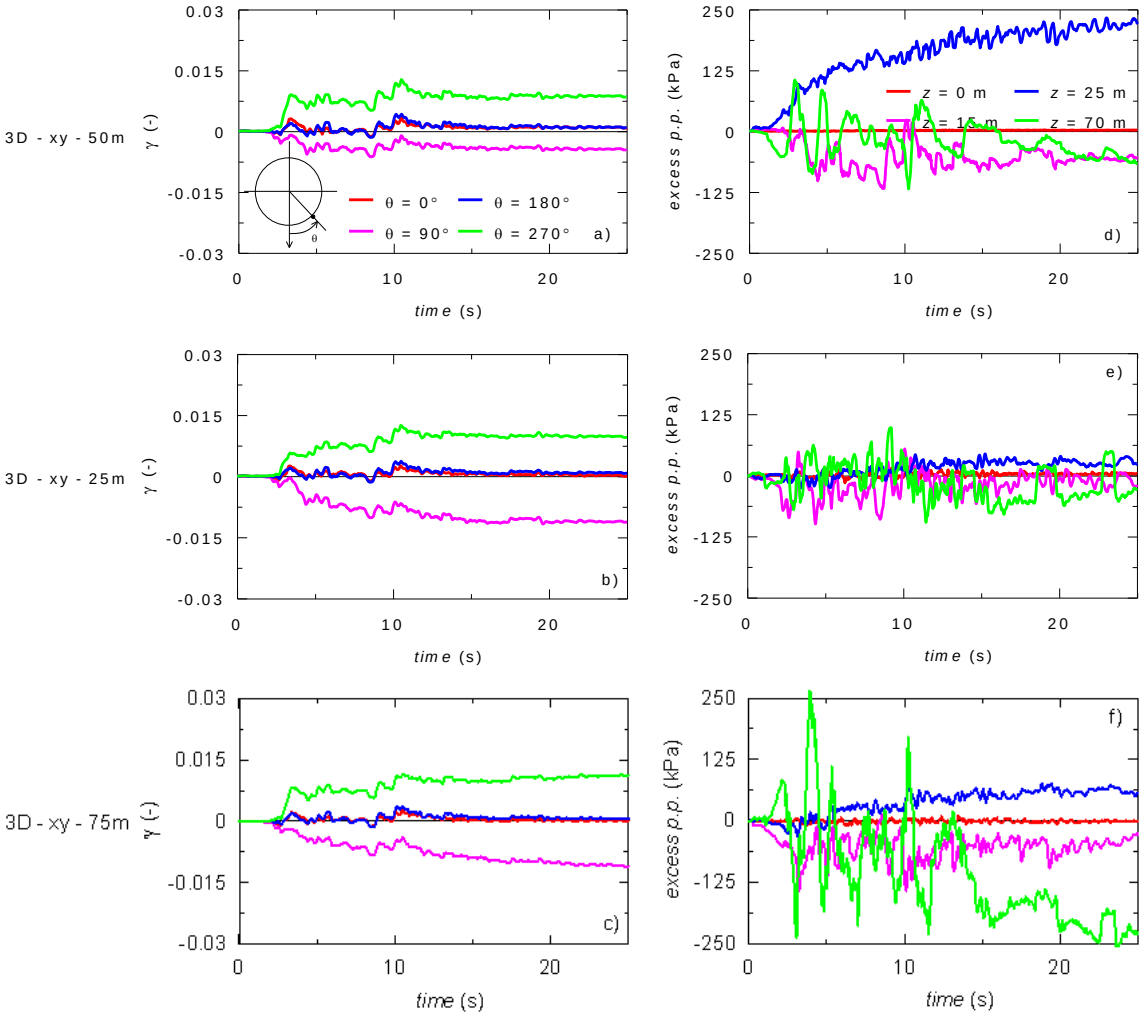

Figure 5.58 Time histories of (a-c) shear strain and (d-f) excess pore pressure of RMW model at a distance of 50m, 25m, and 75m along the tunnel length when both N-S and E-W components applied simultaneously

Figure 5.59 shows the contours of RMW parameter *r*, describing the degree of soil structure, obtained at the end of the seismic event at different sections along the longitudinal length. The contours although generally similar indicate a less pronounced structure degradation induced in the soil deposit at the bottom half below the tunnel at the centre plane of the model (i.e. 50m along the tunnel length) than those at 25m and 75m distance along the tunnel length. This is due to generally higher longitudinal shear strains (γ_{xy} & γ_{yz}) at 25m and 75m marks. This indicates that the imposition of the E-W component has a strong influence on the longitudinal behaviour of the tunnel model. Similarly, the structure degradation in the soil surrounding the tunnel although

generally similar also varies at some degree along the tunnel length as shown in Figure 5.60 consistent with the shear strain levels in the same locations as depicted in Figure 5.58 (a-c). These observations prove that the concurrent application of the two horizontal motions has strong influence on the structure degradation of the soil not only longitudinally along the tunnel length but also transversely although to a much less extent.

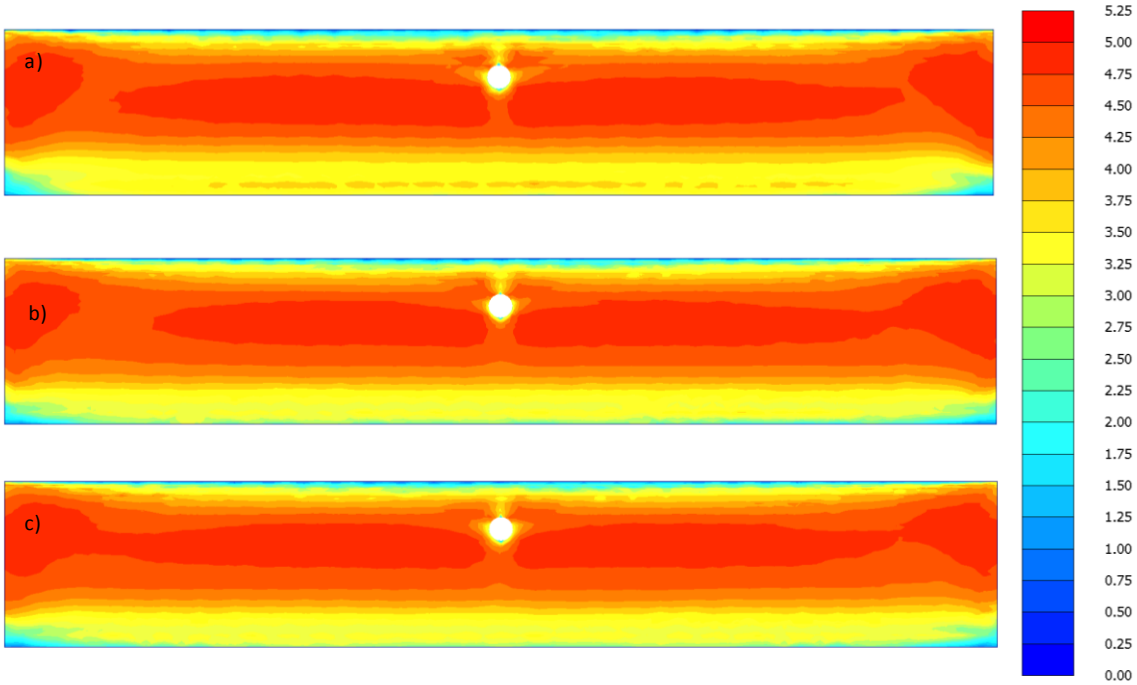

Figure 5.59 Contours of the RMW parameter *r* at the end of the seismic event at a distance of (a) 50m; (b) 25m; and (c) 75m along the tunnel length when both N-S and E-W components applied simultaneously

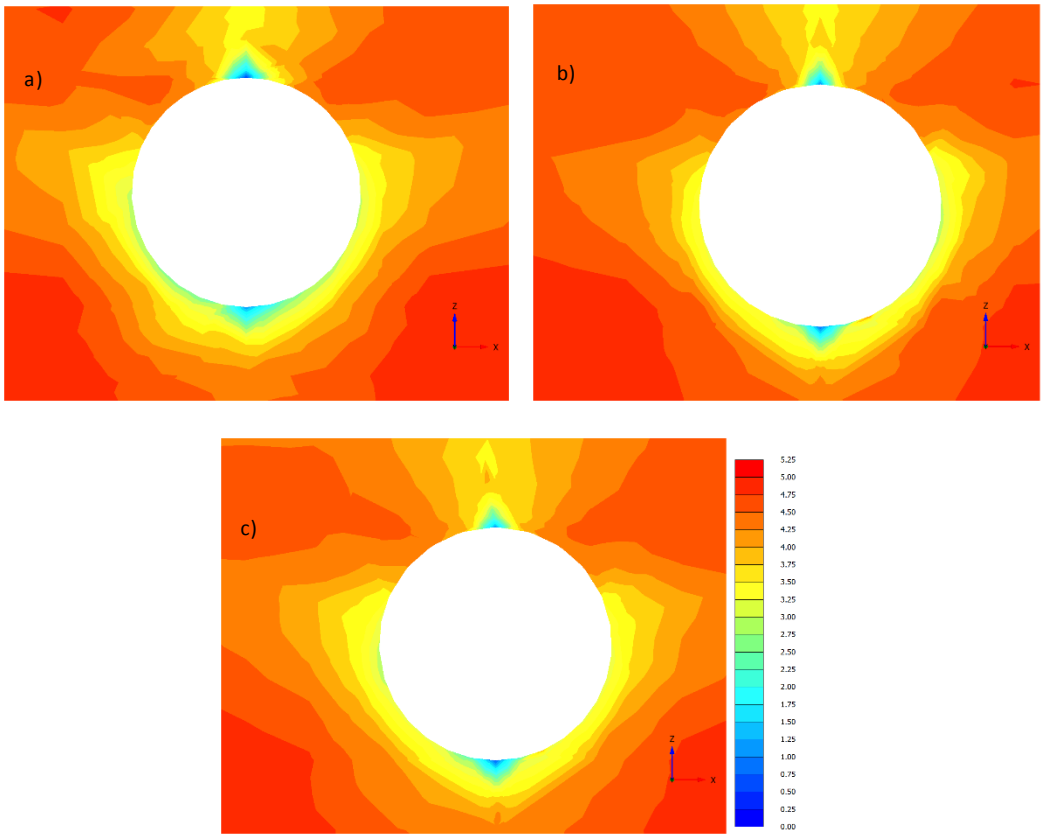

Figure 5.60 Contours of the RMW parameter *r* at the end of the seismic event around the tunnel at a distance of (a) 50m; (b) 25m; and (c) 75m along the tunnel length when both N-S and E-W components applied simultaneously

5.3 Key point summary

The first study shows the 2D seismic behaviour is very similar to the 3D ones, in general, in terms of the transverse forces (i.e. hoop force, transverse bending moment and transverse shear force) in the tunnel lining but more conservative in magnitude because 2D model lacks the ability to disperse the seismic wave longitudinally. On the other hand, the propagation of the wave in the longitudinal direction generates longitudinal forces in the lining (i.e. longitudinal axial force, longitudinal bending moment, longitudinal shear force, torsional moment and in-plane shear force), which cannot be captured by the 2D model.

In the second study, it is evident that the transverse seismic motion heavily dictates the magnitude of the transverse forces and the subsequent imposition of the longitudinal earthquake motion does not significantly affect the transverse forces justifying the common design practice to rely on 2D modelling or one meter strip long of 3D model applying the transverse earthquake component only. However, imposing

the longitudinal component of the earthquake motion in addition to the transverse component has resulted to higher strains in the longitudinal direction and higher degree of soil destructuration which in turn caused further dissipation of the transverse earthquake accelerations in the longitudinal direction. As a consequence, the longitudinal forces, which are normally ignored in the design, can increase substantially which can highly influence the tunnel lining design. The resulting longitudinal forces particularly the longitudinal axial and in-plane shear forces can be quite substantial compared to those from the case where only the transverse seismic loading is imposed into the model. The longitudinal and in-plane shear forces can highly influence the design of the tunnel lining and design of the joints particularly for multi-directional earthquake motion. The magnitude of those forces when ignored, may lead to un-conservative design, compromising the integrity and thereby the safety of the tunnel. Hence, the study highlights the importance of considering the multi-directional effects of the seismic loading in designing tunnels. It also demonstrates that the degradation of the soil structure can influence the dissipation of the seismic wave within the soil thereby affecting not only the longitudinal acceleration but also the transverse and vertical accelerations when considered in the dynamic simulation.

The third study demonstrates that the transverse behaviour of the tunnel throughout the length, when only the transverse earthquake component is applied, remains typically similar in every section, with very slight differences due to the spatial effects, when the degree of destructuration is constant along the length or the soil structure is not considered. On the other hand, the wave scattering and dissipation of the seismic wave longitudinally and corresponding 3D soil-structure interaction responses cause the longitudinal forces to change dramatically along the tunnel length. Some of those variations such as in the case of longitudinal axial and in-plane shear forces can be quite significant and as mentioned earlier, cannot be ignored in the design. It signifies that it is not just the multidirectional seismic loading which can affect heavily the longitudinal forces but also the 3D soil-tunnel interaction effects along the tunnel length. Ignoring these variations in the magnitude of longitudinal forces can lead to unsafe design and therefore these 3D interaction effects should need be considered in every aspect of the seismic design of the tunnels.

Lastly, the inclusion of the longitudinal earthquake component in conjunction with the transverse component has certain influence on the transverse forces along the different sections along the tunnel length but only very slight. This again demonstrates that 2D model or a meter strip of the 3D model can be adequate enough to be used conservatively in the transverse seismic design of the tunnel lining. In contrast, significant differences in magnitude of the longitudinal forces along the length have been observed particularly in the longitudinal axial force and the in-plane shear force due to the wave scattering and complex wave propagation in the longitudinal direction together with the 3D interaction effects of the soil and the tunnel structure along the tunnel length. In addition, the concurrent application of the two horizontal motions has also strong influence on the structure degradation of the soil particularly in the longitudinal direction causing variations in the shear strain along the tunnel length thereby contributing to marked differences in the longitudinal forces along the tunnel length. Thus, the results in this study again highlights the importance of adopting 3D multidirectional seismic loading approach while considering the degradation of the soil structure in natural clays to achieve a realistic and much safer tunnel design.

Chapter 6. Conclusions and future research

6.1 Summary and conclusions

The primary aim of this research is to improve the design of underground structures in natural clayey soils subjected to earthquake loading by increasing the accuracy and reliability through better prediction of tunnel and soil behaviour during seismic action. To achieve this aim, the author investigated the effects of utilising a non-linear advanced soil constitutive model known as Rouiaina Muir-Wood (RMW) model to describe the natural clay soil that interacts with the tunnel during seismic conditions. RMW can capture realistic response of natural clays under seismic loads including non-linear behaviour, hysteretic action, stiffness degradation, pore pressure build-up (for saturated soils), material anisotropy, development of early strains, the response in the small strain region and in particular the degradation of the soil structure caused by irrecoverable plastic strains. Most of which a simpler soil constitutive model in the framework of linear-visco-elastic assumption and elasto-plasticity theory (e.g. Mohr-Coulomb model, Modified Cam Clay model) cannot simulate. Furthermore, it is a well-known fact that the direction of earthquake motions and wave propagation is arbitrary with respect to the axis of the tunnel structure. As such, the author has also investigated the influence of multi-directional earthquake loading on the tunnels by using 3D simulations which causes multi-directional loading for the soil deposit and the tunnel lining and subsequently produces longitudinal effects which can impact the response of the tunnel structure.

The RMW model was implemented into PLAXIS Finite Element software. The soil materials used in this project include a structureless clay material (Marana Capacciotti earth dam material) and a structured clay material (Avezzano clay). The RMW soil parameters were calibrated against experimental data obtained from undrained triaxial compression test, double specimen direct simple shear (DSDSS) and combined resonant column/torsional shear (RC/TS) tests. Equivalent parameters for the reduced single surface version of RMW, effectively representing the Modified Cam Clay (MCC) model, have also been calibrated against the same set of laboratory data for investigation of the effect of the constitutive assumption on dynamic soil-tunnel interaction.

Two earthquake signals with different frequency content have been considered in the dynamic simulations. Both signals reasonably match the response spectrum provided by Eurocode 8 (EC8) for soil type A (rock or other rock-like geological formation). The first signal selected was recorded at the Assisi-Stallone station during the Umbria-Marche earthquake in September 1997 in Assisi, Italy, while the second which has a higher energy content was recorded at the Ulcinj-Hotel Albatros station during the Montenegro earthquake in April 1979 in Albania. The earthquake signals have been applied at the base of the Finite Element mesh models as prescribed horizontal displacement time histories. The case studies were based on large shallow tunnels (10m in tunnel diameter and a tunnel cover of 15m which is less than twice the tunnel diameter) which were found to be more vulnerable to earthquake damage.

In order to optimise the size of the Finite Element (FE) model, which has a good compromise between accuracy and computational time, parametric studies have been conducted to ensure sufficient distance to the lateral boundaries to achieve free-field conditions at the edges of the model. For 2D models, tied degrees of freedom at the lateral boundaries have been applied which are effective in absorbing the energy induced by the seismic action thereby avoiding spurious wave reflections at the boundaries of the soil deposit and therefore sufficient to properly simulate the free-field conditions at the edges of the model. A lateral width of 5 times the soil depth for 2D models with tied-nodes boundary conditions have been adopted although 3 times the soil depth have been found to be sufficient for dynamic simulations of the selected case studies.

For 3D models, viscous boundaries at the lateral sides have been utilised to absorb outgoing wave energy and prevent reflections at the lateral boundaries during the dynamic simulations. This change in boundary conditions is due to unavailability of tied-nodes condition in PLAXIS 3D software. Viscous boundaries, however, can only achieve perfect absorption for angles of incidence greater than 30°. As such, close proximity of the dashpots from the seismic source can cause spurious waves to reflect back. To eliminate the influence of the viscous boundary conditions on the response of the tunnel, the tunnel was placed at as far as possible from the boundaries. An optimised lateral width of 6 times the soil depth and 100m longitudinal dimension for 3D models were found sufficient for dynamic simulations with viscous boundaries.

6.1.1 *2D finite element*

Two case studies have been investigated which are intended to:

1. Highlight the advantage of adopting advanced soil constitutive models over simpler models and;
2. Investigate the effect of varying the key parameters (e.g. initial structure r_0, destructuration rate k) of the advanced model

Influence of soil constitutive model

Comparison between an advanced soil constitutive model (RMW model) and a simpler elasto-plastic model (MCC model) have been performed in PLAXIS 2D FE model adopting the soil parameters for Marana Capacciotti earth dam material. Due to a lack of hysteretic damping provided by the simpler constitutive model, a value of 6% obtained from an equivalent linear 1D simulation with EERA for shear strain levels smaller than 0.1%, has been applied to the bottom 40m of soil to compensate for the deficiency. For RMW, a small amount of 2% Rayleigh damping has been introduced in the dynamic simulations to avoid the propagation of spurious high frequencies, to compensate for the RMW underestimation of damping in the small-strain range and to prevent unrealistic resonance at small strains during wave propagation which can cause numerical divergence. As pointed out by (Bilotta *et al.*, 2014), an amount between 0 and 4% Rayleigh damping does not affect the numerical results in the range of frequency associated with the larger part of the energy content of the input signal but allows smoothing of unrealistic overamplified signal at higher frequency. Both earthquake motions are considered on all case studies.

The results capture a general trend and the conclusions reached from this study can be summarised as follows:

- The soil constitutive model adopted in the modelling and the selection of earthquake plays a significant role on the seismic induced lining loads particularly for shallow tunnels in soft soil.
- Single surface model (MCC) show an overall amplification of the input signals, while an overall deamplification of the maximum acceleration can be observed

for the two-surface model (RMW). Consequently, the maximum shear strain is much higher with MCC than RMW.

- MCC-type models can significantly over-predict the permanent increments of lining forces at the end of the seismic action compared to the kinematic hardening models. This is due to the limited ability of single surface models to accumulate plastic strain during cycles, even with the introduction of Rayleigh damping, while advanced two-surface kinematic hardening models have an inherent plasticity which allows the accumulation of plastic deformation during the unloading stage in every cycle. Consequently, the use of advanced soil models for dynamic analysis, particularly for soft soils, can lead to smaller transverse forces in the tunnel lining resulting in more economic design. Thus, highlighting the benefits of using more advanced constitutive models in tunnel design practice.
- A major disadvantage in using advanced soil model such as RMW for seismic design is the complexity of the analysis which increases the computational time and thus, the computational costs. In engineering practice, the use of advanced soil constitutive model will not be beneficial during the concept and preliminary design due to the time and budget constraint. On the other hand, it can have a major role in the detailed design and construction phases particularly in value engineering by potentially reducing the material cost.

Effect of initial structure and destructuration rate

To investigate the influence of the initial degree structure and its subsequent degradation induced by the seismic loads, two values of the RMW parameter k, which represents the progressive destructuration of a structured soil, have been considered and compared: a case of k equal to 1.5 and another case where k has been set equal to 5.0. The soil adopted to simulate these case studies is the Avezzano clay, a known highly structured Italian clay. To ensure comparability, the initial conditions, i.e. the initial stress level and the initial soil structure r_0 = 5.2 were kept similar for both parametric cases. Both earthquake motions are considered on all case studies.

The findings and conclusions reached from the case studies can be summarised as follows:

- The soil-structure degradation rate does not particularly affect the wave propagation in the deposit but a higher rate leads to higher shear strain levels in the soil deposit due to its softer behaviour.
- Similar to the results of the earlier case study on the influence of the soil constitutive model, it also shows that the higher the energy content of earthquake, the higher the acceleration and associated shear strain induced in the soil and consequently higher forces in the tunnel lining. The energy content of the earthquake also influences the degree of structure degradation. The higher the energy content, the more pronounced structure degradation is induced in the soil. Thus, it highlights the importance of the input motion frequency content in controlling the magnitude of shear strains induced by the earthquake in the tunnel and surrounding deposit.
- A rise in the maximum and minimum values of the lining forces attained during the earthquake motions is predicted when higher rates of soil structure degradation is accounted for. Similarly, when a higher degree of destructuration is allowed to occur in the dynamic simulations, a consistent increase in the hoop force, bending moment and shear force increments accumulated in the tunnel lining can be observed.
- Although a natural clay deposit is characterised by high stiffness and peak strength due to its initial degree of structure, the earthquake loading can induce sufficient stiffness degradation in the soil associated with strain-softening processes, which, in turn, facilitate the transmission of higher loads to the tunnel lining. Therefore, it highlights for the first time the importance of considering structure degradation in the assessment of the dynamic response of shallow tunnels constructed in structured clayey deposits as it can increase the magnitude of the tunnel lining forces. However, the increase caused by destructuration may not be substantial enough to alter the overall tunnel design, as demonstrated by the case study, but nevertheless show its potential in altering the magnitude of the lining forces. Its effect might be more significant in the case of a natural clay with a very high initial soil structure subjected to a very much stronger earthquake, i.e. earthquake with a very high energy content.

6.1.2 *3D finite element*

Three comparative studies were systematically selected and examined as outlined below to highlight the significance of 3D approach in capturing the effects of the direction of seismic wave propagation which is arbitrary with respect to the axis of the structure in conjunction with using an advanced soil constitutive model.

1. Comparison of 2D and 3D results
2. Multidirectional seismic loading effects
3. Effects of multidirectional seismic loading along the tunnel length

2D vs 3D results and multidirectional seismic loading effects

The principal findings derived from the results of those case studies are summarised as follows:

- 2D and 3D transverse results are in satisfactory agreement. However, the 3D model has higher total damping, as the 3D space allows wave propagation and thus energy dissipation in all directions. Therefore, 3D results, in terms of the transverse forces (i.e. hoop force, transverse bending moment and transverse shear force), will be generally lower than 2D due to more space for the seismic wave to propagate in the longitudinal direction.
- It is evident that the transverse earthquake motion (i.e. the wave propagating normally to the tunnel axis) dictates the forces in the transverse direction. Even the imposition of a longitudinal earthquake motion produces comparable yet generally smaller transverse forces which do not significantly affect the results of the transverse forces. This observation justifies and validates the common use of a 2D model which is a conservative approach to design a tunnel section to account for ovaling/racking effects. On the other hand, smaller transverse forces in 3D translate to more economic design.
- The propagation of a horizontal acceleration in the longitudinal direction (i.e. parallel to the tunnel axis) either by applying a transverse earthquake motion only or by applying both transverse and longitudinal earthquake motions concurrently generates longitudinal forces in the lining (i.e. axial compression and extension, longitudinal bending moment, longitudinal shear force, torsional moment and in-plane shear force), which cannot be obtained using a 2D

approach. Some of these forces particularly the longitudinal axial force and in-plane shear can increase substantially in magnitude when both transverse and longitudinal earthquake motions are imposed concurrently. These are essential forces which can heavily influence the decision on the size of the tunnel lining and the design of the joints. Ignoring these forces with a 2D approach can lead to un-conservative design, compromising the integrity and thereby the safety of the tunnel in an earthquake event. Hence, the study highlights the importance of considering the multi-directional effects of the seismic loading in designing tunnels.

- When subjected to transverse earthquake motion only, the structure degradation induced in the soil in both 2D and 3D models are relatively similar. Imposing the longitudinal earthquake component in conjunction with the transverse component increased the destructuration induced in the soil deposit. Correspondingly, the structure degradation has also increased in the soil surrounding the tunnel. The increase in the degree of soil degradation increases the dissipation of the seismic wave in the longitudinal direction thereby affecting not only the longitudinal but also the transverse results (i.e. further reduction in transverse lining forces which has economic design benefit). In contrast, soil with no structure and with limited ability to accumulate plastic strains (e.g. MCC) only affects the longitudinal results. Thus, the soil structure plays a big role in influencing the results of the soil-tunnel interaction in a 3D space during a seismic event.
- The 3D model approach is able to simulate the simultaneous application of a transverse and a longitudinal earthquake event at bedrock, thus effectively reproducing a seismic motion acting at an angle with the tunnel axis. This allows to predict an increase in the axial compression and extension, in-plane shear and longitudinal shear force in the lining. Ignoring these forces may lead to under-designing the tunnel lining, thus potentially compromising the integrity of the underground structure in the longitudinal direction. Nevertheless, the distribution of maximum and minimum longitudinal bending moment and torsional moment depends on the transverse actions only as these forces are predominantly affected by the earthquake components perpendicular to the axis of the tunnel, i.e. transverse component.

- The excess pore water pressures in 3D are relatively higher than 2D. The disparity can be attributed to the higher shear strain levels in the longitudinal direction induced by the 3D interaction effects of the soil and the tunnel structure which cannot be simulated in a 2D model. Imposition of the longitudinal component of the earthquake motion in addition to the transverse component further increases the shear strains in the longitudinal direction resulting to a higher degree of soil destructuration thereby increasing further the magnitude of the pore water pressures.

Effects of multidirectional seismic loading along the tunnel length

The case studies highlight the importance of wave scattering and complex three-dimensional wave propagation and corresponding 3D soil-structure interaction in the analysis of the seismic performance of shallow tunnels in clay deposits by comparing the effects of multidirectional seismic loading across different sections along the tunnel length. The major findings are as follows:

- The application of only the transverse earthquake motion does not alter significantly the transverse behaviour (i.e. hoop force, transverse bending moment and transverse shear force) of the tunnel lining. This demonstrates that the transverse behaviour of the tunnel throughout the length remains typically similar in every section, with slight differences due to the spatial effects, when the degree of destructuration is constant along the length or the soil structure is not considered. This is similarly the case for the longitudinal bending moment and torsional moment as these forces are predominantly affected by the transverse earthquake component.
- On the other hand, the wave scattering and dissipation of the seismic wave longitudinally and corresponding 3D soil-structure interaction responses cause the longitudinal forces to change dramatically along the tunnel length. Some of those variations such as in the case of longitudinal axial and in-plane shear forces can be quite significant and cannot be ignored in the design. It signifies that it is not just the multidirectional seismic loading which can affect heavily the longitudinal forces but also the 3D soil-tunnel interaction effects along the tunnel length. Ignoring these variations in the magnitude of longitudinal forces

can lead to unsafe design and therefore these 3D interaction effects should need be considered in every aspect of the seismic design of the tunnels.

- The application of the longitudinal earthquake motion in conjunction with the transverse ground motion can impact not only the longitudinal forces but also the transverse forces but only very slightly. This demonstrates that 2D model approach can be adequate enough to be used conservatively in the transverse seismic design of the tunnel lining. In contrast, significant differences in magnitude of the longitudinal forces along the length have been observed particularly in the longitudinal axial force and the in-plane shear force due to the wave scattering and complex wave propagation in the longitudinal direction together with the 3D interaction effects of the soil and the tunnel structure along the tunnel length. In addition, the concurrent application of the two horizontal motions has also strong influence on the structure degradation of the soil particularly in the longitudinal direction causing variations in the shear strain along the tunnel length thereby contributing to marked differences in the longitudinal forces along the tunnel length.
- The excess pore water pressure varies along the tunnel length regardless of the direction of the earthquake motion with a more pronounced variation when the transverse and longitudinal earthquake motions were applied simultaneously. However, a similar trend on the build-up of positive and negative pore pressures can be observed for both cases. Likewise, the structure degradation in the soil and around the tunnel along the tunnel length also varies when the two horizontal earthquake motions are applied concurrently.
- Employing 3D model in tunnel dynamics using an advanced soil model can consume huge computational time due to the complexity of the model and the analysis, which translates to huge computational costs. For the case studies presented, dynamic simulations can take months in an ordinary PC. This is a major setback in using this approach in practical design and found to be unpopular in engineering practice. However with the continued fast development of the computing technology, this obstacle can be overcome in the foreseeable future. By then, this approach may prove to be both reliable and cost effective.

Overall, it can be concluded that the 3D multi-directional seismic loading approach using advanced soil models can capture in a much realistic way the wave scattering and complex wave propagation in the longitudinal direction as well as the complex spatial behaviour of tunnels and soil under seismic loading, which a 2D numerical model can underestimate or even ignore. This has significant influence in the design approach for shallow tunnels in structured clays as exemplified by the variations in the tunnel lining forces, soil structure degradation and pore pressures along the longitudinal direction. Hence, this approach increases the accuracy and reliability in predicting tunnel behaviour during seismic action. However, there are still huge opportunities to enhance and refine this approach as discussed in the next section.

6.2 Critical review of the thesis

The 3D method using advanced soil models as discussed above provides a substantial improvement in understanding the significance of a more realistic approach in dealing with dynamic conditions. Its use shows increased accuracy and reliability through better prediction of tunnel and soil behaviour under seismic action. However, there are still a number of limitations in the approach which need to be overcome such as modelling constraints and lack of verification to real-life cases.

Some of these limitations are discussed below.

6.2.1 *Modelling constraints*

As we've seen in the Section 5.1.4, the boundary conditions in dynamic conditions can have a huge impact on the optimised size of the model and thus the results of the simulations. Aside from tied-node and viscous boundary conditions, there are other available boundary conditions such as compliant base and free-field boundary. These other boundary conditions have not been explored and tested in 3D due to an existing flaw which is currently being fixed by the adopted software, i.e. PLAXIS. Another factor which can influence the simulation results is the soil-structure interface properties. Utilising a user-defined model requires interface input data which is not easy to quantify. Conducting sensitivity analyses for different magnitudes of interface data will require a huge amount of computational time thereby preventing the author to explore further its effect on the simulation results.

6.2.2 *Lack of verification to real-life cases or test models*

The approach developed in this thesis lacks validation from real-life case studies or test models. Validating a new approach to actual field or test data will help to verify the effectiveness of the said approach. This was originally planned to be included in this thesis by using the measurement/observation data from the Bolu tunnel in Turkey which collapses during the 1999 Düzce earthquake. However due to the enormous amount of time needed to develop and run the model as well as the computational constraints, this plan has been abandoned.

6.3 Recommendations for further work

Based on the limitations mentioned above, there are several items that can be explored further in the future and extend and possibly improve the work that the author has started. These are as follows:

1. Examine other factors that can influence the soil model as well as the finite element models. These can include exploring the effects of inherent anisotropy of soil fabric which further differentiates the natural clay from reconstituted soils. Although this behaviour has been briefly mentioned in this dissertation, its effects have not been fully explored. Factors which affect the finite element models should also be investigated such as the boundary conditions and soil-structure interface data. Understanding the advantages, disadvantages and limitations of other dynamic boundary conditions (e.g. compliant base, free-field boundary, domain reduction method, etc.) can help find the most suitable solution for this type of geotechnical structure. In addition, quantifying correctly the interface properties particularly for user-defined models can lead to more accurate results. This, however, is not an easy task and requires sensitivity analyses to understand the impact of different magnitudes of interface values thereby the need for further study and demands further simulations.
2. Apply this new 3D approach to real-life cases or test models (e.g. centrifuge) in order to verify its effectiveness. This will require calibration of RMW soil parameters derived from actual soil data and laboratory results. It will also need earthquake data and the physical impact of seismic loading on the soil

and tunnel lining. The results from the actual data or test models and the computer simulations can then be compared to verify the performance of this new approach against real cases. Based on the comparison, possible adjustment or further study and testing might be necessary to refine the input data and thereby establish its capability to predict the actual behaviour of the soil and tunnel lining during earthquake.

3. Conduct a parametric study on the influence of different magnitudes of the initial soil structure r_0 on the tunnel lining forces during an earthquake event which might prove to be of more significance than the rate of destructuration k as demonstrated in the case studies in this dissertation.

Chapter 7. References

Acosta, J.L.G. (2015) 'Dynamic Response of Vertical Sand Drains in a Zone with Seismic Amplification', *From Fundamental to Applications in Geotechnics: Proceedings of the 15th Pan-American Conference on Soil Mechanics and Geotechnical Engineering*. Buenos Aires, Argentina. IOS Press, pp. 1153-1160.

Al-Tabbaa, A. (1987) *Permeability and stress-strain response of speswhite kaolin*. PhD thesis. University of Cambridge.

Al-Tabbaa, A. and Wood, D.M. (1989) 'An experimentally based" bubble'model for clay', *Numerical models in geomechanics. NUMOG III*, pp. 91-99.

Alawaji, H., Alawi, M., Ko, H.Y., Sture, S., Peters, J.F. and Muir Wood, D. (1990) 'Experimental observations of anisotropy in some stress-controlled tests on dry sand', in Boehler, J.P. and Boehler, J.P. (eds.) *Yielding, damage and failure of anisotropic solids*. London: Mechanical Engineering Publications, pp. 251-264.

Amorosi, A. and Boldini, D. (2005) 'Numerical analysis of settlements related to tunnelling: the role of stress-induced anisotropy and structure degradation in fine-grained soils', *Geotechnical Aspects of Underground Construction in Soft Ground: Proceedings of the 5th International Symposium TC28. Amsterdam, the Netherlands, 15-17 June 2005*. CRC Press, p. 465.

Amorosi, A. and Boldini, D. (2009) 'Numerical modelling of the transverse dynamic behaviour of circular tunnels in clayey soils', *Soil Dynamics and Earthquake Engineering*, 29(6), pp. 1059-1072.

Amorosi, A., Boldini, D. and Elia, G. (2010) 'Parametric study on seismic ground response by finite element modelling', *Computers and Geotechnics*, 37(4), pp. 515-528.

Amorosi, A., Boldini, D. and Sasso, M. (2008) *Modellazione numerica del comportamento dinamico di gallerie superficiali in terreni argillosi*. Italia. [Online]. Available at: http://amsacta.unibo.it/2392/.

Amorosi, A., Elia, G., Boldini, D. and Schiavone, F. (2011) 'Seismic ground response analysis: comparison between numerical simulations and observed array data', *Proc. 5th Int. Conf on Earthquake Geotechnical Engineering, Santiago, Chile*. pp. 10-13.

Anastasopoulos, I., Callerio, A., Bransby, M., C. R. Davies, M., El-Nahas, A.A., Faccioli, E., Gazetas, G., Masella, A., Paolucci, R., Pecker, A. and Rossignol, E. (2008) 'Numerical analyses of fault–foundation interaction', *Bulletin of Earthquake Engineering*, 6, pp. 645-675.

Argyroudis, S.A. and Pitilakis, K.D. (2012) 'Seismic fragility curves of shallow tunnels in alluvial deposits', *Soil Dynamics and Earthquake Engineering*, 35, pp. 1-12.

Arias, A. (1970) *Measure of Earthquake Intensity*. Massachusetts Inst. of Tech., Cambridge. Univ. of Chile, Santiago de Chile.

Arthur, J.R.F., Rodriguez del C, J.I., Dunstan, T. and Chua, K.S. (1980) 'Principal stress rotation: a missing parameter', *Journal of the Geotechnical Engineering Division*, 106(4), pp. 419-433.

Assimaki, D., Li, W., Steidl, J. and Schmedes, J. (2008) 'Quantifying Nonlinearity Susceptibility via Site-Response Modeling Uncertainty at Three Sites in the Los Angeles Basin', *Bulletin of the Seismological Society of America*, 98(5), pp. 2364-2390.

Azadi, M. and Hosseini, S.M.M.M. (2010) 'Analyses of the effect of seismic behavior of shallow tunnels in liquefiable grounds', *Tunnelling and underground space technology*, 25(5), pp. 543-552.

Barciaga, T., Taiebat, M., Dafalias, F., Datcheva, M. and Schanz, T. (2016) 'Influence of the mechanical behavior or natural structured soils on the system response in mechanized tunneling', *IV International Workshop on Modern Trends in Geomechanics*. Assisi, Italy, 16–18 May 2016.

Bardet, J.P., Ichii, K. and Lin, C.H. (2000) *EERA: a computer program for equivalent-linear earthquake site response analyses of layered soil deposits*. University of Southern California, Department of Civil Engineering.

Baudet, B. and Stallebrass, S. (2004) 'A constitutive model for structured clays', *Géotechnique*, 54(4), pp. 269-278.

Baudet, B.A. and Ho, E.W.L. (2005) 'Modelling the effects of structure in deep-ocean sediments', *Frontiers in Offshore Geotechnics, ISFOG 2005-Proceedings of the 1st International Symposium on Frontiers in Offshore Geotechnics*.

Belokas, G. and Kavvadas, M. (2010) 'An anisotropic Model for Structured Soils: Part I: Theory', *Computers and Geotechnics*, 37(6), pp. 737-747.

Bian, X., Hong, Z.-S. and Ding, J.-W. (2016) 'Evaluating the effect of soil structure on the ground response during shield tunnelling in Shanghai soft clay', *Tunnelling and Underground Space Technology*, 58, pp. 120-132.

Bilotta, E. (2018) 'Modelling tunnel behaviour under seismic actions: An integrated approach', *9th International Conference on Physical Modelling in Geotechnics (ICPMG 2018)*. London, United Kingdom, 17-20 July 2018. London: CRC Press pp. 3-20.

Bilotta, E., Lanzano, G., Madabhushi, S.P.G. and Silvestri, F. (2014) 'A numerical Round Robin on tunnels under seismic actions', *Acta Geotechnica*, 9(4), pp. 563-579.

Bilotta, E., Lanzano, G., Russo, G., Santucci de Magistris, F. and Silvestri, F. (2007) 'Methods for the seismic analysis of transverse section of circular tunnels in soft ground', *Workshop of ERTC12-Evaluation Committee for the Application of EC8 Special Session XIV ECSMGE, Madrid, Patron Ed., Bologna*.

Bobet, A. (2010) 'Numerical methods in geomechanics', *The Arabian Journal for Science and Engineering*, 35(1B), pp. 27-48.

Bolouri Bazaz, J. and Besharat, V. (2008) 'An Investigation on Seismic Analysis of Shallow Tunnels in Soil Medium', *Journal of Mathematics*.

Borja, R.I., Lin, C.-H. and Montáns, F.J. (2001) 'Cam-Clay plasticity, Part IV: Implicit integration of anisotropic bounding surface model with nonlinear hyperelasticity and ellipsoidal loading function', *Computer methods in applied mechanics and engineering*, 190(26), pp. 3293-3323.

Brinkgreve, R.B.J. and Broere, W. (2015) 'PLAXIS 2D Reference Manual 2015', *Delft, Netherlands2010*.

Brinkgreve, R.B.J., Kumarswamy, S. and Swolfs, W.M. (2015) 'Plaxis 3D Anniversary Edition Manual', *Plaxis bv. The Netherlands. Delft*.

Broere, W. (2016) 'Urban underground space: Solving the problems of today's cities', *Tunnelling and Underground Space Technology*, 55, pp. 245-248.

Brosse, A., Kamal, R.H., Jardine, R.J. and Coop, M.R. (2017) 'The shear stiffness characteristics of four Eocene-to-Jurassic UK stiff clays', *Géotechnique*, 67(3), pp. 242-259.

Brown, D.A., O'Neill, M., Hoit, M., McVay, M., El Naggar, M. and Chakraborty, S. (2001) *NCHRP Report 461–Static and Dynamic Lateral Loading of Pile Groups*. National Academy Press, W.D.C.

Burghignoli, A., Cocciuti, M., Miliziano, S. and Soccodato, F.M. (2003) 'Evaluation of advanced constitutive modelling for cemented clayey soils: A case history', *Mathematical and computer modelling*, 37(5-6), pp. 631-640.

Burghignoli, A., D'Elia, M., Miliziano, S. and Soccodato, F.M. (1999) 'Analisi dei cedimenti di un silo fondato su terreni argillosi cementati', *Rivista Italiana di Geotecnica*, 3, pp. 23-36.

Burghignoli, A., Miliziano, S. and Soccodato, F.M. (2010) 'Cementation effects in two lacustrine clayey soils', *Geotechnical and Geological Engineering*, 28(6), pp. 815-833.

Burland, J.B. (1990) 'On the compressibility and shear strength of natural clays', *Géotechnique*, 40(3), pp. 329-378.

Burland, J.B., Rampello, S., Georgiannou, V.N. and Calabresi, G. (1996) 'A laboratory study of the strength of four stiff clays', *Géotechnique*, 46(3), pp. 491-514.

Cabangon, L.T., Elia, G. and Rouainia, M. (2017) 'Advanced numerical modelling of the transverse behaviour of tunnels under seismic loading', *Proceedings of the Fourth International Conference on Computational Methods in Tunneling and Subsurface Engineering (EURO:TUN 2017)*. Innsbruck, Austria, 18-20 April 2017. pp. 729-737.

Cabangon, L.T., Elia, G. and Rouainia, M. (2018) '3D Numerical Analysis of tunnel behaviour in clayey soils under seismic loads', *16th European Conference on Earthquake Engineering (16ECEE)* Thessaloniki, Greece, 18-21 June 2018.

Cabangon, L.T., Elia, G. and Rouainia, M. (2019) 'Modelling the transverse behaviour of circular tunnels in structured clayey soils during earthquakes', *Acta Geotechnica*, 14(1), pp. 163-178.

Calabresi, G., Rampello, S., Sciotti, A. and Amorosi, A. (2000) 'Diga sulla Marana Capacciotti: Verifiche delle condizioni di stabilità e analisi del comportamento in condizioni sismiche', *Research Rep*.

Callisto, L. and Calabresi, G. (1998) 'Mechanical behaviour of a natural soft clay', *Geotechnique*, 48(4), pp. 495-513.

Cascone, E. and Rampello, S. (2003) 'Decoupled seismic analysis of an earth dam', *Soil Dynamics and Earthquake Engineering*, 23(5), pp. 349-365.

Castro, G. and Christian, J.T. (1976) 'Shear Strength of Soils and Cyclic Loading', *Journal of the Geotechnical Engineering Division*, 102(9), pp. 887-894.

Cha, Y.-H., Cho, G.-C., Hong, E.-S. and Lee, S.-W. (2016) 'A Feasibility Study for the Development of a Vertical Shaft Construction Technique using Ring Cutting', *The 2016 World Congress on Advances in Civil, Environmental, and Materials Research (ACEM16)*. Jeju Island, Korea. Techno-Press.

Chan, A.H.-C. (1988) *A unified finite element solution to static and dynamic problems of geomechanics*. PhD thesis. Swansea University.

Chan, A.H.C. (1993) 'User manual for Diana-Swandyne-II', *School of Civil Engineering. University of Birmingham, Birmingham*.

Chan, A.H.C. and Ou, J.-H. (2008) '3D Numerical Modelling of the Wave-Induced Response Around the Circular Caisson Founded on the Seabed', (48210), pp. 697-704.

Chang, D., Travasarou, T. and Chacko, J. (2008) 'Numerical evaluation of liquefaction-induced uplift for an immersed tunnel', *The 14th world conference on earthquake engineering*. Beijing, China.

Chapman, D.N., Metje, N. and Stark, A. (2017) *Introduction to tunnel construction*. CRC Press.

Charlton, T. and Rouainia, M. (2017) 'The Effect of the Spatial Variability of Clay Structure on Pipeline Uplift Capacity', *Geo-Risk 2017: Impact of Spatial Variability, Probabilistic Site Characterization, and Geohazards*. Denver, Colorado. pp. 340-349. Available at: https://doi.org/10.1061/9780784480717.032 (Accessed: 2018/09/18).

Charlton, T.S. and Rouainia, M. (2016) 'Probabilistic capacity analysis of suction caissons in spatially variable clay', *Computers and Geotechnics*, 80, pp. 226-236.

Charlton, T.S., Rouainia, M. and Gens, A. (2016) 'Numerical analysis of suction embedded plate anchors in structured clay', *Applied Ocean Research*, 61, pp. 156-166.

Chen, S.-L., Lee, S.-C. and Wei, Y.-S. (2016) 'Numerical Analysis of Ground Surface Settlement Induced by Double-O Tube Shield Tunneling', *Journal of Performance of Constructed Facilities*, 30(5), p. 04016012.

Cho, W.-S., Song, K.-I. and Kim, K.-Y. (2014) 'Mechanical behavior of ground due to EPB shield TBM tunnel excavation passing through fractured zone', *Proceedings of the Eight*

International Symposium on Geotechnical Aspects of Underground Construction in Soft Ground. Seoul, Korea. pp. 577-580.

Choudhury, D., Patil, M., Ranjith, P.G. and Zhao, J. (2019) 'Dynamic Tunnel–Soil Interaction in Soft Soils Considering Site-Specific Seismic Ground Response', in Latha G, M. (ed.) *Frontiers in Geotechnical Engineering*. Singapore: Springer Singapore, pp. 249-271.

Cilingir, U. and Madabhushi, S.P.G. (2011) 'A model study on the effects of input motion on the seismic behaviour of tunnels', *Soil Dynamics and Earthquake Engineering*, 31(3), pp. 452-462.

Clayton, C.R.I., Hight, D.W. and Hopper, R.J. (1992) 'Progressive destructuring of Bothkennar clay. implications for sampling and reconsolidation procedures', *Géotechnique*, 42(2), pp. 219-239.

Conti, R., Viggiani, G.B. and Perugini, F. (2014) 'Numerical modelling of centrifuge dynamic tests of circular tunnels in dry sand', *Acta Geotechnica*, 9(4), pp. 597-612.

Coop, M.R., Atkinson, J.H. and Taylor, R.N. (1995) 'Strength, yielding and stiffness of structured and unstructured soils', *Proceedings of the 11th European conference on soil mechanics and foundation engineering, Copenhagen, Denmark*. pp. 55-62.

Cotecchia, F. and Chandler, R.J. (1997) 'The influence of structure on the pre-failure behaviour of a natural clay', *Géotechnique*, 47(3), pp. 523-544.

Cotecchia, F. and Chandler, R.J. (2000) 'A general framework for the mechanical behaviour of clays', *Géotechnique*, 50(4), pp. 431-447.

Curtis, D.J. (1976) 'Discussion on the Circular Tunnel in Elastic Ground', *Geotechnique*, 26(1), pp. 231-237.

D'Elia, M. (2001) *Comportamento meccanico in condizioni cicliche e dinamiche di un'argilla naturale cementata*. PhD thesis. Università di Roma La Sapienza.

d'Onofrio, A., Olivares, L. and Santucci de Magistris, F. (1998) 'Influence of soil structure on the behaviour of two natural stiff clays in the pre-failure range', *II International Symposium on Hard Soil-Soft Rocks*. AA BALKEMA, pp. 497-505.

D'elia, M., Miliziano, S., Soccodato, F.M. and Tamagnini, C. (1999) 'Observed and predicted behaviour of a silo founded on a cemented soft clayey soil', *Pre-failure deformation characteristics of geomaterials. Balkema, Rotterdam*, pp. 741-748.

Dafalias, Y.F. (1987) 'An anisotropic critical state clay plasticity model', *Proceedings of the Second International Conference on Constitutive Laws for Engineering Materials: Theory and Applications*. Tucson, Arizona, U.S.A. Elsevier, pp. 513-521.

Dang, H.K. and Meguid, M.A. (2008) 'Application of a multilaminate model to simulate the undrained response of structured clay to shield tunnelling', *Canadian Geotechnical Journal*, 45(1), pp. 14-28.

Darendeli, M.B. (2001) *Development of a new family of normalized modulus reduction and material damping curves*. PhD thesis. University of Texas, Austin, Texas, USA.

Della Valle, N., Salas Monge, R. and Savin, E. (2014) 'Adoption of shear keys to provide stability to TBM tunnels segmental lining during cross passages construction: The example of Aked tunnel.', *Proceedings of the World Tunnel Congress 2014 – Tunnels for a better Life*. Foz do Iguaçu, Brazil.

DESA, U.N. (2014) 'United Nations, Department of Economic and Social Affairs, Population Division (2014): World Urbanization Prospects, The 2014 Revision, CD-ROM Edition'. UN publications, New York, http://esa.un.org/unpd/wup/FinalReport/WUP2014-Report.pdf.

DESA, U.N. (2019) 'United Nations, Department of Economic and Social Affairs, Population Division: World Urbanization Prospects: The 2018 Revision (ST/ESA/SER.A/420)'. UN publications, New York, https://population.un.org/wup/Publications/Files/WUP2018-Report.pdf.

Dijkstra, J., Broere, W. and Van Tol, A.F. (2006) 'Numerical investigation into stress and strain development around a displacement pile in sand', *Numerical Methods in Geotechnical Engineering*, pp. 595-600.

Dobashi, H., Hatsuku, T., Ichimura, T., Hori, M., Yamada, T., Ohbo, N., Moriguchi, M. and Itami, H. (2008) 'Full 3D seismic response analysis of underground ramp tunnel structure using large-scale numerical computation', *Proceedings of the 14th World Conference on Earthquake Engineering*. Beijing, China. pp. Paper (No. 14-0150).

Dobashi, H., Terashima, Y., Hori, M., Ichimura, T., Ohbo, N., Yamada, T. and Obara, T. (2011) 'Seismic Performance Analysis of Underground Ramp Tunnel Structure using 3-D Massive Numerical Computation', *Proceedings of III ECCOMAS Thematic Conference on Computational Methods in Structural Dynamics and Earthquake Engineering, COMPDYN 2011*. Corfu, Greece, 25–28 May 2011.

Eid, M., Hefny, A., Sorour, T., Zaghloul, Y. and Ezzat, M. (2018) 'Numerical Analysis of Large Diameter Bored Pile Installed in Multi Layered Soil: A Case Study of Damietta Port New Grain Silos Project', *International Journal of Current Engineering and Technology*, 8(02), pp. 218-226.

El-Emam, M.M., Bathurst, R.J. and Hatami, K. (2004) 'Numerical modeling of reinforced soil retaining walls subjected to base acceleration', *13th World Conference on Earthquake Engineering*. Vancouver, B.C., Canada

Elia, G. (2012) 'Equivalent linear versus nonlinear site response analysis' *Recent advances in site response analysis, Imperial College London - Skempton Building*. The Society for Earthquake and Civil Engineering Dynamics.

Elia, G. (2015) 'Lecture Notes on Soil Modelling and Numerical Methods'. Department of Civil Engineering and Geosciences, Newcastle University, UK.

Elia, G., Amorosi, A., Chan, A. and Kavvadas, M. (2010) 'Numerical Prediction of the Dynamic Behavior of Two Earth Dams in Italy Using a Fully Coupled Nonlinear Approach', *International Journal of Geomechanics*, 11(6), pp. 504-518.

Elia, G., Amorosi, A., Chan, A.H.C. and Kavvadas, M.J. (2011) 'Fully coupled dynamic analysis of an earth dam', *Geotechnique*, 61(7), pp. 549-563.

Elia, G. and Rouainia, M. (2010) '2D Finite element analysis of the seismic response of an earth embankment', *SECED Newsletter*, 22(2), pp. 1-5.

Elia, G. and Rouainia, M. (2012) 'Seismic Performance of Earth Embankment Using Simple and Advanced Numerical Approaches', *Journal of Geotechnical and Geoenvironmental Engineering*, 139(7), pp. 1115-1129.

Elia, G. and Rouainia, M. (2014) 'Performance evaluation of a shallow foundation built on structured clays under seismic loading', *Bulletin of Earthquake Engineering*, 12(4), pp. 1537-1561.

Elia, G. and Rouainia, M. (2016) 'Investigating the cyclic behaviour of clays using a kinematic hardening soil model', *Soil Dynamics and Earthquake Engineering*, 88, pp. 399-411.

Elia, G., Rouainia, M. and Panayides, S. (2016) 'Finite Element Modelling of a Deep Excavation in Boston Blue Clay', *Procedia Engineering*, 158, pp. 242-247.

Elia, G., Rouainia, M. and Shahraki, S.N. (2013) 'Blind prediction of the seismic response of tunnels observed in centrifuge experiments', *in Underground The Way to the Future: Proceedings of the World Tunnel Congress (WTC'13)*. pp. 1095-1102.

Ellison, K.C., Masroor, A.M., Almufti, I., Willford, M. and O'Riordan, N. (2015) 'Structure-Soil-Structure Interaction Analysis in a Highly Seismic, Dense Urban Regeneration Zone', *6th International Conference on Earthquake Geotechnical Engineering*. Christchurch, New Zealand.

Ertugrul, N. (2010) *Analysis of Seismic Behavior of Underground Structures: A Case Study on Bolu Tunnels*. Masteral thesis. Middle East Technical University.

Fabozzi, S. and Bilotta, E. (2016) 'Behaviour of a Segmental Tunnel Lining Under Seismic Actions', *Procedia Engineering*, 158, pp. 230-235.

Fabozzi, S., Bilotta, E., Yu, H. and Yuan, Y. (2018) 'Effects of the asynchronism of ground motion on the longitudinal behaviour of a circular tunnel', *Tunnelling and Underground Space Technology*, 82, pp. 529-541.

Fabozzi, S., Licata, V., Autuori, S., Bilotta, E., Russo, G. and Silvestri, F. (2017) 'Prediction of the seismic behavior of an underground railway station and a tunnel in Napoli (Italy)', *Underground Space*, 2(2), pp. 88-105.

Fattah, M.Y., Hamoo, M.J. and Dawood, S.H. (2015) 'Dynamic response of a lined tunnel with transmitting boundaries', *Earthquakes and Structures*, 8(1), pp. 275-304.

Felippa, C.A. (2017) 'Introduction to Finite Element Methods' [Lecture Notes]. Department of Aerospace Engineering Sciences, University of Colorado at Boulder. Available at: https://www.colorado.edu/engineering/cas/courses.d/IFEM.d/.

Fernández Ruiz, J. and Medina Rodríguez, L. (2015) 'Application of an advanced soil constitutive model to the study of railway vibrations in tunnels through 2D numerical models: a real case in Madrid (Spain)', *Revista de la construcción*, 14, pp. 55-63.

Flores, F. and Mayoral, J.M. (2011) 'Static behavior of a tunnel built in very soft clay', *Proceedings of the 2nd International FLAC/DEM Symposium - Continuum and Distinct Element Numerical Modeling in Geomechanics*. Melbourne, Australia, 14-16 February 2011.

Gazetas, G., Gerolymos, N. and Anastasopoulos, I. (2005) 'Response of three Athens metro underground structures in the 1999 Parnitha earthquake', *Soil Dynamics and Earthquake Engineering*, 25(7-10), pp. 617-633.

Gens, A. and Nova, R. (1993) 'Conceptual bases for a constitutive model for bonded soils and weak rocks', *Proc. Int. Conf. on Hard Soils-Soft Rocks*. Athens. pp. 485-494.

Ghosh, B. and Madabhushi, S.P.G. (2004) 'Dynemic Soil Structure Interaction for Layered and Inhomogeneous Ground: A Comparitive Study', *Proceedings of the the 13th World Conference on Earthquake Engineering*. Vancouver, BC, Canada. pp. 1-15.

Godard, J.P. (2002) 'Why go underground', *Urban underground space: a resource for cities, Actes de la conférence internationale de l'ACUUS, Torino*.

Goel, T. and Sonthwal, V.K. (2017) 'A Review on Slope Stability Analysis by Strength Reduction Method using MIDAS GTS', *International Journal of Innovative Research in Science, Engineering and Technology*, 6(8), pp. 17050-17053.

Goit, C.S., Kovács, A. and Thomas, A.H. (2011) 'Advanced numerical modeling in tunnel design - example of a major project in UK', *Proceedings of the 2nd International FLAC/DEM Symposium - Continuum and Distinct Element Numerical Modeling in Geomechanics*. Melbourne, Australia, 14-16 February 2011.

González, N.A., Gens Solé, A., Arroyo Alvarez de Toledo, M. and Rouainia, M. (2011) 'A structured constitutive model for simulating the behaviour of an overconsolidated bonded clay', *Computational plasticity XI: fundamentals and applications: proceedings of the XI International Conference on Computational Plasticity held in Barcelona, Spain, 07-09 September 2011*. Centro Internacional de Métodos Numéricos en Ingeniería (CIMNE), pp. 2-12.

González, N.A., Rouainia, M., Arroyo, M. and Gens, A. (2012) 'Analysis of tunnel excavation in London Clay incorporating soil structure', *Geotechnique*, 62(12), p. 1095.

Graham, J. and Houlsby, G.T. (1983) 'Anisotropic elasticity of a natural clay', *Géotechnique*, 33(2), pp. 165-180.

Grammatikopoulou, A. (2004) *Development, implementation and application of kinematic hardening models for overconsolidated clays*. PhD thesis. Imperial College London.

Gregor, T. and Shobayry, R. (2011) 'Seismic analysis of large underground structures using FLAC 3D', *Proceedings of the 2nd International FLAC/DEM Symposium - Continuum and Distinct Element Numerical Modeling in Geomechanics*. Melbourne, Australia, 14-16 February 2011.

Gu, C., Wang, J., Cai, Y., Yang, Z. and Gao, Y. (2012) 'Undrained cyclic triaxial behavior of saturated clays under variable confining pressure', *Soil Dynamics and Earthquake Engineering*, 40, pp. 118-128.

Gu, Q. (2014) 'Performance and Risk Assessment of Soil-Structure Interaction Systems Based on Finite Element Reliability Methods', *Mathematical Problems in Engineering*, 2014, p. 16.

Gu, S.-c., Zhu, B. and Yang, R.-s. (2007) 'Effect of artificial boundary on seismic response of underground structure [J]', *Journal of Liaoning Technical University*, 3.

Gutierrez, M. and Ishihara, K. (2000) 'Non-Coaxiality and Energy Dissipation in Granular Materials', *Soils and Foundations*, 40(2), pp. 49-59.

Haigh, S.K., Coelho, P.A.L.F. and Madabhushi, S.P.G. (2005) 'On the prediction of dynamic behaviour using numerical and physical modelling', *Proceedings of the 16th International Conference on Soil Mechanics and Geotechnical Engineering*. Osaka, Japan. pp. 2649-2652.

Hashash, Y.M.A., Hook, J.J., Schmidt, B. and I-Chiang Yao, J. (2001) 'Seismic design and analysis of underground structures', *Tunnelling and Underground Space Technology*, 16(4), pp. 247-293.

Hashash, Y.M.A. and Park, D. (2002) 'Viscous damping formulation and high frequency motion propagation in non-linear site response analysis', *Soil Dynamics and Earthquake Engineering*, 22(7), pp. 611-624.

Hashash, Y.M.A., Park, D. and Yao, J.I.C. (2005) 'Ovaling deformations of circular tunnels under seismic loading, an update on seismic design and analysis of underground structures', *Tunnelling and Underground Space Technology*, 20(5), pp. 435-441.

Hashiguchi, K. (1985) 'Two-and three-surface models of plasticity', *Proceedings of the 5th International Conference on Numerical Methods in Geomechanics*. Nagoya, Japan. pp. 285-292.

Hashiguchi, K. (1988) 'A mathematical modification of two surface model formulation in plasticity', *International Journal of Solids and Structures*, 24(10), pp. 987-1001.

Hatzigeorgiou, G.D. and Beskos, D.E. (2010) 'Soil–structure interaction effects on seismic inelastic analysis of 3-D tunnels', *Soil Dynamics and Earthquake Engineering*, 30(9), pp. 851-861.

Hight, D.W., Böese, R., Butcher, A.P., Clayton, C.R.I. and Smith, P.R. (1992) 'Disturbance of the Bothkennar clay prior to laboratory testing', *Géotechnique*, 42(2), pp. 199-217.

Houlsby, G.T. (1985) 'The use of a variable shear modulus in elastic-plastic models for clays', *Computers and Geotechnics*, 1(1), pp. 3-13.

Houlsby, G.T., Amorosi, A. and Rojas, E. (2005) 'Elastic moduli of soils dependent on pressure: a hyperelastic formulation', *Géotechnique*, 55(5), pp. 383-392.

Huang, X., Zhu, Y., Zhang, Z., Zhu, Y., Wang, S. and Zhuang, Q. (2018) 'Mechanical behaviour of segmental lining of a sub-rectangular shield tunnel under self-weight', *Tunnelling and Underground Space Technology*, 74, pp. 131-144.

Huat, B.B.K. and Mohammed, T.A. (2006) 'Finite element study using FE code (PLAXIS) on the geotechnical behavior of shell footings', *Journal of Computer Science*, 2(1), pp. 104-108.

Hudson, M., Idriss, I. and Beikae, M. (1994) *QUAD4M: a computer program to evaluate the seismic response of soil structures using finite element procedures and incorporating a compliant base*. Center for Geotechnical Modeling, Department of Civil and Environmental Engineering, University of California, Davis.

Hung, C.J., Monsees, J., Munfah, N. and Wisniewski, J. (2009) *Technical Manual for Design and Construction of Road Tunnels - Civil Elements*. US Department of Transportation, Federal Highway Administration, National Highway Institute.

Hwang, R.N. and Lysmer, J. (1981) 'Response of buried structures to traveling waves', *Journal of Geotechnical and Geoenvironmental Engineering*, 107(ASCE 16052), pp. 183-200.

Ichimura, T., Tanaka, S., Hori, M., Yamamoto, Y., Dobashi, H., Osada, M., Ohbo, N. and Yamada, T. (2016) 'Full Three-Dimensional Seismic Response Analysis of Underground Structures with Large Complex Cross Sections and Two-Step Analysis Method for Reducing the Computational Costs', *Journal of Earthquake and Tsunami*, 10(05), p. 1640016.

Iervolino, I., Galasso, C. and Chioccarelli, E. (2012) 'REXEL 3.3: Closing the loop of computer aided record selection', *Proceedings of the 15th World Conference on Earthquake Engineering*. pp. 24-28.

Iervolino, I., Galasso, C. and Cosenza, E. (2010) 'REXEL: computer aided record selection for code-based seismic structural analysis', *Bulletin of Earthquake Engineering*, 8(2), pp. 339-362.

Ishibashi, I. and Zhang, X. (1993) 'Unified Dynamic Shear Moduli and Damping Ratios of Sand and Clay', *Soils and Foundations*, 33(1), pp. 182-191.

Jardine, R. (1985) *Investigations of pile-soil behaviour, with special reference to the foundations of offshore structures*. PhD thesis. Imperial College London (University of London).

Jardine, R.J. (1991) 'Some practical applications of a non-linear ground model', *Proc. XECSMFE, Florence*, 1, pp. 223-228.

Jia, J. (2018) 'Dynamic and Cyclic Properties of Soils', in *Soil Dynamics and Foundation Modeling: Offshore and Earthquake Engineering*. Cham: Springer International Publishing, pp. 75-108.

Jin, C. and Chi, S. (2017) 'Elasto-plastic Finite Element Analysis of an Earth-Rockfill Dam Based on Generalized plasticity model', *Proceedings of the 2017 3rd International Forum on Energy, Environment Science and Materials (IFEESM 2017)*. Atlantis Press.

Karstunen, M., Krenn, H., Wheeler, S., Koskinen, M. and Zentar, R. (2005) 'Effect of Anisotropy and Destructuration on the Behavior of Murro Test Embankment', *International Journal of Geomechanics*, 5(2), pp. 87-97.

Katona, M.C. and Zienkiewicz, O.C. (1985) 'A unified set of single step algorithms part 3: The beta-m method, a generalization of the Newmark scheme', *International Journal for Numerical Methods in Engineering*, 21(7), pp. 1345-1359.

Kavvadas, M. and Amorosi, A. (2000) 'A constitutive model for structured soils', *Géotechnique*, 50(3), pp. 263-273.

Kavvadas, M. and Belokas, G. (2000) 'An anisotropic elastoplastic constitutive model for natural soils', *Computer Methods and Advances in Geomechanics: Proceedings of the 10th International Conference on Computer Methods and Advances in Geomechanics, Tucson, Arizona, USA, 7-12 January 2001*. CRC Press, p. 335.

Kawashima, K. (2000) 'Seismic design of underground structures in soft ground: a review', *Geotechnical aspects of underground construction in soft ground*. Balkema, Rotterdam. pp. 3-20.

Khoshnoudian, F. and Shahrour, I. (2002) 'Numerical analysis of the seismic behavior of tunnels constructed in liquefiable soils', *Soils and foundations*, 42(6), pp. 1-8.

Kim, Y. and Jeong, S. (2011) 'Analysis of soil resistance on laterally loaded piles based on 3D soil–pile interaction', *Computers and Geotechnics*, 38(2), pp. 248-257.

Kolymbas, D. (2005) *Tunnelling and tunnel mechanics: A rational approach to tunnelling*. Springer Science & Business Media.

Kommerell, O. (1912) *Statische Berechnung von Tunnelmauerwerk : Grundlagen und Anwendung auf die wichtigsten Belastungsfälle*. Berlin: Wilhelm Ernst & Sohn.

Kontoe, S. (2006) *Development of time integration schemes and advanced boundary conditions for dynamic geotechnical analysis*. PhD thesis. Imperial College, London, UK.

Kontoe, S., Zdravkovic, L., Potts, D.M. and Menkiti, C.O. (2008) 'Case study on seismic tunnel response', *Canadian Geotechnical Journal*, 45(12), pp. 1743-1764.

Kontoe, S., Zdravkovic, L., Potts, D.M. and Menkiti, C.O. (2009) 'Comparison of constitutive models through a case study on seismic response of tunnels', *International Conference on Performance-Based Design in Earthquake Geotechnical Engineering –*

from case history to practice. IS-Tokyo, Japan. London: Taylor & Francis Group, pp. 1051-1059.

Kontoe, S., Zdravkovic, L., Potts, D.M. and Menkiti, C.O. (2011) 'On the relative merits of simple and advanced constitutive models in dynamic analysis of tunnels', *Geotechnique*, 61(10), pp. 815-829.

Kontoe, S., Zdravkovic, L., Potts, D.M. and Salandy, N.E. (2007) 'The use of absorbing boundaries in dynamic analyses of soil-structure interaction problems', *4th Int. Conf. in Earthquake Geotechnical Engineering*. The Technical Committee of Earthquake Geotechnical Engineering (TC4) of the International Society of Soil Mechanics and Geotechnical Engineering (ISSMGE), the Hellenic Scientific Society of Soil Mechanics and Geotechnical Engineering and the Laboratory of Soil Dynamics and Geotechnical Earthquake Engineering of Aristotle University of Thessaloniki.

Korhonen, K.H. and Lojander, M. (1987) 'Yielding of Perno clay', *Proceedings of the 2nd international conference on constitutive laws for engineering materials*. Tucson, Arizona. Elsevier, pp. 1249-1255.

Koskinen, M., Karstunen, M. and Wheeler, S.J. (2002) 'Modelling destructuration and anisotropy of a natural soft clay', *Proc. 5h European Conf on Numerical Methods in Geotechnical Engineering (NUMGE 2002)*. Paris. Presses de l'ENPC, pp. 11-20.

Koungelis, D.K. and Augarde, C.E. (2004) 'Interaction between multiple tunnels in soft ground', in Deeks, A.J. and Hao, H. (eds.) *Developments in mechanics of structures & materials : proceedings of the 18th Australasian Conference on the Mechanics of Structures and Materials, Perth, Australia, 1-3 December 2004*. London: Taylor & Francis, pp. 1031-1036.

Kramer, S.L. (1996) 'Geotechnical earthquake engineering. In prentice–Hall international series in civil engineering and engineering mechanics', *Prentice-Hall, New Jersey*.

Kuesel, T.R. (1969) 'Earthquake Design Criteria for Subways', *Journal of the Structural Division*, 95(6), pp. 1213-1231.

Kuhlemeyer, R.L. and Lysmer, J. (1973) 'Finite Element Method Accuracy for Wave Propagation Problems', *Journal of the Soil Mechanics and Foundations Division*, 99(5), pp. 421-427.

Lagioia, R. and Potts, D.M. (1999) 'The behaviour of shallow foundations on structured soils', *Rivista italiana di Geotecnica*, 33(4), pp. 52-64.

Lambe, T.W. and Whitman, R.V. (1969) *Soil mechanics*. New York: John Willey & Sons Inc.

Lanzano, G., Bilotta, E., Russo, G., Silvestri, F. and Madabhushi, S. (2012) 'Centrifuge Modeling of Seismic Loading on Tunnels in Sand', *Geotechnical Testing Journal*, 35(6), pp. 854-869.

Lanzo, G. and Silvestri, F. (1999) *Risposta sismica locale. Teoria ed esperienze*. Hevelius.

Laver, R. and Soga, K. (2012) 'Numerical simulation of long-term twin-tunnel behaviour at St James's park', in *Geotechnical Aspects of Underground Construction in Soft Ground*. CRC Press, pp. 413-420.

Lee, C.-J. and Sheu, S.-F. (2007) 'The stiffness degradation and damping ratio evolution of Taipei Silty Clay under cyclic straining', *Soil Dynamics and Earthquake Engineering*, 27(8), pp. 730-740.

Leon, A. and Willheim, F. (1910) *Uber die Zerstörung in tunnelartig gelochten Gesteinen*. Wien: Lehmann et Wentzel.

Leroueil, S., Roy, M., La Rochelle, P., Brucy, F. and Tavenas, F.A. (1979) 'Behavior of destructured natural clays', *Journal of Geotechnical and Geoenvironmental Engineering*, 105(6), pp. 759-778.

Leroueil, S. and Vaughan, P.R. (1990) 'The general and congruent effects of structure in natural soils and weak rocks', *Geotechnique*, 40(3), pp. 467-488.

Li, T. (2012) 'Damage to mountain tunnels related to the Wenchuan earthquake and some suggestions for aseismic tunnel construction', *Bulletin of Engineering Geology and the Environment*, 71(2), pp. 297-308.

Liu, H. and Song, E. (2005) 'Seismic response of large underground structures in liquefiable soils subjected to horizontal and vertical earthquake excitations', *Computers and Geotechnics*, 32(4), pp. 223-244.

Liu, W., Hutchinson, T.C. and Stuedlein, A.W. (2015) 'Modeling of Foundation-Soil Systems Using Plane-Strain Elements', *6th International Conference on Earthquake Geotechnical Engineering*. Christchurch, New Zealand.

Low, H.E. (2004) *Compressibility and undrained behaviour of natural Singapore marine clay: Effect of soil structure*. M. Eng thesis. Department of Civil Engineering, National University of Singapore, Singapore.

Lubkowski, Z.A., Pappin, J.W. and Willford, M.R. (2000) 'The influence of dynamic soil structure interaction on the seismic design and performance of an ethylene tank', *Proceedings of the 12th World Conference in Earthquake Engineering*. Auckland, New Zealand.

Lysmer, J. and Kuhlemeyer, R.L. (1969) 'Finite dynamic model for infinite media', *Journal of the Engineering Mechanics Division*, 95(4), pp. 859-878.

Maheshwari, B.K., Truman, K.Z., Naggar, M.H.E. and Gould, P.L. (2004) 'Three-dimensional finite element nonlinear dynamic analysis of pile groups for lateral transient and seismic excitations', *Canadian Geotechnical Journal*, 41(1), pp. 118-133.

Mair, R.J. (1996) 'Settlement effects of bored tunnels', *In: Proc. Int. Symposium on Geotechnical Aspects on Underground Construction in Soft Ground*. AA Balkema, pp. 43-53.

Mašín, D. (2003) 'A kinematic hardening critical state model for anisotropic clays', *Proc. Constitutive Modelling and Analysis of BVP in Geotechnical Engineering, Napoli, Italy*, pp. 253-263.

Matasovic, N. and Vucetic, M. (1995) *Generalized Cyclic-Degradation-Pore-Pressure Generation Model for Clays*.

Mayne, P.W. and Kulhawy, F.H. (1982) 'Ko- OCR Relationships in Soil', *Journal of the Soil Mechanics and Foundations Division*, 108(6), pp. 851-872.

Mayoral, J.M., Sarmiento, N. and Castañon, E. (2015) 'Seismic Response of Floating Tunnel Shafts', *6th International Conference on Earthquake Geotechnical Engineering* Christchurch, New Zealand

McDowell, G.R. and Hau, K.W. (2003) 'A simple non-associated three surface kinematic hardening model', *Géotechnique*, 53(4), pp. 433-437.

Mohammadi-Haji, B. and Ardakani, A. (2018) 'Numerical prediction of circular tunnel seismic behaviour using hypoplastic soil constitutive model', *International Journal of Geotechnical Engineering*, pp. 1-14.

Moldovan, A.R. and Popa, A. (2012) 'Finite element modelling for tunnelling excavation', *Civil Engineering & Architecture*, 55(1), pp. 98-113.

Mroueh, H. and Shahrour, I. (2003) 'A full 3-D finite element analysis of tunneling–adjacent structures interaction', *Computers and Geotechnics*, 30(3), pp. 245-253.

Mróz, Z. (1967) 'On the description of anisotropic workhardening', *Journal of the Mechanics and Physics of Solids*, 15(3), pp. 163-175.

Mróz, Z., Norris, V.A. and Zienkiewicz, O.C. (1979) 'Application of an anisotropic hardening model in the analysis of elasto–plastic deformation of soils', *Geotechnique*, 29(1), pp. 1-34.

Muir-Wood, A.M. (1975) 'The circular tunnel in elastic ground', *Géotechnique*, 25(1), pp. 115-127.

Murianni, A., Zanoli, O. and Parker, E. (2015) 'Evaluation of pipe-soil interaction in liquefied soil', *Frontiers in Offshore Geotechnics III*, pp. 429-434.

Naatänen, A., Wheeler, S.J., Karstunen, M. and Lojander, M. (1999) 'Experimental investigation of an anisotropic hardening model for soft clays', *Proc. 2nd Int. Symp. on Pre-Failure Deformation Characteristics of Geomaterials*. Torino. Balkema, pp. 541-548.

Namazi, E., Mohamad, H., Hong, A.K.B., Hajihassani, M., Jusoh, S.N. and Abad, S. (2012) 'Ground behaviour around a tunnel using various soil models', *Electronic Journal of Geotechnical Engineering*, 17(E), pp. 609-622.

Nash, D., Lings, M., Benahmed, N. and Sukolrat, J. (2007) 'The effects of controlled destructuring on the small strain shear stiffness G 0 of Bothkennar clay', in *Soil Stress-Strain Behavior: Measurement, Modeling and Analysis*. Springer, pp. 287-298.

Ni, B. (2001) *Nonlinear dynamic soil-structure interaction analysis with FLAC*. Masters thesis. University of Auckland.

Ni, B. (2007) *Implementation of a bubble model in FLAC and its application in dynamic analysis*. Doctoral thesis. The University of Auckland.

Nielsen, A.H. (2008) 'Boundary Conditions for Seismic Analysis', *SECED and NAFEMS Seminar: Seismic Analysis using Finite Elements*. London, UK, 5 December 2008.

Oda, M., Nemat-Nasser, S. and Konishi, J. (1985) 'Stress-Induced Anisotropy in Granular Masses', *Soils and Foundations*, 25(3), pp. 85-97.

Oettl, G., Stark, R.F. and Hofstetter, G. (1998) 'A comparison of elastic–plastic soil models for 2D FE analyses of tunnelling', *Computers and Geotechnics*, 23(1), pp. 19-38.

Ohbo, N., Horikoshi, K., Yamada, T., Tachibana, K. and Akiba, H. (2004) 'Dynamic behavior of a underground motorway junction due to large earthquake', *13th World Conference on Earthquake Engineering*. Vancouver, B.C., Canada.

Okamoto, S., Tamura, C., Kato, K. and Hamada, M. (1973) 'Behaviors of submerged tunnels during earthquakes', *Proceedings of the fifth world conference on earthquake engineering*. Rome, Italy. pp. 544-553.

Ou, J.H. and Chan, A.H.C. (2006) 'Three Dimensional Numerical Modelling of Dynamic Saturated Soil and Pore Fluid Interaction', *Proceedings of the Fifth International Conference on Engineering Computational Technology*. Stirlingshire, UK.

Owen, G.N. and Scholl, R.E. (1981) 'Earthquake engineering of large underground structures', *NASA STI/Recon Technical Report N*, 82.

Pakbaz, M.C. and Yareevand, A. (2005) '2-D analysis of circular tunnel against earthquake loading', *Tunnelling and Underground Space Technology*, 20(5), pp. 411-417.

Panayides, S. (2014) *Modelling the Effects of Structure Degradation in Geotechnical Problems*. PhD thesis. University of Newcastle upon Tyne, School of Civil Engineering and Geosciences.

Panayides, S., Rouainia, M. and Muir Wood, D. (2012) 'Influence of degradation of structure on the behaviour of a full-scale embankment', *Canadian Geotechnical Journal*, 49(3), pp. 344-356.

Panayides, S., Rouainia, M. and Osman, A.S. (2010) 'Numerical investigation of the behaviour of suction caissons in structured clays', in Gourvenec, S. and White, D. (eds.) *Frontiers in offshore geotechnics II.* Boca Raton: CRC Press, pp. 759-764.

Park, D., Sagong, M., Kwak, D.-Y. and Jeong, C.-G. (2009) 'Simulation of tunnel response under spatially varying ground motion', *Soil Dynamics and Earthquake Engineering*, 29(11–12), pp. 1417-1424.

Patil, M., Choudhury, D., Ranjith, P.G. and Zhao, J. (2018) 'Behavior of shallow tunnel in soft soil under seismic conditions', *Tunnelling and Underground Space Technology*, 82, pp. 30-38.

Peck, R.B., Hendron, A.J. and Mohraz, B. (1972) 'State of the art of soft-ground tunneling', *N Am Rapid Excav & Tunneling Conf Proc*, 1, pp. 259-286.

Peiris, N. (2000) 'Dynamic soil-structure interaction analysis using LS-DYNA', in *Sixth Young Geotechnical Engineers Symposium*. pp. 7-8.

Penzien, J. (2000) 'Seismically induced racking of tunnel linings', *Earthquake Engineering & Structural Dynamics*, 29(5), pp. 683-691.

Penzien, J. and Wu, C.L. (1998) 'Stresses in linings of bored tunnels', *Earthquake Engineering & Structural Dynamics*, 27(3), pp. 283-300.

Pineda, J.A., Suwal, L.P., Kelly, R.B., Bates, L. and Sloan, S.W. (2016) 'Characterisation of Ballina clay', *Géotechnique*, 66(7), pp. 556-577.

Pinto, P.A. (2012) *Study of Constitutive Models for Soils under Cyclic Loading*. Master's thesis. Universidade Técnica de Lisboa, Lisbon, Portugal, 12 November.

Pitilakis, D., Rovithis, E., Massimino, M. and Gatto, M. (2015) 'Numerical simulation of large-scale soil-foundation-structure interaction experiments in The EuroProteas facility', *Proceedings of the 6th International Conference on Earthquake Geotechnical Engineering*. Christchurch, New Zealand.

Pitilakis, K. and Tsinidis, G. (2014) 'Performance and Seismic Design of Underground Structures', in Maugeri, M. and Soccodato, C. (eds.) *Earthquake Geotechnical Engineering Design*. Springer International Publishing, pp. 279-340.

Pitts, J. (1992) 'Landforms and Geomorphic Evolution of the Islands during the Quaternary', *Physical Adjustment in a Changing Landscape: The Singapore Story, A. Gupta and J. Pitts, eds., Singapore University Press, Singapore*, pp. 83-143.

Potts, D.M. and Zdravković, L.U.h.b.g.c.u.b.i.J. (1999) *Finite element analysis in geotechnical engineering: theory*. Thomas Telford.

Power, M.S., Rosidi, D. and Kaneshiro, J. (1996) *Vol. III Strawman: screening, evaluation, and retrofit design of tunnels*. Buffalo, New York.

Qiao, L., Yuan, C., Miyajima, M. and Zhai, E. (2008) 'Shake-table testing and FLAC modeling of liquefaction-induced slope failure and damage to buried pipelines', in *Geotechnical Earthquake Engineering and Soil Dynamics IV*. pp. 1-10.

Rampello, S. (1993) 'The stress-strain behaviour of natural and reconstituted samples of two overconsolidated clays', *Proc. 1st Int Symp. on Hard Soils-Soft Rocks*, 1, pp. 769-778.

Rampello, S., Cascone, E. and Grosso, N. (2009) 'Evaluation of the seismic response of a homogeneous earth dam', *Soil Dynamics and Earthquake Engineering*, 29(5), pp. 782-798.

Rao, S.S. (2018) *The Finite Element Method in Engineering (Sixth Edition)*. Butterworth-Heinemann.

Reul, O. and Remmel, G. (2010) 'Foundation design for the extension of an existing high-rise building', *International conference on geotechnical challenges in megacities*. Moscow, Russia. pp. 446-453.

Rezania, M., dejaloud, H. and Mousavi Nezhad, M. (2014) 'SCLAY1S-BS : an anisotropic model for simulation of cyclic behaviour of clays', in Soga, K., Kumar, K., Biscontin, G. and Kuo, M. (eds.) *Geomechanics from micro to macro*. CRC Press, pp. 651-655.

Roesset, J.M. (1977) 'Soil amplification of earthquakes', *Numerical methods in geotechnical engineering*, pp. 639-682.

Roscoe, K.H., Basssett, R.H. and Cole, E.R. (1967) 'Principal axes observed during simple shear of a sand', *Proc. Geotech. Conf.* Oslo. pp. 231-237.

Roscoe, K.H. and Burland, J. (1968) *On the Generalized Stress-Strain Behavior of Wet Clays*.

Roscoe, K.H., Schofield, A.N. and Wroth, C.P. (1958) 'On The Yielding of Soils', *Géotechnique*, 8(1), pp. 22-53.

Ross, M. (2004) 'Modeling methods for silent boundaries in infinite media', *Fluid-Structure Interaction, Aerospace Engineering Sciences-University of Colorado at Boulder*, pp. 5519-006.

Rouainia, M., Elia, G., Panayides, S. and Scott, P. (2017) 'Nonlinear Finite-Element Prediction of the Performance of a Deep Excavation in Boston Blue Clay', *Journal of Geotechnical and Geoenvironmental Engineering*, 143(5), p. 04017005.

Rouainia, M. and Wood, D.M. (2000) 'A kinematic hardening constitutive model for natural clays with loss of structure', *Géotechnique*, 50, pp. 153-164.

Sahoo, S., Manna, B. and Sharma, K.G. (2014) 'Seismic Behaviour of Buried Pipelines: 3D Finite Element Approach', *Journal of Earthquakes*, 2014, pp. 1-9.

Saltis, S. (2018) 'Comparing Open Source Software vs Closed Source Software', *https://www.coredna.com/blogs/comparing-open-closed-source-software*.

Sangrey, D.A., Henkel, D.J. and Esrig, M.I. (1969) 'The Effective Stress Response of a Saturated Clay Soil to Repeated Loading', *Canadian Geotechnical Journal*, 6(3), pp. 241-252.

Schubert, W. and Beer, G. (2003) 'Tunnelling - the need for techological developmentl and innovation', in Beer, G. (ed.) *Numerical Simulation in Tunnelling*. Springer Vienna, pp. 7-11.

Shahrour, I., Khoshnoudian, F., Sadek, M. and Mroueh, H. (2010) 'Elastoplastic analysis of the seismic response of tunnels in soft soils', *Tunnelling and Underground Space Technology*, 25(4), pp. 478-482.

Shalabi, F.I. (2017) 'Interaction of Twin Circular Shallow Tunnels in Soils¡ªParametric Study', *Open Journal of Civil Engineering*, Vol.07No.01, p. 16.

Sitarenios, P., Belokas, G. and Kavvadas, M. (2013) 'The incorporation of new isotropic and kinematic hardening rules in an anisotropic constitutive model', *Comp. Geomech.—Proc. Of the 3rd Inter. Symp. On Comp. Geomech.(ComGeo III), Krakow, Poland*. pp. 21-23.

Sivasithamparam, N. (2012) *Development and implementation of advanced soft soil models in finite elements*. PhD thesis. University of Strathclyde.

Sivasithamparam, N., Kamrat-Pietraszewska, D. and Karstunen, M. (2010) 'An anistropic buble model for soft clays', *7th European Conference on Numerical methods in Geotechnical Engineering (NUMGE 2010)*. Trondheim, Norway. Balkema.

Sivasithamparam, N. and Karstunen, M. (2012) 'An anisotropic bubble model for structured clays', *4th International Workshop of Young Doctors in Geomechanics, W (H) YDOC 12*. pp. 43-47.

Sjodin, B. (2016) *What's The Difference Between FEM, FDM, and FVM?* Available at: https://www.machinedesign.com/fea-and-simulation/what-s-difference-between-fem-fdm-and-fvm.

Sliteen, I., Mroueh, H. and Sadek, M. (2011) 'Three-dimensional modeling of the behavior of shallow tunnel under seismic loading', *20ème Congrès Français de Mécanique, 28 août/2 sept. 2011-25044 Besançon, France (FR)*.

St John, C.M. and Zahrah, T.F. (1987) 'Aseismic design of underground structures', *Tunnelling and underground space technology*, 2(2), pp. 165-197.

Stallebrass, S.E. (1990) *Modelling the efects of recent stress history on the behaviour of overconsolidated soils*. PhD thesis. City University London.

Stallebrass, S.E. and Taylor, R.N. (1997) 'The development and evaluation of a constitutive model for the prediction of ground movements in overconsolidated clay', *Géotechnique*, 47(2), pp. 235-253.

Stamos, A.A. and Beskos, D.E. (1995) 'Dynamic analysis of large 3-D underground structures by the bem', *Earthquake engineering & structural dynamics*, 24(6), pp. 917-934.

Stamos, A.A. and Beskos, D.E. (1996) '3-D seismic response analysis of long lined tunnels in half-space', *Soil Dynamics and Earthquake Engineering*, 15(2), pp. 111-118.

Strokova, L.A. (2009) 'Numerical model of surface subsidence during subway tunneling', *Soil Mechanics and Foundation Engineering*, 46(3), pp. 117-119.

Stupazzini, M., Paolucci, R. and Igel, H. (2009) 'Near-Fault Earthquake Ground-Motion Simulation in the Grenoble Valley by a High-Performance Spectral Element Code', *Bulletin of the Seismological Society of America*, 99(1), pp. 286-301.

Suebsuk, J. (2010) *Development of the modified structured cam clay model and finite element implementation*. PhD thesis. Suranaree University of Technoloty, Thailand.

Surarak, C. (2011) *Geotechnical aspects of the Bangkok MRT blue line project*. PhD thesis. Griffith University.

Surarak, C., Likitlersuang, S., Wanatowski, D., Balasubramaniam, A., Oh, E. and Guan, H. (2012) 'Stiffness and strength parameters for hardening soil model of soft and stiff Bangkok clays', *Soils and Foundations*, 52(4), pp. 682-697.

Szerző, Á. and Batali, L. (2017) 'Numerical modelling of piled raft foundations: Modelling particularities and comparison with field measurements', *Proceedings of the 19th International Conference on Soil Mechanics and Geotechnical Engineering*. Seoul, South Korea.

Tamagnini, C., Mašin, D., Costanzo, D. and Viggiani, G. (2006) 'An Evaluation of Different Constitutive Models to Predict the Directional Response of a Reconstituted Fine-Grained Soil', Berlin, Heidelberg. Springer Berlin Heidelberg, pp. 143-157.

Terzaghi, K. (1941) 'Undisturbed clay samples and undisturbed clays', *Journal of the Boston Society of Civil Engineers*, 28(3), pp. 45-65.

Thomas, A., Jayalekshmi, B.R. and Shivashankar, R. (2013) 'Seismic Soil-Structure Interaction Studies on Tall Chimneys', *International Journal of Scientific & Engineering Research*, 4(5), pp. 188-191.

Torcato, D.M.M.F. (2010) *Seismic behaviour of shallow tunnels in stratified ground*. Master's thesis.

Trifunac, M.D. and Brady, A.G. (1975) 'A study on the duration of strong earthquake ground motion', *Bulletin of the Seismological Society of America*, 65(3), pp. 581-626.

Tsinidis, G., Pitilakis, K. and Anagnostopoulos, C. (2016) 'Circular tunnels in sand: dynamic response and efficiency of seismic analysis methods at extreme lining flexibilities', *Bulletin of Earthquake Engineering*, 14(10), pp. 2903-2929.

Tsinidis, G., Pitilakis, K., Heron, C. and Madabhushi, G. (2013) 'Experimental and numerical investigation of the seismic behavior of rectangular tunnels in soft soils', *ECCOMAS Thematic Conference-COMPDYN 2013: 4th International Conference on Computational Methods in Structural Dynamics and Earthquake Engineering, Proceedings-An IACM Special Interest Conference*. Kos, Greece, 12–14 June 2013. pp. 1152-1174.

Valls-Marquez, M. (2009) *Evaluating the capabilities of some constitutive models in reproducing the experimental behaviour of stiff clay subjected to tunnelling stress paths*. Ph.D. thesis. University of Birmingham [Online]. Available at: http://etheses.bham.ac.uk/502/.

Viggiani, G. and Atkinson, J.H. (1995) 'Stiffness of fine-grained soil at very small strains', *Géotechnique*, 45(2), pp. 249-265.

Vlachopoulos, N. and Diederichs, M.S. (2014) 'Appropriate Uses and Practical Limitations of 2D Numerical Analysis of Tunnels and Tunnel Support Response', *Geotechnical and Geological Engineering*, 32(2), pp. 469-488.

Vucetic, M. and Dobry, R. (1991) 'Effect of Soil Plasticity on Cyclic Response', *Journal of Geotechnical Engineering*, 117(1), pp. 89-107.

Wang, G., Lan, H. and Yu, G. (2013) 'A Numerical Study on Artificial Fill Embankment with Liquefiable Foundation Using FLAC', *IACGE 2013: Challenges and Recent Advances in Geotechnical and Seismic Research and Practices*.

Wang, J.N. (1993) *Seismic Design of Tunnels: A Simple State-of-the-art Design Approach*. Parsons Brinckerhoff.

Wang, R., Fu, P. and Zhang, J.-M. (2016) 'Finite element model for piles in liquefiable ground', *Computers and Geotechnics*, 72, pp. 1-14.

Wang, W.L., Wang, T.T., Su, J.J., Lin, C.H., Seng, C.R. and Huang, T.H. (2001) 'Assessment of damage in mountain tunnels due to the Taiwan Chi-Chi earthquake', *Tunnelling and underground space technology*, 16(3), pp. 133-150.

Watson, D., Lloyd, P., Villarreal, R. and Taylor, R. (2018) 'Shallow Cover SEM Tunneling for the Purple Line Project', *North American Tunneling 2018 Proceedings*. Washington D.C., USA. pp. 368-378.

Wheeler, S., Karstunen, M. and Näätänen, A. (1999) 'Anisotropic hardening model for normally consolidated soft clay', *Proc. 7th Int. Symp. on Numerical Models in Geomechanics (NUMOG VII)*. pp. 33-40.

Wheeler, S.J. (1997) 'A rotational hardening elasto-plastic model for clays', *Proceedings of the 14th International Conference on Soil Mechanics and Foundation Engineering*. Hamburg. A.A. Balkema, Rotterdam, pp. 431-434.

Wheeler, S.J., Cudny, M., Neher, H.P. and Wiltafsky, C. (2003a) 'Some developments in constitutive modelling of soft clays', *Proceedings of the International Workshop on Geotechnics of Soft Soils-Theory and Practice, Noordwijkerhoud, the Netherlands*. pp. 17-19.

Wheeler, S.J., Näätänen, A., Karstunen, M. and Lojander, M. (2003b) 'An anisotropic elastoplastic model for soft clays', *Canadian Geotechnical Journal*, 40(2), pp. 403-418.

Wiesmann, E. (1909) 'Ein Beitrag zur Frage der Gebirgs- und Gesteinsfestigkeit', *Schweizerische Bauzeitung*, 53/54(13), pp. 163-165.

Willford, M., Sturt, R., Huang, Y., Almufti, I. and Duan, X. (2010) 'Recent advances in nonlinear soil-structure interaction analysis using LS-DYNA', *Proceedings of the NEA-SSI Workshop*. pp. 6-8.

Wolf, J.P. (1989) 'Soil-structure-interaction analysis in time domain', *Nuclear Engineering and Design*, 111(3), pp. 381-393.

Woodward, P.K. and Griffiths, D.V. (1996) 'Influence of viscous damping in the dynamic analysis of an earth dam using simple constitutive models', *Computers and Geotechnics*, 19(3), pp. 245-263.

Wulandari, P.S. and Tjandra, D. (2015) 'Analysis of Piled Raft Foundation on Soft Soil Using PLAXIS 2D', *Procedia Engineering*, 125, pp. 363-367.

Xu, J., Costantino, C. and Hofmayer, C. (2006) 'Finite element models for computing seismic induced soil pressures on deeply embedded nuclear power plant structures', *ASME Pressure Vessels and Piping Division Conference* Vancouver, BC, Canada p. 11. Available at: http://www.pubs.bnl.gov/documents/32307.pdf.

Yamada, T., Ohbo, N., Itami, H., Ichimura, T. and Hori, M. (2008) 'Three-dimensional analysis method of seismic resistance of large tunnel structure using large-scale numerical computation of soil-tunnel system', *World Tunnel Congress 2008– Underground Facilities for Better Environment and Safety*. pp. 607-615.

Yang, D., Naesgaard, E., Byrne, P.M., Adalier, K. and Abdoun, T. (2004) 'Numerical model verification and calibration of George Massey Tunnel using centrifuge models', *Canadian geotechnical journal*, 41(5), pp. 921-942.

Yashiro, K., Kojima, Y. and Shimizu, M. (2007) 'Historical earthquake damage to tunnels in Japan and case studies of railway tunnels in the 2004 Niigataken-Chuetsu earthquake', *Quarterly Report of RTRI*, 48(3), pp. 136-141.

Yasuhara, K., Hirao, K. and Hyde, A.F. (1992) 'Effects of cyclic loading on undrained strength and compressibility of clay', *Soils and Foundations*, 32(1), pp. 100-116.

Yijun, L. (2003) 'Lecture Notes: Introduction to Finite Element Method'. CAE Research Laboratory, Mechanical Engineering Department, University of Cincinnati. Available at: http://urbana.mie.uc.edu/yliu/FEM-525/FEM-525.htm.

Young, D., Dean, A., Gingery, J.R., Gregor, T. and MacDonald, H.M. (2010) 'Development of Seismic Design Criteria for the Coronado Highway Tunnel', *North American Tunneling 2010 Proceedings*, pp. 365-372.

Yu, H.-S. (2008) 'Non-coaxial theories of plasticity for granular materials', *The 12th international conference of international association for computer methods and advances in geomechanics (IACMAG)*. Goa, India. Citeseer.

Yu, H.-T., Yuan, Y. and Bobet, A. (2013a) 'Multiscale method for long tunnels subjected to seismic loading', *International Journal for Numerical and Analytical Methods in Geomechanics*, 37(4), pp. 374-398.

Yu, H., Yuan, Y. and Bobet, A. (2017) 'Seismic analysis of long tunnels: A review of simplified and unified methods', *Underground Space*, 2(2), pp. 73-87.

Yu, H., Yuan, Y., Chen, Z. and Yu, G. (2009a) 'Numerical Simulation for Large-Scale Seismic Response Analysis of Long-Distance Water-Conveyance Shield Tunnel', *ICPTT 2009: : Advances and Experiences with Pipelines and Trenchless Technology for Water,*

Sewer, Gas, and Oil Applications pp. 1197-1211. Available at: https://ascelibrary.org/doi/abs/10.1061/41073%28361%29127.

Yu, H., Yuan, Y., Chen, Z., Yu, G. and Gu, Y. (2009b) 'Full 3D Numerical Simulation Method and Its Application to Seismic Response Analysis of Water-Conveyance Tunnel', in Yuan, Y., Cui, J. and Mang, H. (eds.) *Computational Structural Engineering*. Springer Netherlands, pp. 349-358.

Yu, H., Yuan, Y., Qiao, Z., Gu, Y., Yang, Z. and Li, X. (2013b) 'Seismic analysis of a long tunnel based on multi-scale method', *Engineering Structures*, 49(0), pp. 572-587.

Yue, Q. and Ang, A.H.S. (2017) '3D reliability evaluation of tunnels under strong-motion earthquakes considering spatial randomness', *Structure and Infrastructure Engineering*, 13(7), pp. 882-893.

Zhang, D.-m., Huang, H.-w., Hu, Q.-f. and Jiang, F. (2015) 'Influence of multi-layered soil formation on shield tunnel lining behavior', *Tunnelling and Underground Space Technology*, 47, pp. 123-135.

Zhang, L. and Liu, Y. (2018) 'Numerical investigations on the seismic response of a subway tunnel embedded in spatially random clays', *Underground Space*.

Zhao, J., Sheng, D., Rouainia, M. and Sloan, S.W. (2005) 'Explicit stress integration of complex soil models', *International Journal for Numerical and Analytical Methods in Geomechanics*, 29(12), pp. 1209-1229.

Zhou, Y., Wu, Y., Shangguan, Z. and Wang, Z. (2018) 'Effects of Spatially Varying Seismic Ground Motions and Incident Angles on Behavior of Long Tunnels', *Advances in Civil Engineering*, 2018, p. 6.

Zienkiewicz, O.C., Bicanic, N. and Shen, F.Q. (1989) 'Earthquake Input Definition and the Trasmitting Boundary Conditions', in Doltsinis, I.S. (ed.) *Advances in Computational Nonlinear Mechanics*. Vienna: Springer Vienna, pp. 109-138.

Zienkiewicz, O.C., Chan, A.H.C., Pastor, M., Schrefler, B.A. and Shiomi, T. (1999) 'Computational Geomechanics with special reference to Earthquake Engineering'.

Zlatanović, E., Broćeta, G. and Popović-Miletić, N. (2013) 'Numerical modelling in seismic analysis of tunnels regarding soil-structure interaction', *Facta universitatis-series: Architecture and Civil Engineering*, 11(3), pp. 251-267.

Appendices

Appendix A Shortlist of soil constitutive models

Behaviour / Soil / Constitutive Model	Soil Type	Cyclic Loading	Non-Linear	Undrained Condition	Pore Pressure Buildup	Material Anisotropy	Stiffness Degradation
Modified Hyperbolic Model (Matasovic) (MKZ)	Clay Sand	✓	✓	✓	✓	✗	✓
Hashash-Park Model (Modified Matasovic)	Clay Sand	✓	✓	✓	✓	✗	✓
MCC with Jardine small strain stiffness model and Rayleigh damping	Clay	✓	✓	✗	✗	✗	✓
Improved Iwan Model	Clay Sand	✓	✓	✓	✓	✗	✓
Structured Cam-Clay (SCC)	Clay	✓	✓	✓	✓	✓	✗
CASM-c Model (Modified CASM)	Clay (NC, OC) Sand	✓	✓	✓	✓	✗	✓
Hypoplastic Model (MCC + Matsuoka-Nakai) (Mašín)	Clay	✓	✓	✓	✓	✓	✓
MCC with Taborda Assumptions (Masing)	Clay	✓	✓	✓	✓	✗	✓

Behaviour / Soil Constitutive Model	Soil Type	Cyclic Loading	Non-Linear	Undrained Condition	Pore Pressure Buildup	Material Anisotropy	Stiffness Degradation
Hardening Model with small strain	Clay Sand	✓	✓	✓	✗	✗	✓
Anisotropic Hardening Model (Mroz)	Clay	✓	✓	✓	✓	✗	✓
Advanced Kinematic Hardening Model (Hashiguchi)	Clay	✓	✓	✓	✓	✗	✓
Iwan-Mroz Model	Clay	✓	✓	✓	✓	✗	✓
Bounding Surface Plasticity Model (Dafalias)	Clay	✓	✓	✓	✓	✓	✓
ECP (École Centrale de Paris) Model	Clay Sand	✓	✓	✓	✓	✗	✓
Borja et al Model (Extended Cam-clay)	Clay	✓	✓	✓	✓	✓	✓
Modified KHSM Model (Modified Rouainia & Muir-Wood Model)	Clay	✓	✓	✓	✓	✓	✓

Behaviour / Soil Constitutive Model	Soil Type	Cyclic Loading	Non-Linear	Undrained Condition	Pore Pressure Buildup	Material Anisotropy	Stiffness Degradation
M2-SKH	Clay	✓	✓	✓	✓	✓	✓
MIT-E3 Model	Clay (NC, MOC)	✓	✓	✓	✓	✓	✓
Nested Yield Surface (Prevost)	Clay Sand	✓	✓	✓	✓	✓	✓
SANICLAY-D-B	Clay	✓	✓	✓	✓	✓	✓
Rouainia & Muir-Wood Model (RMW)	Clay	✓	✓	✓	✓	✓	✓
MSS Model (Kavvadas & Amorosi)	Clay	✓	✓	✓	✓	✓	✓
S3-SKH, AI3- SKH Model (Modified 3-SKH)	Clay (NC, OC) Sand	✓	✓	✓	✓	✗(S3-SKH) ✓(AI3-SKH)	✓
S-CLAY 1 Advanced Models (S-CLAY 1S, BSCLAY 1S)	Clay	✓	✓	✓	✓	✓	✓

Behaviour / Soil Constitutive Model	Coupled Volumetric-Deviatoric Plastic Deformation	Path Dependent UnLoading-Reloading	State Dependency	Non-Linear Stiffness at Small Strain	Early Irreversibility	Non-coaxiality
Modified Hyperbolic Model (Matasovic) (MKZ)	✗	✓	✗	✓	✓	✗
Hashash-Park Model (Modified Matasovic)	✗	✓	✗	✓	✓	✗
MCC with Jardine small strain stiffness model and Rayleigh damping	✓	✓	✓	✓	✗	✗
Improved Iwan Model	✗	✓	✗	✓	✓	✗
Structured Cam-Clay (SCC)	✓	✓	✓	✗	✗	✗
CASM-c Model (Modified CASM)	✓	✓	✓	✓	✗	✗
Hypoplastic Model (MCC + Matsuoka-Nakai) (Mašín)	✓	✓	✓	✓	✗	✗
MCC with Taborda Assumptions (Masing)	✓	✓	✓	✓	✓	✗

Behaviour / Soil Constitutive Model	Coupled Volumetric-Deviatoric Plastic Deformation	Path Dependent UnLoading-Reloading	State Dependency	Non-Linear Stiffness at Small Strain	Early Irreversibility	Non-coaxiality
Hardening Model with small strain	✓	✓	✓	✓	✓	✗
Anisotropic Hardening Model (Mroz)	✓	✓	✓	✓	✓	✗
Advanced Kinematic Hardening Model (Hashiguchi)	✓	✓	✓	✓	✓	✗
Iwan-Mroz Model	✓	✓	✓	✓	✓	✗
Bounding Surface Plasticity Model (Dafalias)	✓	✓	✓	✓	✓	✗
ECP (École Centrale de Paris) Model	✓	✓	✓	✓	✓	✗
Borja et al Model (Extended Cam-clay)	✓	✓	✓	✓	✓	✗
Modified KHSM Model (Modified Rouainia & Muir-Wood Model)	✓	✓	✓	✓	✓	✗

Behaviour / Soil Constitutive Model	Coupled Volumetric-Deviatoric Plastic Deformation	Path Dependent UnLoading-Reloading	State Dependency	Non-Linear Stiffness at Small Strain	Early Irreversibility	Non-coaxiality
M2-SKH	✓	✓	✓	✓	✓	✗
MIT-E3 Model	✓	✓	✓	✓	✓	✗
Nested Yield Surface (Prevost)	✓	✓	✓	✓	✓	✗
SANICLAY-D-B	✓	✓	✓	✓	✓	✗
Rouainia & Muir-Wood Model (RMW)	✓	✓	✓	✓	✓	✗
MSS Model (Kavvadas & Amorosi)	✓	✓	✓	✓	✓	✗
S3-SKH, AI3- SKH Model (Modified 3-SKH)	✓	✓	✓	✓	✓	✗
S-CLAY 1 Advanced Models (S-CLAY 1S, BSCLAY 1S)	✓	✓	✓	✗	✓	✓

Behaviour / Soil Constitutive Model	Structure Degradation	Hysteretic Energy Dissipation	Strain Hardening/ Softening	Hardening Type	Shear Hardening	3D Effects
Modified Hyperbolic Model (Matasovic) (MKZ)	✗	✓	✗		✗	✗
Hashash-Park Model (Modified Matasovic)	✗	✓	✗		✗	✗
MCC with Jardine small strain stiffness model and Rayleigh damping	✗	✓	✓	Isotropic	✗	✓
Improved Iwan Model	✗	✓	✓	Isotropic	✗	✓
Structured Cam-Clay (SCC)	✓	✗	✓	Isotropic	✗	✓
CASM-c Model (Modified CASM)	✗	✓	✓	Isotropic	✗	✓
Hypoplastic Model (MCC + Matsuoka-Nakai) (Mašín)	✗	✓	✓	Isotropic	✗	✓
MCC with Taborda Assumptions (Masing)	✗	✓	✓	Isotropic	✗	✓

Behaviour / Soil Constitutive Model	Structure Degradation	Hysteretic Energy Dissipation	Strain Hardening/ Softening	Hardening Type	Shear Hardening	3D Effects
Hardening Model with small strain	✖	✓	✓	Isotropic	✓	✓
Anisotropic Hardening Model (Mroz)	✖	✓	✓	Isotropic Kinematic	✖	✓
Advanced Kinematic Hardening Model (Hashiguchi)	✖	✓	✓	Isotropic Kinematic	✖	✓
Iwan-Mroz Model	✖	✓	✓	Isotropic Kinematic	✖	✓
Bounding Surface Plasticity Model (Dafalias)	✖	✓	✓	Isotropic Kinematic	✖	✓
ECP (École Centrale de Paris) Model	✖	✓	✓	Isotropic Kinematic	✖	✓
Borja et al Model (Extended Cam-clay)	✖	✓	✓	Isotropic Kinematic	✖	✓
Modified KHSM Model (Modified Rouainia & Muir-Wood Model)	✓	✓	✓	Anisotropic (Elastic) Kinematic (Plastic)	✖	✓

Behaviour / Soil Constitutive Model	Structure Degradation	Hysteretic Energy Dissipation	Strain Hardening/ Softening	Hardening Type	Shear Hardening	3D Effects
M2-SKH	✗	✓	✓	Isotropic Kinematic	✗	✓
MIT-E3 Model	✗	✓	✓	Isotropic Rotational	✗	✓
Nested Yield Surface (Prevost)	✗	✓	✓	Isotropic Kinematic	✗	✓
SANICLAY-D-B	✓	✓	✓	Isotropic Hardening Rotational Hardening Isotropic Destucturation	✗	✓
Rouainia & Muir-Wood Model (RMW)	✓	✓	✓	Isotropic (Elastic) Kinematic (Plastic)	✗	✓
MSS Model (Kavvadas & Amorosi)	✓	✓	✓	Isotropic Kinematic	✗	✓
S3-SKH, AI3- SKH Model (Modified 3-SKH)	✓	✓	✓	Isotropic (Elastic) Kinematic (Plastic)	✗	✓
S-CLAY 1 Advanced Models (S-CLAY 1S, BSCLAY 1S)	✓	✓	✓	Isotropic Rotational Kinematic (BSCLAY 1S)	✗	✓

Behaviour / Soil Constitutive Model	Successfully Implemented in Software	Flow Rule	Parameters
Modified Hyperbolic Model (Matasovic) (MKZ)	Yes (D-MOD)		G_{mo}, τ_{mo}, β, s, δ_r, δ_G, a, b, c, d
Hashash-Park Model (Modified Matasovic)	Yes (DEEPSOIL)		G_{mo}, τ_{mo}, β, s, a, b
MCC with Jardine small strain stiffness model and Rayleigh damping	Yes (ICFEP)	Associated	G, K (κ), λ, M (ϕ'), N (ν) or Γ, α, γ, C, δ, η
Improved Iwan Model	Yes (FLAC 3D)		G_i*, τ_i*, δ, α, a, β, κ
Structured Cam-Clay (SCC)	Yes (AFENA, ABAQUS)	Non-Associated	M*, e^*_{IC}, λ*, κ*, ν*, b, c, γ, ω, $p'_{\gamma,I}$ or $f_{s,i}$, r_1
CASM-c Model (Modified CASM)	Yes (CRISP)	Non-Associated	G, K (κ), ν, λ, M, r, n, h, m, H_U, H_R, k
Hypoplastic Model (MCC + Matsuoka-Nakai) (Mašín)		Non-Associated	N, λ*, κ*, ϕ_c, r, m_R, m_T, R, β_r, χ
MCC with Taborda Assumptions (Masing)	Yes (ICFEP)	Associated	G, K (κ), λ, M (ϕ'), N (ν) or Γ, G_{max}, G_{min}, α_1, n

Behaviour / Soil Constitutive Model	Successfully Implemented in Software	Flow Rule	Parameters
Hardening Model with small strain	Yes (Zsoil, PLAXIS)	Associated (cap yield surface) Non-associated (shear hardening yield surface)	m, E^{ref}_{50}, E^{ref}_{oed}, E^{ref}_{ur}, ν_{ur}, c', ϕ', ψ, G^{ref}_{0}, $\gamma_{0.7}$
Anisotropic Hardening Model (Mroz)		Associated	a, n, m, G_s, K_s,
Advanced Kinematic Hardening Model (Hashiguchi)		Associated	
Iwan-Mroz Model	Yes (NERA)		
Bounding Surface Plasticity Model (Dafalias)		Associated	
ECP (École Centrale de Paris) Model	Yes (CODE_ASTER. GEFDYN)	Non-Associated	
Borja et al Model (Extended Cam-clay)	Yes (SPECTRA)	Associated (Deviatoric) Non-associated (Plasticity)	c, k, μ, α, λ, m
Modified KHSM Model (Modified Rouainia & Muir-Wood Model)		Associated	κ*, v, λ*, m, M, R, B, ψ, k, A, η_0, r_0

Behaviour / Soil Constitutive Model	Successfully Implemented in Software	Flow Rule	Parameters
M2-SKH	Yes (ICFEP)	Associated	G, K (κ), λ, M (ϕ'), N (ν) or Γ, G_{max}, R_b, α
MIT-E3 Model	YES (ABAQUS)	Non-Associated	e_0, K_{0NC}, K, G, ϕ'_{TC}, ϕ'_{TE}, λ, κ_0
Nested Yield Surface (Prevost)	YES (DYNA1D)	Associated	G, H', a, b, c, d, B, x_L, y_L, λ_L
SANICLAY-D-B		Non-Associated	κ, v, λ, M_c, M_e, N, h_0, a_d, C, x, k_i, e, p_0, α, S_i, d
Rouainia & Muir-Wood Model (RMW)	Yes (PLAXIS, FLAC, SWANDYNE)	Associated	κ*, v, λ*, m, M, R, B, ψ, k, A, η_0, r_0
MSS Model (Kavvadas & Amorosi)	Yes (SWANDYNE)	Associated	κ, G/K, λ, c, (ζ_v, η_v) and (ζ_q, η_q), (χ,ψ), γ
S3-SKH, AI3- SKH Model (Modified 3-SKH)	Yes (CRISP)	Associated (S3-SKH) Non-Associated (AI3-SKH)	κ*, N, λ*, M, G, T, S, ψ, s_0, s_f, k
S-CLAY 1 Advanced Models (S-CLAY 1S, BSCLAY 1S)	Yes (CRISP, PLAXIS)	Associated	κ, v', λ_i, λ, M, R, μ, β, ψ, a, b, α_0, x_0 (B-SCLAY 1S) κ, λ, M_c, M_e, x_0, μ, β, a, b, α_0, h_l, h_u, ψ_1, ψ_2, ψ_3 (S-CLAY 1S-BS)

Behaviour / Soil Constitutive Model	Remarks	Points (19 Maximum)
Modified Hyperbolic Model (Matasovic) (MKZ)	Use Masing's rule. The Masing rules underestimates damping at small strains and overestimates damping at large strains.	10
Hashash-Park Model (Modified Matasovic)	Use Masing's rule. The Masing rules underestimates damping at small strains and overestimates damping at large strains.	10
MCC with Jardine small strain stiffness model and Rayleigh damping		11
Improved Iwan Model	Based on theory of incremental plasticity. Use Masings rules. The predicted loops compare well at small and moderate strain amplitudes but not at higher strain.	12
Structured Cam-Clay (SCC)	Not enough reference for cyclic loading.	12
CASM-c Model (Modified CASM)	The ability to accurately predict the behaviour of heavily overconsolidated clay and sand remains a significant advantage of this new unified cyclic model.	13
Hypoplastic Model (MCC + Matsuoka-Nakai) (Mašín)	It allows for the calculation of total strains only. It thus makes no difference between elastic and plastic strains. It strictly excludes tensile stresses in soil.	13
MCC with Taborda Assumptions (Masing)	Use Masing's rule. The Masing rules underestimates damping at small strains and overestimates damping at large strains.	14

Behaviour / Soil Constitutive Model	Remarks	Points (19 Maximum)
Hardening Model with small strain	Although the model has not been designed specifically for dynamic applications, it does have capabilities to describe dynamic soil behaviour to some extent. It does not yet capture material damping at small strain levels (for which Rayleigh damping or viscous damping may be added), and it does not include the accumulationof strain (or pore pressure) with multiple load cycles.	14
Anisotropic Hardening Model (Mroz)		14
Advanced Kinematic Hardening Model (Hashiguchi)		14
Iwan-Mroz Model	Use Masing's rule. The Masing rules underestimates damping at small strains and overestimates damping at large strains.	15
Bounding Surface Plasticity Model (Dafalias)	A major deficiency of this concept is the requirement for the choice of a number of arbitrary functions (such as a mapping rule and a hardening rule) without obvious physical interpretation. On unloading-reloading or a sudden change in the loading path, the models are unrealistic.	15
ECP (École Centrale de Paris) Model		15
Borja et al Model (Extended Cam-clay)		16
Modified KHSM Model (Modified Rouainia & Muir-Wood Model)	Difficult to implement in the program.	16

Behaviour / Soil Constitutive Model	Remarks	Points (19 Maximum)
M2-SKH	The inability of the model to retain a memory of the previous stress history, once yielding is initiated, and hence predicting approximately the same relative stiffness response between compression and extension paths independently of the previous kinematic surface configuration.	16
MIT-E3 Model	Implementation in a computer program is complicated.	16
Nested Yield Surface (Prevost)	Use total stress formulation, therefore the effect of stress history (i.e. OCR) cannot be included in the analysis.	16
SANICLAY-D-B	Not implemented yet in computer program.	16
Rouainia & Muir-Wood Model (RMW)	The model does not have a specific empirical expression for the observed small-strain curves as the Jardine´s models. The model can not sustain tension.	17
MSS Model (Kavvadas & Amorosi)	Too many parameters to establish the model which are difficult to obtain from laboratory tests.	17
S3-SKH, AI3- SKH Model (Modified 3-SKH)	The model has not be used in any practical applications to geotechnical systems.	17
S-CLAY 1 Advanced Models (S-CLAY 1S, BSCLAY 1S)	It has not been used yet for tunnelling problems in particular. Due to the rotated yielding surface in the S-CLAY1 model, the pore water pressures during the undrained shearing stage were underestimated.	17

Appendix B Software selection table, criteria and summary

Sofware Selection – Selection Criteria

		5%	25%	5%	10%	10%	5%	30%	10%	100%
	Code	Availability	Functionality	Adaptability	Capability	Ease of Use	Technical Support	Total Cost	Added Value	Total
Open	SwanDyne 3D + GID	10	8	10	4	5	2	9	10	7.7
	OpenSees + GID	10	10	10	6	5	6	9	10	**8.6**
	Tochnog + GID	10	9	10	4	5	2	9	5	7.45
Close	FLAC 3D	5	10	5	10	10	10	0	10	6.5
	LS-Dyna	5	10	5	5	5	10	1	10	5.8
	PLAXIS 3D/ Dynamic	5	10	5	10	10	10	3	10	**7.4**
	MIDAS GTS NX	5	10	5	10	10	10	4	5	7.2

Code	Availability	Functionality	Adaptability	Capability	Ease of Use	Technical Support	Total Cost	Added Value	Total
SwanDyne 3D + GID	0.5	2	0.5	0.4	0.5	0.1	2.7	1	7.7
OpenSees + GID	0.5	2.5	0.5	0.6	0.5	0.3	2.7	1	**8.6**
Tochnog + GID	0.5	2.25	0.5	0.4	0.5	0.1	2.7	0.5	7.45
FLAC 3D	0.25	2.5	0.25	1	1	0.5	0	1	6.5
LS-Dyna	0.25	2.5	0.25	0.5	0.5	0.5	0.3	1	5.8
PLAXIS 3D/ Dynamic	0.25	2.5	0.25	1	1	0.5	0.9	1	**7.4**
MIDAS GTS NX	0.25	2.5	0.25	1	1	0.5	1.2	0.5	7.2

Criteria								
Scale	Availability	Functionality	Adaptability	Capability	Ease of Use	Technical Support	Total Cost	Added Value (i.e. Publications on Tunnel Dynamics)
10	Free Download	6.4/7 - 7/7	Open	3.7/4 - 4/4	Very Good	Available either free or with cost	£0 - £1000	With
9		5.8/7 - 6.4/7		3.4/4 to 3.7/4			£1000 - £2000	
8		5.2/7 - 5.8/7		3.1/4 to 3.4/4	Good	Available online	£2,000 - £3,000	
7		4.6/7 - 5.2/7		2.8/4 to 3.1/4			£3,000 - £4,000	
5	To be purchased/upgraded	3.4/7 - 4/7	Close with user defined option	2.2/4 - 2.5/4	Moderate	Available but limited	£5,000 - £6,000	Moderate
4		2.8/7 - 3.4/7		1.9/4 - 2.2/4			£6,000 - £7,000	
3		2.2/7 - 2.8/7		1.6/4 - 1.9/4			£7,000 - £8,000	
2		1.6/7 - 2.2/7		1.3/4 - 1.6/4	Difficult	Available but very limited	£8,000 - £9,000	
1		1/7 - 1.6/7		1/4 - 1.3/4			£9,000 - £10,000	
0	Not Available	0/7	Close	0/4	Very Difficult	Not Available	>£10,000	Without